

A SEARCH FOR DARK MATTER THROUGH INVISIBLE
DECAYS OF THE HIGGS BOSON WITH THE ATLAS
DETECTOR AT THE LHC

Joshua Milo Kunkle

A DISSERTATION

in

Physics and Astronomy

Presented to the Faculties of The University of Pennsylvania
in Partial Fulfillment of the Requirements for the Degree of Doctor of Philosophy
2013

Elliot Lipeles, Assistant Professor, Physics
Supervisor of Dissertation

Randall Kamien, Professor, Physics
Graduate Group Chairperson

Dissertation Committee

Joshua Klein, Professor, Physics
I. Joseph Kroll, Professor, Physics
Elliot Lipeles, Assistant Professor, Physics
Andrea Liu, Professor, Physics
Mark Trodden, Professor, Physics



A SEARCH FOR DARK MATTER THROUGH INVISIBLE DECAYS OF THE HIGGS
BOSON WITH THE ATLAS DETECTOR AT THE LHC

COPYRIGHT
2013
Joshua Milo Kunkle

Acknowledgements

My time as a graduate student at Penn was fun, educational, enriching, and inspiring. It was truly one of the best times of my life and I have so many people to thank for it.

My family was always extremely supportive despite the fact that lived over 4000 miles away for most of the time. I owe so much to my mother Lori and my late father Norman who encouraged me and supported me throughout life. I feel their love for me and I know I have their support in whatever endeavor I undertake. My longtime friend Ashley Enderlin was on my side during the entirety of my graduate career. She is my lifelong ally in the pursuit of happiness and I know we have many good times to come.

The faculty at Penn deserve much thanks. I found the department as a whole to be a very intelligent, unique, and congenial group. I would like to thank Joe Kroll, Mark Trodden, Josh Klien, and Andrea Liu for serving on my thesis committee. I owe special thanks to my advisor, Elliot Lipeles, who helped me to find my way through the complexities of physics analysis and be effective in a large collaboration. Elliot is never without an idea and I strive to attain the same level of knowledge and insight. I also owe many thanks to the other high energy faculty at Penn. I worked closely with Joe Kroll for some time and I found his input to be extremely helpful. I was also fortunate to have some good discussions with Evelyn Thomson when I sat in her office in my early years. Brig Williams is the fearless leader of the Penn army. I leaned from his physics insight and thoroughly enjoyed my interactions with him. I would also like to thank the staff at Penn. Jean O'boyle was always helpful in making anything happen, even on a short time scale. The electronics group at Penn provided a lot of support and I always learned something talking to them. I would like to thank Paul Keener who set up the tier three at Penn and spent the next few years answering our complaints about it. This system was essential in facilitating many of the results in this thesis. The post-docs at Penn were an essential component of the group. I benefited from their mentoring and I hope to apply the skills I learned from them in the future.

I would like to thank the MuLan group and in particular my undergraduate advisor, Dave

Hertzog. I was fortunate to be introduced to particle physics by such a great group of people working on a very interesting experiment. Although I've developed much more now, I still take lessons from my time with this group.

I would also like to thank the thousands of people who spent many years to develop, build, and maintain the LHC and the ATLAS detector. Thanks to the colleagues who I've worked with over the years on analysis projects. None of the results would have happened without people working together towards a common goal. This is possibly a once in a lifetime project and I'm glad to have been a small part of it.

The students I interacted with while at Penn and CERN made the experience extremely enjoyable. Liz Hines was my cooper pair from beginning to end. I spent over three years as Ryan Reece's flat mate. He strongly influenced my taste in music and I was thoroughly enriched by discussions with him in physics, philosophy, or whatever else came up. Ryan and I also had a lot of fun with Devin Harper who also inspired me to develop a particular method of background estimation that is highlighted throughout this thesis. And then there's the rest of the Penn army. If I were to write something about each one of you this acknowledgments page would be half the size of this thesis. So I won't. I'll just say that working with this group has been a truly amazing experience. I've never known such an intelligent, diverse, and fun-loving group of people. You all have enriched my life in so many ways. The only way I can do it justice is to take what I learned from all of you and pass it on to whoever I meet in the future. I wish you all the best!

Finally, I'd like to thank Nature. The fact that we live in a universe that has parameters such that galaxies, stars, and intelligent life can develop is amazing. Thanks for putting the mass of the Higgs boson in such an interesting place. So what's up with dark matter anyways?

ABSTRACT

A SEARCH FOR DARK MATTER THROUGH INVISIBLE DECAYS OF THE HIGGS
BOSON WITH THE ATLAS DETECTOR AT THE LHC

Joshua Milo Kunkle

Elliot Lipeles

Diboson physics provides insight into a wide variety of processes that are produced copiously at the LHC. Of particular interest are events where leptons and neutrinos are produced, strong signatures of electroweak physics. The study of electroweak physics is essential to understanding the Standard Model and in searches for phenomena outside the Standard Model. The most sensitive channels that contributed to the discovery of the Higgs boson searched for decays to dibosons. This thesis will present four analyses that utilize charged leptons and neutrinos whose presence are inferred from the missing transverse momentum.

Two measurements of Standard Model cross sections will be presented. The WW cross section is measured using 34 pb^{-1} of data collected in 2010 and is one of the earliest measurements of diboson processes at the LHC. The ZZ cross section is measured using 4.6 fb^{-1} of data collected in 2011. A search for the Higgs in the WW decay channel is presented also using 4.6 fb^{-1} of data collected in 2011. This analysis did not have the sensitivity to discover the Higgs boson, but when data were added in 2012 this channel contributed significantly to its discovery.

Finally a search for anomalous invisible decays of the Higgs boson using 4.6 fb^{-1} of data taken in 2011 and 13.1 fb^{-1} of data taken in 2012 will be presented. This search is sensitive to new physics that couples to the Higgs boson that would result in an increased rate of decays to invisible particles. One possible scenario is that dark matter couples to the Higgs boson. If the mass of the dark matter particle is less than half of the mass of the Higgs boson decays to dark matter increase its invisible branching fraction. Dark matter is a significant contribution to the makeup of the universe, but

very little is known about it. This search provides additional limits on how dark matter can couple to the Standard Model. No excess of events is observed in this search and limits are placed on the allowed invisible branching fraction. These limits are interpreted in the context of simple Higgs portal models to place constraints on the allowed dark matter mass and interaction cross section. The results are compared with current limits on dark matter and place significant restrictions on the allowed dark matter mass and cross section within these models.

Contents

Acknowledgements	iii
Abstract	vi
Contents	vii
List of Tables	xii
List of Figures	xiii
1 Introduction	1
2 Observations and theoretical motivations	3
3 The Standard Model of particle physics	7
3.1 The Higgs boson at the LHC	8
3.2 Open questions	11
3.3 The structure of the proton	13
3.4 Particle interactions with matter	14
3.4.1 Ionization by charged particles	15
3.4.2 Bremsstrahlung	15
3.4.3 Transition radiation	16
3.4.4 Photon interactions	16
3.4.5 Strong force interactions	19
4 Dark matter	20
4.1 The WIMP hypothesis	21
4.2 Observational evidence for dark matter	21

4.3	Searches for dark matter	23
4.3.1	Scattering experiments	23
4.3.2	Cosmic searches	25
4.3.3	Collider searches – LHC	26
4.4	The Higgs and dark matter – Higgs portal models	26
5	The LHC	29
5.1	Beam parameters	30
5.2	The CERN accelerator complex	32
5.3	Luminosity determination	34
5.4	Pileup interactions	34
5.5	Standard LHC operation	35
5.6	The scale of physics at the LHC	36
6	The ATLAS experiment	38
6.1	The inner detector	40
6.1.1	The pixel detector	40
6.1.2	The semiconductor tracker	41
6.1.3	The transition radiation tracker	42
6.1.3.1	TRT monitoring	42
6.2	Calorimeters	43
6.2.1	Liquid argon calorimeters	44
6.2.2	The tile calorimeter	45
6.3	Muon spectrometer	46
6.4	Trigger	47
6.5	Data taking conditions	47
6.6	Monte Carlo simulation	48
6.7	Coordinate system	49
7	Common object selection	50
7.1	Tracks	51
7.2	Calorimeter clusters	51
7.3	Electrons	51
7.4	Muons	53
7.5	Jets	53
7.6	Primary vertex	54

7.7	Missing transverse momentum	55
7.7.1	E_T^{miss} derived quantities	56
7.7.2	Track based E_T^{miss}	56
7.7.3	E_T^{miss} performance	58
7.7.3.1	True E_T^{miss} scale	58
7.7.3.2	Sources of fake E_T^{miss}	58
7.7.3.3	Fake E_T^{miss} modeling in simulation	60
7.7.3.4	Simulation of pileup multiplicity	60
7.7.3.5	Modeling min-bias events	61
8	Standard Model measurements	65
8.1	$W^+W^- \rightarrow \ell^- \nu_\ell \ell^+ \bar{\nu}_\ell$ cross section measurement	67
8.1.1	Analysis overview	68
8.1.2	Data and simulation samples	69
8.1.3	Object reconstruction	69
8.1.3.1	Electrons	70
8.1.3.2	Muons	70
8.1.3.3	Jets	70
8.1.3.4	Missing transverse momentum	70
8.1.4	Event selection	70
8.1.5	Signal acceptance	73
8.1.6	Background estimation	74
8.1.6.1	Z/γ^* background estimate	74
8.1.6.2	Top background estimate	77
8.1.6.3	W + jets background estimate	78
8.1.6.4	Diboson background estimate	79
8.1.7	Results	79
8.1.8	Summary	80
8.2	$ZZ \rightarrow \ell^+ \ell^- \nu_\ell \bar{\nu}_\ell$ cross section measurement	80
8.2.1	Analysis overview	82
8.2.2	Data and simulation samples	83
8.2.3	Object selection	85
8.2.3.1	Electrons	85
8.2.3.2	Muons	85
8.2.3.3	Jets	86

8.2.3.4	Missing transverse momentum	86
8.2.4	Event selection	86
8.2.5	Background estimation	87
8.2.5.1	Combined $WW + \text{top} + Z \rightarrow \tau\tau$ estimate	90
8.2.5.2	Z/γ^* background estimate	90
8.2.5.3	$W + \text{jet}$ background estimate	91
8.2.6	Cross section and fiducial volume definition	92
8.2.7	Signal acceptance	93
8.2.8	Results	94
8.2.9	Differential cross sections and limits on anomalous triple gauge couplings	94
8.2.10	Summary	95
9	Search for the Higgs boson in the $W^+W^- \rightarrow \ell^+\nu\ell^-\bar{\nu}$ channel	97
9.1	Observation of the Higgs boson	98
9.2	$H \rightarrow W^+W^{(*)-} \rightarrow \ell^+\nu\ell^-\bar{\nu}$ search	98
9.2.1	Analysis overview	100
9.2.2	$H \rightarrow WW$ signal	100
9.2.3	Object and event selection	101
9.2.4	E_T^{miss} studies	104
9.2.5	Background estimates	105
9.2.6	Results	106
9.2.7	Summary	107
10	Search for invisible decays of the Higgs boson	108
10.1	Standard Model expectation	109
10.2	Analysis overview	110
10.3	Data and simulation samples	111
10.4	Object selection	112
10.5	Event selection	113
10.6	Background estimation	115
10.6.1	ZZ and WZ backgrounds	115
10.6.2	Combined $WW + \text{top} + Z \rightarrow \tau\tau$ estimate	116
10.6.3	Z/γ^* background estimate using ABCD method	116
10.6.4	Z/γ^* background estimate using single photon method	117
10.6.5	Inclusive W background estimate	117

10.7 Results	117
10.8 Dark matter interpretation of branching ratio limits	118
11 Z/γ^* background estimate using single photons	123
11.1 Motivation	124
11.2 Compatibility between single photon and Z/γ^* events	124
11.3 Basic single photon method	126
11.3.1 Modeling possibilities	126
11.3.2 Sample compatibility and normalization	127
11.3.3 p_T^γ weighting	127
11.3.4 Additional weights	129
11.3.5 Weighting by the average number of pileup interactions	130
11.3.6 Photon identification	131
11.3.7 Photon selection	132
11.3.8 Single photon kinematic distributions	133
11.3.9 Single lepton and dilepton control regions	135
11.3.10 Background subtraction	138
11.3.11 Photon vertexing – converted photons	139
11.3.11.1 Trident suppression	140
11.3.12 Data driven dijet prediction and normalization of single photon simulation	141
11.3.13 Improved estimate of $W \rightarrow e\nu_e$ background	145
11.3.14 Application – $ZZ \rightarrow \ell^+\ell^-\nu\bar{\nu}$	147
11.3.15 Application – ZH, H \rightarrow invisible	153
11.4 Extended single photon method	154
11.4.1 Application – $H \rightarrow WW$	159
12 Conclusions	165
Bibliography	168

List of Tables

3.1	The known particle content of the Standard Model and their assigned quantum numbers and mass.	9
8.1	Final state decay modes in WW events.	67
8.2	Relevant quantities used in Equation 8.1 to estimate the systematic uncertainty on the Z/γ^* background.	76
8.3	Predicted Z/γ^* contribution in the signal region from three Monte Carlo generators in each analysis channel.	77
8.4	Top background estimates from the simulation and two independent data driven methods.	78
8.5	Estimated $W + \text{jets}$ background in the WW signal region.	79
8.6	The number of observed events, the expected number of events, and the contribution from each background for the ee , $\mu\mu$, and $e\mu$ channels.	80
8.7	Final state decay modes of ZZ events.	82
8.8	Reconstruction efficiencies for the ZZ signal.	93
8.9	The number of observed events, the expected number of events, and the contribution from each background for the ee and $\mu\mu$ channels.	94
8.10	Measured ZZ cross sections with uncertainties.	94
9.1	The predicted number of signal events for the signal having $m_H = 125$ GeV as well as the estimated background contributions with the observed number of events in the zero jet signal region.	106
10.1	Expected background, expected signal, and observed number of events for the 2011 and 2012 data periods.	118
10.2	Values for variables used in Equations 4.1 through 4.6.	120
11.1	Single photon triggers and their average prescales for the 2011 and 2012 data samples.	133
11.2	Data-driven Z background estimates using the single photon method.	153

List of Figures

3.1	Self consistency test of the Higgs sector of the Standard Model from the electroweak fit produced by the Gfitter collaboration.	11
3.2	Feynman diagrams for the primary Higgs production mechanisms.	12
3.3	Higgs production cross section and branching fractions as a function of the Higgs mass.	12
3.4	Parton distribution functions derived for $Q^2 = 10\text{GeV}^2$ and $Q^2 = 10^4\text{GeV}^2$	14
3.5	Fractional energy loss of an electron in matter for energies between 1 MeV and 1 GeV.	16
3.6	The interaction cross section of photons in matter for energies between 1 eV and 100 GeV.	18
4.1	The evolution of the dark matter density in the early universe.	22
4.2	The rotation curve for galaxy NGC 3198.	23
4.3	The CMB anisotropy power spectrum for various values of Ω_b	24
4.4	Limits on the dark matter scattering cross section from direct detection experiments.	25
4.5	The measured positron spectra from the AMS-02, PAMELA, and Fermi-LAT experiments.	26
4.6	Feynman diagrams for the decay of the Higgs boson into dark matter particles, scattering of dark matter particles off of a nucleon with the exchange of a Higgs boson, and the annihilation of dark matter into standard model particles.	28
5.1	Cross sectional diagram of an LHC dipole.	31
5.2	Diagram of the CERN accelerator complex.	33
5.3	Integrated luminosity versus time in year for the three years of data taking. The integrated luminosity in 2010 was quite small relative to the following years and is only visible at the bottom of the plot.	34
5.4	The distribution of the number of pileup interactions for 2011 and 2012 data taking.	35
5.5	A representative 24 hour period of LHC running.	36
5.6	Production cross sections for a number of processes near LHC energies.	37
6.1	Diagram of the ATLAS detector systems.	39
6.2	Diagram of the ATLAS inner detector systems.	40
6.3	Discriminator thresholds at which the noise rate is 300 kHz for 1/32 of one half of the TRT barrel and the noise rate averaged over parts of the detector and offset to a common value as a function of the instantaneous luminosity.	43
6.4	Diagram of the ATLAS inner detector systems.	44
6.5	Diagram of the accordion structure of the LAr calorimeter showing the sensor granularity.	45

7.1	Probability to reconstruct the incorrect primary vertex as a function of the number of pileup vertices.	55
7.2	Diagram of the Axial E_T^{miss} calculation.	57
7.3	The linearity of the reconstructed E_T^{miss} with respect to the true E_T^{miss}	58
7.4	The width of the x and y components of E_T^{miss} as a function of the $\sum E_T$ in data and simulation.	60
7.5	The correlation between the number of reconstructed vertices and $\langle \mu \rangle$	61
7.6	Comparisons of track properties in min-bias collisions between data and simulations having different min-bias tunes.	62
7.7	The E_T^{miss} distribution in $Z \rightarrow \ell\ell$ events using 3.5 fb^{-1} of 2011 data.	63
7.8	Comparisons of track related variables in $Z \rightarrow \ell\ell$ events between data and simulation with no $\langle \mu \rangle$ correction.	64
7.9	Comparisons of track related variables in $Z \rightarrow \ell\ell$ events between data and simulation with $\langle \mu \rangle$ scaled by 0.83.	64
8.1	Summary of Standard Model cross section measurements at ATLAS.	66
8.2	Feynman diagrams for the production of WW events and their decay to lepton pairs.	68
8.3	Dilepton mass distributions for the ee , $\mu\mu$, and $e\mu$ channels.	71
8.4	$E_T^{\text{miss,rel}}$ distributions for the ee , $\mu\mu$, and $e\mu$ channels after the veto on the Z mass in the ee and $\mu\mu$ channels.	72
8.5	Jet multiplicity distribution for the three channels combined after the Z mass veto and the $E_T^{\text{miss,rel}}$ cut.	72
8.6	$E_T^{\text{miss,rel}}$ distributions for the ee , $\mu\mu$, and $e\mu$ channels after all cuts except $E_T^{\text{miss,rel}}$	73
8.7	$E_T^{\text{miss,rel}}$ distribution for data and simulation for events selected within the Z control region for the ee and $\mu\mu$ channels.	75
8.8	Comparison of the $E_T^{\text{miss,rel}}$ distributions between ee , $\mu\mu$, and $e\mu$ channels	76
8.9	Production and decay of Z boson pairs decaying to the $\ell^+\ell^-\nu\bar{\nu}$ final state. The TGC vertex is not allowed in the Standard Model	81
8.10	Truth level comparison of the ZZ signal simulated with MC@NLO, SHERPA, and POWHEGBOX.	84
8.11	Invariant mass distributions after the baseline dilepton selection in the ee and $\mu\mu$ channels.	87
8.12	Axial E_T^{miss} distributions after the $M_{\ell\ell}$ cut in the ee and $\mu\mu$ channels.	87
8.13	Jet multiplicity distributions after the $M_{\ell\ell}$ and Axial E_T^{miss} cuts in the ee and $\mu\mu$ channels.	88
8.14	Axial E_T^{miss} distributions after all cuts except for Axial E_T^{miss} in the ee and $\mu\mu$ channels.	88
8.15	Jet multiplicity distributions after all cuts except for the jet veto in the ee and $\mu\mu$ channels.	89
8.16	Dilepton mass distributions after all cuts in the ee and $\mu\mu$ channels.	89
8.17	Differential cross section measurements unfolded to the generator level.	95
8.18	$p_T^{\ell\ell}$ distribution with predictions from various anomalous TGC predictions.	96
8.19	Combined anomalous TGC limits compared to limits from LEP and the Tevatron. This measurement significantly improves on previous limits.	96
9.1	Final signal selection plots for the $H \rightarrow \gamma\gamma$, $H \rightarrow ZZ^{(*)} \rightarrow \ell^+\ell^-\ell^+\ell^-$, and $H \rightarrow W^+W^{(*)-} \rightarrow \ell^+\nu\ell^-\bar{\nu}$ channels.	99
9.2	The observed and expected local probability for all channels contributing to the Higgs boson discovery.	99
9.3	Feynman diagram for the production of a Higgs boson via gluon fusion and decay to WW in the fully leptonic final state.	101

9.4	Dilepton mass distributions in the ee , $\mu\mu$, and $e\mu$ channels after the baseline lepton selection.	103
9.5	$E_T^{\text{miss,rel}}$ distributions in the ee , $\mu\mu$, and $e\mu$ channels after the baseline lepton selection.	103
9.6	Jet multiplicity for the three channels combined after the $E_T^{\text{miss,rel}}$ and $M_{\ell\ell}$ cuts are applied.	103
9.7	Transverse mass distribution for the three channels combined after all signal cuts are applied.	104
9.8	Expected and observed 95% confidence level limits on the allowed range of Higgs masses.	106
10.1	Feynman diagram for the associated production of a Higgs boson with a Z boson.	110
10.2	Feynman diagrams representing invisible decays of the Higgs boson.	110
10.3	E_T^{miss} distributions for the ee and $\mu\mu$ channels after the $M_{\ell\ell}$ cut is applied.	114
10.4	$\Delta\phi(E_T^{\text{miss}}, E_T^{\text{miss,track}})$ distributions for the ee and $\mu\mu$ channels after the $M_{\ell\ell}$ cut is applied.	114
10.5	Fractional p_T difference distributions for the ee and $\mu\mu$ channels after the $M_{\ell\ell}$ cut is applied.	115
10.6	Jet multiplicity distributions for the ee and $\mu\mu$ channels after the $M_{\ell\ell}$ cut is applied.	115
10.7	Final E_T^{miss} distributions for the 2011 and 2012 data taking periods.	119
10.8	The 95% CL limit on the production cross section times branching ratio for Higgs mass hypotheses between 115 GeV and 300 GeV.	119
10.9	$1 - CL$ for the invisible branching ratio for a Standard Model Higgs boson having $m_H = 125$ GeV.	120
10.10	Limits on $\lambda_{h\chi\chi}$ vs m_χ for scalar, vector, and majorana fermion dark matter in the Higgs portal model.	121
10.11	Limits on $\sigma_{\chi N}$ vs m_h . Limits calculated from the invisible branching ratio limits presented in this note are shown for the scalar, vector, and majorana fermion cases.	121
11.1	Feynman diagrams for the tree level production of Z/γ^* and single photons.	125
11.2	An example of p_T^γ weights derived for the single photon method.	129
11.3	Distributions of the average number of pileup interactions for single photon triggers in the 2011 and 2012 data taking periods.	130
11.4	Photon reconstruction efficiency with respect to true photons for the loose and tight working points.	131
11.5	Photon trigger efficiency turn-on curves.	133
11.6	Photon trigger weighting scheme in the 2012 data sample.	134
11.7	Photon trigger weighting scheme in the 2011 data sample.	135
11.8	Distributions of E_T^{miss} , p_T^γ , track E_T^{miss} , $\Delta\phi(\gamma, E_T^{\text{miss}})$, and jet multiplicity for events having exactly one tight, isolated, unconverted photon and no identified leptons. The calorimeter isolation distribution is shown with the photon isolation cut applied.	136
11.9	Distributions of E_T^{miss} , p_T^γ , track E_T^{miss} , and $\Delta\phi(\gamma, E_T^{\text{miss}})$, for events having exactly one tight, isolated, unconverted photon, no reconstructed jets, and no identified leptons.	137
11.10	Single photon plus lepton control regions.	138
11.11	The difference between the z positions of the primary vertex and the extrapolated photon origin using the calorimeter cluster.	140
11.12	E_T^{miss} distributions in events having a 2 track converted photon before suppression of trident fakes from electrons and after.	141
11.13	Variables used to reject electrons faking 2 track converted photons.	142
11.14	A diagrammatic explanation of the dijet background estimate and single photon normalization procedure.	143

11.15	Calorimeter isolation distribution of photon candidates that pass the tight identification criteria.	144
11.16	Comparison of the weights derived in the three schemes used to estimate the dijet background and the $\gamma + \text{jet}$ process.	144
11.17	Comparison of the isolation distribution for the three dijet estimation schemes and of the E_T^{miss} for the three schemes after the isolation cut is applied.	145
11.18	Calorimeter isolation distributions of photon candidates where all tight cuts except three variables derived from layer 1 quantities that are largely uncorrelated with isolation.	146
11.19	Fake factors for an electron that passes the medium++ identification criteria to fake a photon that passes the tight identification criteria.	147
11.20	Axial E_T^{miss} distributions in the ee and $\mu\mu$ channel for the $ZZ \rightarrow \ell^+ \ell^- \nu \bar{\nu}$ analysis.	149
11.21	Comparison of the $\Delta\phi(Z, E_T^{\text{miss}})$ distributions between the data and the single photon model in the ee and $\mu\mu$ channels.	149
11.22	Axial E_T^{miss} distributions for each of three bins in $p_T^{\ell\ell}$	150
11.23	Axial E_T^{miss} distributions for each of three bins in m_T	151
11.24	Axial E_T^{miss} distributions for each of three bins in $\Delta\phi(\ell, \ell)$	152
11.25	Distributions of $\Delta\phi(Z, E_T^{\text{miss}})$ and $\Delta\phi(E_T^{\text{miss}}, E_T^{\text{miss,track}})$ for the ee and $\mu\mu$ channels with no $\Delta\phi(Z, E_T^{\text{miss}})$ correction.	155
11.26	Distributions of $\Delta\phi(Z, E_T^{\text{miss}})$ and $\Delta\phi(E_T^{\text{miss}}, E_T^{\text{miss,track}})$ for the ee and $\mu\mu$ channels with the $\Delta\phi(Z, E_T^{\text{miss}})$ correction.	156
11.27	Distributions of E_T^{miss} for the ee and $\mu\mu$ channels and fractional p_T difference for the ee and $\mu\mu$ channels.	157
11.28	Schematic of the merging procedure for a single dilepton event.	158
11.29	E_T^{miss} distributions in the ee and $\mu\mu$ channels.	160
11.30	$E_T^{\text{miss,rel}}$ distributions in the ee and $\mu\mu$ channels.	161
11.31	$fRecoil$ distributions in the ee and $\mu\mu$ channels.	161
11.32	Track E_T^{miss} distributions in the ee and $\mu\mu$ channels.	162
11.33	m_T distributions in the ee and $\mu\mu$ channels.	162
11.34	The predicted $Z + \text{jet}$ m_T distribution using the extended single photon method in the ee and $\mu\mu$ channels.	163
11.35	Determination of the statistical uncertainty of the $Z + \text{jets}$ prediction using the bootstrapping method.	164

CHAPTER 1

Introduction

Dark matter is one of the most compelling signatures for the existence of physics beyond the Standard Model. Its presence in the universe has been unambiguously established by observing its gravitational influence. The measured density of dark matter is larger than the density of ordinary matter by a factor of five. Despite its abundance, little information is known about dark matter at the particle level. A promising model for dark matter is that it is massive and that it experiences weak interactions. The LHC is currently exploring the electroweak scale so LHC experiments may be able to detect dark matter. A search for dark matter produced in invisible decays of the Higgs boson is presented in this dissertation. The analysis places limit on the invisible branching fraction of the newly discovered Higgs boson. The limit is interpreted within simple Higgs portal models where the dark matter particle only couples to Standard Model particles through the Higgs boson. Through the Higgs portal model limits are placed on the allowed coupling between dark matter and the Higgs. The limits are also interpreted as a limit on the dark matter scattering cross section and the results are compared to results from dark matter direct detection experiments.

This dissertation also presents measurements of two Standard Model cross sections and a search for the Higgs boson. Standard Model measurements are important to establish an understanding of the detector and the reconstruction of physics objects. Understanding the Standard Model is essential to searches for new physics to which Standard Model backgrounds are often backgrounds. The discovery of the Higgs boson was a major goal of the LHC program. This goal was realized with the announcement of its discovery in 2012. A summary of the discovery of the Higgs is given and a search in the WW decay channel is described.

All of the measurements presented utilize final states that have two leptons and large missing transverse momentum (E_T^{miss}) from escaping neutrinos. A common issue with each measurement presented is the rejection of backgrounds that have no escaping neutrinos, but can have large E_T^{miss} from fake sources. In the dilepton plus E_T^{miss} final state the Z/γ^* process is the main fake E_T^{miss}

background. My work focused on the rejection of this background and methods to estimate the contamination of this background in the signal region. I developed method that uses single photon events to model the E_T^{miss} distribution in Z/γ^* events.

This thesis is organized as follows. Chapter 2 discusses the experimental inputs and the theoretical progression that produced the current theory of the Standard Model. Chapter 3 outlines the basic theoretical structure of the Standard Model. Special attention is given to the physics of the proton, which is important to understanding collisions at the LHC, and the physics of particle interactions with matter, which underly the detector technologies used. Chapter 5 describes the LHC and outlines the basic functionality of the accelerator. Chapter 6 presents the ATLAS detector. The reconstruction of particles in ATLAS is outlined in Chapter 7. Special attention is given to the E_T^{miss} , an essential component of all the measurements presented in this thesis. Chapter 8 presents measurements of the WW and ZZ cross sections. Chapter 9 briefly discusses the discovery of the Higgs boson and presents a search for the Higgs boson in the WW decay channel. Chapter 10 presents a search for invisible decays of the Higgs boson and places limits on dark matter couplings to the Higgs boson. A method to model the fake E_T^{miss} distribution in Z/γ^* events using single photon events is presented in Chapter 11. Finally Chapter 12 gives concluding remarks.

CHAPTER 2

Observations and theoretical motivations

The Standard Model is an extremely successful theory that codifies our understanding of three of the four known forces of nature. The Standard Model is an observationally motivated theory. It has been constructed over the last 200 years by advancing theory to incorporate a growing body of experimental evidence. The theory as it exists today describes nearly all of the available experimental data¹ and has been tested to extreme accuracy. For example the prediction of the magnetic moment of the electron agrees with experiment to one part per trillion. A brief discussion of the observational inputs and the impact of those observations on the theory is instructive. The following discussion is not strictly historical and only a sampling of the relevant results will be covered.

The development of the Standard Model is interwoven with related discoveries that were essential in defining the underlying structure of the theory. Einstein first proposed a new structure of space time in his 1905 paper on Special Relativity. Einstein realized that the speed of light is a constant while space and time are not. Theories must be constructed so that they are invariant under Lorentz transformations that respect this structure of space-time. In addition the underlying physics of the Standard Model is that of quantum mechanics. Our understanding of the laws obeyed by particles at the smallest scale feeds into the field theories that comprise the Standard Model. These two discoveries occurred while the elements of the Standard Model were being collected and were essential to building a consistent theory.

The first force, besides gravity, that humans studied in detail was the electromagnetic force. Through the 1800's electric and magnetic phenomena were studied as separate subjects. Hans Ørsted first discovered that electric currents create magnetic fields in 1820. The realization that the electric and magnetic forces were in fact two expressions of the same force can be considered the first unification of forces. The theoretical unification of the electric and magnetic forces was completed in the theory of electromagnetism formulated by Maxwell in 1873. It was known at this time that light was very closely related to electromagnetic phenomena, but a complete theory of light and its interaction with matter particles did not exist until the development of quantum electrodynamics (QED) in 1940 by Feynman.

The need for the strong force was clear upon the discovery of the neutron by Chadwick in 1932. With the discovery of the neutron, the current model of the nucleus – that it is composed of a bound state of protons and neutrons – was realized. However, the electromagnetic force alone can not describe how positively charged protons and neutral neutrons are tightly bound into the nucleus and a new strong force is needed. Further insight into the nature of the strong force was obtained by studying the structure of nucleons in deep inelastic scattering of electrons off of protons. As the

¹Some measurements of Standard Model quantities are expected to disagree because of statistical fluctuations. However experimental data also exist that do not fit within the Standard Model. Some of these cases will be described in Section 3.2.

momentum of the probing electron is increased the kinematics of the scattered particles indicate that the scatter is off of a bound state of point-like particles rather than a single particle with a finite radius. The nucleon is therefore composed of more fundamental particles that were later identified as quarks. More evidence for the existence of quarks was provided by the host of new particles that were discovered by collision experiments in the 1950's. The newly discovered particles were organized by their quantum numbers of isospin and strangeness. The classification of the new particles motivated Gell-Mann and Zweig to develop the quark model in 1964 which described how quarks combine to create the newly observed particles. The full quark model was realized with the discovery of the charm, bottom, and top quarks (although the existence of the top quark was not established experimentally until 1995, after the establishment of the quark model). The quarks must be held together by a force carrier, the gluon, which was identified in three jet events at the PETRA accelerator. In 1970 the complete description of the strong force, quantum chromodynamics (QCD), was developed by Polizer, Wilczek, and Gross.

The presence of a weak force was first indicated by the observation of radioactive decays. The neutron is unique among many of the early hadronic particles that were discovered because of its long decay lifetime. Particles that decay through the strong force have very short lifetimes, on the order of 10^{-23} seconds, while the neutron has a lifetime of approximately 920 seconds. This large difference indicates the presence of a new force that is much weaker than the strong force. Another input to the theory was the existence of neutrinos posited by Pauli in 1930. In studies of beta decay it was apparent that some of the energy in the decay was missing. The missing energy was attributed to the momentum carried by an invisible particle, the neutrino. This is very similar to how the presence of neutrinos are inferred from measuring the missing transverse momentum in particle collisions. These observations were successfully merged into an effective four-fermion theory of weak interactions by Fermi in 1933. Fermi's theory was not renormalizable, but it could describe the known weak processes. In the current theory of electroweak interactions a W boson is exchanged, but the energies available at the time were well below the mass of the W boson where Fermi's theory is applicable. Fermi's theory was superseded by a theory of electroweak interactions formulated by Glashow, Weinberg, and Salam in the 1960s. The theory successfully explained the weak charged current interaction and also predicted a weak neutral current interaction. The weak neutral current interaction was discovered shortly after by the Gargamelle experiment in 1973, confirming the theory of electroweak interactions. The theory predicted the existence of two charged W bosons and a neutral Z boson. Both the W and Z particles were discovered at CERN's SPS accelerator in 1983. The theory had one remaining problem – the W and Z bosons must be massless in the theory. A solution proposed by Higgs, Englert, and Brout was to produce the masses via

spontaneous symmetry breaking. A new scalar field is added to the theory which attains a non-zero vacuum expectation value. In this process the W and Z bosons attain a mass while the photon remains massless. The Higgs mechanism predicts an additional particle, the Higgs boson, associated to excitations of the Higgs field. The discovery of a Higgs boson in 2012 proved the existence of the particle and completed the story of electroweak symmetry breaking.

The discovery of the Higgs boson is a strong confirmation of the theory, but there exists tantalizing evidence for new physics that is not contained in the model. From the theory perspective, corrections to the mass of the Higgs boson from loop diagrams are not controlled. It is possible that the bare mass of the Higgs boson is chosen to almost exactly cancel the loop corrections, but this fine tuning is unnatural. The more natural solution is to introduce new physics that also enters into the loop correction to the Higgs mass and cancels the other contributions. The nature of this new physics is unknown, but many theories exist that attempt to solve this problem. The most compelling motivations for new physics comes from experimental observations. The presence of dark energy and dark matter are not explained by the Standard Model. While including dark energy into the Standard Model is far off, dark matter provides strong evidence for the existence of additional particles. The determination of the particle nature of dark matter is our best insight into new physics and will be a central theme of this dissertation.

CHAPTER 3

The Standard Model of particle physics

The Standard Model is an $SU(3)_C \times SU(2)_{T^3}^L \times U(1)_Y$ gauge theory. Each term represents a symmetry group whose transformation properties describe the interactions among a set of particles. Each symmetry gives rise to a conserved charge via Noether's theorem. The mathematical group structure is the special unitary group, $SU(N)$. The unitary group, $U(N)$, describes the symmetry of all $N \times N$ hermitian matrices. The special unitary group adds the requirement that the $N \times N$ matrix is traceless. The $U(1)$ group is the symmetry of a single phase. The $SU(N)$ group is spanned by $N^2 - 1$ basis vectors – the generators of the group. This also corresponds to the number of force carriers in the theory.

The first term, $SU(3)_c$, describes the strong force that acts on the quarks which possess a three state color charge (r,g,b) that is exchanged among eight gluons. The second term, $SU(2)_{T^3}^L$, describes the electroweak force. The superscript, L, indicates that the symmetry only exists among left handed particles. Every left handed lepton and quark carries an isospin quantum number that is exchanged among three weak gauge bosons, W^1 , W^2 , and W^3 . The third term, $U(1)$, is another component of the electroweak force. The weak hypercharge, Y, is the conserved charge and it has a gauge boson, B. However, the W^1 , W^2 , W^3 bosons and the B boson are not the particles observed in nature. To produce the observed particles – two massive W bosons, the massive Z boson, and the massless photon – the $SU(2)$ and $U(1)$ components are spontaneously broken. The W^3 and B bosons of the unbroken theory mix to form the observed Z and photon. The amount of mixing is determined by the Weinberg angle, θ_w , and must be measured by experiment. The $SU(2)_{T^3}^L \times U(1)_Y$ symmetry is broken by the non-zero masses of the W and Z gauge bosons. In the theory the gauge bosons acquire their masses from the Higgs mechanism. The Higgs mechanism adds a potential to the Lagrangian such that perturbations around the zero of the field are not stable and a non-zero expectation value is obtained. Excitations of the field about the vacuum expectation value are the manifestation of the Higgs boson. This mechanism of mass generation is extended to the quarks and leptons through Yukawa couplings.

The full particle content of the Standard Model and the quantum numbers assigned to each particle is shown in Table 3.1.

3.1 The Higgs boson at the LHC

The LHC is designed to find the Higgs boson or to rule out its existence over a large range of viable masses. The best lower limit on the Higgs mass, before results from the LHC were available, was a limit of 114.4 GeV from LEP [3]. Although there was no experimental upper limit on the Higgs mass, there are good reasons to expect the mass to be small. Indirect constraints on the Higgs mass are derived from electroweak fits [4] that are sensitive to its mass through loop corrections. Loop

particle	mass (GeV)	Q	I ₃	Y	C
e_L	5.11×10^{-4}	-1	1/2	-1	-
μ_L	0.106	-1	1/2	-1	-
τ_L	1.777	-1	1/2	-1	-
ν_{eL}	$< 2 \times 10^{-9\dagger}$	0	-1/2	1	-
$\nu_{\mu L}$	$< 2 \times 10^{-9\dagger}$	0	-1/2	1	-
$\nu_{\tau L}$	$< 2 \times 10^{-9\dagger}$	0	-1/2	1	-
e_R	5.11×10^{-4}	-1	0	-2	-
μ_R	0.106	-1	0	-2	-
τ_R	1.777	-1	0	-2	-
W^\pm	80.4	± 1	± 1	0	-
Z	91.2	0	0	0	-
γ	$< 1 \times 10^{-27\ddagger}$	0	0	0	-
H	125.5 [§]	0	-1/2 [△]	1 [△]	-
u_L	$2.3 \times 10^{-3}\text{✕}$	2/3	1/2	1/3	r,g,b
c_L	1.3✕	2/3	1/2	1/3	r,g,b
t_L	174	2/3	1/2	1/3	r,g,b
d_L	$4.8 \times 10^{-3}\text{✕}$	-1/3	-1/2	1/3	r,g,b
s_L	$9.5 \times 10^{-2}\text{✕}$	-1/3	-1/2	1/3	r,g,b
b_L	4.2✕	-1/3	-1/2	1/3	r,g,b
u_R	$2.3 \times 10^{-3}\text{✕}$	2/3	0	4/3	r,g,b
c_R	1.3✕	2/3	0	4/3	r,g,b
t_R	174	2/3	0	4/3	r,g,b
d_R	$4.8 \times 10^{-3}\text{✕}$	-1/3	0	-2/3	r,g,b
s_R	$9.5 \times 10^{-2}\text{✕}$	-1/3	0	-2/3	r,g,b
b_R	4.2✕	-1/3	0	-2/3	r,g,b
g	0	0	0	0	r,g,b \otimes $\overline{\text{r,g,b}}$

Table 3.1: The known particle content of the Standard Model and their assigned quantum numbers and mass. All masses are taken from the particle data group [1] unless otherwise indicated

[†] The exact neutrino masses are not known, but the observation of neutrino oscillations means that they must have a non zero mass. Only the mass differences are known and the mass hierarchy is not yet known.

[‡] The photon is considered to be massless in the theory. The quoted number is the current best experimental limit on the photon mass.

[§] The latest mass measurement from the ATLAS experiment [2].

[✕] Bare masses for all but the top quark cannot be directly measured because all quarks except for the top quark are measured in bound states. A specific mass calculation scheme must be used and the results can vary between schemes.

[△] Quantum numbers are given for the Higgs field. The physical Higgs particle carries no quantum numbers.

corrections to the W and top propagators relate the Higgs mass to the W and top mass. The mass of the W boson and the top quark are most sensitive, but constraints are also derived from the values of the Z width, $\sin \theta_w$, and α_s measured at LEP and SLD [5, 6] and G_F measured from the muon lifetime [7]. The combined fit places the most probable higgs mass at 94 GeV with an uncertainty of approximately 25 GeV. Now that the Higgs boson has been discovered and its mass has been measured these relations are over constrained and the self-consistency of the electroweak sector of the Standard Model can be checked. Figure 3.1 shows the consistency between the measured Higgs boson mass and the electroweak parameters. The vertical and horizontal green bands show the measured top mass and W mass respectively and their uncertainties. The gray shaded area shows the 1σ and 2σ allowed Higgs masses from the electroweak fit not including the top mass, W mass or Higgs mass. The blue shaded areas shows the fit when the Higgs mass is included in the fit. The blue shaded area and the two green bands nearly intersect indicating that the Standard Model is indeed self consistent.

The Higgs boson is produced in five modes at the LHC. Figure 3.2 shows the Feynman diagrams for each process and Figure 3.3(a) shows the production cross section of each process as a function of the mass of the Higgs boson. The Higgs couples weakly to the light quarks in the proton so the main production mechanism is through the fusion of two gluons into a loop that is dominated by top and bottom quarks. The rate of gluon fusion depends strongly on the center of mass energy because of the behavior of the gluon parton distribution function (see Section 3.3). The next largest production mechanism for $m_H > 100$ GeV is through vector boson fusion (VBF). The associated production of a Higgs boson with a W or Z boson are the next largest cross sections and associated production with a $t\bar{t}$ pair has the smallest cross section. The gluon fusion process was the main production mode that contributed to the discovery of the Higgs boson. The other channels provide complimentary measurements of the coupling of various particles to the Higgs boson. With the full 2012 dataset a small number of events are expected in the VBF channel and in the WH and ZH channels. However, these channels do not have enough signal to claim discovery of the Higgs boson alone. Searches in the $t\bar{t}H$ channel are underway, but require more data to be sensitive to the Standard Model production rate. In the future the LHC will collect enough data to measure all production mechanisms.

The branching fraction to various final states also depends on the Higgs mass. Figure 3.3(b) shows the branching fractions for masses between 80 GeV and 200 GeV. The couplings to the gauge bosons are the largest followed by the Yukawa couplings to the heaviest fermions. Therefore above $m_h \sim 180$ GeV the branching ratio is shared between WW and ZZ . If the mass is above 350 GeV decays to top quark pairs also have a sizeable branching fraction. Below 180 GeV one of the Z

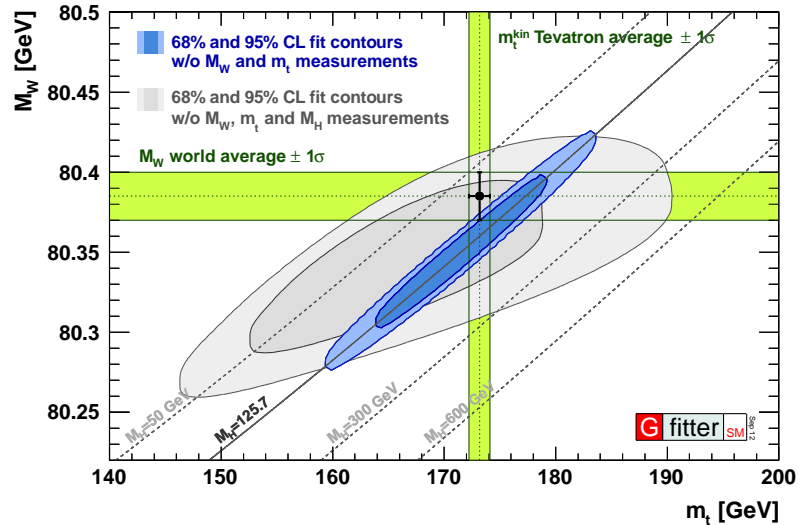


Figure 3.1: Self consistency test of the Higgs sector of the Standard Model from the electroweak fit produced by the Gfitter collaboration [4]. The W and top quark masses are the most sensitive to the Higgs mass and are shown on the y and x axes respectively. The green bands show the measured W and top quark masses. The intersection of the two green bands gives the allowed Higgs mass range from these two inputs. The diagonal lines show contours of constant Higgs masses. The allowed mass range from the remaining inputs to the electroweak fit are shown in gray. The blue regions include the measured Higgs mass in the electroweak fit. The blue allowed region falls close to the intersection of the W and top quark masses indicating the consistency of the Standard Model.

bosons in the ZZ final state must be off-shell and the decay width to ZZ decreases. This also occurs in the WW decay channel when the mass falls below 160 GeV and one of the W bosons must be off-shell. At low masses, where the WW and ZZ decays are highly suppressed by the off-shell boson, the decay to $b\bar{b}$, $\tau^+\tau^-$, $c\bar{c}$, and gg dominate. The first three are Yukawa couplings and only depend on the mass of the decay particle. The Higgs boson does not couple directly to gluons, but the gg final state can proceed through a loop – the inverse of the gluon fusion production. The decay to two photons also proceeds through a loop. In this case the two photons couple to the Higgs boson through a W loop or through a top quark loop.

3.2 Open questions

Despite physicists' efforts in assembling the Standard Model, it still does not describe all observed phenomena. Some of the most compelling open questions are,

- What regulates the Higgs mass? (Also known as the hierarchy problem). Loop corrections to the Higgs mass indicate that it should be much larger than the electroweak scale. To bring the mass to the electroweak scale either the bare mass must be chosen such that it nearly ex-

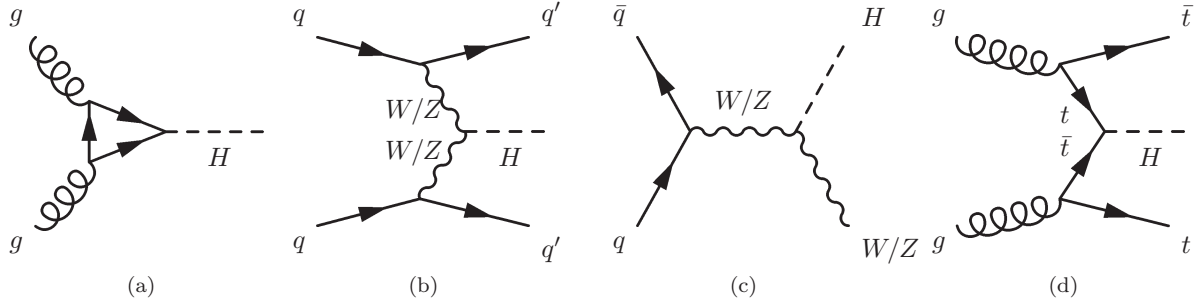


Figure 3.2: Feynman diagrams for the primary Higgs production mechanisms. The processes are, gluon fusion (a), vector boson fusion (b), associated production (c), and $t\bar{t}H$ (d).

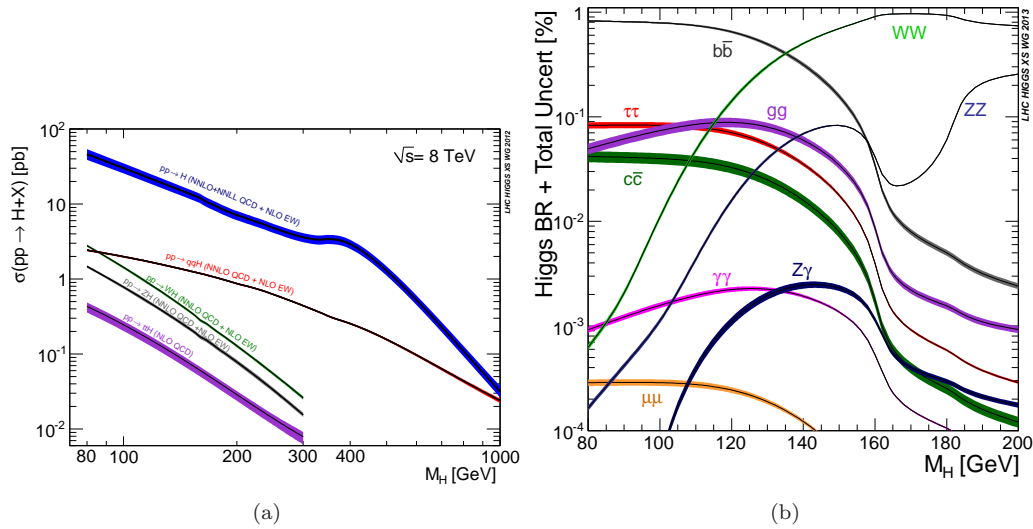


Figure 3.3: Higgs production cross section (a) and branching fractions (b) as a function of the Higgs mass.

actly cancels the loop contributions or a new theory needs to be introduced to cancel the loop corrections. A common proposed solution to the hierarchy problem is Supersymmetry. Supersymmetry proposes the existence of a new symmetry and doubles the number of particles. The new particles enter the loop diagrams for the Higgs mass and exactly cancel the contributions from their partner particles in the Standard Model. Supersymmetric particles are expected to have masses near the electroweak scale, and may be found at the LHC. Currently no direct evidence for Supersymmetry has been found.

- Do the four forces unify? The unification of the electroweak and strong forces of the Standard Model and gravity is currently an unsolved problem. String theories attempt to unify the four forces, but this unification can only occur near the Planck scale. Although it is theoretically

possible for string theory to produce the Standard Model, no experimental confirmation is available. Other theories such as Randall-Sundrum models propose an additional dimension of space time to explain the weakness of gravity.

- What is the nature of dark energy? Dark energy accounts for the energy density that causes the accelerating expansion of the universe. The source of dark energy is unknown and it is unaccounted for in the Standard Model. Dark energy is included in the standard model of cosmology by including a cosmological constant in the Einstein equation. This provides an accurate description of the expansion of the universe but does not point to the underlying nature of dark energy.
- What is the nature of dark matter? Dark matter is the observed non-luminous matter that is four times more abundant than normal matter. No known particle species can account for the dark matter, so its presence is a strong indication of physics beyond the Standard Model. Many experiments are searching for dark matter through its hypothetical weak interaction, including the LHC. Our current understanding of dark matter is described in Chapter 4 and Chapter 10 presents a search for dark matter produced in invisible decays of the Higgs boson.

3.3 The structure of the proton

The LHC collides protons in order to achieve the highest energy particle collisions. The use of protons is a trade off with respect to using a fundamental particle such as an electron. Protons produce much less synchrotron radiation and can be accelerated to much higher energies.² The drawback to colliding protons is that they are composite objects, consisting of three bound valence quarks surrounded by a sea of gluons and quarks. In a given collision it is impossible to know which partons collided.³ In order to reproduce the correct cross sections, the probability for a given parton to be involved in a collision is needed. The parton distribution function (PDF) for a given parton in the proton depends on the momentum transfer (Q^2) at which the collision occurs. Figure 3.4 shows the PDFs for each parton for two values of Q^2 . The PDFs must be measured. Although they can be measured at the LHC, the best measurements of the proton PDFs were made in electron proton collisions at the HERA accelerator. The PDFs measured at HERA are not directly applicable to proton collisions at the LHC because collisions occur at a higher Q^2 at the LH at the LHCC. Fortunately, for the values of Q^2 probed at HERA and the LHC, perturbative calculations in QCD can extrapolate from lower Q^2 to higher Q^2 using the DGLAP equations [8, 9, 10].

²The power radiated through synchrotron radiation depends on the relativistic γ to the sixth power.

³In fact it is possible to distinguish gluon collisions from quark collisions by measuring the properties of final state jets but for this discussion they are assumed to be indistinguishable.

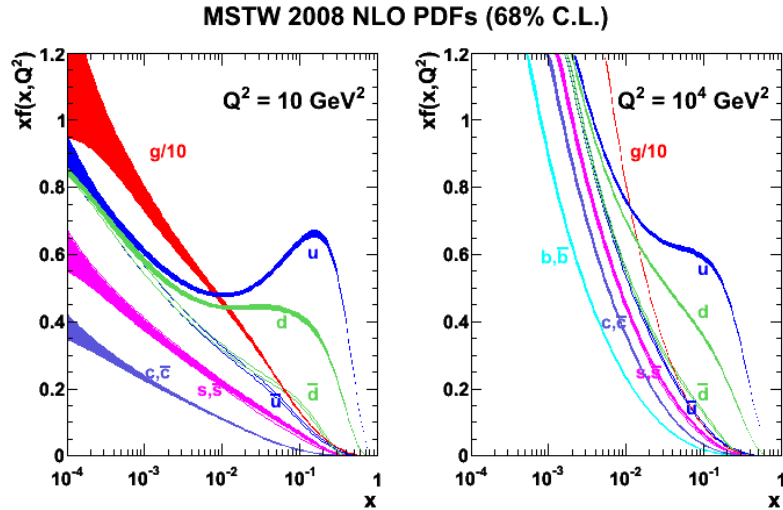


Figure 3.4: Parton distribution functions derived for $Q^2 = 10 \text{ GeV}^2$ and $Q^2 = 10^4 \text{ GeV}^2$. The y axis is proportional to the probability of finding a given parton having that value of the Bjorken scaling variable, x , shown on the x axis. At the energies of the LHC the low x gluons have enough energy to produce electroweak physics making gluon collisions the dominant production mode for many processes studied at the LHC. The gluon function rises so rapidly that it is divided by a factor of 10 so that it is visible on the plot. The PDF sets are provided by MSTW [11].

3.4 Particle interactions with matter

An understanding of how particles interact with matter is essential to the construction of particle detectors at the LHC. Detector design takes advantage of the properties of particle interactions with matter to have the best performance for measuring specific particles. Calorimeters must fully contain particle showers and provide an accurate measurement of the original energy of the particle. Tracking detectors must also utilize particle interactions to measure space points as particles pass through the detector. However, the material in the tracking detectors must be kept at a minimum so that the energy of the particle is not significantly decreased as it passes through the tracker and into the calorimeter. Muons are unique in that they pass through the calorimeters without stopping.⁴ The presence of a high momentum particle outside of the calorimeter is a good indication that the particle is a muon. Tracking detectors are added outside of the calorimeters to obtain additional measurements of the muon's momentum.

Multiple interaction phenomena exist that depend on the density of the material as well as the mass, charge, and momentum of the particle. All of these phenomena must be accounted for when considering how a particle interacts with the detector. The strength of interactions can be strongly dependent on momentum so there are multiple energy regimes where one or another type of

⁴Muons having $p_T > 5 \text{ GeV}$ usually do not stop in the calorimeter, but lower momentum muons may be stopped.

interaction dominates. The physics of particle interactions with matter is covered in many references, including [1, 12, 13, 14].

3.4.1 Ionization by charged particles

The dominant electromagnetic interaction for most charged particles is through ionization. The small mass of the electron makes energy loss via bremsstrahlung significant; this process is discussed in the next section. As charged particles traverse matter, they interact with electrons in atomic orbitals. This form of energy loss is given by the Bethe formula. The energy loss is approximately proportional to the density of the material and is inversely proportional to $\beta^2 = (v/c)^2$. Therefore for high energy particles $\beta \approx 1$ and the energy loss via ionization is constant. As a high energy particle traverses matter, it loses energy at a rate that is approximately constant with energy as long as $\beta \approx 1$. When β falls significantly below one the energy loss increases quickly causing a large portion of the energy to be lost at the end of its trajectory. This peak in energy loss is called the Bragg peak.

Ionization is the main process by which particles are detected in silicon and gaseous detectors. In semiconductor devices a bias voltage is applied across a bulk region depleting it of free charge carriers. As a charged particle traverses the bulk region, electrons are liberated and flow under the bias voltage to charge collection and readout devices. For high energy particles the amount of energy lost via ionization in a silicon device is typically 1 - 100 keV depending on the density and thickness of the traversed material [14]. Therefore high energy charged particles at the LHC lose a small fraction of their momentum in the silicon detectors.⁵ In gaseous detectors a charged particle liberates electrons from gas molecules which travel to a charge collector under the influence of an applied voltage. The amount of energy deposited in a gaseous detector is small due to the relatively low density of the gas.

3.4.2 Bremsstrahlung

When charged particles traverse a material, they scatter off of atoms causing the path of the particle to change slightly. This acceleration causes the particle to emit bremsstrahlung radiation. The power radiated via bremsstrahlung is strongly dependent on the relativistic γ factor, scaling as γ^6 . Therefore bremsstrahlung radiation is only significant for electrons or very high energy pions or muons. The radiation length, χ_0 , is used as a figure of merit for energy loss by electrons having momentum above about 10 MeV where losses by bremsstrahlung dominate. It is defined as the distance an electron travels before its momentum is reduced to $1/e$ of its original momentum. Figure 3.5

⁵This is not the case for electrons, which lose much more energy through bremsstrahlung.

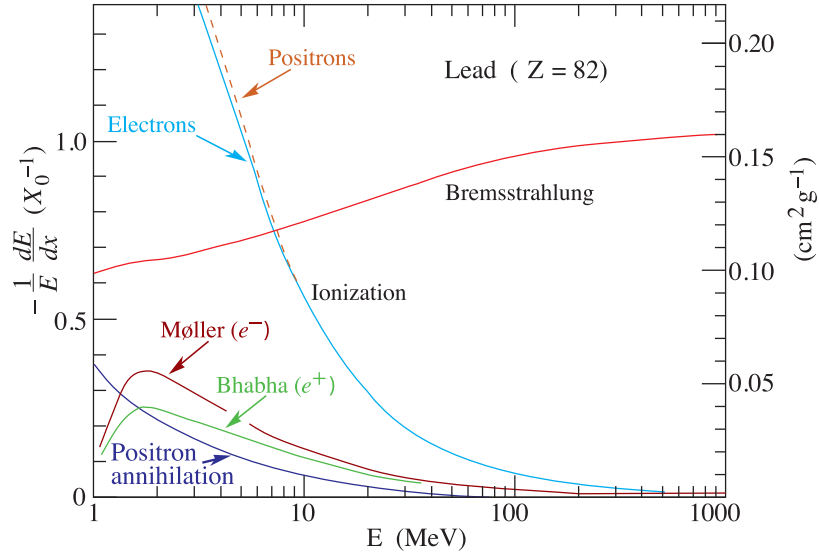


Figure 3.5: Fractional energy loss of electrons in matter for energies between 1 MeV and 1 GeV. The dominant interaction is highly dependent on the electron momentum. At low energy ionization losses dominate while at high energy losses via bremsstrahlung dominate. Courtesy of the particle data group [1].

shows the average energy loss per radiation length for electrons over a large range of momentum. The ionization interaction dominates at low momentum and bremsstrahlung dominates at high momentum. For high p_T electrons in ATLAS large energy losses through bremsstrahlung is common in the inner detector.

3.4.3 Transition radiation

Transition radiation is used in the ATLAS transition radiation tracker detector (TRT) to identify electrons. When a charged particle passes between two mediums having diffractive indices the particle emits radiation in the form of photons. The radiated power depends on the relativistic γ factor and is only significant for high momentum electrons or very high momentum (> 1 TeV) pions or muons. The ATLAS TRT is designed so that particles pass through many layers of radiator material and a special detection threshold identifies transition radiation photons. The presence of transition radiation can therefore be used to discriminate electrons from pions.

3.4.4 Photon interactions

Photon interactions in matter are dominated by three processes, the strength of which depends on the momentum of the photon. Figure 3.6 shows the interaction cross section for photons in copper and lead over a wide range of momentum. Photons can Rayleigh scatter off of an atom or

can be absorbed by an atom, causing an orbital excitation of an electron. These effects dominate if the momentum of the photon is below 1 MeV. In this regime there are absorption resonances where the photon energy closely matches the excitation energy of an orbital. The excited atom quickly returns to its ground state by emission of one or more photons. At energies around 1 MeV Compton scattering of photons off of electrons dominates the energy loss. Above 1 MeV the energy is sufficient to convert into an electron-positron pair. The conversion is not allowed in vacuum because of momentum conservation, but in matter the photon can transfer momentum to an atomic nucleus or electron and split into an electron-positron pair. This process dominates the energy loss at energies above 10-100 MeV. Pair production closely resembles the bremsstrahlung process and the interaction length defined for electrons also appears in the conversion probability for photons. The probability for a photon to convert is $e^{-7/9dx/x_0}$. In one radiation length, therefore, the probability for a photon to pair produce is 54%.

With the above interactions in mind for photons and electrons, their behavior in particle detectors can be completely understood. When a high energy electron traverses the inner detector it tends to lose energy via bremsstrahlung. Because the electron is moving in a magnetic field, the radiated photon is emitted in the original direction of the electron before it interacted while the electron bends more because it has lost energy. The radiated photons are collected in the calorimeter along with the electron so that the original electron energy can be accurately reconstructed. When the electron enters the calorimeter it undergoes bremsstrahlung radiation, emitting photons. If the photon momentum is large enough it will pair produce an electron and positron, each of which can radiate more photons through bremsstrahlung. Eventually electrons are stopped via ionization losses and photons are absorbed by atoms. These processes produce an electromagnetic shower that can be measured in the detector. The shower develops both along the original particle's trajectory and transverse to it. The transverse width of the shower is measured with the Molière radius which defines a circle in which 90% of the electromagnetic shower is contained. The Molière radius does not depend on the energy of the particle, only on the density of the stopping material. Two different detector technologies are used to record electromagnetic showers, homogeneous calorimetry and sampling calorimetry. The former design is used in the CMS electromagnetic calorimeter and the latter is used in all calorimeters in ATLAS and the hadronic calorimeter in CMS. Homogeneous calorimeters use dense, transparent crystals and attempt to collect all the light emitted from the electromagnetic shower. A sampling calorimeter only measures a fraction of the total energy. The total energy is proportional to the energy deposited allowing the total energy to be calculated.

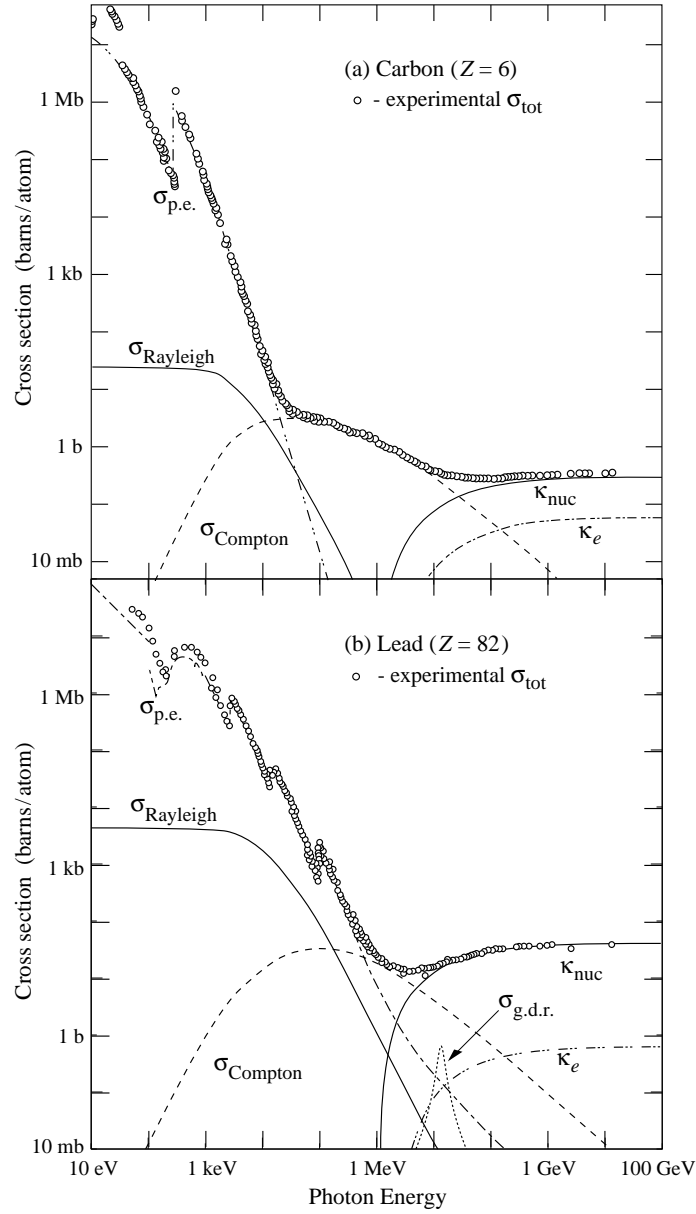


Figure 3.6: The interaction cross section of photons in matter for energies between 1 eV and 100 GeV in copper (top) and lead (bottom). At low energy photons are absorbed by exciting an atomic electron to a higher orbital ($\sigma_{\text{p.e.}}$). At high energies the photon produces an electron-positron pair in the presence of an atomic nucleus (κ_{nuc}) or an electron in an atomic orbital (κ_e). Rayleigh scattering (σ_{Rayleigh}) and Compton scattering (σ_{Compton}) also contribute to the total scattering cross section.

3.4.5 Strong force interactions

All hadrons interact with material through strong interactions with nuclei. Charged hadrons also experience energy loss through ionization, but strong interactions usually dominate. The stopping power of hadrons in materials is measured by the hadronic interaction length, λ_0 , defined as the mean free path of the particle in the material. The strong force is short ranged, so the probability for a hadron to interact strongly with a nucleus is approximately the cross section for it to collide with the nucleus. Therefore λ_0 depends mostly on the density of the material. When high energy hadrons interact with a nucleus, it is usually broken up and many secondary particles are produced. These secondary particles can also interact with nuclei causing a shower of particles. Hadronic showers are measured in a dedicated calorimeter in ATLAS. The hadronic calorimeter is placed outside of the electromagnetic calorimeter so that electrons and photons are contained within the electromagnetic calorimeter while more massive hadronically interacting particles pass through the hadronic calorimeter. A portion of a hadronic shower occurs in the electromagnetic calorimeter so the measurements from both types of calorimeters are added to measure the energy of a hadronic shower.

CHAPTER 4

Dark matter

Numerous observations have established the existence of non-luminous, non-baryonic matter in the universe. In fact the observed dark matter density is larger than the density of baryonic matter by a factor of four. Despite the abundance of dark matter, little information is known about it. The only evidence for dark matter is from cosmological measurements of its gravitational interaction and no theory exists to explain it at the particle level. Neutrinos are a possible candidate because they only interact weakly, but this possibility has been largely ruled out by measurements of the cosmic microwave background (CMB). Measurements of the CMB are sensitive to the relative density of the components that make up the universe. To agree with CMB measurements dark matter should be non-relativistic so it contributes to the matter density of the universe. A dark matter candidate should therefore be heavy whereas neutrinos are very light and they tend to move at relativistic speeds.

4.1 The WIMP hypothesis

The most accepted model for dark matter is that it is weakly interacting and massive (WIMP). It must be massive so that it has a non-relativistic velocity and contributes to the matter density of the universe. The possibility that it must interact weakly arises from the evolution of the dark matter density with the expansion of the universe.⁶ The hypothesis is that in the early universe ($t < 10^{-9}$ s) dark matter is in thermal equilibrium with other particle species. As the universe expands and cools the rate of interactions begins to decrease. Eventually there is not enough thermal energy to sustain dark matter interactions and the dark matter density “freezes out” to a constant value. The time of freeze out and thus the remaining (relic) dark matter density only depends on the mass and interaction cross section of the dark matter particle. Figure 4.1 shows the evolution of the dark matter density as it freezes out. The observed relic density predicts that the interaction cross section is on the same order as weak interactions. This supports the idea that new physics should exist near the electroweak scale to solve the hierarchy problem and is referred to as the “WIMP miracle”.

4.2 Observational evidence for dark matter

The first well established observation of the presence of dark matter was from measurements of the rotation curves of galaxies [15, 16]. Velocities of points along the plane of the galaxy are determined from the relative Doppler shift of common emission lines. Measurements of the density profile of luminous matter in galaxies indicate that the matter density should fall off roughly as \sqrt{R} where R is the distance of the source from the galactic center. Instead we observe that the radial velocity is

⁶It should also be noted that if dark matter only interacts gravitationally then we have no chance of identifying it at the particle level.

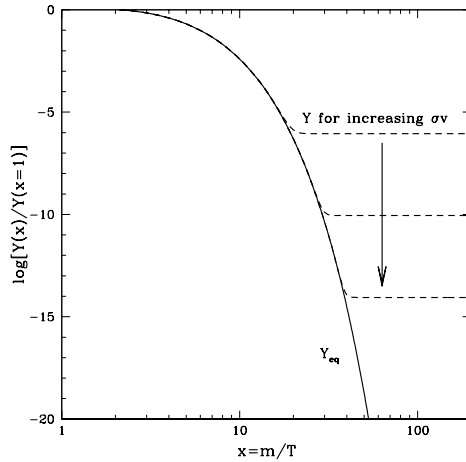


Figure 4.1: The evolution of the dark matter density in the early universe. The y axis is the comoving number density of dark matter particles, defined to account for the expansion of the universe; the density of a species in equilibrium decreases as the volume of the universe increases while the comoving density of a species in equilibrium is constant. The comoving density at which dark matter freezes out depends only on its interaction cross section. The cross section that reproduces the observed relic dark matter density is on the same scale as weak interactions.

approximately constant in R indicating that a large fraction of the matter content of the galaxy is non-luminous. Figure 4.2 shows the rotation curve for one exemplary galaxy, NGC 3198. The “halo” curve shows the prediction for only a dark matter halo and the “disk” curve shows the prediction for only the luminous matter in the galaxy. The data fall far from the distribution expected from luminous matter and is only only consistent with a combination of both dark matter halo and luminous matter.

Further proof of the existence of dark matter comes from weak lensing experiments [17, 18]. As light passes near a massive object its trajectory is bent as it passes through warped space-time. In these measurements a galaxy cluster is observed in the foreground with a number of visible background galaxies. The distortion in the shape of the background galaxies is used to determine the mass density profile of the galaxy cluster. Measurements of the luminous matter disagree significantly with the mass measured through gravitational lensing. Therefore dark matter is assumed to account for the remaining matter.

Measurements of anisotropies of the Cosmic Microwave Background (CMB) provide additional evidence of the presence of Dark Matter. Acoustic oscillations between baryonic matter, radiation, and dark matter created density perturbations in the early universe. These perturbations persisted until they were revealed by the CMB photons that were released during recombination when the universe became transparent to photons. The contributions of these different species is extracted from the power spectrum of the angular size of anisotropies on the CMB. Figure 4.3 shows the power

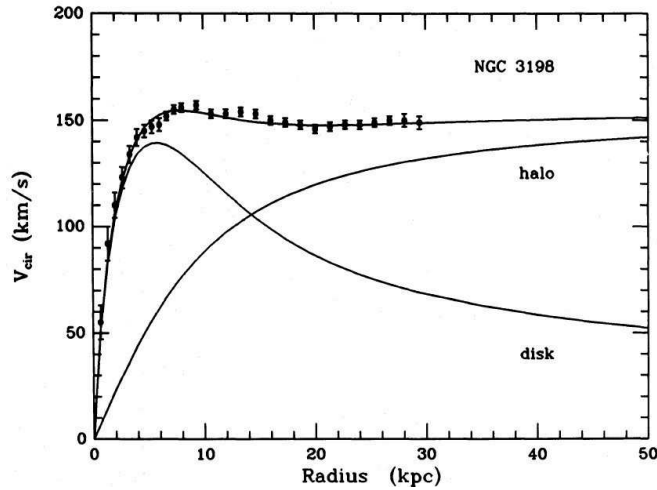


Figure 4.2: The rotation curve for galaxy NGC 3198. The solid line labeled “disk” is the contribution from the baryonic matter, calculated using luminous sources. The solid line labeled “halo” is the contribution from the dark matter halo. The data fall far from the distribution expected from luminous matter and is only only consistent with a combination of both dark matter halo and luminous matter.

spectrum predicted from different density parameters of baryonic matter (Ω_b). The data measured by WMAP are shown as red points [19, 20]. The total matter density, $\Omega_b + \Omega_{DM}$, is held constant. The power spectrum depends on a number of input parameters which are extracted with a fit to the data. The effect on the power spectrum from varying Ω_b is complicated, but clearly the data distinguish between values of Ω_b . These measurements provide the best estimate of the dark matter density. Recent results from WMAP determine the dark matter density to be 0.227 ± 0.014 [20].

4.3 Searches for dark matter

The presence of dark matter has been well established through measurements of its gravitational interaction. A complete understanding of the nature of dark matter also requires identifying it at the particle level. In other words, we must be able to observe its weak interactions. A number of direct detection experiments have been developed to detect dark matter. Dark matter may also be produced in collisions at the LHC. The following sections describe these searches.

4.3.1 Scattering experiments

Dark matter direct detection experiments are designed to observe dark matter by observing it scattering off of nuclei in a sensitive detector. The earth travels through the dark matter halo of our galaxy and in a rare number of cases a dark matter particle scatters in the detector. Direct

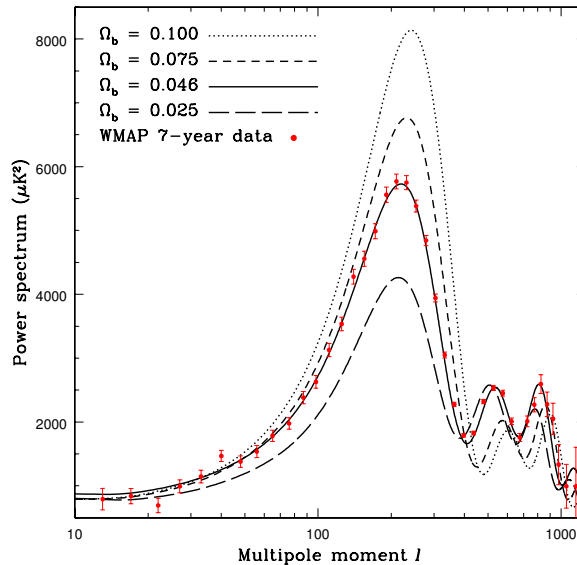


Figure 4.3: The CMB anisotropy power spectrum for various values of Ω_b [19]. The total matter density, $\Omega_b + \Omega_{DM}$, is held constant. Variations in Ω_b cause the first peak to change amplitude and changes the position of higher order peaks. The data are consistent with $\Omega_b = 0.046$.

detection detectors must be placed far underground to shield them from backgrounds from cosmic showers. There are two methods for observing dark matter signals. One method is to search for an excess of events over a low rate background. The other method uses the annual modulation of events produced by the varying velocity of the earth through the dark matter halo as it orbits the sun. This method helps to reduce backgrounds that are constant with time, but introduces other backgrounds that are correlated with the time in the year.

Direct detection experiments are sensitive to both the mass of the dark matter particle and its interaction cross section. The sensitivity to the mass arises from the ability to detect the recoiling nucleus. If the dark matter mass is too low, the momentum transferred to the nucleus is too small and it cannot be detected. The cross section also depends on the mass because the amount of dark matter is known and fixed. As the mass increases the density must decrease to compensate. Therefore at high mass the sensitivity also decreases.

Figure 4.4 shows limits on the interaction cross section and mass from various dark matter experiments. Exclusion limits have been provided by a number of experiments including XENON [21, 22], CDMSII [23], EDELWEISS [24, 25], ZEPLIN-III [26], COUPP [27], and SIMPLE [28]. Some experiments have reported an observation of a dark matter signal, including CRESST [29], DAMA [30], and CoGeNT [31]. The most recent observation from the CDMS collaboration [32] provides compelling evidence an 8.6 GeV dark matter particle. Not all of the observations are consistent with each other and some results are disputed by the community. Direct detection experiments make no

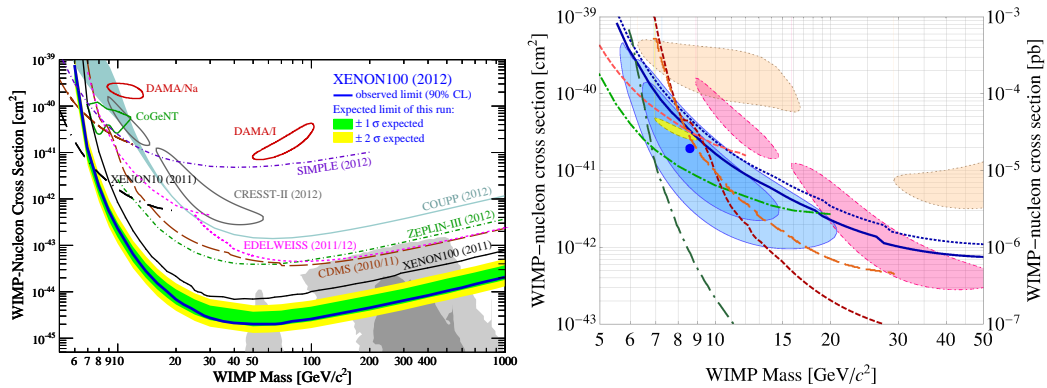


Figure 4.4: Limits on the dark matter scattering cross section from direct detection experiments from the XENON collaboration [21] (a) and from the CDMS collaboration [32] (b). Figure (b) is a zoom in of figure (a) that adds the recent observation from the CDMS collaboration. The closed contours show observations and the solid and dashed lines show limits. In Figure (b) the CDMS observation using silicon detectors is shown in the blue contours, the pink contour is from CRESST, the orange contour is from DAMA/LIBRA, and the yellow contour is from COGENT. The blue solid line interprets the new CDMS silicon detector data as a limit and the dashed blue line combines with previous CDMS data using silicon detectors. The dark green line is the limit from XENON100, the light green line is the limit from XENON10, the dark and light red dashed lines are two CDMS limits using germanium detectors, and the orange line is the limit from EDELWEISS. The limits disagree with some of the observations and some observations disagree with others. The reasons for the disagreements are unknown and many of the results are disputed within the community.

a priori assumption about the mechanism by which dark matter particles interact with Standard Model particles, but interpretations of the results usually assume that the interaction is through the exchange of a Higgs boson. If dark matter couples to the Standard Model through the Higgs boson it may be detectable at the LHC.

4.3.2 Cosmic searches

A number of experiments have been developed to measure the cosmic ray signature of dark matter annihilation. The AMS-02 experiment [33] has recently published results that extend previous results made by the PAMELA [34] and Fermi-LAT [35] experiments among others. Experiments search for dark matter annihilations by measuring the spectrum of positrons relative to the spectrum of electrons in cosmic rays. Positrons are created when cosmic rays interact with the interstellar medium. The ratio of positrons to electrons falls with momentum from this source. If two dark matter particles having mass M_{DM} annihilate the positron fraction should increase up to an energy of M_{DM} and sharply drop off when the kinematic limit is reached. A sharp peak is not observed because the decay particles can lose energy through secondary collisions. Figure 4.5 shows the positron spectrum from the AMS-02, PAMELA, and Fermi-LAT experiments [33]. Results from

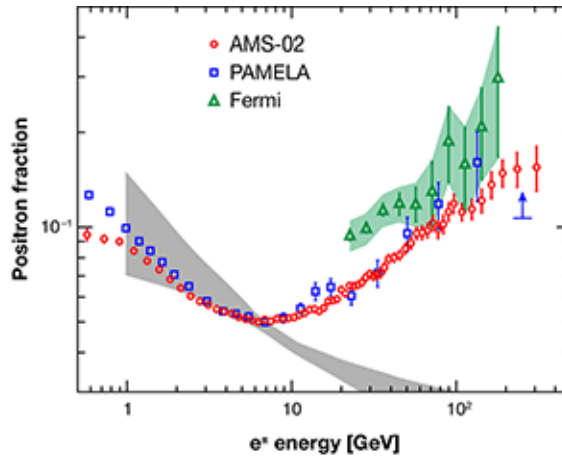


Figure 4.5: The measured positron spectra from the AMS-02 [33], PAMELA [34], and Fermi-LAT [35] experiments. All experiments show a rise in the positron spectrum above about 10 GeV.

the three experiments confirm the existence of a rise in the positron spectrum at momenta above about 10 GeV. The cause of the rise is unknown, but no sharp cutoff has been observed to indicate the annihilation of a massive particle. Future data from the AMS-02 experiment will explore the positron fraction at higher momenta.

4.3.3 Collider searches – LHC

Searches for dark matter at the LHC are performed by identifying the production of single, high p_T particles and large missing transverse momentum. The production of dark matter in proton-proton collisions is parameterized with an effective theory that assumes that an unknown heavy particle mediates the interaction between the initial state particles and dark matter. Such searches have been performed at ATLAS and CMS in final states having a single photon [36, 37] and in final states having a single jet [38, 39]. A search is underway in the ATLAS experiment in events having a single Z boson as well. Searches for dark matter in decays of the Higgs boson are also underway at ATLAS. In this case the Higgs boson decays to undetectable dark matter particles and must be produced with one or more tagging objects. Chapter 10 presents such a search when the Higgs boson is produced in association with a Z boson. A search in the VBF production channel is also underway. To date, no searches at the LHC have reported an observation of dark matter.

4.4 The Higgs and dark matter – Higgs portal models

Higgs Portal models [40, 41, 42] make a simple, ad-hoc extension to the Standard Model by introducing a new particle that couples to only the Higgs boson. The interaction strength is introduced

with a coupling constant, $\lambda_{h\chi\chi}$. In this model dark matter can be detected through three related interactions, scattering, annihilation, and Higgs decay. Within this model the cross section for each process is expressed in terms of $\lambda_{h\chi\chi}$. Figure 4.6 shows Feynman diagrams for the decay, scattering, and annihilation processes. The three diagrams all contain a vertex that is proportional to $\lambda_{h\chi\chi}$. Using the Feynman rules for these diagrams the Higgs partial width and scattering cross section are determined in terms of $\lambda_{h\chi\chi}$. The Higgs partial width for the decay to dark matter particles for the scalar, vector, and fermion cases is given in Equations 4.1, 4.2, and 4.3 respectively.

$$\Gamma^{\text{Scalar}}(h \rightarrow \chi\chi) = \frac{\lambda_{h\chi\chi}^2 v^2}{64\pi m_h} \left[1 - \left(\frac{2m_\chi}{m_h} \right)^2 \right]^{1/2} \quad (4.1)$$

$$\Gamma^{\text{Vector}}(h \rightarrow \chi\chi) = \frac{\lambda_{h\chi\chi}^2 v^2}{256\pi m_\chi^4 m_h} [m_h^4 - 4m_\chi^2 m_h^2 + 12m_\chi^4] \left[1 - \left(\frac{2m_\chi}{m_h} \right)^2 \right]^{1/2} \quad (4.2)$$

$$\Gamma^{\text{Majorana}}(h \rightarrow \chi\chi) = \frac{\lambda_{h\chi\chi}^2 v^2 m_h}{32\pi \Lambda^2} \left[1 - \left(\frac{2m_\chi}{m_h} \right)^2 \right]^{3/2} \quad (4.3)$$

The partial width is a function of only the Higgs boson mass, the dark matter mass, the vacuum expectation value, and the coupling constant. Note the introduction of a cutoff scale, Λ in the fermionic case. In this case the Higgs interaction operator has dimension five and is non-renormalizable. A cutoff scale is added that assumes the presence of new physics at a higher energy scale which would produce a renormalizable theory. This model does not purport to be a complete model, so the addition of this cutoff scale does not invalidate it. For the scattering process the dark matter-nucleon cross section is given for the for the scalar, vector, and fermion cases in Equations 4.4, 4.5, and 4.6 respectively.

$$\sigma_{\chi N}^{\text{Scalar}} = \frac{\lambda_{h\chi\chi}^2 \text{Scalar}}{16\pi m_h^4} \frac{m_N^4 f_N^2}{(m_\chi + m_N)^2} \quad (4.4)$$

$$\sigma_{\chi N}^{\text{Vector}} = \frac{\lambda_{h\chi\chi}^2 \text{Vector}}{16\pi m_h^4} \frac{m_N^4 f_N^2}{(m_\chi + m_N)^2} \quad (4.5)$$

$$\sigma_{\chi N}^{\text{Majorana}} = \frac{\lambda_{h\chi\chi}^2 \text{Majorana}}{4\pi \Lambda^2 m_h^4} \frac{m_\chi^2 m_N^4 f_N^2}{(m_\chi + m_N)^2} \quad (4.6)$$

The cross section has an additional dependence on the nucleon mass, m_N and the form factor, f_N which quantifies the coupling strength between the Higgs boson and the Nucleon. This form factor is determined using lattice calculations and suffers from large theoretical uncertainties [40]. These theoretical uncertainties will not be included in the comparison plots.

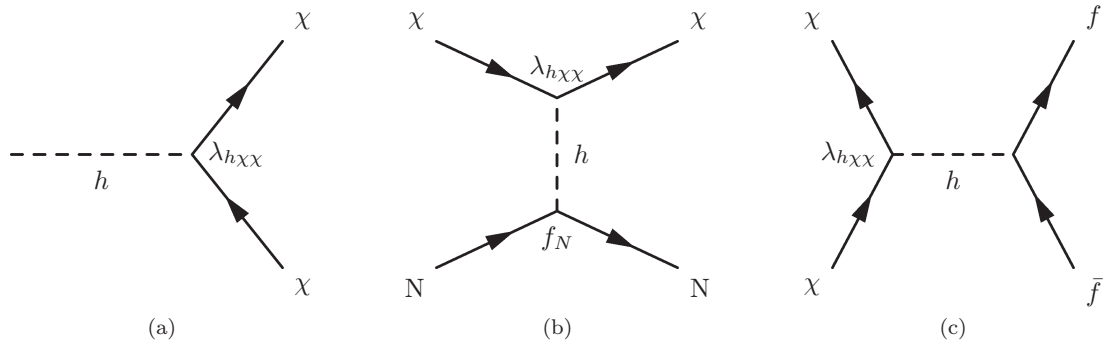


Figure 4.6: Feynman diagrams for the decay of the Higgs boson into dark matter particles (a), scattering of dark matter particles off of a nucleon with the exchange of a Higgs boson (b), and the annihilation of dark matter into standard model particles (c). The Higgs-dark matter interaction vertex has a coupling constant of $\lambda_{h\chi\chi}$ in each diagram. In the scattering diagram the Higgs-nucleon coupling strength is parameterized with a form factor, f_N .

CHAPTER 5

The LHC

The Large Hadron Collider (LHC) [43] is the highest energy particle collider in operation and has often been referred to as the largest scientific instrument ever built. The collider resides in an underground ring that is 27 km in circumference and approximately 100 m below the surface. The ring was originally built for the large electron positron collider (LEP) and has been reused for the LHC. Two counter-rotating beams of protons are directed through 1232 superconducting dipoles cooled to 1.9 Kelvin. Figure 5.1 shows a cross section of a dipole magnet. To store a 7 TeV proton beam, the magnets are supplied with a maximum current of 12 kA to produce a field of 8.3 Tesla. Over 5000 additional magnets are used to focus the beam and for orbit correction.

The LHC collides protons with a design center of mass energy of 14 TeV. For the first three years of its operation the LHC did not collide at its maximum energy because of a problem with the connections between the magnets. The center of mass energy was 7 TeV in 2010 and 2011 and was increased to 8 TeV in 2012. The LHC will turn on in 2015 after repairs and upgrades at a higher center of mass energy, most likely between 13 TeV and 14 TeV. The proton beams are accelerated and bunched using radio frequency cavities operating at 400 MHz. A beam dump system is instrumented for each beam. The beam dump is a long cylinder made of a carbon based material and is the only object that can absorb the entire LHC beam without being destroyed. There are many reasons for the beam to be dumped. The LHC is implemented with a complex interlock system that automatically dumps the beam if beam losses are too large, it begins to deviate from its nominal orbit too far, or if a magnet quenches. The LHC nominally holds 2808 bunches with 25 ns between bunches. In the 2012 run, bunches were separated by 50 ns allowing a total of 1380 filled bunches. Protons are brought into collision in four interaction points around the ring. At each interaction point an experiment is built to study the collisions. Two experiments, ATLAS and CMS, are general purpose detectors, while LHC-b studies b-quarks, and ALICE is designed to study heavy ion collisions. At each interaction point the beams are squeezed to increase the proton density. In ATLAS and CMS the beams are squeezed to a transverse width of 16 μm . Protons are supplied to the LHC by a complex of accelerators at CERN that have been built and repurposed since CERN's inception in 1954. An exhaustive account of this extremely complex machine is beyond the scope of this dissertation, but the key features and functionality will be presented.

5.1 Beam parameters

This section aims to introduce the basic formalism for storage and acceleration of charged particle beams. Particle beams are stored using dipole magnetic fields. The Lorentz force law describes the behavior of a charged particle in a uniform magnetic field,

$$F = qv \times \vec{B} \tag{5.1}$$

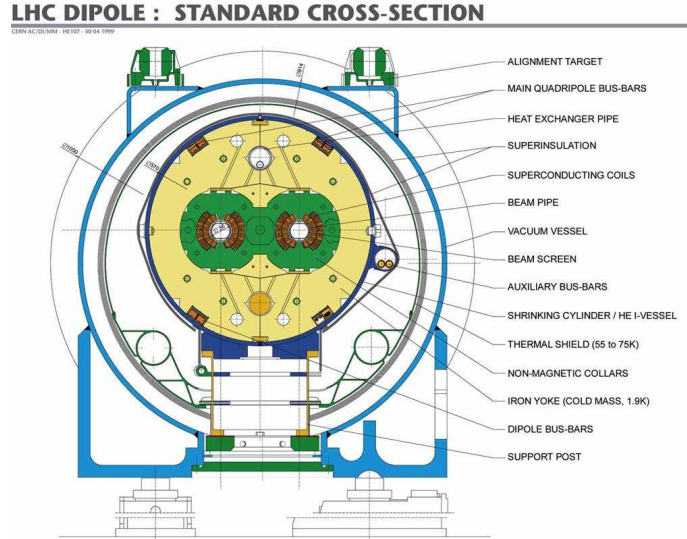


Figure 5.1: Cross sectional diagram of an LHC dipole.

Assuming that the magnetic field is perpendicular to the motion of the particle and the particles have charge e , the momentum of the particle expressed in GeV/c is

$$p = 0.3BR \quad (5.2)$$

where the magnetic field is measured in Tesla and the radius is measured in meters. Therefore, protons having momentum $7 \text{ TeV}/c$ contained in a circle of radius 2.8 km (approximately $2/3$ of the circumference of the LHC is dedicated to dipole bending magnets) require a magnetic field of 8.3 T . Higher energies can only be reached by installing stronger magnets or building a tunnel with a larger radius.

The LHC (as well as any modern proton accelerator) uses an alternating gradient design. Such a design is often referred to as a FODO lattice. The beam is alternatively focused (F) and defocused (D) in the vertical and horizontal coordinates achieving an overall focusing in both coordinates. The O in FODO refers to any other instrumentation such as bending magnets placed in between the focusing magnets.

In a very simplified model of a proton synchrotron the beam position in a given coordinate follows a wave equation. This is a good assumption because the focusing and defocusing effects of the lattice produce wave-like motion. The equation of motion in the x coordinate is

$$\ddot{x} - Kx = 0$$

where K parameterizes the magnetic forces acting on the beam. Solutions to this equation are complicated and in practice must be computed numerically, but basic properties of the wave equation

apply. One particularly important issue is that of resonances. If the wave frequency matches a resonant frequency of the machine the beam position will grow uncontrollably and the beam will be lost. Therefore the resonances of the machine must be mapped out and the beam must be tuned so that no resonances are encountered. This is particularly challenging while the beam is being accelerated because the tune can move and cross a resonance.

The LHC aims to search for rare processes and do to so it must achieve the maximum number of proton collisions. The proton collision rate is measured by the instantaneous luminosity. The instantaneous luminosity depends on beam parameters and is given in Equation 5.3,

$$\mathcal{L} = \frac{N_1 N_2 n_b f_{rev}}{4\pi\sigma_x\sigma_y} F \quad (5.3)$$

where N_1, N_2 are the number of protons per bunch in each beam, n_b is the number of bunches, f_{rev} is the revolution frequency, $\sigma_{x,y}$ is the width of the beam in the transverse directions, and F is a reduction factor that accounts for the fact that the beams do not collide head on, but at an angle. Therefore, to increase the luminosity one can increase the number of protons per bunch, increase the number of bunches, or squeeze the beam more at the interaction point to reduce $\sigma_{x,y}$.

5.2 The CERN accelerator complex

Protons are provided to the LHC only after passing through a number of accelerators. Protons must be accelerated over nine orders of magnitude, from thermal velocities to the final LHC energy. The LHC cannot perform this full acceleration, but instead protons must be provided at a minimum energy of 450 GeV. A complex of accelerators is required to accelerate protons over such a large energy range. Each accelerator progressively increases the momentum of the proton beam until it is finally injected into the LHC and further accelerated to the final collision energy. Figure 5.2 shows a diagram of the CERN accelerator complex highlighting the injection chain for various particle beams.

Protons are sourced from a bottle of hydrogen gas. Gas is injected into a duoplasmatron [44] at a rate of 1.1 Hz. The duoplasmatron heats the gas to create a plasma and an electric potential separates the protons from the electrons and accelerates the protons to 90 keV. The protons then enter the radio frequency quadrupole (RFQ) [45, 46]. The RFQ is a 3m long apparatus that consists of four veins that produce an alternating electric quadrupole field. The radius of the veins is sinusoidally modulated in the beam direction creating a longitudinal electric field. The RFQ therefore bunches, focuses, and accelerates the beam up to an energy of 750 keV. At this point the proton bunch enters linac2 [47], a drift tube linear accelerator that accelerates the protons up to 50 MeV. At this point it is no longer feasible to use linear accelerators, and the protons are transferred to the booster to

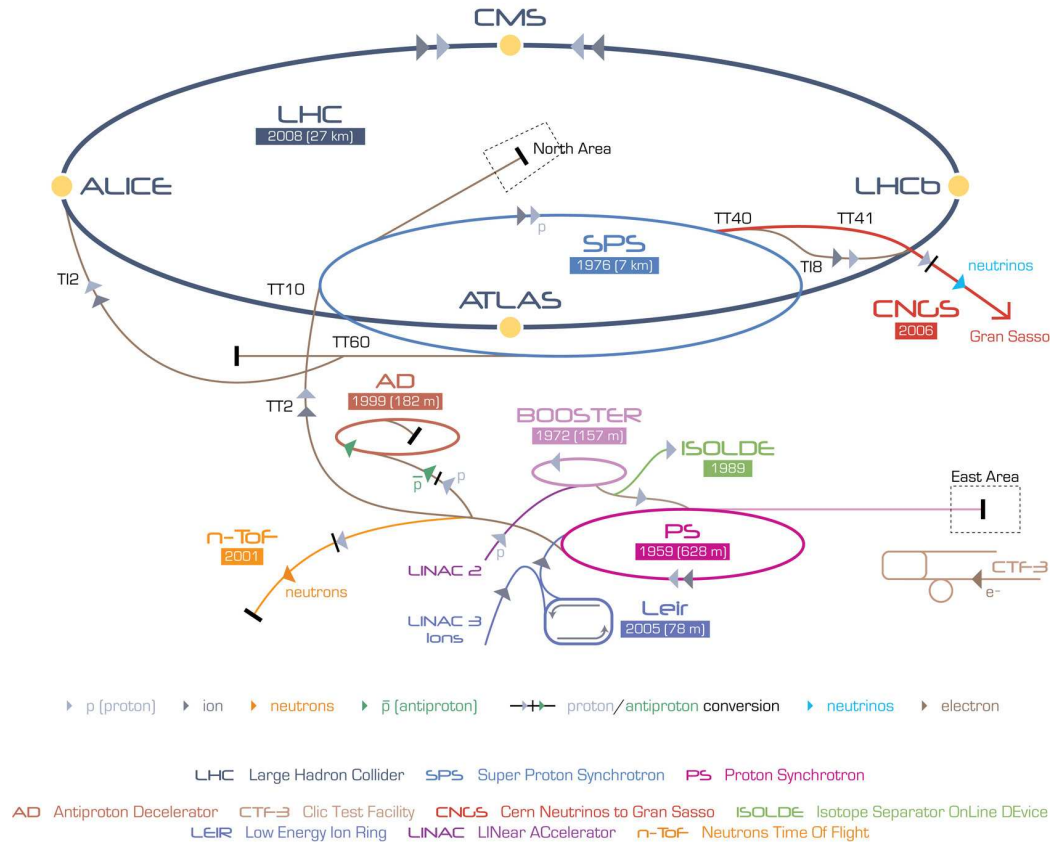


Figure 5.2: Diagram of the CERN accelerator complex. The injection chains for various types of particles is indicated by the colored arrows.

the proton synchrotron (PSB) [48]. The PSB has four parallel beam pipes in a 157 m circumference ring. The proton bunch from the linac is split into four bunches which are accelerated to 1.4 GeV, each in a separate beam pipe. Proton bunches are then transferred to the Proton Synchrotron (PS) [49, 50]. This machine is 628 m in circumference and further accelerates proton bunches to 26 GeV. Proton bunches from the PS are split into 12 smaller bunches and injected into the Super Proton Synchrotron [51] (SPS). The SPS is 7 km in circumference and was CERN's largest proton accelerator before the LHC was built. The SPS accelerates protons to 450 GeV and finally injects the protons into the LHC. This acceleration chain repeats until both LHC rings are filled with the required number of proton bunches. The LHC then accelerates the proton beams to final collision energy, which was 3.5 TeV in 2010 and 2011, and 4 TeV in 2012.

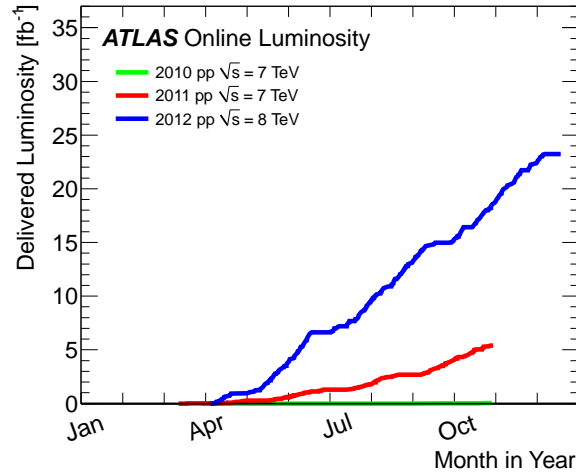


Figure 5.3: Integrated luminosity versus time in year for the three years of data taking. The integrated luminosity in 2010 was quite small relative to the following years and is only visible at the bottom of the plot.

5.3 Luminosity determination

The luminosity is determined by dedicated Van der Meer (VdM) scans [52]. The VdM scan measures σ_x and σ_y from Equation 5.3 by separating the beam and measuring the collision rate as the beams are brought into collision. The bunch populations, N_1 and N_2 , are measured using dedicated fluxgate magnetometer devices situated around each beam pipe [53]. These devices measure the beam current by measuring the magnetic field produced by the beam. The bunch population is measured for each of the bunches and can change by 10-20% from bunch to bunch. The luminosity measurement occurs only once or twice per year and must be extrapolated to the entire run period. A number of ATLAS sub-detectors are used to independently measure the luminosity. The measurements are calibrated to the VdM scan and then extrapolated to the entire run period. Luminosity values are provided for each luminosity block, a 1 to 2 minute period of time where the beam conditions are assumed to be stable (see also Section 6.4). The luminosity is summed over all luminosity blocks used for data analysis to determine the total integrated luminosity. Figure 5.3 shows the integrated luminosity vs time for 2010, 2011, and 2012 data taking periods.

5.4 Pileup interactions

The number of proton-proton interactions that occur when two LHC bunches cross follows a Poisson distribution and depends on the min-bias cross section and the instantaneous luminosity,

$$\langle N \rangle = \sigma_{mb} \mathcal{L}_{inst}. \quad (5.4)$$

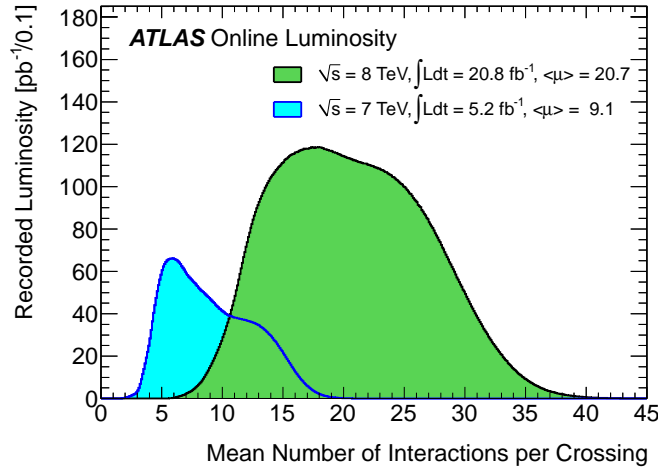


Figure 5.4: The distribution of the number of pileup interactions for 2011 (blue) and 2012 (green) data taking.

When $\langle N \rangle$ is less than one the probability of getting more than one collision per crossing is small. However, as the instantaneous luminosity increases it becomes more common for multiple proton-proton interactions to occur in the same crossing. When a hard scatter interaction is identified for analysis these additional interactions are referred to as pileup interactions. Figure 5.4 shows the distribution of the pileup multiplicity for 2011 and 2012 data taking. Pileup interactions are a trade-off; higher pileup accompanies higher luminosity, but detector measurements degrade because of the addition of energy from pileup collisions.

5.5 Standard LHC operation

A typical 24 hr period of LHC running is shown in Figure 5.5. Both LHC beams are filled with batches of protons from the SPS. The filling period usually lasts for between one half hour and one hour as multiple SPS batches are required to fill the LHC. Once the beams are filled they are ramped to the final collision energy. To accelerate the beam while keeping it in the proper orbit requires the RF and magnet systems to work in concert. The magnet current must increase at exactly the rate that the RF system increases the energy of the beam. Once the beam reaches its full energy, magnets near each collision point squeeze the beams and direct them into collision. Then, once all accelerator adjustments are finished, stable beams are declared and the experiments can begin recording data. The LHC operators attempt to keep the LHC in stable beams conditions for as long as possible to maximise the amount of data recorded by the experiments. The beam intensity decreases during a run mainly because protons are lost in collisions, but losses are possible from beam collimation as

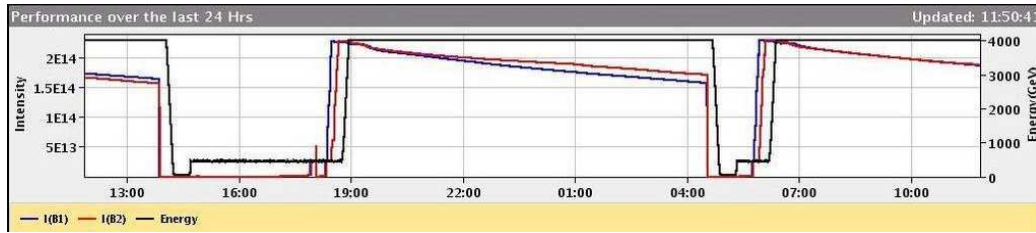


Figure 5.5: A representative 24 hour period of LHC running.

well. At the programmed end of a run, or when a beam interlock is tripped, the beam is dumped. Following a beam dump the magnet current is reduced to accept a 450 GeV beam and the process is repeated.

5.6 The scale of physics at the LHC

Over the full 2012 running period, approximately 2000 trillion proton-proton collisions occurred in ATLAS. The need for such a large number of collisions is driven by the relatively low cross section of processes of interest the LHC. Figure 5.6 shows the production cross section of many processes at collision energies accessible to the LHC. A major focus of the LHC experimental program and of this dissertation is the production of electroweak bosons. The W boson has the highest production rate, but this rate is a factor of 10^6 smaller than the min-bias production rate. Furthermore, the rate of Higgs boson production is a factor of 10^4 smaller than the W production rate. This large difference in production rate requires the LHC to provide a large number of collisions and the experiments to quickly and efficiently filter out the small fraction of interesting collisions.

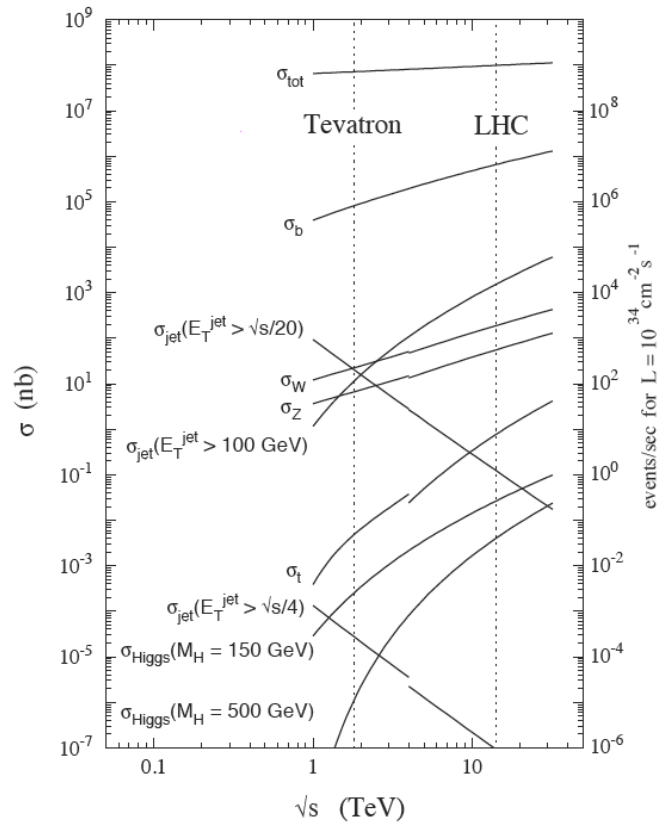


Figure 5.6: Production cross sections for a number of processes near LHC energies. The right axis shows the event rate assuming an instantaneous luminosity of $10^{34} \text{ cm}^2/\text{s}$. In 2012 the peak instantaneous luminosity was approximately $0.7 \times 10^{34} \text{ cm}^2/\text{s}$ and higher values are expected to be achieved in the future.

CHAPTER 6

The ATLAS experiment

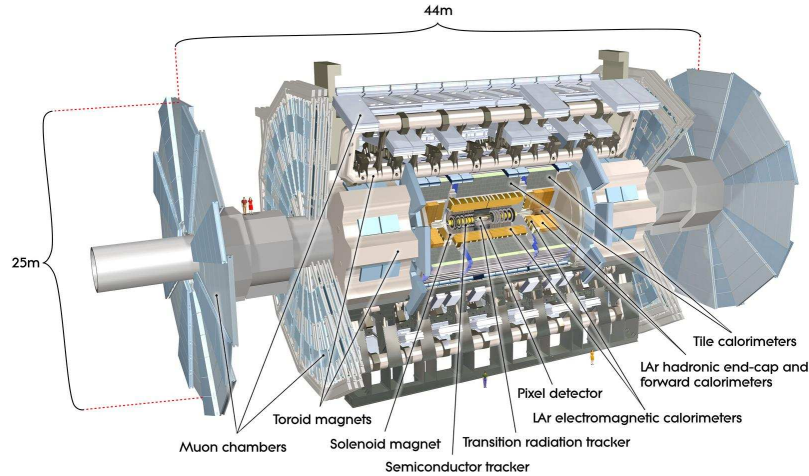


Figure 6.1: Diagram of the ATLAS detector systems.

The ATLAS detector [54] is a general purpose particle detector situated at interaction point 1 of the LHC. The experiment incorporates a number of technologies to record as many interesting collisions as possible and provide the most complete event reconstruction. Figure 6.1 shows a diagram of the ATLAS detector. The detector system nearest to the interaction point is the inner detector, which is divided into three subsystems, the pixel detector, the SCT, and the transition radiation tracker (TRT). The inner detector is immersed in a magnetic field of 2 Tesla provided by a superconducting solenoid surrounding it. The tracking detectors measure the momentum of charged particles within $|\eta| < 2.5$. The TRT also provides electron identification information. The electromagnetic (EM) calorimeter lies beyond the solenoid, and fully contains the showers from electromagnetic and fully interacting electrons and photons to measure their energy. Hadronically interacting particles pass through the EM calorimeter to the hadronic calorimeter. The hadronic calorimeter stops all particles except for muons and neutrinos.⁷ Beyond the hadronic calorimeter lies the muon spectrometer (MS). The MS measures the momenta of muons outside of the calorimeters. A toroidal magnet system surrounding the barrel and endcaps cause muons to bend in the MS so that their momenta can be measured. A three-tier trigger system is used to identify and record interesting events. The trigger must reduce the event rate from 20 MHz to approximately 500 Hz. The exact output rate is not fixed, but it must average a rate of approximately 500 Hz so that all recorded events can be stored within the allocated storage space.

⁷In rare cases very high momentum particles punch through the hadronic calorimeter. In addition any new particles that interact only weakly also pass through without interacting.

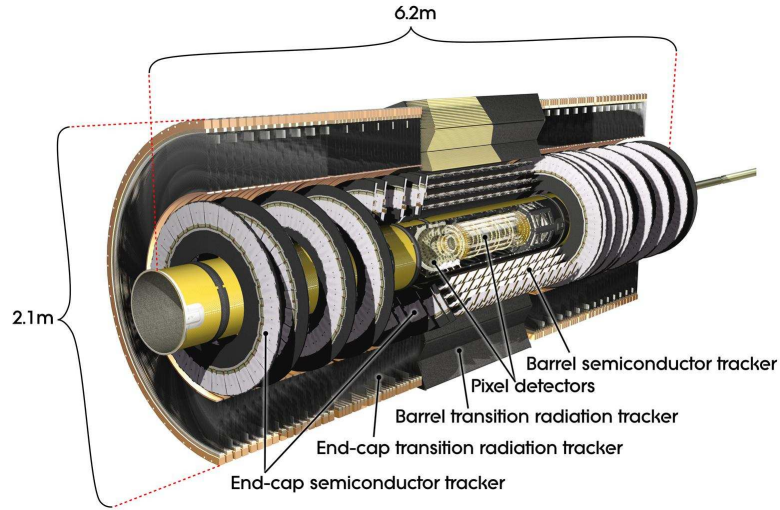


Figure 6.2: Diagram of the ATLAS inner detector systems.

6.1 The inner detector

The inner detector is divided into three sub-detectors. The two sub-detectors closest to the interaction point use silicon devices to achieve the highest granularity to provide the best track position and momentum resolution. The outermost detector is a gaseous straw detector which improves the momentum resolution without the high cost of a silicon based detector. Figure 6.2 shows a diagram of the inner detector.

6.1.1 The pixel detector

The pixel detector [55, 56] uses silicon pixel technology to provide high granularity for precision tracking within the high track multiplicity environment. The proximity to the collision point and the high granularity of the detector allows the reconstruction of secondary vertices from b-meson decays that travel on average $c\tau \sim 0.5$ mm before decaying. The detector consists of three barrel layers, at radii of 4.3 cm, 10.1 cm, and 13.2 cm from the center of the beam pipe and five disks on either side of the barrel situated longitudinally from 0.5 m to 0.9 m from the center of the barrel. The principle component of the pixel detector is a sensor module. The entire pixel detector is comprised of more than 4000 modules having dimensions of approximately $16 \text{ cm} \times 60 \text{ cm}$. Each module contains 46080 individual pixel cells having dimensions of $50 \mu\text{m}$ in the ϕ direction and $400 \mu\text{m}$ in z . On each module, pixel cells are read out by 16 front end chips bump-bonded to the silicon sensor. Additional electronics on the opposing side of the silicon sensor manage trigger, timing, configuration, and data readout.

Pixel sensors are composed of an n-type semiconductor providing negatively charged electron charge carriers. A p-type semiconductor is placed on the side opposing the bump-bonded readout chips. A voltage ranging between 200 V and 600 V is applied at the p-type side while the bump-bonded side is held at ground. When a particle passes through the semiconductor, electrons are liberated and drift towards the bump-bonded readout. Immediately under each bump-bond is a region that has higher doping to attract the drifting electrons to the bump-bond. The current from the collected electrons is amplified and discriminated in the front end chip. The discriminator threshold is configurable and is set so that signal pulses are efficiently identified while noise is sufficiently rejected. The leading edge time and time over threshold are saved for each pixel that has a signal passing the threshold. This information is stored on a buffer and is read out if a level 1 trigger accept signal is received.

6.1.2 The semiconductor tracker

The semiconductor tracker (SCT) also uses silicon technology and lies outside of the pixel detector. Four barrel modules and eighteen endcap disks (nine on either side of the barrel) make up the SCT. The SCT has 2112 modules in the barrel and 1976 barrels in the endcap. Each module has two back-to-back readout sensors which are slightly offset at stereo angle of $40 \mu\text{m}$ to provide resolution along the long axis of the sensor. Each readout sensor has two silicon wafers each having 768 sensing strips of length 6.3 cm and with a pitch of $80 \mu\text{m}$. Matching strips are connected together so that each channel reads out a $12.6 \text{ cm} \times 80 \mu\text{m}$ area. The total number of readout channels is approximately 6 million. During nominal LHC collisions the hit occupancy of the SCT is approximately 5%. The noise occupancy is required to be less than 1% of the hit occupancy to ensure good tracking efficiency. The hit resolution of an SCT module is $17 \mu\text{m}$ in the $R - \phi$ direction and $580 \mu\text{m}$ in the z direction in the barrel and radial direction in the endcap. The SCT is designed so that most tracks within $|\eta| < 2.5$ cross at least four SCT layers corresponding to eight sensor modules. A track having $|\eta| < 1.17$ is fully contained within the barrel.

The SCT sensors work much like the pixel sensors. The bulk material is an n-type semiconductor with a bias voltage between 100 V and 500 V. The sensors are connected to a p-type deposition and are held at ground. When a charged particle passes through the semiconductor electrons are liberated and flow towards the sensor. Front end electronics amplify and discriminate the input and record when a hit occurs. The data are stored in a pipeline and are read out if a level-1 trigger accept signal is received.

6.1.3 The transition radiation tracker

The transition radiation tracker (TRT) is a gaseous straw detector that lies outside of the SCT. A mixture of 70% Xenon, 27% CO₂ and 3% O₂ of gas fills approximately 350,000 sensing straws. The barrel detector has approximately 50,000 straws that are 1.5 m in length arranged parallel to the beam. A glass bead in the center of the wire separates wire into two 0.75 m sensitive sections. The endcap detectors consist of 20 straw wheels on either side of the barrel. Endcap straws are approximately 35 cm in length and are arranged radially. Tracks are fully contained in the barrel within $|\eta| < 0.62$ and in the endcap within $|\eta| < 2.0$. On average, a track has 35 TRT hits. Despite the poorer resolution of an individual straw relative to the silicon detectors, the large number of hits at a large radius significantly improves the tracking resolution.

A TRT straw has a diameter of 4 mm with a sensing wire in the center. The straw is filled with a gas mixture that ionizes when a charged particle passes through. The sensing wire is held at ground and the wall is held at a high negative voltage (typically 1 kV to 2 kV). When a charged particle passes through the wire, ions are created along the path of the particle and drift towards the sensing wire. Charge is collected at the end of the wire and the signal is amplified and passed to a discriminator. The discriminator records pulses at two thresholds, a low threshold for tracking, and a high threshold to identify transition radiation. The low-threshold discriminator records the presence of a signal over threshold in 3.125 ns intervals to provide pulse width information. Data are stored in memory on the front end and are read out if a level-1 trigger accept signal is received. The time over threshold for a given pulse determines the distance between the sensing wire and the closest approach of the particle. Therefore, the position measurement is more precise than the physical size of the straw.

The TRT provides tracking measurements and electron identification by detecting transition radiation (see Section 3.4.3 for a discussion on transition radiation). A radiator material is placed between the straws that causes the electron to radiate photons as it passes through regions having different dielectric constants. Transition radiation photons cause a much higher signal in the sensor and are identified by a higher level discriminator threshold than is used for normal tracking.

6.1.3.1 TRT monitoring

The response of the TRT electronics is scanned periodically. Consistent scanning over time allows the state of the TRT to be monitored for long term effects. Of particular concern is the effect of radiation on the gain of the pulse amplifier. Changes in the gain can be monitored by measuring the noise amplitude. The rate at which noise pulses are accepted depends on the discriminator threshold. In this scan the rate at which the discriminator threshold is passed by noise pulses is scanned

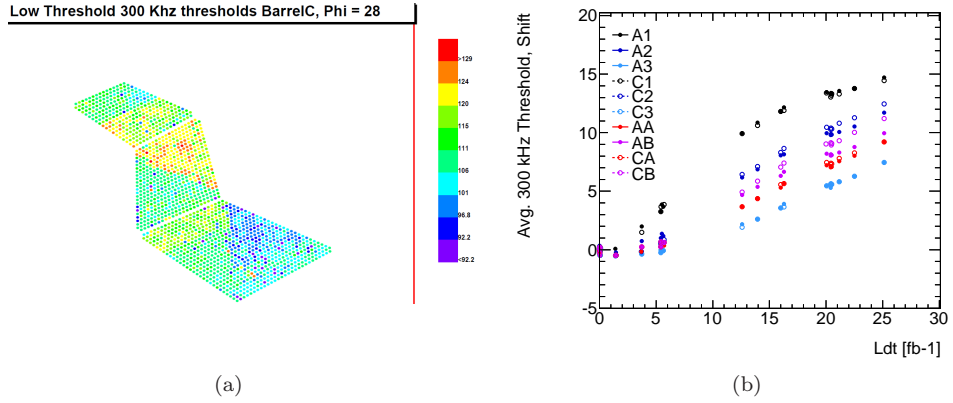


Figure 6.3: Discriminator thresholds at which the noise rate is 300 kHz for 1/32 of one half of the TRT barrel (a) and the noise rate averaged over parts of the detector and offset to a common value as a function of the instantaneous luminosity (b). The change in threshold indicates an effect on the gain of the pulse amplifier from radiation.

as a function of the discriminator threshold. The benchmark rate is 300 kHz – the rate that gives approximately 2% detector occupancy. The value of the discrimination threshold at which the rate is closest to 300 kHz is recorded for every channel. Figure 6.3(a) shows a graphical representation of the benchmark threshold for 1/32 of one half of the TRT barrel. Regular scans were performed throughout the 2011 and 2012 data taking periods. Figure 6.3(b) shows the benchmark threshold averaged over different parts of the detector and offset to a common value plotted as a function of integrated luminosity. A clear trend is present in the thresholds indicating an effect from the radiation dose. The changes in threshold are well within the dynamic range of the discriminator. Future monitoring will be important to understanding the effects of radiation on the readout electronics.

6.2 Calorimeters

The ATLAS calorimeters provide energy measurements for electromagnetically interacting electrons and photons in the electromagnetic (EM) calorimeter and all hadrons up to $|\eta| < 4.8$ in the tile and endcap calorimeters. Two types of detection technologies are used. In the EM calorimeter and endcap calorimeters, sensors are interleaved with lead absorbers and liquid argon. In the tile calorimeter, lead tiles are interleaved with scintillating tiles. Figure 6.4 shows a diagram of the calorimeters in ATLAS.

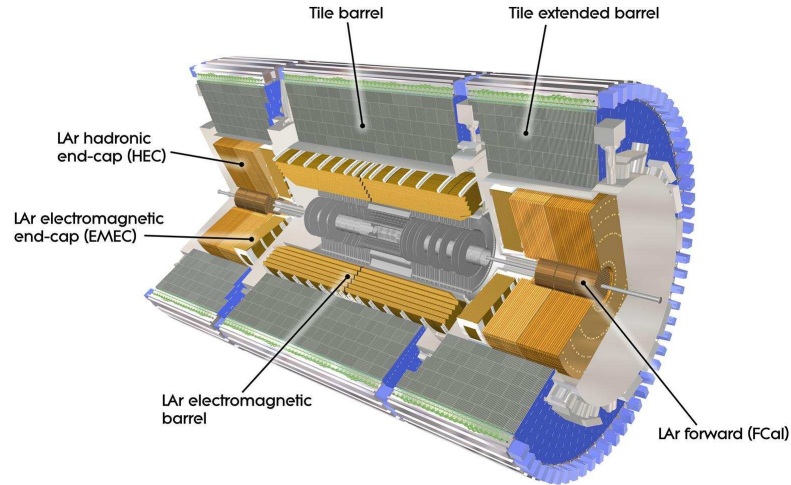


Figure 6.4: Diagram of the ATLAS inner detector systems.

6.2.1 Liquid argon calorimeters

The EM barrel and endcap calorimeters, the hadronic endcap calorimeter (HEC), and the forward calorimeters (FCal) employ a design that interleaves copper sensors and lead absorbers with liquid argon flowing on either side. The copper sensors are composed of three layers with the outer layers held at high voltage and the inner layers held at ground. When a particle enters the calorimeter it begins to shower when it interacts with the high density lead. The secondary particles created by the shower ionize the liquid argon and the ions drift towards the high voltage sensors. The charge is collected via capacitive coupling between the outer copper layers and the inner layer and the signal is digitized with a 16 bit ADC before being read out.

The EM barrel calorimeter covers $|\eta| < 1.4$ and is designed to be hermetic in ϕ . The barrel is divided at $\eta = 0$ into two halves. Figure 6.5 shows a diagram of a section of the EM barrel. Each half has 1024 accordion-shaped copper electrodes spaced between accordion-shaped absorbers. The accordion shape ensures that there is no ϕ dependence on the particle energy measurement. The copper sensor accordions have three segments in depth (radially from the interaction point). The first layer has fine segmentation in η to provide shower shape measurements. The second layer occupies most of the radial depth and is where most of the energy is collected. The third layer has the coarsest segmentation and collects the end of showers from high p_T electrons and photons. The barrel calorimeter has a total of approximately 10^5 readout channels. A liquid argon presampler is added in front of the barrel calorimeter and is used to correct for the energy lost by the particle in the solenoid and cryostat walls.

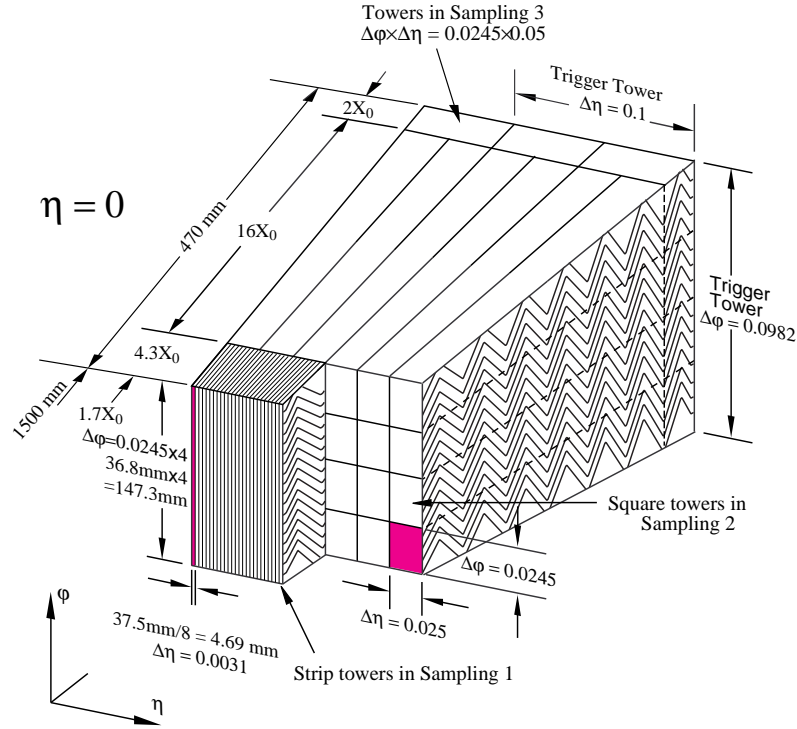


Figure 6.5: Diagram of the accordion structure of the LAr calorimeter showing the sensor granularity.

The EM endcap calorimeter is instrumented similarly to the barrel calorimeter with 96 accordion sensors in each endcap. The endcaps extend EM calorimetry by covering $1.375 < |\eta| < 3.2$. Each endcap has approximately 30,000 readout channels. The HEC provides hadronic calorimetry between $1.5 < |\eta| < 3.2$ and is placed behind the EM endcap detector. The HEC is composed of copper plates oriented perpendicular to the beam axis. Liquid argon flows in between absorber and sensor plates and the signal is collected similarly to the barrel and endcap calorimeters. Three forward calorimeters cover $3.2 < |\eta| < 4.9$. To cope with the high radiation environment, a higher density design is used. Liquid argon channels are created by the space between a bulk absorber made of copper in the first FCal module (closest to the beam spot in z) and tungsten in the other two module and copper tubes that lie parallel to the beam axis. The signal is collected by electrodes inserted in the tube. The three FCal have approximately 30,000 readout channels.

6.2.2 The tile calorimeter

The tile calorimeter measures the energy of hadronically interacting particles in a barrel section between $|\eta| < 1.0$ and extended barrel sections between $0.8 < |\eta| < 1.7$. The detector is composed of alternating lead absorbing tiles and scintillating tiles. As a particle traverses the hadronic calorime-

ter, it showers in the lead tiles and the shower creates scintillation light as it passes through the tiles. The light is collected by wavelength-shifting fibers and directed towards photomultiplier tubes at the edge of the detector. Pulses from the photomultiplier tubes are shaped and passed to an ADC which measures the energy with 16 bit dynamic range.

6.3 Muon spectrometer

The muon spectrometer lies outside of the calorimeters to measure the momenta of muons that pass through. Muons that enter the barrel muon system within $|\eta| < 1.0$ pass through a toroidal magnetic field generated by eight large toroidal superconducting magnets oriented symmetrically in phi. The toroidal field is approximately 0.5 Tesla in the bulk, but depends heavily on the distance from the magnet. Two endcap toroid systems complete the toroidal field for muons having $1.4 < |\eta| < 2.7$. Four detector technologies are used in the muon system. Monitored drift tubes (MDT) and cathode strip chambers (CSC) provide precision tracking measurements and resistive plate chambers (RPC) and thin gap chambers (TGC) provide trigger information. The various detector technologies are:

- Monitored Drift Tubes – Approximately 370000 tubes are arranged longitudinally in the barrel and azimuthally in the endcap wheels. The tubes are 30 mm diameter aluminum cylinders with a sensing wire in the center. The tubes are filled with a gas that is easily ionized by charged particles. Ions are attracted towards a central wire that is held at high voltage. The signal is read out by electronics at the end of the wire.
- Cathode strip chambers – CSCs are placed at high pseudorapidity and closer to the beam spot than the MDTs. The chambers are multiple wire proportional chambers with strip readouts as the cathode. A gas fills the chamber and ions that are produced drift to the cathode strips where the signals are read out. The CSCs have a total of 67000 readout channels.
- Resistive plate chambers – RPCs provide trigger information in the barrel. Two resistive plates are placed close together with a gas gap in between. Ionized particles are attracted towards readout strips. The narrow gap and the choice of gas mixture creates a fast pulse that can be used for triggering.
- Thin gap chambers – TGSs are used for triggering in the endcap. The design is a multiple wire proportional chamber with wire pitch, readout pitch, and gas mixture chosen to create a quick pulse that can be used for triggering.

6.4 Trigger

A three-level trigger system selects interesting events for offline storage and data analysis. The first level trigger (L1) is implemented in hardware to provide a quick trigger decision to the front end electronics. The second level trigger (L2) and third level trigger, called the event filter (EF) are implemented in software and provide a more accurate measurement of event kinematics. The L2 trigger only runs on regions of interest (ROI) provided by the level 1 trigger and the EF implements a full event reconstruction. The size of the buffers on the front end electronics are limited and the level one trigger must make a decision within $2.5 \mu\text{s}$ of the collision or data are lost. This corresponds to 100 beam crossings at a bunch spacing of 25 ns. The L1 trigger must reduce the data rate from the 40 MHz collision rate to 75 kHz. Level one trigger signals are received from the muon system, the electromagnetic calorimeter, the hadronic calorimeter, and the forward calorimeter. Trigger objects are defined based on which sub-detector fired the trigger and are categorized into muons, electromagnetic deposits, central jets, forward jets, and $E_{\text{T}}^{\text{miss}}$. The threshold for the various objects is configurable and triggers may be prescaled to reduce their rate. The level two trigger receives data from ROIs where the level one trigger fired. The number of regions of interest that are identified depend on the event topology, but the full event data is available to the level two trigger if necessary. The level two trigger runs basic event reconstruction in the ROIs and provides a decision within 1 to 10 ms. The output rate of the level 2 trigger must be less than 1 kHz. The EF trigger does a full event level reconstruction and a more detailed calculation of particle momentum and energies. The EF reduces the output rate to approximately 400 Hz. The full data from each event is approximately 1 Mb in size.

6.5 Data taking conditions

The performance and the integrity of the data readout of each sub-detector is monitored throughout the data taking period. The information is saved for each lumi block, a period of time corresponding to approximately two minutes of data taking. If any sub-detector performs non-optimally the data recorded during that time is labeled as such. A good runs list (GRL) defines the set of data in which all sub-detectors required for a given analysis are performing optimally. Events that fail the good runs list requirement are removed from the analysis and the total luminosity analyzed is calculated with respect to data that pass the good runs list.

6.6 Monte Carlo simulation

The data collected at the LHC is a mix of many processes. For example, dilepton events can originate from a number of electroweak processes including Z , WW , ZZ , and $t\bar{t}$. A prediction of each contributing process is required in order to understand the makeup of the data and to determine which event selection is optimal for selecting a given signal process. In principle, predictions of differential distributions amounts to solving the matrix element of a given process, but in practice the matrix elements can be difficult or impossible to solve analytically. Additional complication arises from the nature of collisions at the LHC. Collisions can occur between different partons in the proton, and a single proton-proton collision can create hundreds of final state particles. The simulation must also include the effects of pileup. The only way to successfully make predictions is to simulate events using the Monte Carlo method. The basic Monte Carlo method integrates a function by filling a space spanned by the function by throwing random numbers. When sufficient statistics are collected the integral of the function is simply the number of throws that fall below the function divided by the total number of throws. In the Monte Carlo simulation used for the LHC the integration occurs over multiple dimensions. This includes the matrix element, the parton distribution functions, and the probability for additional initial state radiation and final state radiation. Although Monte Carlo simulation can be complicated, its advantage is that it closely mimics the randomness of proton collisions. Each random sampling in the multidimensional space considered by the simulation corresponds to one event and many events are generated to cover the multidimensional space of interest. This simplistic description outlines the basic methods used, but often optimizations are made to improve the computational speed and accuracy of the simulation.

A number of different Monte Carlo generators are used in ATLAS. Each generator is designed to simulate a certain set of processes, but they handle event generation in different manners. Generators such as Pythia and Alpgen are tree level generators – only tree level diagrams are simulated and no loop calculations are included. Sherpa and MC@NLO are next to leading order generators, allowing a loop to enter the calculation. Many other generators exist and are discussed as needed in the analysis sections. Often generators predict slightly different kinematics for the same process. In many cases a generator is chosen that best models the data. Differences in the predictions from different generators are also used to evaluate systematic uncertainties in the theory.

Complete event simulation adds additional steps to the generation process to accurately reproduce the LHC environment. The remnants of the colliding protons must be simulated. When a hard collision occurs between two partons, the remaining partons break up, leaving tracks in the detector. The probability for multiple interactions of partons also exists and must be simulated. Event generators produce quarks and gluons in the final state. However, the strong force dictates

that quarks and gluons cannot be isolated, so when a single quark or gluon is produced, additional quarks and gluons are pulled out of the vacuum. These additional particles form into a collimated cone that points along the direction of the original quark or gluon. This process of hadronization must also be included in the event simulation. The high luminosity of the LHC beams produces multiple proton-proton interactions in a bunch crossing. A selected event is therefore composed of the hard scatter of interest plus a number of minimum bias interactions which must be included in the event simulation.

Once an event is fully generated, all final state particles, which can number in the hundreds or thousands, are propagated through the detector and the detector response is simulated. The propagation of charged particles depends on a detailed map of the magnetic field and of the position and properties of every passive and active detector element. These objects are simulated in a GEANT4 model of the detector. As particles pass through detector elements a probabilistic model of particle interactions with matter determines the energy lost. Every sub-detector employs a dedicated simulation to map the deposited energy into a signal that would be produced by such a deposition. The simulated detector signals are saved in the same format as they are for data. Through this procedure the signature of any type of event is simulated. It should be noted that additional corrections are usually derived to correct the simulation to the data, but in many cases the simulation performs quite well.

6.7 Coordinate system

All detector elements and particle paths are labeled using a right handed spherical coordinate system centered at the middle of the beam pipe and in the center of the detector along the beam pipe. Nominally the distribution of the positions of proton-proton collisions is centered at $(x, y, z) = (0, 0, 0)$. Coordinates are usually expressed as (r, ϕ, θ) or (r, ϕ, η) where r is the radial component, ϕ is the azimuthal angle, and θ is the zenith angle. Often particle trajectories use the pseudorapidity, η , instead of θ , where

$$\eta = -\ln\left(\tan\left(\frac{\theta}{2}\right)\right).$$

The use of η over θ is preferred because the particle multiplicity is approximately constant as a function of η .

CHAPTER 7

Common object selection

The following chapters present multiple independent analyses that select final state electrons, muons, and jets and use E_T^{miss} to identify the presence of neutrinos. Much of the identification criteria for these objects is the same across these analyses. However, the analyses presented span three years of data taking during which the identification criteria used to select these objects were improved. This section describes the baseline identification criteria for these objects. Any differences with respect to a particular analysis are described therein.

7.1 Tracks

The track reconstruction first identifies a set of hits in the detector that are consistent with a particle track and then runs a track fit on the points to extract the track parameters. The Kalman track fitting algorithm is used for tracks recorded in ATLAS [57, 58]. A track fit is carried out iteratively starting with hits in just the pixel and the first layer of the SCT. The fitted track parameters are extrapolated to identify candidate hits in the full SCT and is refit with the additional points. Quality cuts and overlap criteria are applied and passing tracks are extended into the TRT. A final track fit includes hits from the full inner detector. Tracks having a minimum p_T of 500 MeV are used for physics analyses presented here.

7.2 Calorimeter clusters

Calorimeter clusters are constructed from groups of individual calorimeter cells [59]. The nominal clustering algorithm used in ATLAS is called topological clustering. A topological cluster is built by iteratively adding cells surrounding a seed cell. A seed cell has a measured energy $4 \times \sigma_{\text{noise}}$ where σ_{noise} is the cell's RMS noise energy. All cells surrounding the seed cell having $2 \times \sigma_{\text{noise}}$ are included and all neighbors to those having any positive signal are included to recover tails of the energy deposit. Cells can only be associated to one calorimeter cluster. Clusters that have multiple separated energy depositions are split into separate clusters. The cluster energy is measured at the electromagnetic scale and is calibrated to match the response of single hadrons from simulation. Further corrections are applied to account for noise and pileup contributions.

7.3 Electrons

Electrons traverse the inner detector producing tracking hits and stop in the electromagnetic calorimeter (EM) leaving a narrow shower (see Section 3.4 for a description of electromagnetic interactions in matter and Section 6.2.1 for a description of the EM calorimeter). Electrons are seeded from EM calorimeter showers using a sliding window technique [59]. Calorimeter clusters are matched to

inner detector tracks in a loose $\Delta\eta \times \Delta\phi$ window of 0.05×0.1 . The matched track momentum must be at least 10% of the cluster energy. Wider matching criteria in $\Delta\phi$ and the large allowance for the momentum difference between the track and the cluster account for energy loss via bremsstrahlung in the inner detector. Additional cuts are applied on a number of shower shape variables that discriminate between narrow electromagnetic showers produced by electrons and jets that have wider showers and more hadronic activity. The variables used and the cuts applied on those variables are defined at three working points: `loose`, `medium`, and `tight`. The three working points trade off between real electron identification efficiency and background rejection. The `loose` working point has the highest efficiency, but also the largest background contamination while `tight` has the lowest efficiency, but rejects more background. A background rejection of approximately 500, 5000, and 50000 is achieved for the `loose`, `medium`, and `tight` working points respectively [60]. In 2011 and 2012 the identification criteria were optimized to account for the effects of increased luminosity and the working points were correspondingly updated to `loose++`, `medium++` and `tight++`. The analyses presented in this dissertation utilize the `tight` and `medium++` working points. Additional cuts are applied on the electron track quality that also depend on the working point. To reject electrons from photon conversions, a hit in the pixel b-layer is required if the track crosses an active b-layer module. The track also must have a minimum number of hits in the silicon detectors. The TRT is used to identify electrons through transition radiation by requiring that a fraction of hits in the TRT pass the high-threshold tag (see Section 3.4.3 for a description of transition radiation and Section 6.1.3 for a description of the TRT).

An electron is rejected if it falls in a region of the calorimeter where disabled cells or readout boards affect the cluster energy measurement. Cuts on the z_0 and d_0 significance remove non-collision backgrounds, electrons from heavy flavor decay, photon conversions, and particles from pileup interactions. In order to further reject jet backgrounds, electrons must be isolated from additional calorimeter deposits and inner detector tracks. The transverse energy of calorimeter clusters or tracks is measured within a cone around the object defined by $\Delta R = \sqrt{(\Delta\phi)^2 + (\Delta\eta)^2} < X$. Typical values for X range between 0.1 and 0.4. The track isolation variable is labeled as `ptCone` and the calorimeter isolation variable is labeled as `EtCone`. A numerical suffix indicates the value of X used – for example `ptCone30` uses a cone of $\Delta R = 0.3$. The track isolation sums all track momenta around an object, excluding the object itself. The calorimeter isolation is the scalar sum of calorimeter clusters falling within the defined cone. It does not include the electron cluster energy itself and is corrected for energy contributions from pileup interactions. Most electrons are also reconstructed as jets and must be removed from the list of jet objects using an overlap procedure. Overlap removal may be performed with respect to other objects, and the exact procedure is analysis

dependent.

The electron energy is measured using the calorimeter cluster. The track p_T measurement is not used because the electron radiates energy via bremsstrahlung radiation as it passes through the Inner Detector material (see Section 3.4.2 for a description of bremsstrahlung radiation). If the electron track has more than four silicon detector hits, the track η and ϕ are used to complete the four-vector. Otherwise, the cluster η and ϕ are used. In 2012 the electron track measurements were improved by refitting electron tracks using a Gaussian Sum Fitter [61] that allows for energy loss at points where matter is traversed in the track fit.

The electron energy scale and resolution are measured in data using events from the Z resonance mass peak [60]. A comparison is made to the simulated Z lineshape to extract p_T and η dependent smearing factors to correct the simulated Z lineshape to agree with the data.

7.4 Muons

Muons are identified using the *Staco Combined* algorithm [59] which performs a statistical combination between a muon spectrometer track and a matched inner detector track. Quality cuts are applied on the inner detector track to ensure that it is well measured. The track must have a minimum number of hits in the silicon and TRT detectors: one hit in the pixel b-layer and two hits in the entire pixel detector, 6 hits in the SCT, less than 3 holes (where a hit is expected but not observed) in the entire silicon detector, and an η dependent requirement of the number of hits in the TRT. Cuts are applied on the z_0 and the d_0 significance of the inner detector track relative to the primary vertex. These cuts reduce backgrounds from heavy flavor decays, cosmic muons, and other non-collision backgrounds. To further reject muons produced in heavy flavor jets, muons are required to be isolated. Both calorimeter based and track based isolation variables are used that follow the same calculation that is used for electrons.

As in the electron case the muon energy scale and resolution are measured in data using events from the Z resonance mass peak [62]. A comparison is made to the simulated Z lineshape to extract p_T and η dependent smearing factors to correct the simulated Z lineshape to agree with the data.

7.5 Jets

Quarks and gluons produced in pp collisions hadronize to produce a collimated shower of charged and neutral particles collectively called a jet. Jet reconstruction consists of grouping calorimeter clusters into one object that best estimates the direction and momentum of the original particle. Jet reconstruction can also be performed on tracks, but all jets used herein use calorimeter clusters.

Jets are reconstructed using the anti- k_t algorithm [63] with a distance parameter of $R = 0.4$. The jet energy is measured at the same scale as deposits in the electromagnetic calorimeter (EM scale) and is corrected to most accurately recover the true jet energy [64]. Jets are first corrected for energy deposits from pileup collisions with weights that depend on the pileup multiplicity and the number of reconstructed primary vertices. An energy calibration that corrects to the hadronic scale is derived from simulation. Finally additional in-situ corrections are applied to achieve the final jet energy. The corrections are derived from Z + jet, γ + jet, and dijet events [65]. Jet energy scale uncertainties are also derived using these methods.

Jets originating from pileup collisions are rejected by requiring a minimum jet vertex fraction (JVF). The JVF is the momentum fraction of tracks pointing to the jet area that originate from the highest $\sum p_{T,\text{track}}^2$ vertex. Jets that originate from pileup vertices have few tracks from the highest $\sum p_{T,\text{track}}^2$ vertex pointing to it and therefore have JVF near zero. For jets originating from the highest $\sum p_{T,\text{track}}^2$ vertex most of the pointing tracks originate from this vertex and the jet has JVF near one. Jets that have no associated tracks are assigned $\text{JVF} = -1$ and are not vetoed by the JVF requirement. The specific JVF cuts depend on the pileup conditions and are therefore analysis dependent.

Jets initiated by a b-quark tend to have sufficiently long lifetimes such that a secondary vertex from the B hadron decay can be identified. Multiple algorithms are implemented to identify b-quark initiated jets including the SV1, IP3D, and JetFitter algorithms [66]. The SV1 algorithm attempts to find a secondary vertex among the tracks associated to a jet. The IP3D algorithm uses the impact parameters of tracks associated to a jet in a likelihood ratio technique. The JetFitter algorithm uses the topology of b-hadron and c-hadron decays within the jet. For 2012 data, an additional algorithm, MV1, combines the SV1, IP3D, and JetFitter algorithms in a neural network to take full advantage of the b-tagging power of the three methods.

7.6 Primary vertex

The primary vertex, the pp interaction vertex from which the high p_T objects in the event originate, is identified as the vertex that has the largest scalar sum of track p_T associated with it. The primary vertex identification efficiency depends on the final state objects present in the event because they are included in the primary vertex determination. For dilepton events the efficiency is near 95%. Figure 7.1 shows the primary vertex reconstruction efficiency for events having various final state objects.

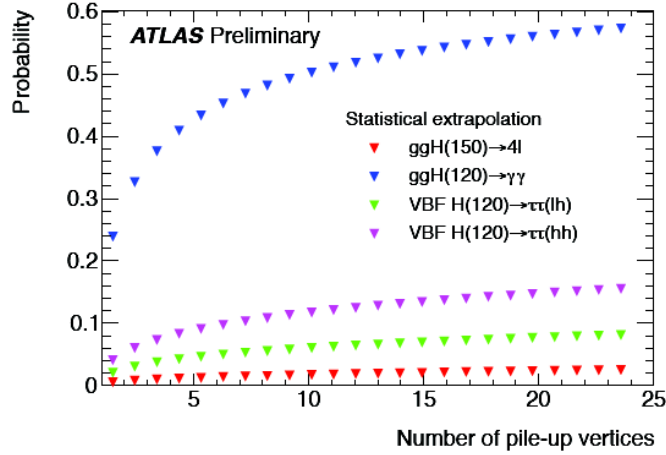


Figure 7.1: Probability to reconstruct the incorrect primary vertex as a function of the number of pile-up vertices. Events having multiple final state leptons have less than 5% miss-identification probability, while events having photons can have over 50% miss-identification probability.

7.7 Missing transverse momentum

The missing transverse momentum (E_T^{miss}) measures the momentum imbalance in the transverse plane to identify particles that escape detection. The E_T^{miss} , defined as $E_T^{\text{miss}} = -\sum_i \vec{p}_T^i$, is the vector that balances the summed transverse momentum of all objects in the event. Two versions of E_T^{miss} are used in the analyses presented here. In 2010, a simple E_T^{miss} definition, LOCHADTOPO, which sums the calibrated transverse energy of all calorimeter clusters was used. The transverse momentum of any identified muons are also added into LOCHADTOPO. In 2011 and 2012, a refined calculation of E_T^{miss} , RefFinal, was used. This definition sums the calibrated transverse momenta of all identified objects and adds any calorimeter cluster that is not associated to an identified object. This calculation provides a better E_T^{miss} resolution by using the momenta of calibrated objects [67, 68]. The RefFinal calculation is,

$$E_{x(y)}^{\text{miss,RefFinal}} = E_{x(y)}^{\text{miss,electron}} + E_{x(y)}^{\text{miss,\gamma}} + E_{x(y)}^{\text{miss,\tau}} + E_{x(y)}^{\text{miss,jets}} + E_{x(y)}^{\text{miss,soft}} + E_{x(y)}^{\text{miss,\mu}} + E_{x(y)}^{\text{miss,calo-\mu}} \quad (7.1)$$

where each term is the negative sum of the momenta of all objects associated to that term. The calculation includes the calibrated momenta of all identified electrons, photons, tau leptons, jets, and muons. Specific quality criteria, identification cuts, and p_T cuts are applied on each object. All calorimeter clusters that are not associated to an object are included in the $E_{x(y)}^{\text{miss,soft}}$ term. In the $E_{x(y)}^{\text{miss,soft}}$ term was originally separated into a soft jets term and a cell out term. The soft jets term consists of low p_T jets that fail the p_T requirement of the $E_T^{\text{miss,jets}}$ term. All other unclustered energy enters the cell out term. Near the end of the 2012 data taking run these two terms were combined. An energy flow method is used to improve the resolution of calorimeter clusters in the soft

term. In the energy flow calculation a match between inner detector tracks and calorimeter clusters is attempted. If a track match is successful, the cluster E_T measurement is replaced with the track p_T measurement. The $E_{x(y)}^{\text{miss,calo}-\mu}$ term accounts for double counting of muon energy deposits in the calorimeter. If a muon is isolated from nearby jets by $\Delta R > 0.3$, the combined muon momentum measurement is used which corrects for energy loss in the calorimeter. In this case $E_{x(y)}^{\text{miss,calo}-\mu}$ is zero. If a muon is not isolated its energy loss in the calorimeter cannot be distinguished from the jet energy. In this case the muon momentum is measured using only the muon spectrometer and the estimated energy loss in the calorimeter is included in $E_{x(y)}^{\text{miss,calo}-\mu}$.

7.7.1 E_T^{miss} derived quantities

It is often useful to combine E_T^{miss} with other kinematic variables to take advantage of correlations between the invisible and visible final state particles. The $E_T^{\text{miss,rel}}$ variable is introduced to reduce the impact of lepton or jet momentum mismeasurements. It is defined as

$$E_T^{\text{miss,rel}} = \begin{cases} E_T^{\text{miss}} & \text{if } \Delta\phi \geq \pi/2 \\ E_T^{\text{miss}} \times \sin \Delta\phi & \text{if } \Delta\phi < \pi/2 \end{cases} \quad (7.2)$$

where $\Delta\phi$ is the difference in ϕ between the E_T^{miss} vector and the nearest lepton or jet. If the E_T^{miss} is near a lepton or jet $E_T^{\text{miss,rel}}$ is small. Large values of $E_T^{\text{miss,rel}}$ are attained if the E_T^{miss} is large and does not point along a lepton or jet. Distributions of $E_T^{\text{miss,rel}}$ are shown for the HWW analysis in Figure 9.5.

The Axial E_T^{miss} variable takes advantage of the correlation between E_T^{miss} and the dilepton p_T when the dilepton system is boosted against the object that produces the E_T^{miss} . Axial E_T^{miss} is defined as

$$\text{Axial } E_T^{\text{miss}} = -E_T^{\text{miss}} \times \cos \Delta\phi(\vec{p}_T^{\ell\ell}, E_T^{\text{miss}}) \quad (7.3)$$

Figure 7.2 shows a diagram of the Axial E_T^{miss} calculation. Axial E_T^{miss} is equivalent to E_T^{miss} when the E_T^{miss} is directly back-to-back with the dilepton p_T . When the E_T^{miss} is exactly perpendicular to the dilepton p_T , Axial E_T^{miss} is zero. Axial E_T^{miss} is negative when the E_T^{miss} points in the same hemisphere as the dilepton p_T and is positive if the E_T^{miss} points in the opposite hemisphere. Axial E_T^{miss} distributions are shown in Figures 8.12 and 8.14 for the $ZZ \rightarrow \ell^+ \ell^- \nu \bar{\nu}$ analysis.

7.7.2 Track based E_T^{miss}

A track based E_T^{miss} ($E_T^{\text{miss,track}}$) provides a complimentary measurement of the missing transverse momentum in an event. The $E_T^{\text{miss,track}}$ is the inverse of the vector sum of the transverse momenta of all tracks that are consistent with having originated from the primary vertex. The two definitions

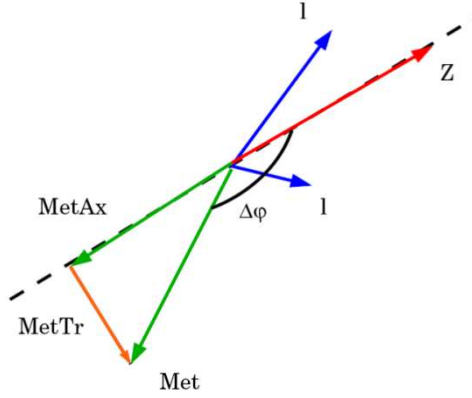


Figure 7.2: Diagram of the Axial E_T^{miss} calculation. In the diagram Axial E_T^{miss} is labeled as **MetAx**. Axial E_T^{miss} is equivalent to E_T^{miss} if the E_T^{miss} is directly back-to-back with the $\vec{p}_T^{\ell\ell}$, otherwise the value is reduced by the cosine of the angle between them and is linear with true E_T^{miss} .

are complimentary; the E_T^{miss} includes the momenta of all particles within $|\eta| < 4.9$, but is pileup dependent while $E_T^{\text{miss,track}}$ is pileup independent, but only includes charged particles within $|\eta| < 2.5$. Therefore, $E_T^{\text{miss,track}}$ and E_T^{miss} are used together to achieve more rejection of fake E_T^{miss} backgrounds.

The $E_T^{\text{miss,track}}$ sums all good tracks originating from the primary vertex having $p_T > 500$ MeV and $|\eta| < 2.5$. To remove poorly measured tracks, they must have at least one hit in the pixel detector and at least five hits in the SCT detector. To ensure that the tracks originate from the primary vertex, the d_0 with respect to the highest $\sum p_T^{\text{track}^2}$ vertex must be less than 1.5 mm and $z_0 \sin \theta < 1.5$. The factor of $\sin \theta$ accounts for the poorer z_0 resolution for tracks at lower θ (higher η).

This dissertation focuses on events that have multiple electrons or muons. In a small number of cases the track associated with an electron or muon is not included in the $E_T^{\text{miss,track}}$ calculation. In these cases the electron or muon momentum is included instead. To improve the resolution of $E_T^{\text{miss,track}}$ the momentum from all electron tracks are replace with the cluster measurement. The cluster measurement is better than the track measurement because undergo bremsstrahlung radiation in the inner detector causing the track momentum measurement to be biased to because lower values. The calorimeter cluster collects the radiated photons and is a more accurate measurement of the electron's momentum.

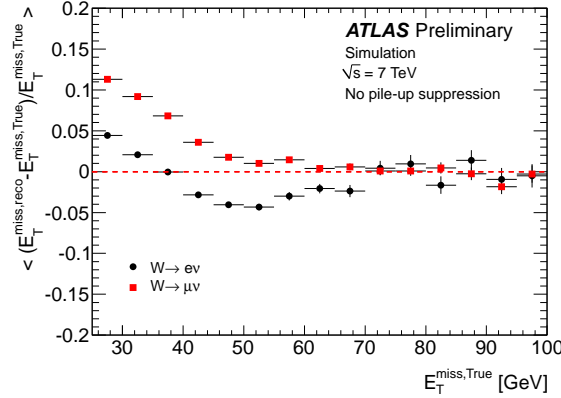


Figure 7.3: The linearity of the reconstructed E_T^{miss} with respect to the true E_T^{miss} . At low true E_T^{miss} the reconstructed E_T^{miss} is affected by other activity in the event causing the scale to be discrepant. At high E_T^{miss} the reconstructed E_T^{miss} is dominated by the true E_T^{miss} component and the scale agrees to within a few percent.

7.7.3 E_T^{miss} performance

There are two components to the performance of the E_T^{miss} calculation: the E_T^{miss} resolution in fake E_T^{miss} events and the scale in true E_T^{miss} events. In events where there is no true E_T^{miss} , the measured E_T^{miss} is fake and dominated by the detector resolution. Having the best fake E_T^{miss} resolution is needed to reject fake E_T^{miss} backgrounds. In true E_T^{miss} events the reconstructed E_T^{miss} should accurately measure the true E_T^{miss} . The performance in both true and fake E_T^{miss} events is important to the identification of true E_T^{miss} events and rejection of fake E_T^{miss} events.

7.7.3.1 True E_T^{miss} scale

The true E_T^{miss} scale and linearity is derived using $W + \text{jet}$ simulation. The scale is given by the mean of the difference between the reconstructed and true E_T^{miss} relative to the true E_T^{miss} , $\langle E_T^{\text{miss, reco}} - E_T^{\text{miss, true}} / E_T^{\text{miss, true}} \rangle$. The linearity of the scale is the dependence of the scale on $E_T^{\text{miss, true}}$. Figure 7.3 shows the scale as a function of $E_T^{\text{miss, true}}$. At small values of $E_T^{\text{miss, true}}$, the reconstructed E_T^{miss} is affected by other activity in the event and the scale can be off by as much as 10%. At large $E_T^{\text{miss, true}}$, it dominates over the other activity and the reconstructed value agrees with the true value to within a few percent and is fairly linear with true E_T^{miss} .

7.7.3.2 Sources of fake E_T^{miss}

Sources of fake E_T^{miss} are separated into three categories: missed particles, Gaussian resolution from pileup and the underlying event, and non-Gaussian tails. Missed particles are those that fall outside of the detector acceptance; $|\eta| < 4.9$ for particles that stop in the calorimeter and $|\eta| < 2.7$ for

muons. Holes in the calorimeter and muon system also contribute to this term. The effect of lost particles on the E_T^{miss} resolution is small, with other sources dominating the E_T^{miss} resolution. Non-Gaussian tails result from lepton or jet mismeasurement. The resolution on these objects is generally not Gaussian and tends to have long tails where the object's momentum is measured to be lower than the true value. Catastrophic mismeasurements resulting in either higher or lower momentum measurements can cause large E_T^{miss} tails as well. The resolution from pileup and the underlying event contributes significantly to fake E_T^{miss} . This contribution is particularly troublesome because the resolution scales with the number of pileup interactions.

The E_T^{miss} resolution in fake E_T^{miss} events is important for rejecting fake E_T^{miss} backgrounds when selecting events that have true E_T^{miss} . When the fake E_T^{miss} resolution increases, the background rejection cut must be increased or additional cuts must be applied to reduce the background contamination at the expense of signal efficiency. The resolution depends strongly on the amount of activity in the event. The energy measurement of each calorimeter deposit has an uncertainty based on the cluster resolution. With more activity in the detector, the E_T from more calorimeter deposits are added into the E_T^{miss} calculation. The uncertainties on the cluster E_T add in quadrature, increasing the uncertainty and therefore the resolution on the E_T^{miss} . The x and y components of fake E_T^{miss} are Gaussian distributed and the RMS of these distributions are used to measure the affect of the fake E_T^{miss} . To a good approximation the resolution scales with the square root of the $\sum E_T$, the scalar sum of all energy deposits in the event. Figure 7.4 shows the width of the x and y components of E_T^{miss} versus $\sum E_T$ in both $Z + \text{jets}$ data and simulation. This distribution fits well to a square root function.

Given that the E_T^{miss} is a quadrature sum of the x and y components, the fake E_T^{miss} distribution can be derived analytically. A quadrature sum of two Gaussian distributed variables follows a Rayleigh distribution,

$$f(\xi, \sigma) = \frac{\xi}{\sigma^2} e^{-\xi^2/2\sigma^2}$$

Where the x and y components of E_T^{miss} are assumed to have the same resolution, σ , and the ξ is E_T^{miss} . The mean of a Rayleigh distribution is $\sigma\sqrt{\pi/2}$. Therefore the mean of the fake E_T^{miss} distribution depends only on the width of the distributions of the x and y components of E_T^{miss} and scales as the square root of the total energy deposited. Thus the mean of the Gaussian component of fake E_T^{miss} depends on the activity in the event and in particular on the number of pileup collisions. The distribution of the number of pileup interactions is shown in Figure 5.4. This distribution increased rapidly in 2011 and again in 2012 making the understanding of fake E_T^{miss} particularly important.

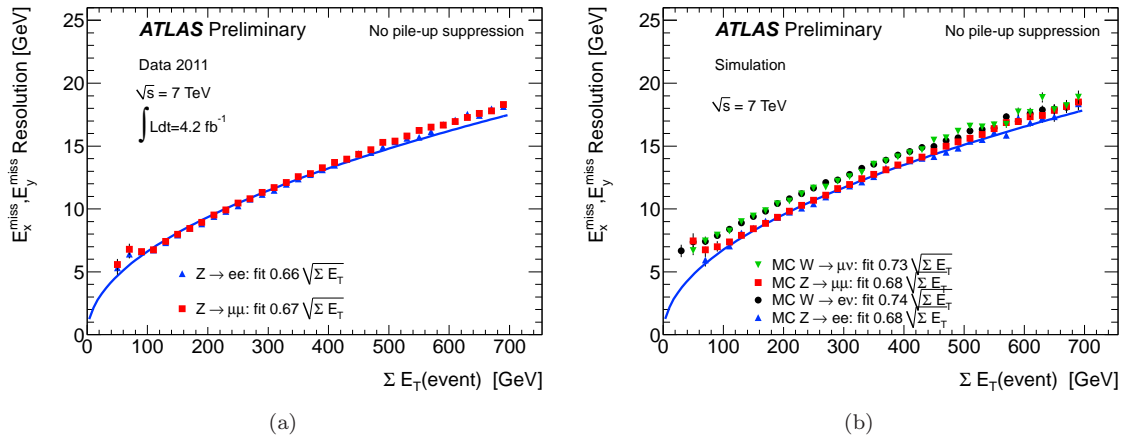


Figure 7.4: The width of the x and y components of E_T^{miss} as a function of the ΣE_T in data (a) and simulation (b). The distributions agree between data and simulation and fit well to a square root function.

7.7.3.3 Fake E_T^{miss} modeling in simulation

Fake E_T^{miss} is notoriously difficult to model in simulation. The shape of the simulated fake E_T^{miss} resolution depends on the modeling of the underlying event, hadronic recoil from the hard scatter, the number of pileup interactions, and simulation of the detector response. The effects from pileup have a significant impact on E_T^{miss} resolution and are particularly troublesome because they scale with instantaneous luminosity. Therefore, it is essential to correctly simulate the number of pileup interactions as well as the kinematics of those distributions.

7.7.3.4 Simulation of pileup multiplicity

Simulated events are generated with a pileup multiplicity ($\langle \mu \rangle$) that approximates the distribution in data. Perfect agreement is difficult to achieve because the simulation is often created before all the data are recorded. Therefore, the simulated distribution is generated to cover the expected distribution in data and is weighted to match the final data distribution. In simulation, $\langle \mu \rangle$ is simply the number of additional min-bias interactions added in the event. In data events, $\langle \mu \rangle$ is a measured quantity. Instead of relying on tracking measurements, which have limited η coverage and can miss pileup vertices, $\langle \mu \rangle$ is extrapolated in data from the beam current measured using beam monitors. The average number of pileup interactions is extrapolated from the instantaneous luminosity using Equation 7.4,

$$N_{PU} = \mathcal{L} \times \sigma_{mb} \quad (7.4)$$

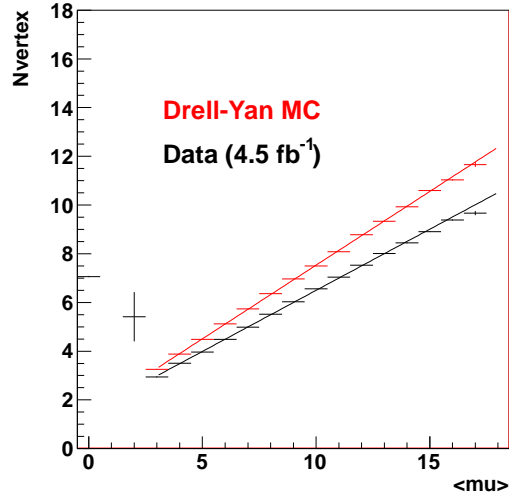


Figure 7.5: The correlation between the number of reconstructed vertices and $\langle \mu \rangle$. The red points are from the simulation and the black points are from data. A clear difference in slope is observed and a correction factor of 0.89 is derived to correct the simulation.

The only other parameter entering the calculation is the min-bias cross section, σ_{mb} . If σ_{mb} is incorrect the measured $\langle \mu \rangle$ distribution will not reflect the true number of pileup interactions. When the simulated $\langle \mu \rangle$ distribution is reweighted to the incorrect data distribution it is apparent in the E_T^{miss} modeling in the simulation. Any discrepancy caused by an incorrect σ_{mb} can be resolved by shifting the data distribution to compensate. The ATLAS experiment has measured the min-bias cross section [69] to be 60.3 ± 2.1 mb, but extrapolating this measurement from the fiducial volume of the detector to the inclusive cross section is difficult. Therefore the cross section calculated using Pythia is used instead. The accuracy of the σ_{mb} used in the calculation is checked by measuring the number of reconstructed primary vertices vs $\langle \mu \rangle$ in both data and simulation. The slope of this line is essentially the vertex reconstruction efficiency, but if $\langle \mu \rangle$ is measured incorrectly the slope is also affected. If the slope in data is different than the slope in simulation the pileup has not been correctly accounted for. Figure 7.5 shows this comparison and a clear difference in slope is observed. A correction factor of 1.11 is derived to bring the simulation into agreement with the data. The $\langle \mu \rangle$ in each data event is multiplied by the correction factor and the simulation is reweighted to match the scaled $\langle \mu \rangle$ distribution.

7.7.3.5 Modeling min-bias events

Pileup is simulated by overlaying the simulated hard scatter event with multiple min-bias collisions simulated with Pythia. Simulation of min-bias collisions is difficult because of the non-perturbative

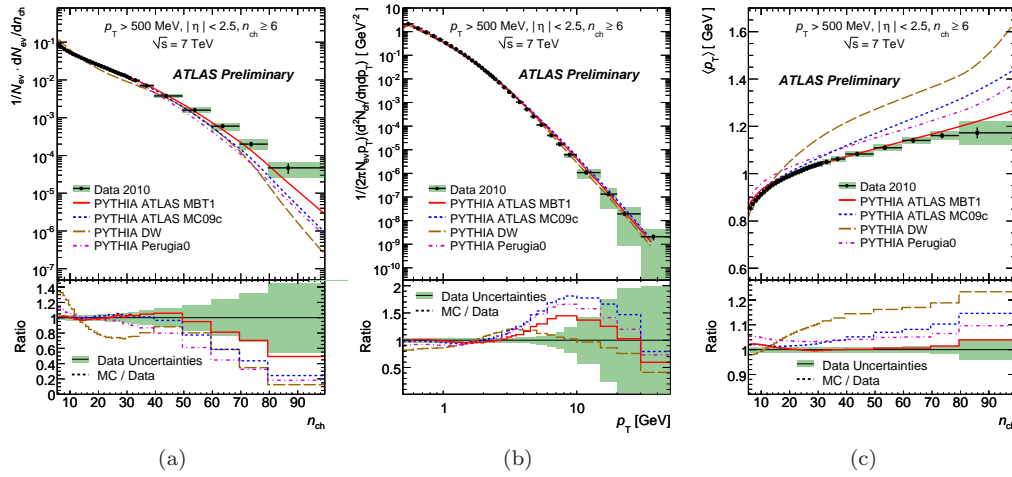


Figure 7.6: Comparisons of track properties in min-bias collisions between data and simulations having different min-bias tunes. Plot (a) shows the multiplicity of charged particles. Plot (b) shows the differential rate – effectively the cross section – of charged particles. Plot (c) shows the average track p_T versus charged particle multiplicity.

nature of the collisions. Parameters in the min-bias simulation must be tuned in order to reproduce a number of low level distributions including the charged particle multiplicity and particle p_T in individual collisions [70]. The first tuning is derived in the first small fraction of data recorded in each new data taking period (once or twice per year). Min-bias collisions are recorded using an unbiased trigger and distributions relevant to the tuning are compared between data and simulation. The tuning procedure adjusts simulation parameters to best reproduce the data distributions. However Pythia as well as other event generators do not have enough tunable parameters to completely describe the data. Figure 7.6 compares the charged particle multiplicity, the differential rate of charged particles, and the average charged particle p_T vs the number of charged particles. Some tunes agree better than others, but there is no tune that agrees within uncertainties across the entire distributions. These small disagreements are amplified by the number of pileup interactions – on average 22 in 2012 data. The combined effect of these mismodelings translate into the modeling the fake E_T^{miss} resolution.

Issues with the pileup modeling in the simulation first appeared when the instantaneous luminosity rapidly increased in 2011. In early 2011 data most crossings had zero or one proton-proton interaction. After the increase in luminosity the average number of pileup interactions increased to five. Figure 7.7 compares the E_T^{miss} distribution between data and simulation in a $Z \rightarrow \ell\ell$ selection with 3.5 fb^{-1} of 2011 data. Discrepancies of up to 50% are observed between the data and simulation. This discrepancy is a result of poor modeling of simulated pileup interactions. In the

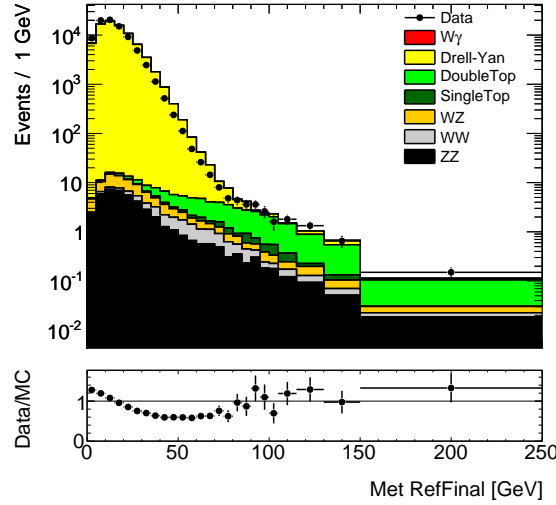


Figure 7.7: The E_T^{miss} distribution in $Z \rightarrow \ell\ell$ events using 3.5 fb^{-1} of 2011 data. The fake E_T^{miss} simulation does not correctly reproduce the E_T^{miss} distribution showing disagreements as large as 50%.

same selection, tracking level variables are compared with simulation to indicate the source of the mismodeling. Figure 7.8(a) plots the sum of the momenta of tracks associated to the primary vertex. This distribution is well modeled by simulation, indicating that the discrepancy does not arise from the simulation of the hard interaction. Figure 7.8(b) shows the sum of the momenta of tracks using all tracks in the event and Figure 7.8(c) shows the charged particle multiplicity. Large discrepancies are observed between data and simulation in both distributions. An ad-hoc solution that improves the E_T^{miss} modeling without retuning the simulation is achieved by scaling $\langle \mu \rangle$ in the same manner used for correcting the number of simulated pileup events as described in Section 7.7.3.4. Scaling $\langle \mu \rangle$ essentially increases or decreases the amount of pileup that is modeled. Figures 7.8(b) and 7.8(c) indicate that the nominal simulation contains too much pileup. Therefore $\langle \mu \rangle$ can be shifted down to correct for these discrepancies. Figure 7.9 shows the same tracking distributions after rescaling $\langle \mu \rangle$ by a factor of 0.83 and much better agreement is observed in the distributions sensitive to pileup.

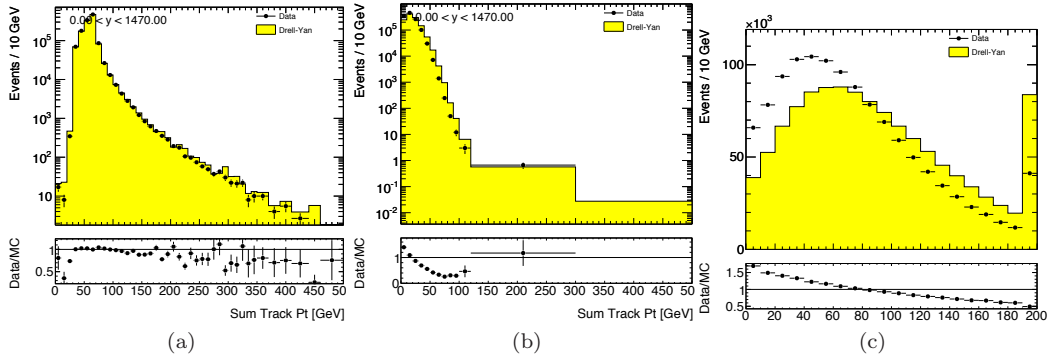


Figure 7.8: Comparisons of track related variables in $Z \rightarrow \ell\ell$ events between data and simulation with no $\langle \mu \rangle$ correction. The sum p_T of tracks from the primary vertex (a) are modeled well by simulation. When tracks from all vertices are considered, the simulated sum p_T of tracks (b) shows disagreement with the data. The charged particle multiplicity using tracks from all vertices (c) also disagrees. These disagreements point to tuning issues in the min-bias simulation.

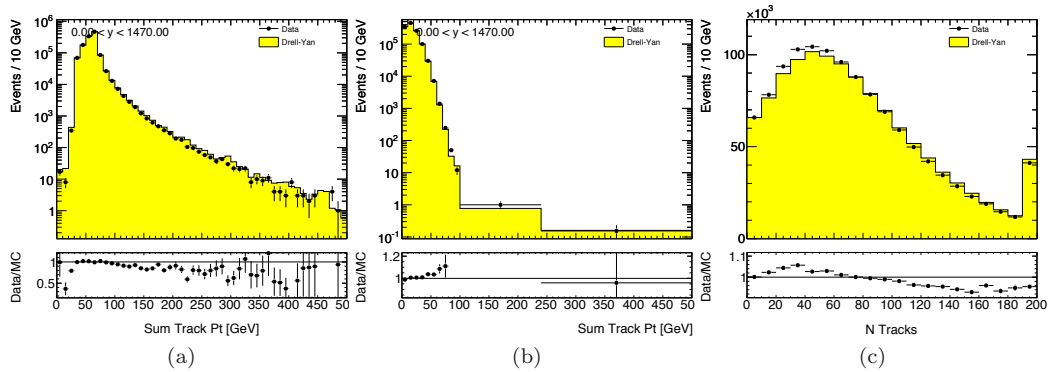


Figure 7.9: Comparisons of track related variables in $Z \rightarrow \ell\ell$ events between data and simulation with $\langle \mu \rangle$ scaled by 0.83. Relative to Figure 7.8, the modelling of the pileup sensitive distributions, (b) and (c), are improved.

CHAPTER 8

Standard Model measurements

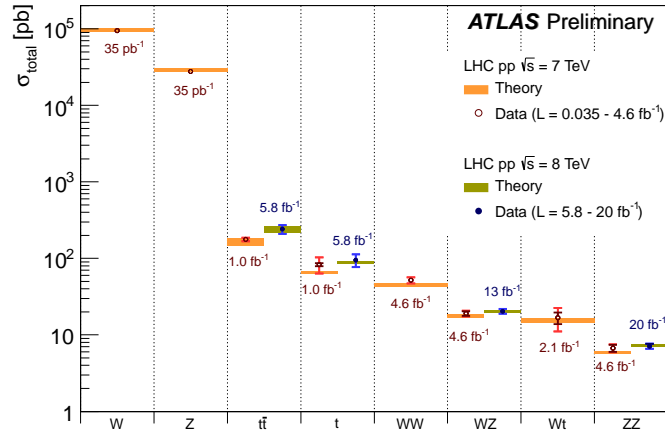


Figure 8.1: Summary of Standard Model cross section measurements at ATLAS. The open points show measurements made at $\sqrt{s} = 7$ TeV and their uncertainties while the closed points show measurements made at $\sqrt{s} = 8$ TeV. The measured cross sections are compared with the theory predictions.

As a prerequisite to searching for new phenomena at the LHC it is essential to validate the standard model by measuring quantities predicted by the theory and confirmed by previous experiments. A significant component of this validation is in measuring the cross section of Standard Model processes. These measurements also provide a testing ground for understanding event level objects such as electrons, muons, jets, and missing transverse momentum (E_T^{miss}). Many Standard Model processes are also backgrounds to searches for new physics. Therefore establishing an understanding of Standard Model processes provides the baseline upon which we search for new physics.

The ATLAS experiment has measured the cross sections of a number of Standard Model processes. Figure 8.1 summarizes many of the Standard Model cross section measurements made to date. All measurements show good agreement with the theory prediction. The following sections will detail two measurements, the first measurement of the WW cross section at ATLAS in the fully leptonic final state ($W^+W^- \rightarrow \ell^+\nu\ell^-\bar{\nu}$), and the first measurement of the ZZ cross section at ATLAS where one Z boson decays to charged leptons and the other decays to neutrinos ($ZZ \rightarrow \ell^+\ell^-\nu\bar{\nu}$). Both measurements rely on the dilepton + E_T^{miss} final state, but differ in their signal selection cuts.

Both $W^+W^- \rightarrow \ell^+\nu\ell^-\bar{\nu}$ and $ZZ \rightarrow \ell^+\ell^-\nu\bar{\nu}$ events are backgrounds to the search for invisible decays of the Higgs boson presented in Chapter 10. The ZZ background is the dominant Standard Model process in the invisible Higgs search. WW contributes to approximately 5% of the background. $W^+W^- \rightarrow \ell^+\nu\ell^-\bar{\nu}$ is also the main background to the search for the Higgs boson in the WW decay channel presented in Chapter 9.

Decay mode	Branching Fraction (%)
$jjjj$	45.7
$\ell\nu jj$ ($\ell = e, \mu, \tau$)	43.8
$\ell\nu\ell\nu$ ($\ell = e, \mu, \tau$)	10.5
Fully Leptonic breakdown	
$\ell\nu\ell\nu$ ($\ell = e, \mu, \tau; \tau \rightarrow e\nu_e\nu_\tau$ or $\mu\nu_\mu\nu_\tau$) [This Analysis]	6.45
$\ell\nu\tau\nu + \tau\nu\tau\nu$ ($\ell = e, \mu; \tau \rightarrow h$)	4.05

Table 8.1: Final state decay modes in WW events. This analysis selects fully leptonic events, but hadronic decays of tau leptons are not selected. The fully leptonic branching fraction is broken down to show the branching fraction that this analysis is sensitive to. Individual particle branching fractions are taken from the Particle Data Group [1].

8.1 $W^+W^- \rightarrow \ell^-\nu_\ell\ell^+\bar{\nu}_\ell$ cross section measurement

The WW cross section was first measured at ATLAS using 34 pb^{-1} of data taken in 2010 at $\sqrt{s} = 7 \text{ TeV}$ [71] and is the focus of this section. This measurement has since been updated to include 4.6 fb^{-1} of data taken in 2011 at $\sqrt{s} = 7 \text{ TeV}$ [72]. This process has also recently been measured with the CMS detector at $\sqrt{s} = 7 \text{ TeV}$ [73]. Previous measurements of WW production were made in e^+e^- collisions at LEP [74, 75, 76, 77] and in $p\bar{p}$ collisions at the Tevatron [78, 79]. WW events are mainly produced through t-channel and u-channel interactions of a quark, anti-quark pair. Approximately 3% of WW events are produced via gluon fusion at $\sqrt{s} = 7 \text{ TeV}$. Figure 8.2 shows the Feynman diagrams representing the production and leptonic decay of WW . The possible decay modes of W bosons creates three distinct classes of final states: fully hadronic – when both W bosons decay to quarks, semi-leptonic – when one W boson decays to leptons and the other decays to quarks, and fully leptonic – when both W bosons decay to leptons. Table 8.1 shows the possible final states of WW events and their branching fractions. This analysis selects WW events in the fully leptonic decay mode. While the fully leptonic decay mode has the smallest branching fraction, it has far fewer backgrounds than the other decay modes. The fully leptonic branching fraction in Table 8.1 is further broken down to show the branching fraction to which this analysis is sensitive, when both W bosons decay to electrons or muons or to taus that subsequently decay to an electron or muon. After the final selection the ratio of signal to background of more than four. The theoretical cross section, calculated at next-to-leading order in QCD, is $44 \pm 3 \text{ pb}$. Including the fully leptonic branching ratio selected by this analysis, 96 events are expected before background reduction cuts are applied.

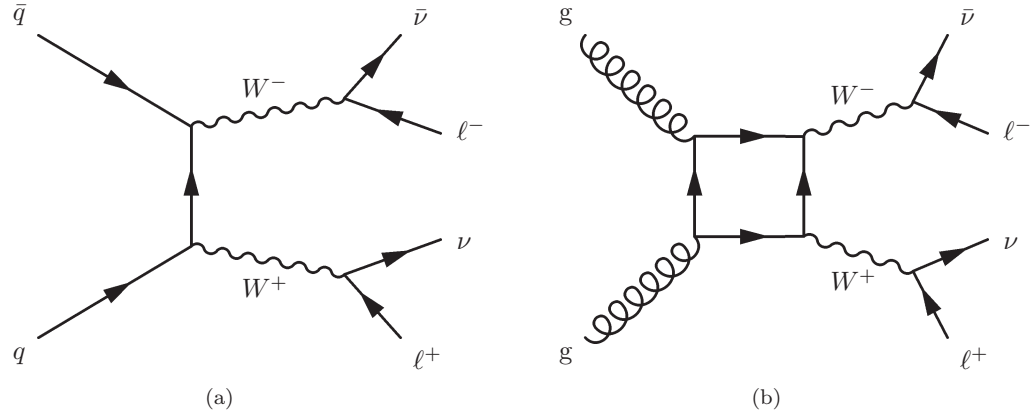


Figure 8.2: Feynman diagrams for the production of WW events and their decay to lepton pairs. Diagram (a) shows the t -channel interaction of a quark and anti-quark. This is the main WW production process. Diagram (b) shows W pair produced through gluon fusion. Although gluon-gluon interactions occur at a higher rate than $q\bar{q}$ interactions at the LHC, the loop in the gluon fusion case suppresses this production mode which contributes approximately 6% of the total cross section at 7 TeV.

8.1.1 Analysis overview

Candidate events are selected by requiring exactly two reconstructed opposite sign electrons or muons. Events are separated into three decay channels based on the leptons present in the final state – ee , $e\mu$, and $\mu\mu$. This selection is completely dominated by non- WW backgrounds and additional cuts that use the missing momentum resulting from the escaping neutrinos as well as jet information must be applied to reject these backgrounds. The main backgrounds are,

- **Top** – Events where a $t\bar{t}$ pair is produced are similar to the signal having two W bosons plus two b -quarks in the final state. Events where a top quark is produced singly with a W boson also fake the signal, but are produced at a lower rate than $t\bar{t}$. A jet veto removes a majority of the top background. This background is approximately 43% of the total in the same flavor channels and 27% in the $e\mu$ channel.
- **W + jets** – This process constitutes a background when the W decays leptonically and a jet fakes the second lepton. Although the rate of this process is much larger than the signal, the lepton identification largely rejects this background. W + jets contributes to 19% of the total background in the same flavor channels and 36% in the $e\mu$ channel.
- **Z + jets** – Events where a Z boson is produced and decays to charged leptons dominate the ee and $\mu\mu$ channels. There is also a contribution from $Z \rightarrow \tau\tau \rightarrow \mu\nu_\mu\nu_\tau e\nu_e\nu_\tau$ in the $e\mu$ channel. Cuts on the dilepton mass and the E_T^{miss} reduces this to a negligible background in the ee and

$\mu\mu$ channels and 17% of the background in the $e\mu$ channel where the $E_{\text{T}}^{\text{miss}}$ cut is reduced to improve the signal efficiency.

- WZ – The signal is faked when a WZ pair decays fully leptonically and one of the Z decay leptons is lost. This background is rejected by requiring exactly two leptons in the event and is a fairly small background. WZ events are 35% of the background in the same flavor channels and 18% of the background in the $e\mu$ channel.
- ZZ – Fully leptonic or semi-leptonic decays of ZZ are rejected by vetoing events near the Z mass and this low rate background is negligible.
- $H \rightarrow WW \rightarrow \ell\nu\ell\nu$ – At the time that this measurement was performed the Higgs boson had not yet been discovered. Indeed the Higgs boson does exist, but for this analysis the selection is not optimized for Higgs decays which tend to have low $M_{\ell\ell}$. This background is therefore considered negligible.
- Dijets – In order for dijet events to fake the signal both jets must fake a lepton. This background is negligible.

8.1.2 Data and simulation samples

The data were recorded at $\sqrt{s} = 7$ TeV during the 2010 data run. The data are required to be recorded during stable beam conditions and during nominal detector performance. Events are triggered with single lepton triggers that select events having a 15 GeV electron or 13 GeV muon.

The signal is modeled with MC@NLO [80] and ggWW [81] where the former models quark initiated events and the latter models gluon fusion production. Inclusive W and Z production are simulated using ALPGEN [82] which implements a leading order calculation with the emission of up to five final state partons. The remaining backgrounds, $t\bar{t}$, Wt , WZ , and ZZ are simulated using MC@NLO. The simulated particles are propagated through the detector and its response is implemented in a GEANT4 [83] model.

8.1.3 Object reconstruction

As discussed previously this analysis selects final state electrons and muons. Jets and $E_{\text{T}}^{\text{miss}}$ must be reconstructed for background rejection. This section describes details specific to this analysis and a generic discussion of each object is given in Chapter 7.

8.1.3.1 Electrons

Electron reconstruction and identification follows the description in Section 7.3 using the 2010 `tight` identification criteria [84]. Electrons must have $p_T > 20$ GeV and $|\eta| < 2.47$, but with the transition region between the barrel and endcap calorimeters within $1.37 < |\eta| < 1.52$ excluded. Electrons must be isolated from nearby calorimeter deposits with `Etcone30` < 6 GeV. The electron track must have $z_0 < 10$ mm and d_0 significance less than 10.

8.1.3.2 Muons

Muons are reconstructed using the *Staco Combined* algorithm as described in Section 7.4. Muons are required to have $p_T > 20$ GeV and $|\eta| < 2.4$ so that the track is contained in the inner detector volume. An additional cut requires that the momentum measured by the muon spectrometer (MS) is consistent with the momentum measured by the inner detector (ID), $|p_T^{\text{ID}} - p_T^{\text{MS}}|/p_T^{\text{ID}} < 0.5$. Muons must be isolated from nearby tracks by requiring that `ptCone20`/ $p_T < 0.1$.

8.1.3.3 Jets

Jets are reconstructed as described in Section 7.5. Jets must have $p_T > 20$ GeV and $|\eta| < 3$. The number of pileup interactions was quite low in the 2010 run so no pileup suppression of jets is applied.

8.1.3.4 Missing transverse momentum

The E_T^{miss} is reconstructed using the LOCHADTOPO method as described in Section 7.7. An alternate definition, $E_T^{\text{miss,rel}}$, described in Section 7.7.1 is used to reduce the impact of mismeasured leptons. This also helps to reduce the background in the $e\mu$ channel from $Z \rightarrow \tau\tau$ because the τ lepton p_T is effectively mismeasured because of the escaping decay neutrinos.

8.1.4 Event selection

Events are first selected with a baseline dilepton selection. Events must have two opposite charge electrons or muons passing the identification criteria above. Three lepton channels are allowed, ee , $\mu\mu$, and $e\mu$. Figure 8.3 shows the dilepton mass distributions for each channel. In the same flavor channels the $Z/\gamma^* \rightarrow \ell\ell$ process dominates. The contribution from $Z/\gamma^* \rightarrow \tau\tau$ in the $e\mu$ channel is relatively small and $t\bar{t}$ events dominate. To reduce the background from Z boson events in the same flavor channels, events having $|M_{\ell\ell} - M_Z| < 10$ GeV are removed. The world average Z mass is used for M_Z [1]. In addition we require $M_{\ell\ell} > 15$ GeV in all channels to avoid low mass resonances. Further reduction of Z/γ^* events is achieved by requiring $E_T^{\text{miss,rel}} > 40$ GeV in the ee and $\mu\mu$

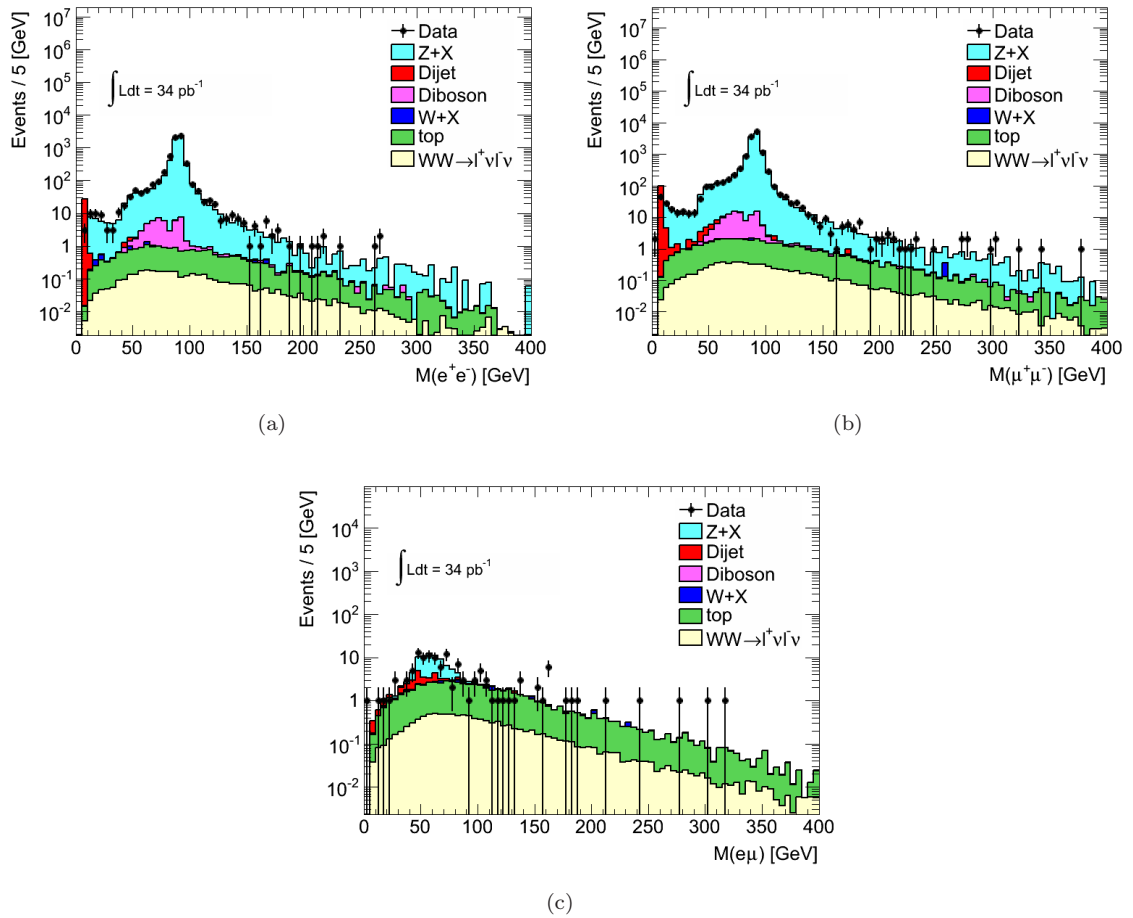


Figure 8.3: Dilepton mass distributions for the ee (a), $\mu\mu$ (b), and $e\mu$ (c) channels. At this stage of the cutflow Z and $t\bar{t}$ events dominate the selection.

channels and $E_T^{\text{miss,rel}} > 20$ GeV in the $e\mu$ channels. Figure 8.4 shows the $E_T^{\text{miss,rel}}$ distribution for each channel. The cut in the $e\mu$ channel is allowed to be lower because fewer Z/γ^* events contaminate the $e\mu$ channel. After the $E_T^{\text{miss,rel}}$ cuts are applied $t\bar{t}$ events dominate the selection. Figure 8.5 shows the jet multiplicity distribution after the Z mass veto and $E_T^{\text{miss,rel}}$ cuts are applied. The zero jet bin is mostly comprised by the signal while the $t\bar{t}$ background tends to have one or more jets. Therefore a jet veto is applied to remove most of the $t\bar{t}$ background. Figure 8.6 shows the $E_T^{\text{miss,rel}}$ distributions for each channel with all cuts except $E_T^{\text{miss,rel}}$ applied illustrating the purity that is achieved by applying a $E_T^{\text{miss,rel}}$ cut to events with a Z veto and jet veto applied.

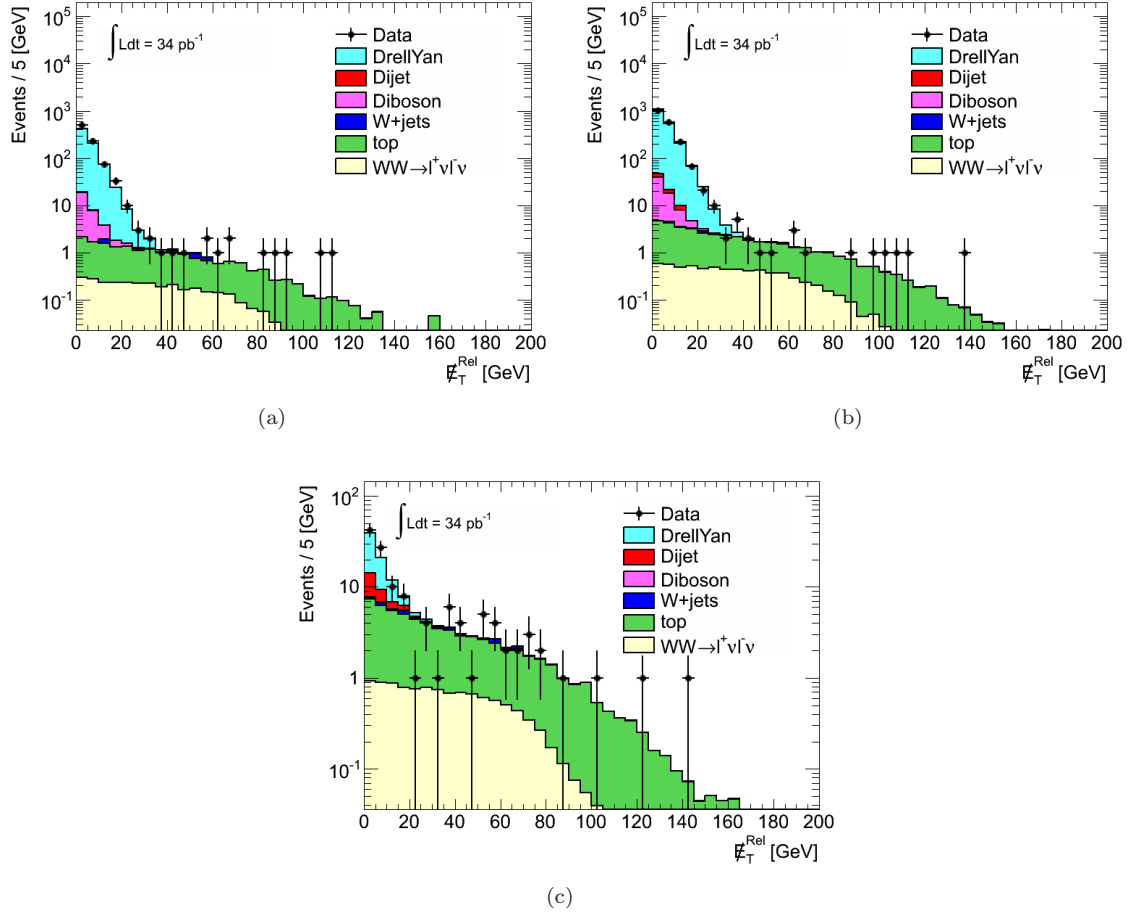


Figure 8.4: $E_T^{\text{miss,rel}}$ distributions for the ee (a), $\mu\mu$ (b), and $e\mu$ (c) channels after the veto on the Z mass in the ee and $\mu\mu$ channels.

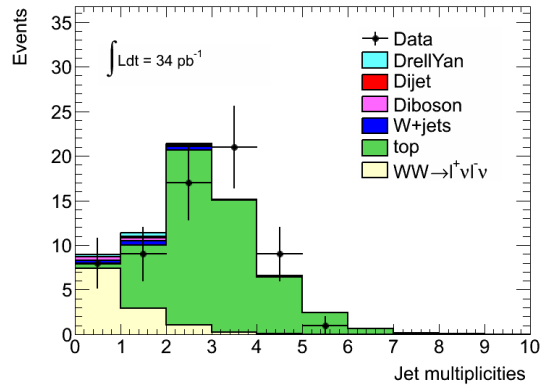


Figure 8.5: Jet multiplicity distribution for the three channels combined after the Z mass veto and the $E_T^{\text{miss,rel}}$ cut. The zero jet bin is dominated by the WW signal while higher jet multiplicities are dominated by $t\bar{t}$ events.

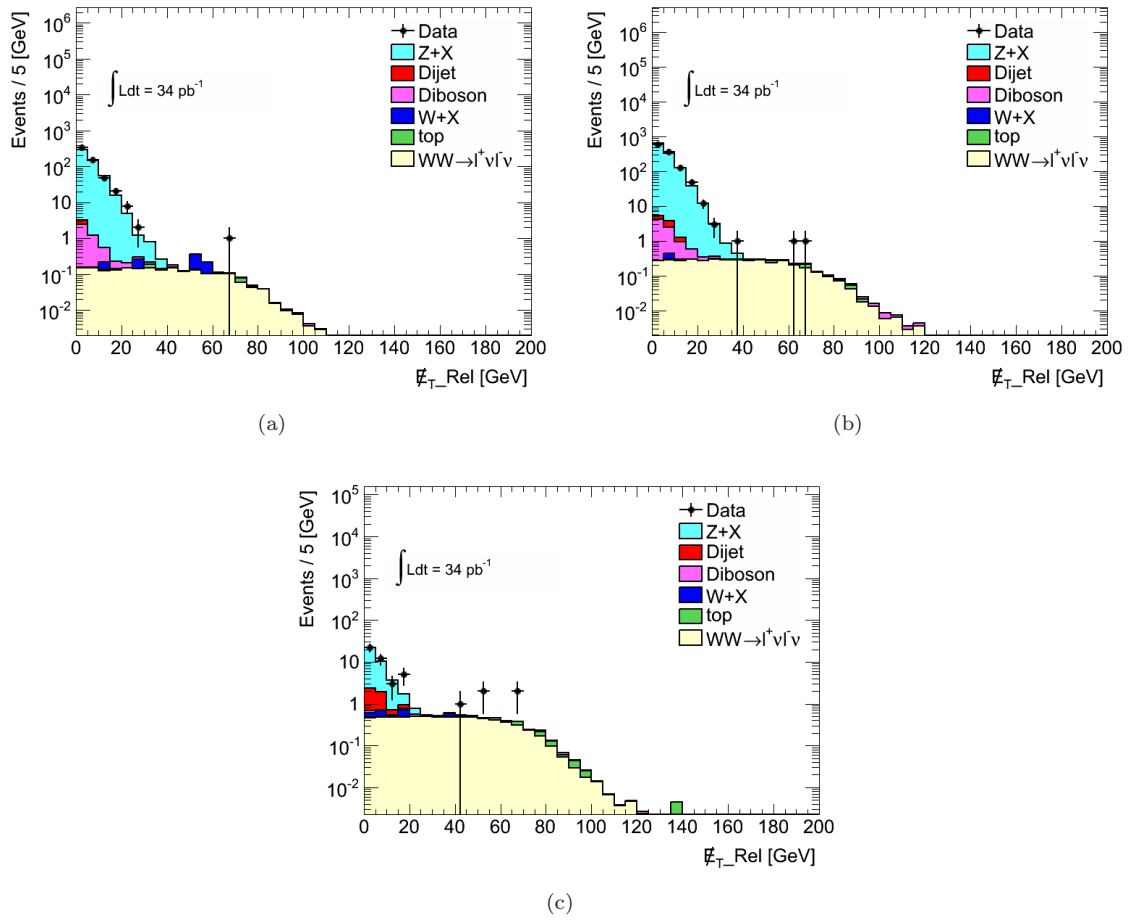


Figure 8.6: $E_T^{\text{miss,rel}}$ distributions for the ee (a), $\mu\mu$ (b), and $e\mu$ (c) channels after all cuts except $E_T^{\text{miss,rel}}$.

8.1.5 Signal acceptance

In order to calculate the WW cross section, the signal selection efficiency must be determined. The signal selection accepts only a small phase space of WW decays. The efficiency allows the measurement made within the fiducial acceptance of the analysis to be extrapolated to the total WW production cross section. The signal acceptance is separated into two terms, the fiducial acceptance and reconstruction efficiencies. The fiducial acceptance is determined from the simulated WW samples. Uncertainties on the fiducial acceptance result from varying the proton PDF in the CTEQ 6.6 PDF set [85] and varying the Q^2 of the interaction. An additional uncertainty is evaluated from the acceptance difference with respect the MSTW2008 PDF set [11]. The combined systematic uncertainty is 1.2%. The trigger efficiency, lepton identification efficiencies, and jet veto efficiency in the simulation are corrected to the data efficiencies. The trigger and lepton

reconstruction efficiencies are measured using a tag-and-probe method in a pure sample of $Z \rightarrow \ell\ell$ events selected in data, and are also measured in $Z \rightarrow \ell\ell$ simulation. Scale factors for both the trigger and lepton reconstruction efficiencies are near unity. The lepton momentum uncertainties are derived from comparing the measured Z width in data and simulation. The combined uncertainty on trigger and lepton reconstruction efficiencies and lepton momentum scale uncertainties is 4.2%. To reduce the uncertainty on the jet energy scale and resolution a jet veto scale factor is derived by calculating the jet veto efficiency in a pure sample of $Z \rightarrow \ell\ell$ in data and in simulated events. The jet veto scale factor is 0.97 and has a 6% systematic uncertainty. An additional systematic of 0.5% is assessed from the effects of pileup interactions. The luminosity uncertainty of 3.4% is measured using dedicated van der Meer beam scans [86] (see also Section 5.3).

8.1.6 Background estimation

Data driven methods are used to estimate most of the backgrounds in this analysis. The Z/γ^* , $t\bar{t}$, and $W+$ jets backgrounds are estimated using data driven methods and the remaining diboson backgrounds are estimated using simulation.

8.1.6.1 Z/γ^* background estimate

The Z/γ^* background is rejected by a factor of approximately 10^5 in the same flavor channels by application of the Z veto cut and in all channels by the $E_T^{\text{miss,rel}}$ cut. The simulation does not a priori correctly model the $E_T^{\text{miss,rel}}$ distribution as and a data driven method is preferred. Section 7.7.3.3 discusses the issues with modeling E_T^{miss} in the simulation.

A partially data driven method uses the Z peak region, which is vetoed in the signal selection, to check the $E_T^{\text{miss,rel}}$ modeling in the simulation. This method uses the observed discrepancy between the $E_T^{\text{miss,rel}}$ distributions in data and simulation within the Z peak region and applies that discrepancy as a systematic to the background predicted from simulation in the signal region. The method assumes that the mechanism that causes a discrepancy between data and simulation is independent of the invariant mass of the sample. The event selection begins with the baseline dilepton selection as in 8.1.4. Events must fall in the Z control region ($|M_{\ell\ell} - M_Z| < 10$ GeV) and the jet veto is applied. This selection provides a large sample of Z events having relatively little WW signal contamination. The data are then compared to the prediction from simulation. Figure 8.7 shows the $E_T^{\text{miss,rel}}$ distributions for data and simulation in the Z control region. Assuming that any discrepancy between data and the simulation arises from Z/γ^* mismodeling of the E_T^{miss} distribution,

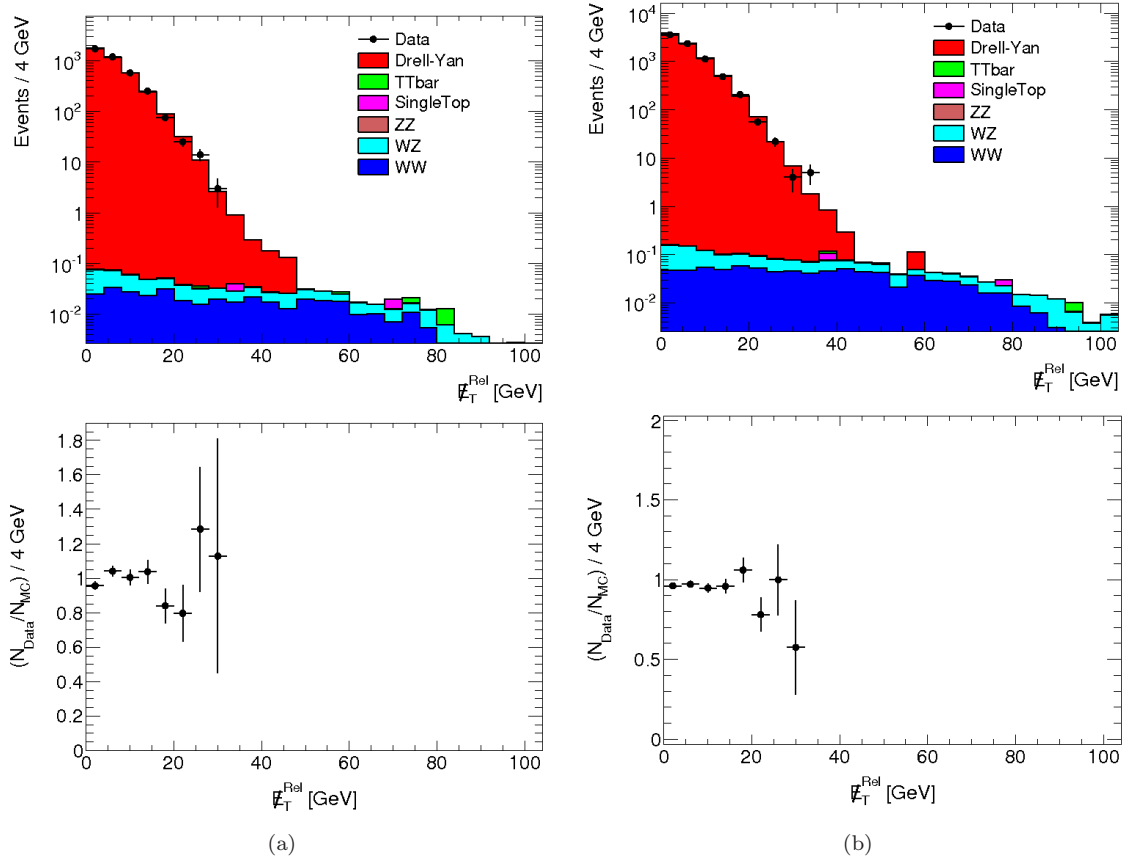


Figure 8.7: $E_T^{\text{miss,rel}}$ distribution for data and simulation for events selected within the Z control region for the ee (a) and $\mu\mu$ (b) channels. The bottom plots show the ratio of data to simulation.

the discrepancy is quantified as

$$S = \frac{N_{\text{Data}}(E_T^{\text{miss,rel}} > 30 \text{ GeV}) - N_{\text{MC}}(E_T^{\text{miss,rel}} > 30 \text{ GeV})}{N_{\text{DY}}(E_T^{\text{miss,rel}} > 30 \text{ GeV})} \quad (8.1)$$

Where N_{Data} is the number of data events, N_{MC} is the number of events predicted by the sum of all simulated samples and N_{DY} is the number of events predicted by the Z/γ^* simulation alone. A $E_T^{\text{miss,rel}}$ cut of 30 GeV is used because no data exist in the Z control region above $E_T^{\text{miss,rel}} = 35$ GeV. Since a 30 GeV cut already selects events well on the tails of the $E_T^{\text{miss,rel}}$ distribution, it is assumed that the result obtained with this cut value is applicable to the analysis cut value of 40 GeV. The relevant quantities from Equation 8.1 are shown in Table 8.2.

For both channels the S value is negative indicating that the simulation over estimates the data. Since the S values provide a handle on the amount by which the simulation disagrees with data, the absolute values are used. The two channels are combined in a weighted average to give

Channel	N_{Data}	N_{MC}	N_{DY}	S
ee	2	2.89 ± 0.43	2.4 ± 0.42	-0.38 ± 0.61
$\mu\mu$	5	5.97 ± 0.62	4.88 ± 0.61	-0.20 ± 0.47

Table 8.2: Relevant quantities used in Equation 8.1 to estimate the systematic uncertainty on the Z/γ^* background.

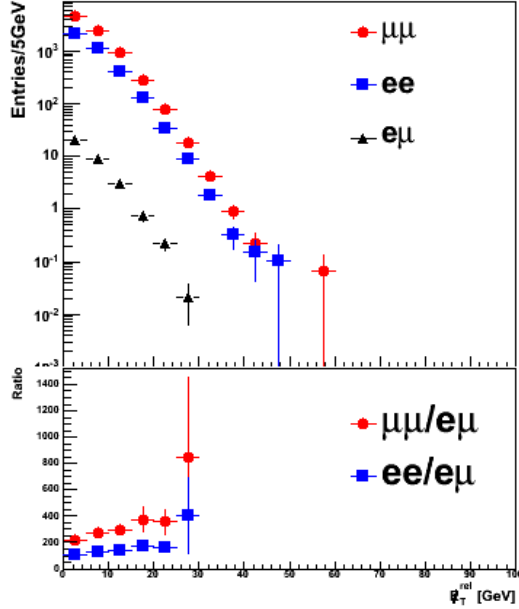


Figure 8.8: Comparison of the $E_T^{\text{miss,rel}}$ distributions between ee , $\mu\mu$, and $e\mu$ channels. The bottom plot is a ratio of ee to $e\mu$ and $\mu\mu$ to $e\mu$.

a prediction of 0.27 ± 0.37 . Both the S value and its uncertainty are sensitive to the discrepancy, so as a conservative estimate the value and its error are added linearly to give a final background uncertainty of 64%.

The uncertainty obtained from the ee and $\mu\mu$ channels is applied to the $e\mu$ channel. This is a conservative estimate because the simulation is expected to better predict real E_T^{miss} from τ decays. In order for the value to apply, the $E_T^{\text{miss,rel}}$ distributions must be similar between the $e\mu$ channel and the ee and $\mu\mu$ channels. Figure 8.8 shows that the shapes agree well between the same flavor and $e\mu$ channels. The presence of a small slope in the ratio plot indicates that the $e\mu$ channel tends to have lower $E_T^{\text{miss,rel}}$ than the ee or $\mu\mu$ channels. In this case, applying the systematic determined from the same flavor channels is a conservative over estimate of the systematic for the $e\mu$ channel.

The central value of the Z/γ^* background is taken from the ALPGEN simulation. Where the simulation has zero events in the signal region, an upper limit is used. The prediction from the

Generator	ee	$\mu^+\mu^-$	$e\mu$	combined
ALPGEN	$0.00 \pm 0.10 \pm 0.07$	$0.01 \pm 0.10 \pm 0.07$	$0.22 \pm 0.06 \pm 0.15$	$0.23 \pm 0.15 \pm 0.17$
MC@NLO	$0.02 \pm 0.01 \pm 0.01$	$0.06 \pm 0.02 \pm 0.04$	$0.27 \pm 0.07 \pm 0.18$	$0.35 \pm 0.07 \pm 0.18$
PYTHIA	$0.00 \pm 0.01 \pm 0.01$	$0.05 \pm 0.02 \pm 0.03$	$0.24 \pm 0.06 \pm 0.16$	$0.29 \pm 0.07 \pm 0.16$

Table 8.3: Predicted Z/γ^* contribution in the signal region from three Monte Carlo generators in each analysis channel. Entries show the statistical uncertainty first and the systematic uncertainty second. The systematic uncertainties are derived from the data driven estimate.

ALPGEN simulation is checked with events generated using MC@NLO and PYTHIA. Table 8.3 compares the predictions from the three generators which all agree within statistical and systematic uncertainties.

8.1.6.2 Top background estimate

The $t\bar{t}$ and Wt backgrounds mimic the dilepton signal when both W bosons decay leptonically. These events are also accompanied with one or more b-quark initiated jets and additional jets from ISR and FSR emission of quarks or gluons. Figure 8.5 shows the jet multiplicity distribution for Z vetoed events having large $E_T^{\text{miss,rel}}$. This background is largely rejected by selecting events with zero reconstructed jets. A small fraction of top events have zero reconstructed jets because they fall below the p_T threshold or fall outside of the jet acceptance in η . Two data driven methods are used to predict the number of top background events in the signal region.

The first method (method A) compares the prediction from simulation to the data separately in the 2 and 3 jet control region and in the 4 or more jets control region. The ratio of data to simulation in the control region is applied to the prediction from simulation in the zero jet bin as shown in Equation 8.2. Sources of systematic uncertainties arise from the non top background subtraction, variation of the jet E_T threshold, and variations of the rate of initial and final state radiation.

$$N_{\text{Top}}^{\text{Estimated}}(N_{\text{jet}} = 0) = N_{\text{Top}}^{\text{MC}}(N_{\text{jet}} = 0) \times \frac{N_{\text{data}}(\text{control region})}{N_{\text{Top}}^{\text{MC}}(\text{control region})} \quad (8.2)$$

The second method (method B) of estimating the top background derives a jet veto efficiency in a b-tag control region. The SV1 b-tagging algorithm described in Section 7.5 is used to identify b-quark initiated jets. Events are selected by applying the full signal selection except for the jet veto and instead requiring one or more b-tagged jets. The jet veto efficiency, P_1^{Btag} , is the ratio of the number of events have zero additional jets to the number of events having one or more additional jets. A b-tag requirement is not made on the additional jets. The square of P_1^{Btag} is the probability for a $t\bar{t}$ or Wt event that has two or more jets to be reconstructed as a zero jet event. The ratio of P_1^{Btag} between data and simulation is applied to the efficiency of the jet veto cut from simulation. Equation 8.3 shows this calculation where P_2^{MC} is the jet veto efficiency measured from

Method	MC	Method A	Method B
Prediction	0.53 ± 0.12	0.55 ± 0.10 ($N_{jet} = 2\&3$) $0.52^{+0.20}_{-0.17}$ ($N_{jet} \geq 4$)	$0.25^{+0.50}_{-0.25}$

Table 8.4: Top background estimates from the simulation and two independent data driven methods. All results are consistent within uncertainties and the background predicted from simulation is used as the central value.

simulation. The measured jet veto efficiency, P_2^{Data} is then applied to the number of events passing the full selection except the jet veto to estimate the number of events in the zero jet bin as shown in Equation 8.4. Sources of systematics from the jet energy scale uncertainty and from statistical uncertainty in the b-tag control region are considered.

$$P_2^{Data} = \left(P_1^{Btag,Data}\right)^2 \frac{P_2^{MC}}{\left(P_1^{Btag,MC}\right)^2} \quad (8.3)$$

$$N_{Top}^{Data}(\ell\ell + E_T^{\text{miss}}, 0j) \approx N_{Top}^{Data}(\ell\ell + E_T^{\text{miss}}) \left(P_1^{Btag,Data}\right)^2 \frac{P_2^{MC}}{\left(P_1^{Btag,MC}\right)^2}, \quad (8.4)$$

Table 8.4 gives the estimated background from both methods as well as from the simulation. The two control regions considered in method A give consistent results. Method B predicts a background that is smaller than Method A by a factor of two, but the results are consistent within the large statistical and systematic uncertainties. Both methods validate that the simulation correctly predicts the top background, and the background estimate from the simulation is used.

8.1.6.3 W + jets background estimate

Events in which a single W boson is produced with additional jets can mimic the signal when a jet fakes a lepton. Although the rate at which jets fake leptons is small, the W production rate is much larger than the signal making this a small, but non-negligible background. This background is estimated by selecting events enriched in W bosons that have a fully identified lepton and an object passing an alternate loose lepton definition that is enriched in jets. The loose lepton definition inverts identification cuts on electrons and inverts the isolation cuts on muons. The selected events are weighted by a p_T dependent fake factor that quantifies the probability for a loose lepton to be identified as a signal lepton. The fake factor is determined in a dijet triggered sample. Contributions from W and Z bosons in this sample are rejected and residual contributions are subtracted using simulation. The background estimation after all selection cuts is given in Equation 8.5 for the same

flavor channels and Equation 8.6 for the $e\mu$ channel where one must consider the probability for either an electron or muon to be faked. Table 8.5 shows the estimated $W + \text{jets}$ background.

$$N_{W+\text{jet Bkg}}^{ee(\mu\mu)} = f_{e(\mu)} \times N_{e+\text{Jet-Rich } e(\mu+\text{Jet-Rich } \mu)} \quad (8.5)$$

$$N_{W+\text{jet Bkg}}^{e\mu} = f_e \times N_{\mu \text{ ID} + \text{Jet-Rich } e} + f_\mu \times N_{\text{elec. ID} + \text{Jet-Rich } \mu} \quad (8.6)$$

Channel	Estimated $W + \text{jet}$ background
ee -channel	$0.08 \pm 0.05(\text{stat.}) \pm 0.03(\text{syst.})$
$\mu\mu$ -channel	$0 \pm 0.29(\text{stat.}) \pm 0.10(\text{syst.})$
$e\mu$ -channel	$0.46 \pm 0.12(\text{stat.}) \pm 0.17(\text{syst.})$
$ee + \mu\mu + e\mu$ -channel	$0.54 \pm 0.32(\text{stat.}) \pm 0.21(\text{syst.})$

Table 8.5: Estimated $W + \text{jets}$ background in the WW signal region.

8.1.6.4 Diboson background estimate

Diboson production other than WW can present small backgrounds to this measurement. Events where a WZ pair are produced become a background when both bosons decay to charged leptons and one of the Z leptons is lost. Cases where the W lepton is lost are removed by the Z mass veto. Events where a pair of Z bosons or $Z + \gamma$ are produced are also largely removed by the Z mass veto. $W + \gamma$ events are largely reduced because the photon must fake a lepton. All diboson backgrounds are estimated from simulation giving a combined estimate of 0.39 ± 0.06 (syst.).

8.1.7 Results

After the full WW selection 8 events are observed with an expected background of 1.72 events. Table 8.6 summarizes the number observed events, the number of expected events from simulation and the expected background for each channel and for all channels combined.

The WW cross section is extracted using Equation 8.7 where N_{obs} is the observed number of events, N_{bkg} is the estimated background, ϵ is the combined reconstruction efficiency, \mathcal{A} is the acceptance efficiency, \mathcal{L} is the integrated luminosity, and Br is the branching ratio. A likelihood function for Poisson statistics is used to extract the WW cross section. The likelihood function, shown in Equation 8.8, separates the contribution from each channel in the product. The WW cross section is determined by maximizing the log likelihood function for σ^{WW} . The measured WW cross section is,

$$\sigma^{WW} = 40_{-16}^{+20}(\text{stat.}) \pm 7(\text{syst.})\text{pb.}$$

The measurement is consistent with the theoretical value of 46 pb. The uncertainty on the measurement is dominated by the available statistics. More recent measurements of the WW cross section yield more precise results.

$$\sigma^{WW} = \frac{N_{obs} - N_{bkg}}{\epsilon \mathcal{A} \mathcal{L} Br} \quad (8.7)$$

$$F = \ln \prod_{i=1}^3 \frac{(N_{sig}^i + N_{bkg}^i)^{N_{obs}^i} e^{-(N_{sig}^i + N_{bkg}^i)}}{N_{obs}^i!}, \quad N_{sig}^i = \sigma^{WW} Br^i \epsilon^i \mathcal{A}^i \mathcal{L} \quad (8.8)$$

Final State	$e^+e^- E_T^{\text{miss}}$	$\mu^+\mu^- E_T^{\text{miss}}$	$e^\pm\mu^\mp E_T^{\text{miss}}$
Observed Events	1	2	5
Expected WW Signal	$0.79 \pm 0.02 \pm 0.09$	$1.61 \pm 0.04 \pm 0.14$	$4.46 \pm 0.06 \pm 0.44$
Backgrounds			
Top(MC)	$0.04 \pm 0.024 \pm 0.02$	$0.14 \pm 0.06 \pm 0.07$	$0.35 \pm 0.10 \pm 0.19$
W +jets (data-driven)	$0.08 \pm 0.05 \pm 0.03$	$0 \pm 0.29 \pm 0.10$	$0.46 \pm 0.12 \pm 0.17$
Z +jets (MC/data-driven)	$0 \pm 0.10 \pm 0.07$	$0.01 \pm 0.10 \pm 0.07$	$0.22 \pm 0.06 \pm 0.15$
$WZ, ZZ, W/Z + \gamma$ (MC)	$0.05 \pm 0.01 \pm 0.006$	$0.10 \pm 0.004 \pm 0.009$	$0.23 \pm 0.05 \pm 0.023$
Total Background	$0.17 \pm 0.11 \pm 0.08$	$0.25 \pm 0.31 \pm 0.15$	$1.26 \pm 0.17 \pm 0.31$

Table 8.6: The number of observed events, the expected number of events, and the contribution from each background for the ee , $\mu\mu$, and $e\mu$ channels.

8.1.8 Summary

The WW production cross section was measured using 34 pb^{-1} of data from the 2010 run taken at $\sqrt{s} = 7 \text{ TeV}$. Eight signal events were observed, with 1 event in the ee channel, 2 events in the $\mu\mu$ channel and 5 events in the $e\mu$ channel. A total of 1.26 background events were expected giving a signal to background ratio greater than 4. The measured cross section of $40_{-16}^{+20}(\text{stat.}) \pm 7(\text{syst.})$ agrees well with the next-to-leading order prediction of $46 \pm 3 \text{ pb}$.

8.2 $ZZ \rightarrow \ell^+\ell^-\nu_\ell\bar{\nu}_\ell$ cross section measurement

This section presents a measurement of the ZZ cross section using 4.6 fb^{-1} of data taken during the full 2011 data run with beams colliding at an energy of $\sqrt{s} = 7 \text{ TeV}$. Pairs of Z bosons are produced mainly through collisions of quark, anti-quark pairs. Approximately 6% of ZZ events are produced via gluon fusion at $\sqrt{s} = 7 \text{ TeV}$. Figure 8.9 shows the Feynman diagrams for the production and decay of ZZ to the $\ell^+\ell^-\nu\bar{\nu}$ final state. This analysis was published in combination with a similar measurement in the $llll$ final state [87]. This measurement was recently made with the

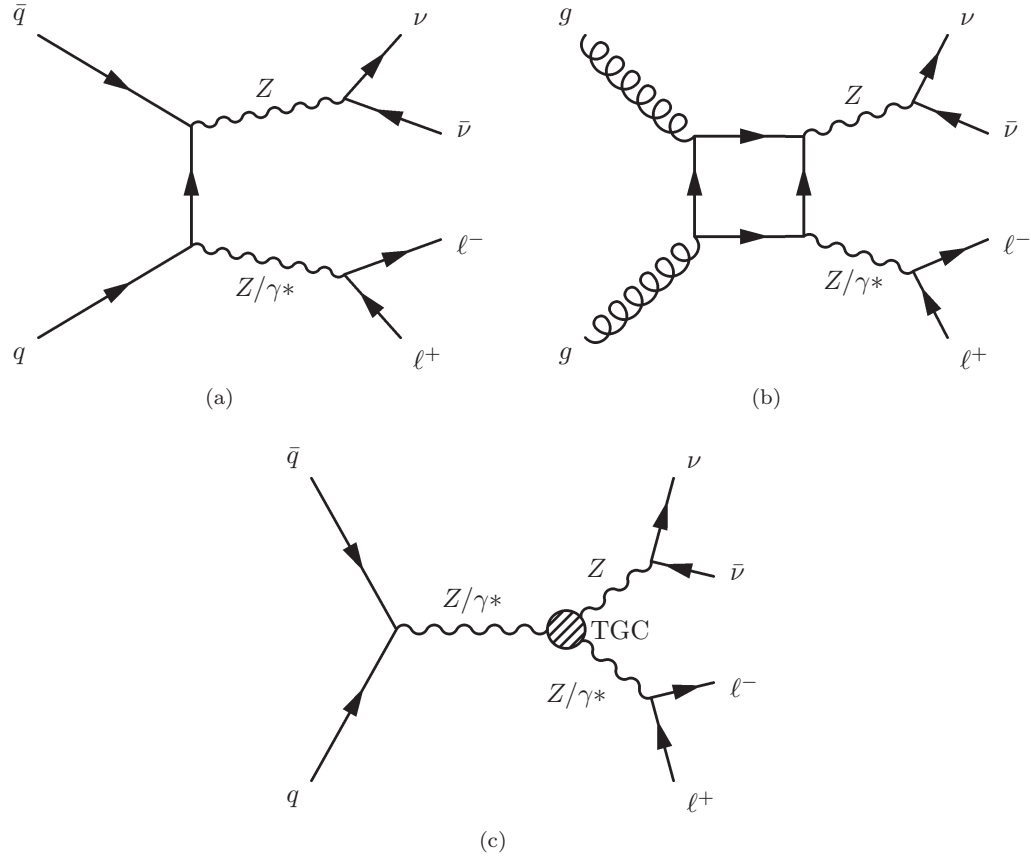


Figure 8.9: Production and decay of Z boson pairs decaying to the $\ell^+\ell^-\nu\bar{\nu}$ final state. A majority of ZZ events are produced via quark-anti quark collisions (a). Approximately 6% of ZZ events are produced via gluon fusion (b). Diagram (c) proceeds via a triple gauge coupling which is not allowed in the Standard Model. Limits are placed on the allowable magnitude of the triple gauge coupling.

CMS detector at $\sqrt{s} = 7$ TeV [73]. Measurements of the ZZ production cross sections have also been made in e^+e^- collisions at LEP [88, 89, 90, 91] and in $p\bar{p}$ collisions at the Tevatron [92, 93]. Table 8.7 shows the possible decay modes of ZZ events and their branching fractions. This final state has the second-smallest branching fraction, but also suffers from fewer backgrounds than the higher rate decay modes. The ZZ cross section is measured within the fiducial acceptance of the analysis and is extrapolated to the full production cross section. Fiducial cross sections are measured differentially as a function of p_T , $\Delta\phi(\ell, \ell)$, and m_T by unfolding the reconstructed distributions to the truth level. In addition limits are placed on anomalous triple gauge couplings (aTGC). Figure 8.9(c) shows the aTGC diagram which does not exist in the Standard Model. We consider all possible extensions to the Standard Model Lagrangian that would produce an aTGC and set limits on the magnitude of those terms.

Decay mode	Branching Fraction (%)
$j\bar{j}j\bar{j}$	48.9
$j\bar{j}\nu\nu$	28.0
$j\bar{j}l\bar{l}$ ($l = e, \mu, \tau$)	14.1
$\nu\nu\nu\nu$	4.0
$l\bar{l}\nu\nu$ ($l = e, \mu$) [This Analysis]	2.7
$l\bar{l}\nu\nu$ ($l = \tau$)	1.3
$l\bar{l}l\bar{l}$ ($l = e, \mu, \tau$)	1.0

Table 8.7: Final state decay modes of ZZ events. This analysis selects events containing two opposite-sign charged leptons and two neutrinos. Contributions from leptonic decays of tau leptons are negligible because event level cuts largely reject these events. Individual particle branching fractions are taken from the Particle Data Group [1].

8.2.1 Analysis overview

This measurement identifies ZZ events in the $l\bar{l} + E_{\text{T}}^{\text{miss}}$ final state with one Z boson decaying to charged leptons and the other Z boson decaying to neutrinos. The basic event selection is therefore a same flavor, opposite sign lepton pair having an invariant mass near the Z boson mass and large $E_{\text{T}}^{\text{miss}}$ from the escaping neutrinos. This event selection suffers from a number of non- ZZ backgrounds and additional cuts must be added to reject these backgrounds. After the full event selection described below the ratio of signal to background is approximately one. The background processes that contribute are,

- WZ – This process becomes a background when both bosons decay leptonically and the W decay lepton is not identified. This background is the largest and contributes to approximately 56% of the total background.
- WW – A pair of leptonically decaying W bosons fake the signal when the invariant mass of the decay leptons lies close to the Z mass. WW events constitute approximately 29% of the total background.
- Top – Top quark pairs ($t\bar{t}$) produce the same signature as WW but with additional jets. Events where a top quark is produced singly with a W boson also produce a similar signature, but at a lower rate than $t\bar{t}$. A jet veto is applied to reject these backgrounds. This background is approximately 12% of the total background.
- $Z + \text{jets}$ – Events where a single Z boson is produced have no escaping neutrinos and are largely rejected by requiring large $E_{\text{T}}^{\text{miss}}$. In a small fraction of events the measured $E_{\text{T}}^{\text{miss}}$ fluctuates to pass the cut and enters the signal region. This process is approximately 4% of the total background.

- $W + \text{jets}$ – In order for $W + \text{jet}$ events to enter as a background a jet must fake a lepton and the invariant mass between the real and faked lepton pair must be near the Z boson mass. The probability for a jet to fake a lepton is small, but the rate of $W + \text{jet}$ events is much larger than the signal. This background small, but not negligible and contributes 3% of the total background.
- dijets – Similar to the $W + \text{jets}$ background, this process is a background when two jets fake leptons, the lepton invariant mass is near the Z mass peak, and the reconstructed $E_{\text{T}}^{\text{miss}}$ fluctuates to be large. This high rate process is reduced to less than 1% of the background.
- $H \rightarrow WW, H \rightarrow ZZ$ – Higgs production is a negligible background to this measurement. In $H \rightarrow WW$ events the dilepton invariant mass falls below the Z mass peak and in $H \rightarrow ZZ$ the $E_{\text{T}}^{\text{miss}}$ tends to be smaller than the signal selection cut.

8.2.2 Data and simulation samples

This measurement uses 4.6 fb^{-1} of data taken during the 2011 data taking period at $\sqrt{s} = 7 \text{ TeV}$. The data are required to have been recorded during stable beam conditions and during nominal detector and data readout performance. Data are recorded using unrescaled single electron and single muon triggers. As the instantaneous luminosity increased during the 2011 data taking period, it was necessary to increase the p_{T} threshold at which the lepton triggers were unrescaled. Therefore events were selected using different triggers depending on which trigger was unrescaled. The highest p_{T} threshold used was 22 GeV for electrons and 18 GeV for muons.

The ZZ signal and background processes are modeled with a variety of leading order (LO) and next-to-leading order (NLO) generators. The ZZ signal is modeled using the MC@NLO [80] generator and is cross-checked using the POWHEGBOX [94, 95, 96] and SHERPA [97] generators. The simulated particles are interfaced to a GEANT4 [83] model of the detector. Small differences are expected from these two generators because MC@NLO uses the narrow width approximation while POWHEGBOX and SHERPA do not. In addition SHERPA and POWHEGBOX treat FSR differently; in POWHEGBOX the entire $\ell\nu\nu$ system is affected by lepton FSR while in SHERPA only the leptonic decay is affected. Truth level mass and p_{T} distributions are compared between these generators in Figure 8.10. The contribution from gluon-gluon fusion is not included in the simulation and the cross section of the signal sample is increased by 6% to compensate. A systematic uncertainty is applied to account for differences in event kinematics between gluon-gluon fusion and $q\bar{q}$ collisions.

The WZ background is simulated using HERWIG [98], the WW background is simulated with MC@NLO, $W/Z + \gamma$ events are simulated with MADGRAPH [99], and $t\bar{t}$ and single top events are simulated using MC@NLO. The ALPGEN [82] generator is used to simulate Z/γ^* and W events.

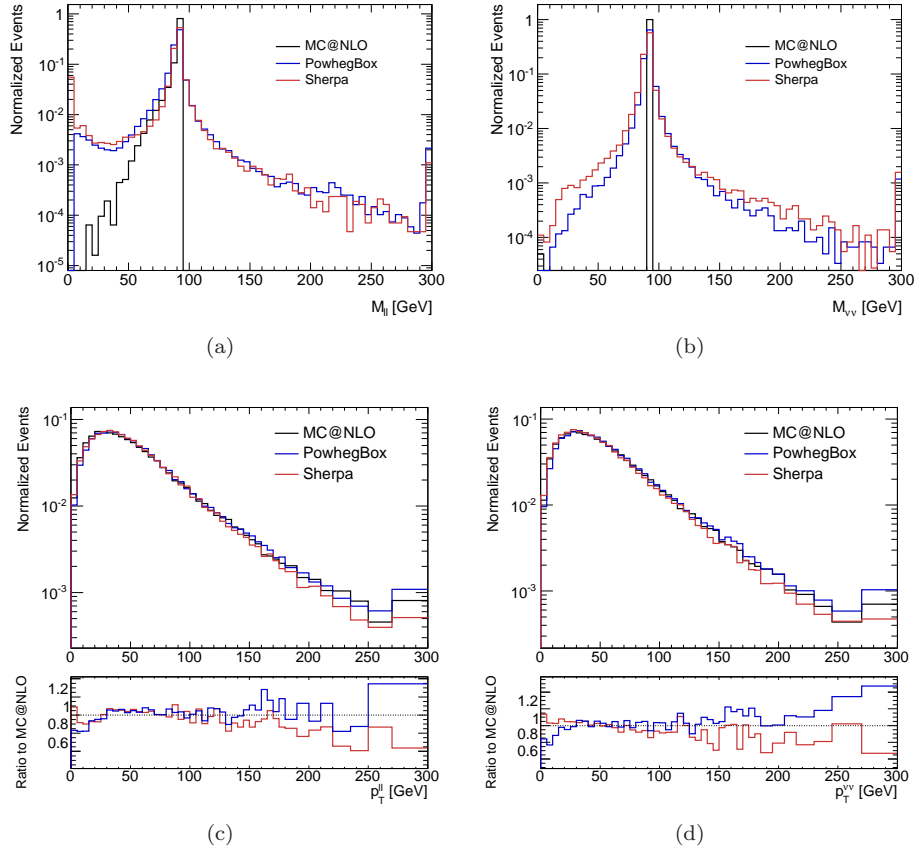


Figure 8.10: Truth level comparison of the ZZ signal simulated with MC@NLO, SHERPA, and POWHEGBOX. Plots (a) and (b) compare the dilepton and dineutrino mass. MC@NLO uses the narrow width approximation which generates Z bosons only at the peak of the mass distribution. In the case of the leptonically decaying Z boson FSR causes lower $M_{\ell\ell}$. Differences between SHERPA and POWHEGBOX are attributed to the treatment of FSR. In SHERPA the entire $\ell\nu\nu$ system is affected by FSR whereas POWHEGBOX treats each Z boson separately. Figures (c) and (d) show $p_T^{\ell\ell}$ and $p_T^{\nu\nu}$ distributions respectively. Good agreement is observed between the three generators. The bottom panels of Figures (c) and (d) show the ratio of the SHERPA and POWHEGBOX samples to the MC@NLO sample. In figures (b), (c), and (d) a cut is applied on the dilepton mass distribution to match the analysis cut, $76 \text{ GeV} < M_{\ell\ell} < 106 \text{ GeV}$.

The simulation is used to estimate the WZ and $W\gamma$ backgrounds while all other backgrounds are estimated using data-driven techniques.

8.2.3 Object selection

This analysis reconstructs electrons and muons to identify leptonically decaying Z bosons. The E_T^{miss} is used to identify the Z boson that decays to neutrinos. Jets must also be identified to implement a jet veto that rejects the top background. A general description of the reconstruction of analysis is given in Chapter 7. The following sections describe details of the selection of these objects specific to this analysis.

8.2.3.1 Electrons

Electrons are reconstructed as described in Section 7.3. The `medium++` identification criteria is used, which is similar to the medium working point, but was optimized for 2011 data taking. Electrons are required to have $p_T > 20$ GeV, and at least one electron in a di-electron event must have $p_T > 25$ GeV to ensure that the trigger efficiency is on plateau. Electrons are also selected having $p_T > 10$ GeV to veto an additional third electron that falls below the $p_T > 20$ GeV requirement. Electrons are required to have $|\eta| < 2.47$ so that the electron track is contained within the inner detector and the electron shower avoids a transition between the calorimeters. The transition region between the barrel and endcap calorimeters between $1.37 < |\eta| < 1.52$ has degraded electron performance, but is included to increase the signal acceptance. The calorimeter isolation requirement is $\text{EtCone30}/E_T < 0.14$ and the track isolation requirement is $\text{ptCone30}/E_T < 0.13$. Electrons are rejected if they fall within $\Delta R = 0.1$ of a fully identified muon to ensure that the same object is not reconstructed as both an electron and a muon.

8.2.3.2 Muons

Muons are identified following the description in Section 7.4. Muons must have $p_T > 20$ GeV and $|\eta| < 2.4$ so that the muon track traverses the inner detector. Muons are selected with $p_T > 10$ GeV to veto an additional third muon that falls below the $p_T > 20$ GeV requirement. The calorimeter isolation requirement is $\text{EtCone30}/p_T < 0.14$ and the track isolation requirement is $\text{ptCone30}/p_T < 0.15$. The z_0 of the inner detector track with respect to the primary vertex must be less than 1 mm and the d_0 significance must be less than 3.

8.2.3.3 Jets

Jets are reconstructed as described in Section 7.5. Jets must have $p_T > 25$ GeV and $|\eta| < 4.5$. To remove jets from pileup collisions, we require $|\text{JVF}| < 0.75$.

8.2.3.4 Missing transverse momentum

The `RefFinal` E_T^{miss} calculation is used as described in Section 7.7. In signal events the E_T^{miss} is expected to be back-to-back with the leptonically decaying Z boson. Therefore to enhance the sensitivity to the signal, the Axial E_T^{miss} definition described in Section 7.7.1 is used.

8.2.4 Event selection

A baseline dilepton event selection requires exactly two opposite sign, same flavor electrons or muons having $p_T > 20$ GeV. Events are separated into two channels based on the final state leptons present, ee , and $\mu\mu$. To reduce the background from WZ where the p_T of the W decay lepton falls below 20 GeV a veto is applied on any additional electrons or muons having $10 \text{ GeV} < p_T < 20 \text{ GeV}$. Figure 8.11 shows the dilepton mass distribution in each channel. A majority of signal events have on-shell Z bosons causing the dilepton mass distribution to peak at the Z mass. To remove backgrounds that do not peak at the Z mass such as WW and $t\bar{t}$ the dilepton mass is required to be consistent with the Z mass, $76 \text{ GeV} < M_{\ell\ell} < 106 \text{ GeV}$. This selection is dominated by Z/γ^* events and further cuts are applied to purify the signal selection.

A cut is applied on the Axial E_T^{miss} distribution to reject Z/γ^* events. Figure 8.12 shows the Axial E_T^{miss} distribution for events that pass the $M_{\ell\ell}$ cut. The fake E_T^{miss} background is centered around zero while the signal tends to have large and positive Axial E_T^{miss} . A cut of Axial $E_T^{\text{miss}} > 75$ GeV is applied to remove a majority of the Z/γ^* background. After the Axial E_T^{miss} cut, backgrounds having real E_T^{miss} dominate. Figure 8.13 shows the jet multiplicity after the $M_{\ell\ell}$ and Axial E_T^{miss} cuts are applied. The signal prefers the zero jet bin while the top background tends to have two or more jets. A jet veto is applied to reject the $t\bar{t}$ and Wt backgrounds while keeping most of the signal. In signal events having no high p_T jets the two Z bosons are produced back-to-back and have approximately the same p_T . The E_T^{miss} , which measures the p_T of the invisibly decaying Z boson, should therefore be similar in magnitude to $p_T^{\ell\ell}$. Therefore a cut on the fractional p_T difference, $|E_T^{\text{miss}} - p_T^{\ell\ell}|/p_T^{\ell\ell} < 0.4$, is applied to select signal events. Any Z/γ^* events that pass the Axial E_T^{miss} cut most likely do not have high $p_T^{\ell\ell}$ and therefore have large fractional p_T difference and fail the cut. This cut, applied in addition to the Axial E_T^{miss} cut implies a minimum $p_T^{\ell\ell}$ cut of $75/1.4$. To illustrate the effect of the jet veto and Axial E_T^{miss} cuts, figure 8.14 shows the Axial E_T^{miss} with all cuts applied except Axial E_T^{miss} and figure 8.15 shows the jet multiplicity distribution after

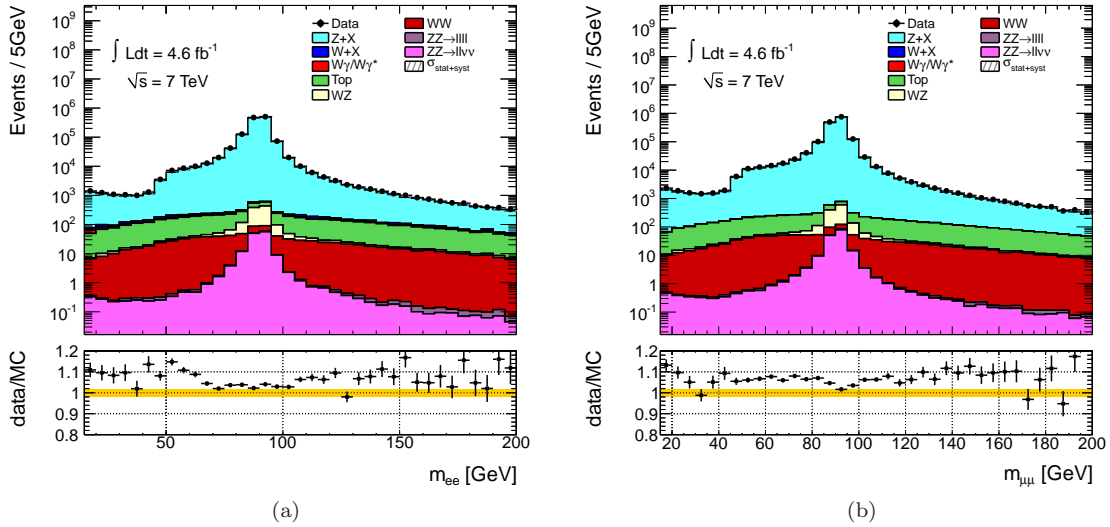


Figure 8.11: Invariant mass distributions after the baseline dilepton selection in the ee (a) and $\mu\mu$ (b) channels.

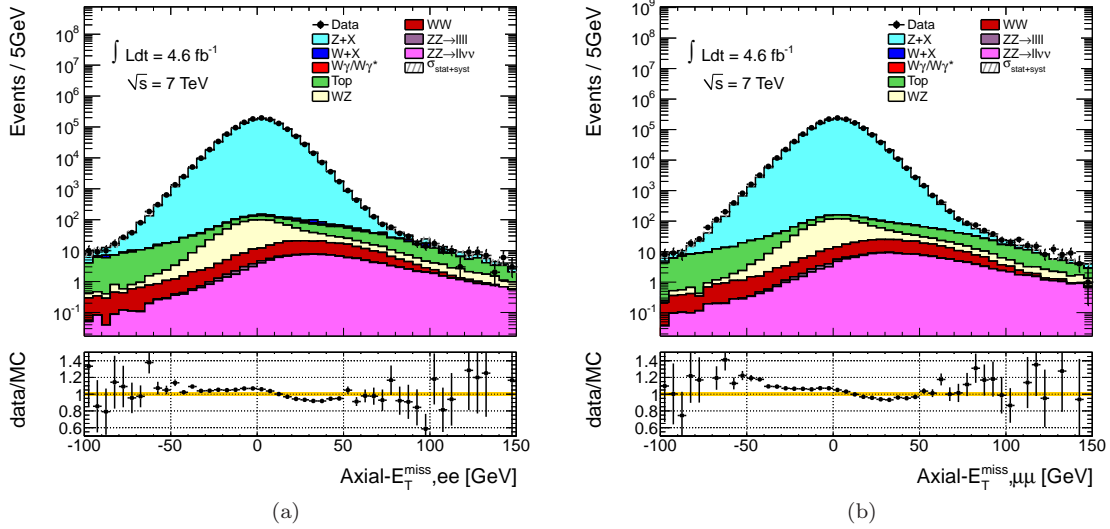


Figure 8.12: Axial E_T^{miss} distributions after the $M_{\ell\ell}$ cut in the ee (a) and $\mu\mu$ (b) channels.

all cuts except the jet veto. Figure 8.16 shows $M_{\ell\ell}$ after all cuts. A peak consistent with the Z mass is observed from the presence of signal $ZZ \rightarrow \ell^+ \ell^- \nu \bar{\nu}$ events.

8.2.5 Background estimation

A number of processes present backgrounds to this measurement. After the full signal selection approximately half of the selected events are expected to be from background processes. Therefore

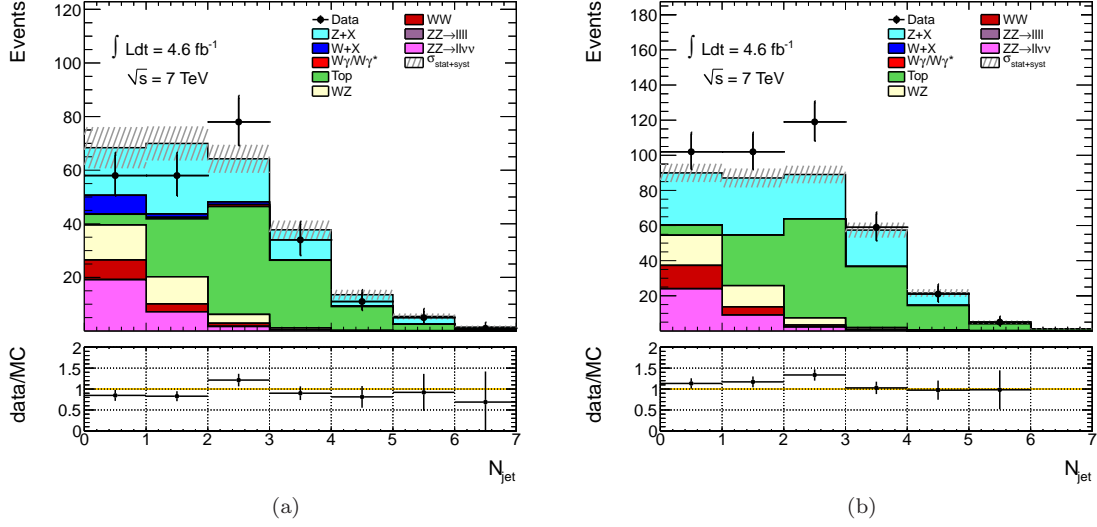


Figure 8.13: Jet multiplicity distributions in the ee (a) and $\mu\mu$ (b) channels after the $M_{\ell\ell}$ and Axial E_T^{miss} cuts are applied.

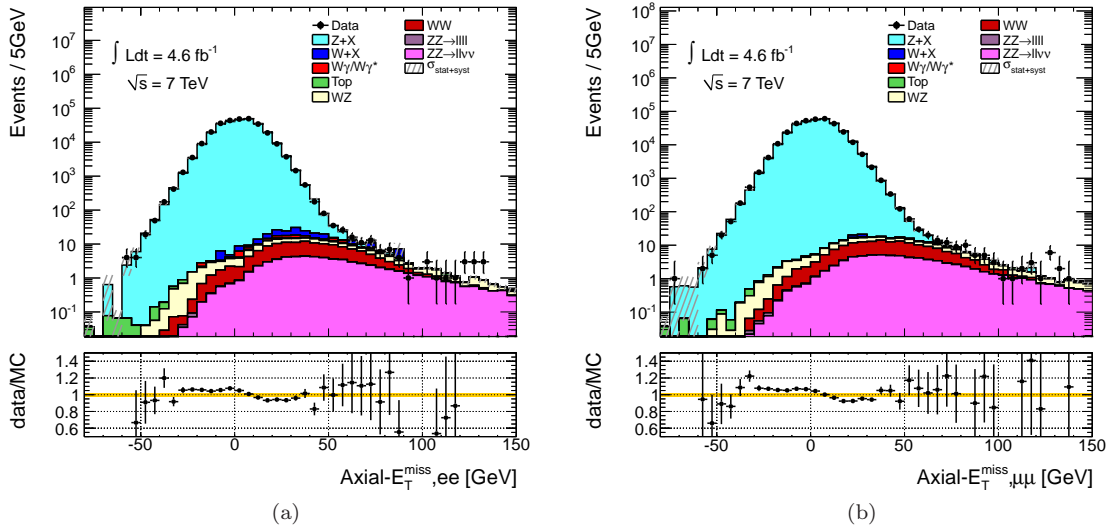


Figure 8.14: Axial E_T^{miss} distributions after all cuts except for Axial E_T^{miss} in the ee (a) and $\mu\mu$ (b) channels.

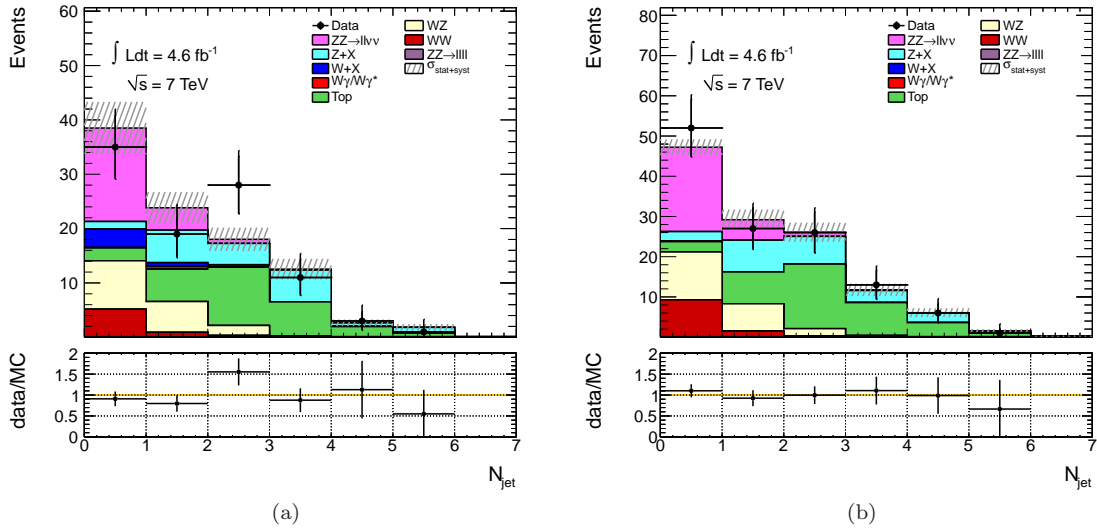


Figure 8.15: Jet multiplicity distributions after all cuts except for the jet veto in the ee (a) and $\mu\mu$ (b) channels.

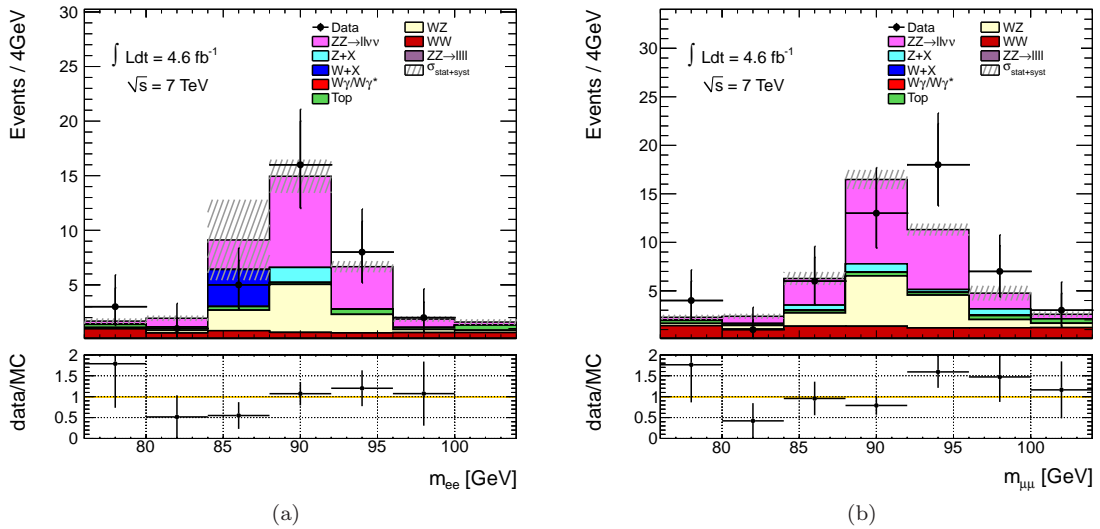


Figure 8.16: Dilepton mass distributions after all cuts in the ee (a) and $\mu\mu$ (b) channels.

it is essential to accurately predict these backgrounds. All backgrounds are estimated using data driven techniques except for the WZ background which is estimated using the simulation.

8.2.5.1 Combined $WW + \text{top} + Z \rightarrow \tau\tau$ estimate

The combination of the WW , top , and $Z \rightarrow \tau^+\tau^-$ backgrounds is estimated using the $e\mu$ control region. These backgrounds all exhibit flavor symmetry; the branching fraction to $e\mu$ is twice the branching fraction to ee or $\mu\mu$. The $e\mu$ control region is essentially signal free. The only possible signal contamination occurs when the leptonically decaying Z boson decays to tau leptons, but these events fall below the $M_{\ell\ell}$ window considered for the analysis. Differences in lepton identification and reconstruction efficiencies are corrected using the Z resonance in the ee and $\mu\mu$ channels. The estimate in the ee and $\mu\mu$ channels are,

$$N_{ee}^{est} = N_{e\mu}^{data} \times k_{ee}, \quad k_{ee} = \frac{1}{2} \sqrt{N_{ee}^{data}/N_{\mu\mu}^{data}} \quad (8.9)$$

$$N_{\mu\mu}^{est} = N_{e\mu}^{data} \times k_{\mu\mu}, \quad k_{\mu\mu} = \frac{1}{2} \sqrt{N_{\mu\mu}^{data}/N_{ee}^{data}} \quad (8.10)$$

The number of $e\mu$ events, $N_{e\mu}^{data}$, are corrected for small backgrounds by subtracting the contribution from processes that do not exhibit the flavor symmetry using simulation. Systematic uncertainties are derived from a closure test using simulation and from uncertainties in subtracting backgrounds using simulation. The uncertainty on the estimate is dominated by statistical uncertainties.

8.2.5.2 Z/γ^* background estimate

The Z/γ^* background is estimated using a single photon control region. The method will be briefly described here; see Chapter 11 for a complete description. Single photon events are selected as a proxy to Z/γ^* events because they both have no true E_T^{miss} . The E_T^{miss} is therefore dominated by fake sources in both samples. Using data events avoids the modeling issues in simulation that are discussed in Section 7.7.3.3. In addition, single photon events are produced through the same processes as Z/γ^* events. Single photons provide a high statistics control region because they are produced at a similar rate to Z/γ^* , but do not suffer from the 3% lepton branching fraction. The principle difference between single photon and Z/γ^* events is that Z/γ^* are massive while photons are not. This difference manifests its self in the difference between the photon p_T distribution (p_T^γ) and the $p_T^{\ell\ell}$ distribution. To account for this difference the p_T^γ distribution is reweighted to match the $p_T^{\ell\ell}$ distribution.

Photons are selected using single photon triggers of varying p_T thresholds. Photon triggers having low p_T thresholds must be prescaled to reduce the rate. The prescale is relatively smaller for higher

threshold triggers and the 80 GeV trigger threshold is not prescaled in 2011 data. Events that pass prescaled triggers must be corrected to reproduce the correct pileup distribution. Trigger prescales are changed between data runs and within runs to maintain a constant trigger rate. At higher instantaneous luminosity the trigger prescales are increased. The number of pileup interactions scales with the instantaneous luminosity causing the prescaled triggers to be biased towards lower pileup conditions. To correct for the bias, the distribution of the average number of pileup interactions for prescaled triggers is weighted to match the distribution for the unprescaled trigger.

After the p_T^γ and prescale weights are applied the Axial E_T^{miss} and fractional p_T difference cuts are applied to the single photon distribution where p_T^γ replaces the $p_T^{\ell\ell}$ in both definitions. Systematics are derived from dijet contamination, subtraction of real E_T^{miss} backgrounds in the single photon sample using simulation, and the performance of the single photon method in a low Axial E_T^{miss} control region.

8.2.5.3 $W + \text{jet}$ background estimate

The $W + \text{jet}$ background is estimated using a matrix method. The matrix maps the reconstructed lepton type (tight, loose) to the true lepton type (real, fake). The loose lepton definition is enhanced in jet fakes and is used as a baseline to estimate the probability for a jet to fake a tight lepton. The source of fake leptons depends on the lepton flavor. Electrons are faked by decays in flight from heavy flavor jets, by light flavor jets where the jet topology passes the electron identification cuts and by photon conversions. The loose electron definition loosens the PID requirement and removes the isolation cuts. Muons are faked mainly by heavy flavor decays in flight. The loose muon definition removes the isolation cuts. The terms in the matrix consist of lepton efficiencies measured in a pure Z sample and loose lepton fake factors derived in a dijet control region. Using the loose and tight (denoted L and T respectively) definitions there are four types of events, TT, LT, TL, and LL. The matrix maps these four types events to the true composition of the event having real and fake (denoted R and F respectively) leptons, RR, RF, FR, FF. The matrix equation is,

$$\begin{bmatrix} N_{TT} \\ N_{TL} \\ N_{LT} \\ N_{LL} \end{bmatrix} = \begin{bmatrix} r_1 r_2 & r_1 f_2 & f_1 r_2 & f_1 f_2 \\ r_1(1-r_2) & r_1(1-f_2) & f_1(1-r_2) & f_1(1-f_2) \\ (1-r_1)r_2 & (1-r_1)f_2 & (1-f_1)r_2 & (1-f_1)f_2 \\ (1-r_1)(1-r_2) & (1-r_1)(1-f_2) & (1-f_1)(1-r_2) & (1-f_1)(1-f_2) \end{bmatrix} \times \begin{bmatrix} N_{RR} \\ N_{RF} \\ N_{FR} \\ N_{FF} \end{bmatrix} \quad (8.11)$$

where N_{XX} is the number of events having the signatures described above, r_1 and r_2 are the true lepton efficiencies for the leading and subleading leptons respectively, and f_1 and f_2 are the probabilities for a loose lepton to fake a tight lepton for the leading and subleading leptons respectively. The

lepton efficiencies and jet fake factors depend on the p_T of the object and are binned accordingly. The number of estimated $W + \text{jets}$ is,

$$N_{W+\text{jets}} = \sum_i^{\text{events}} N_{RF}^i \times r_1^i \times f_2^i + N_{FR}^i \times f_1^i \times r_2^i \quad (8.12)$$

Where N_{FR} and N_{RF} are determined from solving Equation 8.11.

The lepton reconstruction efficiency is determined using a selection of pure Z events. Events are required to have one tight and one loose lepton and the invariant mass must be within 5 GeV of the Z mass. The efficiency determined as a function of p_T is the fraction of loose leptons in this selection that pass the tight identification criteria. The jet fake factor is determined in a jet rich control region. Events are selected with a jet trigger and are required to have exactly one loose lepton. Sources of true leptons are vetoed and the remaining true lepton background is subtracted using simulation. The fake factor is the fraction of loose leptons in this selection that pass the tight identification criteria.

8.2.6 Cross section and fiducial volume definition

The cross section is measured within the fiducial volume of this analysis and this measurement extrapolated to the total phase space. The fiducial cross section suffers from fewer uncertainties than the total cross section and allows for a comparison with theory by measuring the ZZ rate with fewer uncertainties. The fiducial cross section is given by,

$$\sigma_{zz}^{\text{fiducial}} = \frac{N_{\text{obs}} - N_{\text{bkg}}}{C_{ZZ}\mathcal{L}} \quad (8.13)$$

Where C_{ZZ} is the reconstruction efficiency within the fiducial volume,

$$C_{ZZ} = \frac{N_{\text{final reco.}}^{\text{MC}}}{N_{\text{generator}}^{\text{MC in fiducial volume}}} \times \left[\frac{\epsilon_{\text{trig}}^{\text{data}}}{\epsilon_{\text{trig}}^{\text{MC}}} \times \frac{\epsilon_{\text{reco}}^{\text{data}}}{\epsilon_{\text{reco}}^{\text{MC}}} \times \frac{\epsilon_{\text{jet veto}}^{\text{data}}}{\epsilon_{\text{jet veto}}^{\text{MC}}} \right] \quad (8.14)$$

The first term measures the reconstruction efficiency using simulation and the terms in the brackets correct the lepton trigger and reconstruction efficiencies and the jet veto efficiency to those measured in data. The total cross section is measured by including an additional factor, A_{ZZ} , which is the efficiency of the fiducial volume selection relative to the full phase space. The full phase space considered is all events where both Z/γ^* are on shell having masses between $66 \text{ GeV} < M_Z < 116 \text{ GeV}$. A_{ZZ} is given by

$$A_{ZZ} = \frac{N_{\text{generator}}^{\text{MC in fiducial volume}}}{N_{\text{generator}}^{\text{total}}} \quad (8.15)$$

The total cross section is,

$$\sigma_{zz}^{\text{total}} = \frac{N_{\text{obs}} - N_{\text{bkg}}}{BR(ZZ \rightarrow \ell\ell\nu\nu)A_{ZZ}C_{ZZ}\mathcal{L}} \quad (8.16)$$

	ee channel	$\mu\mu$ channel	combined
A_{ZZ}			$0.081 \pm 0.001 \pm 0.005$
C_{ZZ}	$0.625 \pm 0.005 \pm 0.024$	$0.766 \pm 0.005 \pm 0.015$	$0.695 \pm 0.004 \pm 0.014$

Table 8.8: Reconstruction efficiencies for the ZZ signal determined from POWHEGBOX simulation. A_{ZZ} is the efficiency for generated events to fall in the fiducial volume and C_{ZZ} is the efficiency for generated events in the fiducial volume to be reconstructed. C_{ZZ} is measured for each channel and A_{ZZ} is assumed to be the same in both channels.

The fiducial volume definition should closely resemble the event selection and events that fail the fiducial selection should not pass the nominal event selection. The fiducial definition is,

- Exactly two opposite sign electrons or muons having $p_T > 20$ GeV and $|\eta| < 2.5$
- $76 \text{ GeV} < M_{\ell\ell} < 106 \text{ GeV}$
- Axial $E_T^{\text{miss}} - -p_T^{\nu\nu} \times \cos(\Delta\phi(p_T^{\nu\nu}, p_T^{\ell\ell})) > 75 \text{ GeV}$
- Fractional p_T difference $- |p_T^{\ell\ell} - p_T^{\nu\nu}|/p_T^{\ell\ell} < 0.4$
- Jet Veto – no particle level jets having $p_T > 25 \text{ GeV}$ and $|\eta| < 4.5$ with electron-jet overlap removal, $\Delta R(e, j) > 0.3$
- leptons cannot overlap because of isolation requirements $- \Delta R(\ell, \ell) > 0.3$

8.2.7 Signal acceptance

As described previously the signal acceptance is separated into two terms. Table 8.8 shows the efficiencies and their uncertainties. The efficiency of the fiducial volume selection, A_{ZZ} , is determined using POWHEGBOX simulation. Uncertainties on A_{ZZ} are derived from comparisons to aMC@NLO [100] and from variations by a factor of two on the renormalization and factorization scale. An additional uncertainty accounts for the 6% contribution from the gluon fusion process which is not included in the POWHEGBOX simulation. The affect of gluon fusion is evaluated using a sample generated with gg2zz [101]. The total uncertainty on A_{ZZ} is 6.3%. The uncertainty on C_{ZZ} is derived from comparisons to other simulations and from uncertainties on lepton reconstruction, lepton energy scale, jet energy scale, E_T^{miss} scale, and the jet veto efficiency. The total combined uncertainty on C_{ZZ} is 2.1%. The luminosity uncertainty is 1.8%, an improvement on the 3.4% uncertainty used in earlier 2011 analysis and in particular the analysis presented in Section 9.2.

Final State	$e^+e^- E_T^{\text{miss}}$	$\mu^+\mu^- E_T^{\text{miss}}$	$\ell\ell + E_T^{\text{miss}}$
Observed Events	35	52	87
Expected ZZ Signal	$18.2 \pm 0.5 \pm 1.9$	$22.1 \pm 0.6 \pm 2.2$	$40.3 \pm 0.4 \pm 4.0$
Backgrounds			
WZ (MC)	$8.9 \pm 0.5 \pm 0.4$	$11.9 \pm 0.5 \pm 0.3$	$20.8 \pm 0.7 \pm 0.5$
$W\gamma$ (MC)	$0.1 \pm 0.1 \pm 0.1$	$0.1 \pm 0.1 \pm 0.1$	$0.2 \pm 0.1 \pm 0.1$
$WW + \text{top} + Z \rightarrow \tau\tau$ (data-driven)	$8.5 \pm 2.1 \pm 0.5$	$10.6 \pm 2.6 \pm 0.6$	$19.1 \pm 3.3 \pm 0.8$
$Z + \text{jets}$ (data-driven)	$2.6 \pm 0.7 \pm 1.0$	$2.7 \pm 0.8 \pm 1.2$	$5.3 \pm 1.1 \pm 1.6$
$W + \text{jets}$ (data-driven)	$0.7 \pm 0.3 \pm 0.3$	$0.7 \pm 0.2 \pm 0.2$	$1.4 \pm 0.4 \pm 0.4$
Total Background	$20.8 \pm 2.2 \pm 1.2$	$26.1 \pm 2.7 \pm 1.4$	$46.9 \pm 2.7 \pm 3.5$

Table 8.9: The number of observed events, the expected number of events, and the contribution from each background for the ee and $\mu\mu$ channels.

Fiducial, ee channel	$4.9^{+2.2}_{-1.9}(\text{stat.})^{+0.9}_{-0.9}(\text{syst.}) \pm 0.1(\text{lumi})$ fb
Fiducial, $\mu\mu$ channel	$7.1^{+2.1}_{-1.9}(\text{stat.})^{+0.9}_{-0.9}(\text{syst.}) \pm 0.1(\text{lumi})$ fb
Fiducial, combined	$12.5^{+3.0}_{-2.8}(\text{stat.})^{+1.0}_{-1.1}(\text{syst.}) \pm 0.2(\text{lumi})$ fb
Total, combined	$5.7^{+1.4}_{-1.3}(\text{stat.})^{+0.7}_{-0.6}(\text{syst.}) \pm 0.1(\text{lumi})$ pb

Table 8.10: Measured ZZ cross sections with uncertainties.

8.2.8 Results

The number of observed events and the expectation from each background is shown in Table 8.9. The observed number of events is consistent with the prediction from signal plus the background expectation. Approximately half of the observed events are expected to be from signal events. The measured cross section is extracted by maximizing a likelihood function for the best fit cross section. The results for both the fiducial and total cross sections are shown in Table 8.10.

8.2.9 Differential cross sections and limits on anomalous triple gauge couplings

To further facilitate the comparison with theory differential cross sections are measured in three distributions, $p_T^{\ell\ell}$, $\Delta\phi(\ell, \ell)$, and the transverse mass, m_T . Differential cross sections are measured within the fiducial acceptance as defined above in Section 8.2.6. Measured distributions are unfolded to the truth level distributions. A matrix derived from simulation maps the reconstructed distribution to the truth level distribution and accounts for bin-to-bin migration. Additional systematic uncertainties are assessed to account for uncertainties in deriving the matrix from simulation. Figure 8.17 shows the unfolded differential cross section measurements.

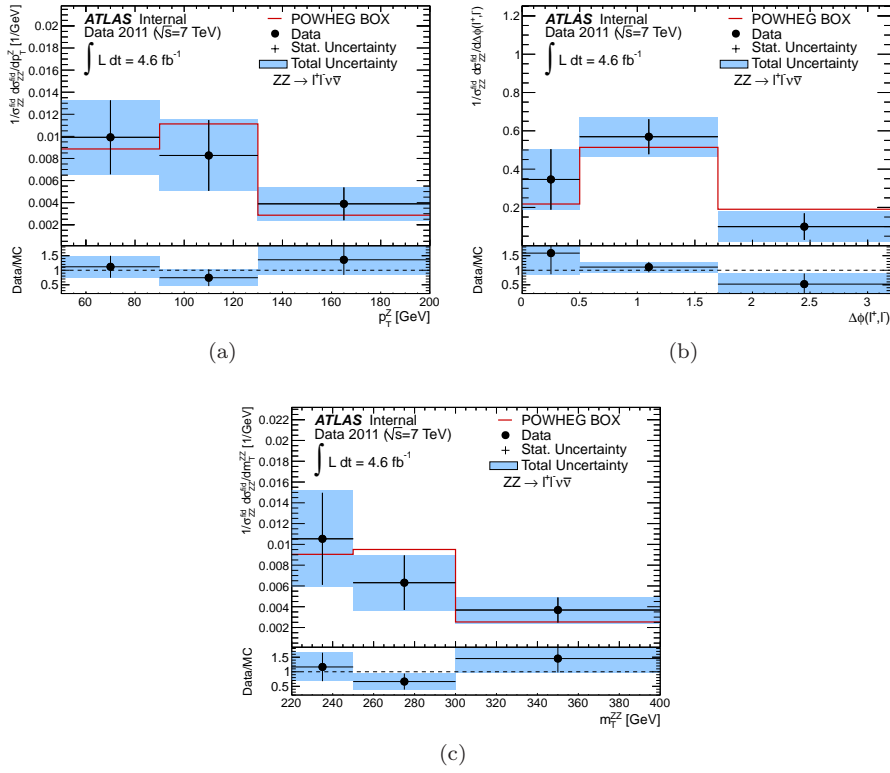


Figure 8.17: Differential cross section measurements unfolded to the generator level. The blue band shows the total uncertainty on the measurement and is compared to the POWHEGBOX simulation shown by the red line.

Limits are placed on possible extensions to the Standard Model that result in an anomalous $ZZ\gamma$ or ZZZ triple gauge coupling following the method developed by Baur and Rainwater [102]. Anomalous TGCs tend to increase the ZZ cross section at high p_T^Z . The $ZZ \rightarrow \ell\ell\nu\nu$ channel is particularly sensitive to this enhancement because it produces large E_T^{miss} and $p_T^{\ell\ell}$. Figure 8.18 shows the binned $p_T^{\ell\ell}$ distribution with predictions from aTGC enhancements. In Figure 8.19 the combined result from this analysis and the $llll$ channel are combined and compared to previous measurements at LEP [103] and the Tevatron [104].

8.2.10 Summary

The ZZ cross section was measured in the $\ell\ell\nu\nu$ final state at $\sqrt{s} = 7$ TeV using 4.6 fb^{-1} of data taken during the 2011 data run. The cross section was measured within the fiducial acceptance of the analysis and was extrapolated to measure the total ZZ cross section. Differential cross sections were provided in $p_T^{\ell\ell}$, $\Delta\phi(\ell, \ell)$, and m_T and limits were set on anomalous triple gauge couplings. Results were combined with similar measurements in the $llll$ channel. The measured total cross

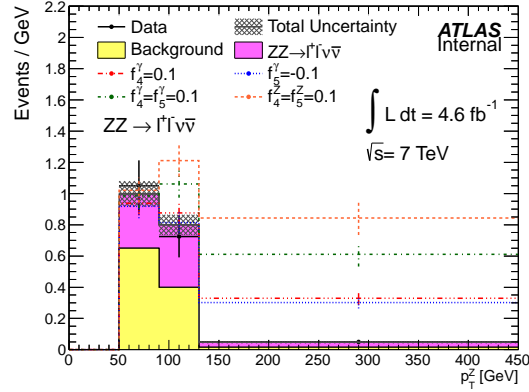


Figure 8.18: $p_T^{\ell\ell}$ distribution with predictions from various anomalous TGC predictions.

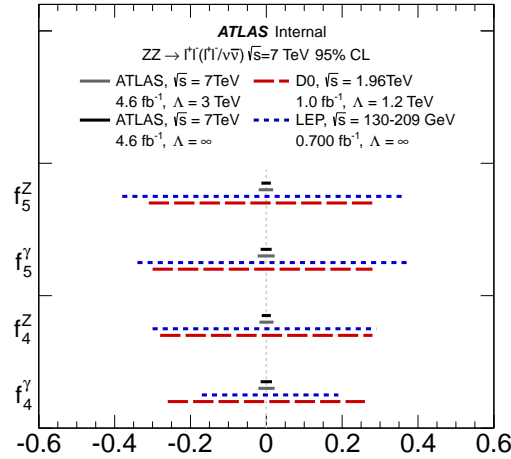


Figure 8.19: Combined anomalous TGC limits compared to limits from LEP and the Tevatron. This measurement significantly improves on previous limits.

section of $5.7_{-1.3}^{+1.4}(\text{stat.})_{-0.6}^{+0.7}(\text{syst.}) \pm 0.1(\text{lumi})$ pb agrees well with the cross section measured in the $llll$ channel, $7.0_{-0.8}^{+0.9}(\text{stat.})_{-0.3}^{+0.4}(\text{syst.}) \pm 0.1(\text{lumi})$ pb and with the theoretical NLO prediction of $5.89_{-0.18}^{+0.22}$ pb. The higher center of mass energy and higher luminosity of the LHC facilitates much improved limits on anomalous triple gauge couplings over LEP and the Tevatron.

CHAPTER 9

Search for the Higgs boson in the $W^+W^- \rightarrow \ell^+\nu\ell^-\bar{\nu}$ channel

9.1 Observation of the Higgs boson

On July 4, 2012 the CMS and ATLAS experiments each announced 5σ evidence for the discovery of a Higgs-like boson [105, 106]. In the year since the discovery, additional data have been used to measure the spin of the new boson, providing further confirmation that a Higgs boson [107] was discovered (see Section 3.1 for details on Higgs properties). The discovery of the Higgs boson marked a significant milestone in the history of particle physics and completed a major goal of the LHC program. Three channels contributed significantly to the discovery: $H \rightarrow \gamma\gamma$, $H \rightarrow ZZ^{(*)} \rightarrow \ell^+\ell^-\ell^+\ell^-$, and $H \rightarrow W^+W^{(*)-} \rightarrow \ell^+\nu\ell^-\bar{\nu}$. Once the leptonic decay branching ratios are taken into account, $H \rightarrow W^+W^{(*)-} \rightarrow \ell^+\nu\ell^-\bar{\nu}$ has the highest rate, but it also suffers from large backgrounds and has poor mass resolution. The $H \rightarrow \gamma\gamma$ channel has no additional branching ratio and has the second highest rate. The Higgs mass is fully reconstructed in this channel, but the signal lies under a large continuum $\gamma\gamma$ background. $H \rightarrow ZZ^{(*)} \rightarrow \ell^+\ell^-\ell^+\ell^-$ has the lowest rate because of the 1% branching fraction to four charged leptons (see Table 8.7), but a Higgs mass peak is reconstructed on top of a relatively small background. Figure 9.1 shows the final signal selection plots for the three channels. An excess of events is observed in all three channels and the $H \rightarrow \gamma\gamma$ and $H \rightarrow ZZ^{(*)} \rightarrow \ell^+\ell^-\ell^+\ell^-$ show a mass peak near 125 GeV. Figure 9.2 shows the local probability (p_0) – the probability that the observed number of events is due to a statistical fluctuation of the background – for each channel and for the combination of all channels. The $H \rightarrow ZZ^{(*)} \rightarrow \ell^+\ell^-\ell^+\ell^-$ and $H \rightarrow \gamma\gamma$ channels show an excess of 3.6σ and 4.5σ respectively near 125 GeV and a broad 2σ excess is observed in the $H \rightarrow W^+W^{(*)-} \rightarrow \ell^+\nu\ell^-\bar{\nu}$ channel. The combination of the three channels shows the presence of a signal with 6σ significance meaning that that probability that the observed excesses is due to fluctuation of the background is 1 in 10^9 .

9.2 $H \rightarrow W^+W^{(*)-} \rightarrow \ell^+\nu\ell^-\bar{\nu}$ search

The WW decay mode is particularly useful in the search for the Higgs boson. For Higgs masses above twice the W mass the two W bosons are on-shell and the Higgs decays to WW most of the time (see Section 3.1 for a discussion of Higgs branching fractions). At lower masses the WW decay rate begins to drop as one W boson must be off shell. This channel therefore provides the best Higgs exclusion above 140 GeV and is competitive with other channels down to approximately 120 GeV. The $H \rightarrow WW$ process is identified in the fully leptonic decay mode giving it a $\ell\ell + E_T^{\text{miss}}$ signature. Similar to the WW cross section measurement presented in Section 8.1, the fully leptonic branching fraction is the smallest, (see Table 8.1) but also has the smallest background. A particularly challenging element of this analysis is separating the $H \rightarrow WW$ signal from the continuum WW

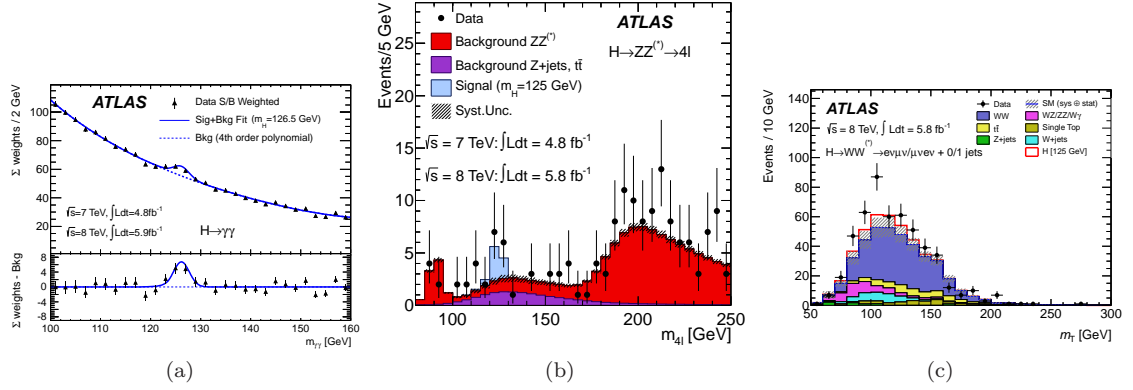


Figure 9.1: Final signal selection plots for the $H \rightarrow \gamma\gamma$ (a), $H \rightarrow ZZ^{(*)} \rightarrow \ell^+\ell^-\ell^+\ell^-$ (b), and $H \rightarrow W^+W^{(*)-} \rightarrow \ell^+\nu\ell^-\bar{\nu}$ (c) channels. Events in Figure (a) are weighted by the sensitivity of each $H \rightarrow \gamma\gamma$ sub-channel to show the sensitivity of all sub-channels combined.

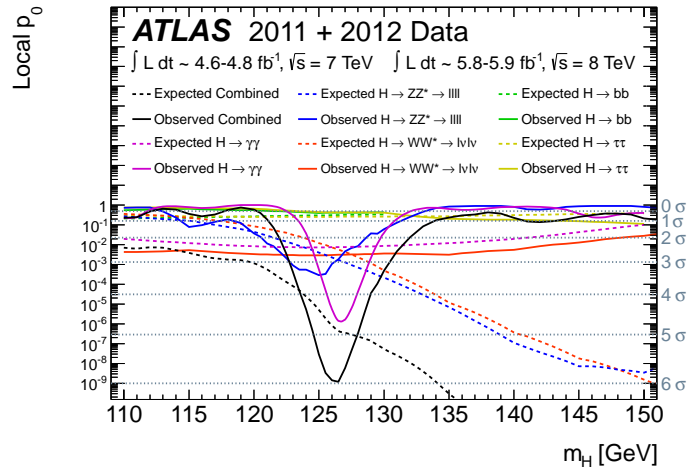


Figure 9.2: The observed and expected local probability for all channels contributing to the Higgs boson discovery. The $H \rightarrow \gamma\gamma$ and $H \rightarrow ZZ^{(*)} \rightarrow \ell^+\ell^-\ell^+\ell^-$ channels both show excess events at significances of 4.5σ and 3.6σ respectively near 125 GeV. The $H \rightarrow W^+W^{(*)-} \rightarrow \ell^+\nu\ell^-\bar{\nu}$ channel has poor mass resolution, but observes a broad excess at a significance of 2.8σ . The combined significance is 6σ – sufficient to claim discovery of a Higgs-like boson. The $H \rightarrow b\bar{b}$ and $H \rightarrow \tau^+\tau^-$ channels do not have enough sensitivity in this dataset to observe a signal at the predicted standard model rate.

background. The Higgs signal is discriminated from the WW background using topological cuts that are sensitive to the spin of the WW system. The W decay is fully parity violating such that the anti-matter decay particle is preferentially emitted along the spin of the W . When the W bosons originate from a spin 0 Higgs boson, the spins of the W bosons must be opposite. The left-handed nature of the weak interaction means that W^- bosons must decay to an anti-neutrino and the W^+ boson must decay to a neutrino. This causes the two charged leptons to be preferentially emitted in the same direction. Continuum WW production occurs through a mixture of the spins of the initial state quarks and the leptons instead tend to be back-to-back. Therefore the azimuthal separation between the two charged leptons ($\Delta\phi(\ell, \ell)$) is used to discriminate $H \rightarrow WW$ from continuum WW production. This channel has a poor mass resolution because the E_T^{miss} measures only the sum of the neutrino momenta and only transverse information is available. The best measure of the WW mass is the transverse mass (m_T) defined as $m_T = \sqrt{(E_T^{\ell\ell} + E_T^{\text{miss}})^2 - |p_T^{\ell\ell} + E_T^{\text{miss}}|^2}$ which measures the mass using only transverse quantities. The transverse mass distribution is used as the final signal discriminant.

9.2.1 Analysis overview

This section reports on a search for $H \rightarrow WW$ using 4.6 fb^{-1} of data recorded with beams colliding at $\sqrt{s} = 7 \text{ TeV}$ from the full 2011 data run. This result was published in Ref [108] and has been updated to include the full 2011 and 2012 datasets in [109]. This quantity of data could not provide enough sensitivity to observe the Higgs boson, but a large range of masses, between 127 GeV and 233 GeV were excluded. The equivalent search was performed in this channel with the CMS detector [110] and masses between 129 GeV and 270 GeV were excluded. The CMS result has also been updated to include the full 2011 and 2012 datasets [111]. This channel was a major contribution to the Higgs mass exclusion from the Tevatron [112] which excluded masses between 147 GeV and 180 GeV.

Events are separated into three channels based on the final state leptons present: ee , $e\mu$, and $\mu\mu$. The transverse momentum carried by the escaping neutrinos is identified as large E_T^{miss} . The analysis is additionally separated into zero jet, one jet, and two jet channels. The zero jet channel has the highest sensitivity because it has the smallest background from top events. The one jet channel suffers from the top background, but adds additional sensitivity. The two jet channel selects Higgs bosons produced via VBF but has little sensitivity in the 2011 dataset.

9.2.2 $H \rightarrow WW$ signal

The main Higgs production mechanism is through gluon fusion. Figure 9.3 shows the production of a Higgs boson and subsequent decay to the final state of interest. The gluon fusion production

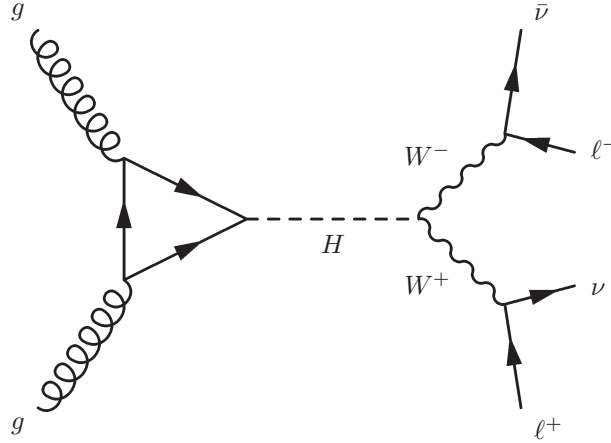


Figure 9.3: Feynman diagram for the production of a Higgs boson via gluon fusion that decays to WW with the subsequent decay to the fully leptonic final state.

cross section is calculated to next-to-next-to leading order in QCD [113]. For a Higgs boson having $m_H = 125$ GeV the cross section is 15.13 pb. The production proceeds through a quark loop that is dominated by the top and bottom quarks because they have the largest Yukawa couplings to the Higgs boson. Calculations show that the corrections to the cross section from adding higher order terms are large, leading to a large uncertainty on the Higgs production cross section. The signal is simulated using the POWHEG [94, 95, 96] generator. Samples are generated for a number of Higgs mass hypotheses between 110 GeV and 600 GeV.

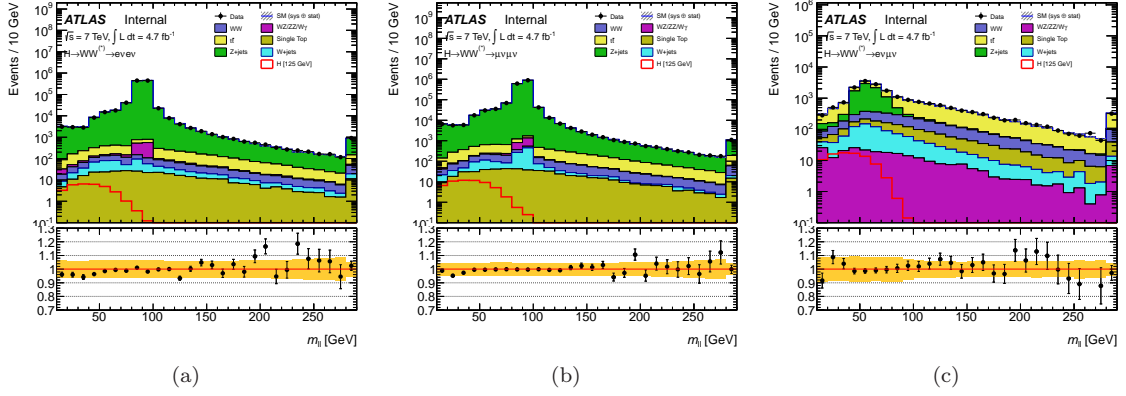
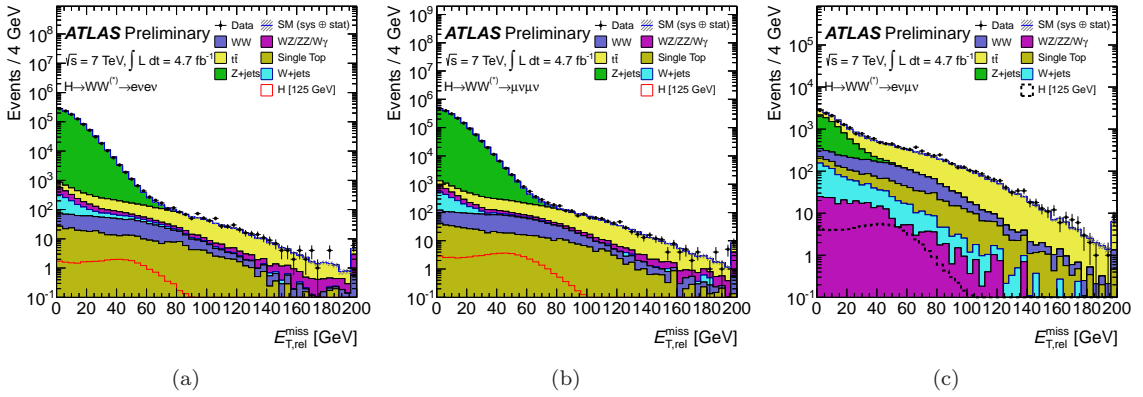
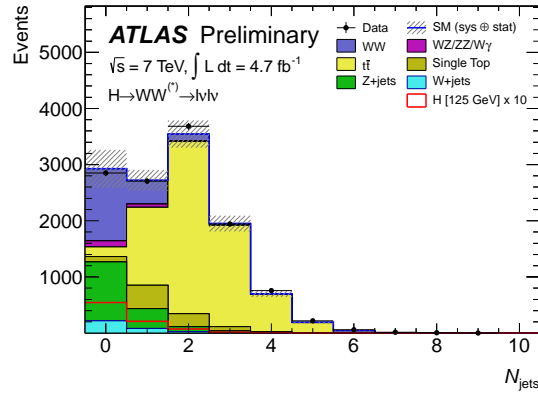
The predicted number of signal events depends on the mass hypothesis. The production cross section decreases as the Higgs mass increases, and the branching ratio to WW depends strongly on the Higgs mass when it is below a mass of 160 GeV (see Section 3.1 for a discussion of Higgs production rates and branching fractions). In retrospect, the Higgs boson that was discovered has a mass of approximately 125 GeV. The production cross section at this mass is 15.3 pb and the branching fraction to WW is 21.5%. Including the branching fraction to the fully leptonic final state, approximately 1000 $H \rightarrow W^+W^{(*)-} \rightarrow \ell^+\nu\ell^-\bar{\nu}$ events are produced in the 2011 dataset. Background rejection cuts further reduce the available signal events.

9.2.3 Object and event selection

At low Higgs masses one of the W bosons is off-shell and one decay lepton tends to have low p_T . To have the best signal efficiency the lepton p_T requirement should therefore be low. However, low p_T leptons are often faked by jets, and the $W + \text{jet}$ background increases if the p_T requirement is lower. To balance these two effects, electrons and muons are required to have $p_T > 15$ GeV. To reduce the $W + \text{jet}$ background, electrons are required to pass the `tight++` requirement and both electrons

and muons must pass tight calorimeter and track isolation. Sections 7.3 and 7.4 give a detailed description of electron and muon reconstruction. The E_T^{miss} is reconstructed using the **RefFinal** algorithm as described in Section 7.7. To reduce the impact of lepton mismeasurements on the E_T^{miss} the $E_T^{\text{miss,rel}}$ definition is used. Jets are reconstructed using the anti- k_t algorithm as described in Section 7.5. To remove jets originating from pileup vertices we require $|\text{JVF}| > 0.75$.

The baseline event selection requires two opposite sign electrons, muons, or an electron and a muon, making three channels: ee , $\mu\mu$, and $e\mu$. At least one final state lepton must match a trigger object and the matching lepton must have $p_T > 25$ GeV so that the trigger efficiency is on plateau. Since the background composition is different between the same flavor and $e\mu$ channels, different cuts are made where necessary. In the same flavor channels, the Z resonance and low mass resonances are vetoed by requiring $M_{\ell\ell} > 12$ GeV and $|M_{\ell\ell} - M_Z| > 15$ GeV while in the $e\mu$ channel we require $M_{\ell\ell} > 10$ GeV. Figure 9.4 shows the dilepton mass distributions for each channel. The prediction for a Higgs boson having $m_H = 125$ GeV is shown in red. The dilepton invariant mass from a low mass Higgs boson tends to be small. For Higgs mass hypothesis below $m_H = 200$ GeV the invariant mass requirement is $M_{\ell\ell} < 50$ GeV. For higher mass hypothesis, the invariant mass must be less than 150 GeV except for the Z mass window which is vetoed in the ee and $\mu\mu$ channels. The Z/γ^* background is largely removed by requiring $E_T^{\text{miss,rel}} > 45$ GeV in the same flavor channels and $E_T^{\text{miss,rel}} > 25$ GeV in the $e\mu$ channel. In the $e\mu$ channel the cut is lowered because there is less background from $Z \rightarrow \tau\tau$ than from $Z \rightarrow ee$ and $Z \rightarrow \mu\mu$ in the same flavor channels. Figure 9.5 shows the $E_T^{\text{miss,rel}}$ distributions for each channel. As described previously the analysis is separated into events having zero, one, and two jets with a VBF signature. The zero jet analysis provides the most sensitivity and will be the focus of the event selection. Figure 9.6 shows the jet multiplicity distribution for all channels combined after $E_T^{\text{miss,rel}}$ and $M_{\ell\ell}$ cuts are applied. The zero jet bin has the smallest background from top events and a majority of the signal. At this stage of the signal selection, the contribution of Z/γ^* events still dominates the selection. In Z/γ^* events that pass the jet veto, the $p_T^{\ell\ell}$ tends to be small while in signal events having zero jets $p_T^{\ell\ell}$ is approximately equal to E_T^{miss} . Therefore, to further reject the Z/γ^* background, we require $p_T^{\ell\ell} > 45$ GeV in the same flavor channels and $p_T^{\ell\ell} > 30$ GeV in the $e\mu$ channel. To take advantage of the spin correlation in $H \rightarrow WW$ to discriminate it from continuum WW , the azimuthal opening angle of the two leptons must be $\Delta\phi(\ell, \ell) < 1.8$ for Higgs mass hypothesis below $m_H = 200$ GeV. For higher masses the leptons tend to be farther apart and this cut is not applied. The final discriminating variable is the transverse mass. Figure 9.7 shows the transverse mass for all channels combined. The expectation for a $m_H = 125$ GeV signal is shown in black.


 Figure 9.4: Dilepton mass distributions in the ee (a), $\mu\mu$ (b), and $e\mu$ channels (c) after the baseline lepton selection.

 Figure 9.5: $E_T^{\text{miss,rel}}$ distributions in the ee (a), $\mu\mu$ (b), and $e\mu$ channels (c) after the baseline lepton selection.

 Figure 9.6: Jet multiplicity for the three channels combined after the $E_T^{\text{miss,rel}}$ and $M_{\ell\ell}$ cuts are applied.

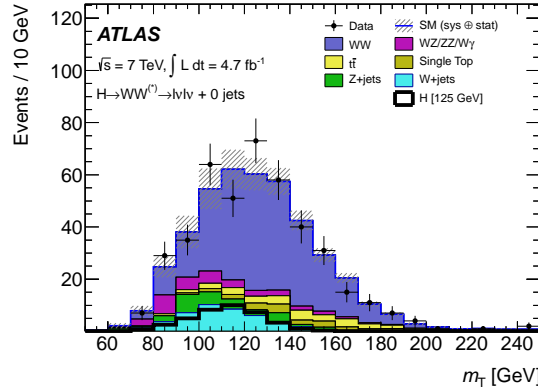


Figure 9.7: Transverse mass distribution for the three channels combined after all signal cuts are applied.

9.2.4 E_T^{miss} studies

The E_T^{miss} performance is an essential element to this analysis, particularly in the ee and $\mu\mu$ channels where the large Z/γ^* background is large and must be suppressed. As is evident in Figure 9.5 a compromise must be made between rejecting the Z/γ^* background and preserving signal events. The complicated decay topology of the WW system causes the signal to have a broad $E_T^{\text{miss,rel}}$ distribution that cuts off by 100 GeV. Low $E_T^{\text{miss,rel}}$ events are caused by low neutrino momentum or when the E_T^{miss} points near a lepton. The distribution cuts off at high $E_T^{\text{miss,rel}}$ because the E_T^{miss} only measures the combined neutrino momentum which is a combination of the momenta and decay topology of the two W bosons. This differs from the $ZZ \rightarrow \ell^+\ell^-\nu\bar{\nu}$ case described in Section 8.2 where the E_T^{miss} can be much larger because it measures the momentum of just one particle. The goal of understanding the E_T^{miss} is to reduce the Z/γ^* background as much as possible while maintaining an acceptable signal efficiency.

The efficiency of the $E_T^{\text{miss,rel}}$ (or E_T^{miss}) cut depends on the fake met resolution. The $E_T^{\text{miss,rel}}$ distribution falls rapidly, by approximately one order of magnitude for every 20 GeV in $E_T^{\text{miss,rel}}$. Therefore the efficiency of the $E_T^{\text{miss,rel}}$ cut is highly sensitive to the various sources of fake E_T^{miss} . Many improvements were made in the terms that contribute to $E_T^{\text{miss,rel}}$ during the 2011 data taking period. The calculation of the muon E_T^{miss} term was improved, the jet calibration was improved, the cluster calibration was changed, and the simulation was retuned. The retuning caused the simulated E_T^{miss} distribution to significantly disagree with the distribution in data. These changes motivated studies of the E_T^{miss} resolution and pileup modeling. The results of these studies were described in Section 7.7.3.3. In particular, the improved understanding of the pileup modeling led to the development of pileup rescaling that effectively adjusts the amount of simulated pileup and led to

improvements in future simulations.

9.2.5 Background estimates

Backgrounds are a challenging aspect of this analysis. As shown in Figure 9.7 the signal is small compared to the WW background and in addition other backgrounds from top, $W + \text{jets}$, $Z + \text{jets}$, and diboson processes contribute at a similar level as the signal.

The WW background is estimated using simulation. A correction to the normalization of the simulation is derived in a WW rich control region where all event cuts are applied except for the $\Delta\phi(\ell, \ell)$ cut and where $M_{\ell\ell} > M_Z + 15$ GeV. in the same flavor channels and $M_{\ell\ell} > 80$ GeV in the $e\mu$ channel. The normalization factor derived in the control region is then applied to the simulation in the signal region.

The top background is estimated using a similar method as used in the WW cross section measurement described in Section 8.1.6.2. A jet veto probability is determined a control region having at least one b-tagged jet. The square of the jet veto probability is applied to the number of top events with no jet veto applied to predict the number of top events in the zero jet bin.

The $W + \text{jets}$ background estimate uses a fake factor method similar to that described in Section 8.1.6.3 for the WW cross section measurement. Loose lepton definitions which are enhanced in jet fakes are constructed for electron and muons. The probability for a jet to fake each loose lepton type is derived in a jet rich control region. The fake factor is determined as a function of the p_T of the faking object. The signal selection is applied to events having one nominal lepton and one loose lepton and the derived fake factors are applied to the loose leptons to determine the $W + \text{jets}$ background.

The Z/γ^* background in the same flavor channels is estimated using the Z rich control region that is vetoed in the signal selection. In the $e\mu$ channel the background from Z/γ^* is smaller and is estimated using simulation. The ratio of events passing the nominal $E_T^{\text{miss,rel}}$ cut of 45 GeV to the number of events in the $20 \text{ GeV} < E_T^{\text{miss,rel}} < 45 \text{ GeV}$ is measured in the Z control region. This ratio is applied to the $20 \text{ GeV} < E_T^{\text{miss,rel}} < 45 \text{ GeV}$ of the signal selection to estimate the number of Z/γ^* events passing the nominal cut. Estimates of this background were also made using the single photon method and are described in Section 11.4.1.

The backgrounds from other diboson processes such as $W\gamma$, WZ , and ZZ are estimated using simulation.

Signal	WW	$WZ/ZZ/W\gamma$	top	Z/γ^*	$W + \text{jets}$	Total bkg	Observed
39.0 ± 0.2	276 ± 17	33 ± 2	45 ± 3	28 ± 6	44 ± 1	425 ± 26	429

Table 9.1: The predicted number of signal events for the signal having $m_H = 125$ GeV as well as the estimated background contributions with the observed number of events in the zero jet signal region. Note that the final results are obtained from a fit to the m_T distribution and the signal sensitivity is greater than what is reflected by the results in this table.

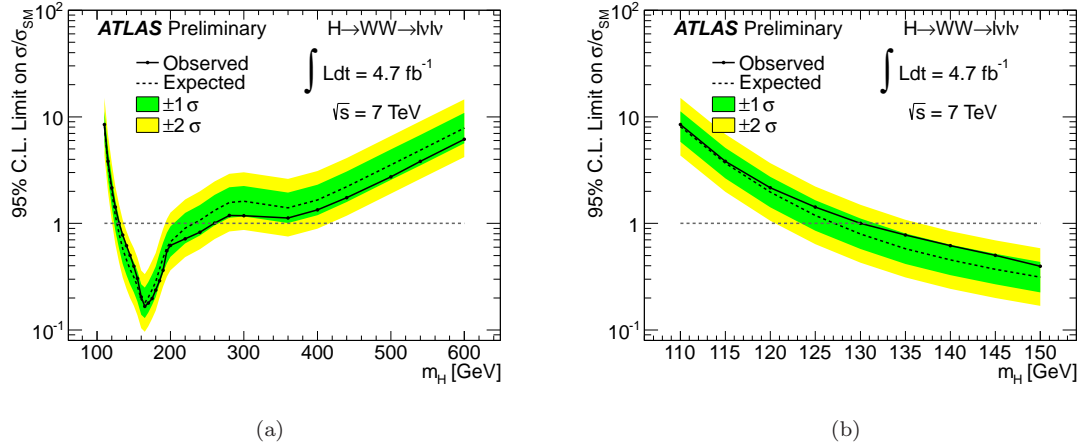


Figure 9.8: Expected and observed 95% confidence level limits on the allowed range of Higgs masses. Figure (a) shows the limits between $110 \text{ GeV} < m_h < 600 \text{ GeV}$ and (b) shows the limit in the low mass region only. Higgs masses between 130 GeV and 260 GeV are excluded at 95% confidence.

9.2.6 Results

Table 9.1 shows the number of observed events and the expected number of signal and background events. No significant discrepancy is observed over the background prediction and a log likelihood function is used to extract limits on the allowed Higgs masses. The likelihood function is composed of Poisson terms for each lepton and jet bin channel and is further binned in m_T to increase sensitivity to the signal. Terms for the WW and $t\bar{t}$ control regions are included in the likelihood function to extract the normalization of those backgrounds. Limits on the allowed range of Higgs masses are shown in Figure 9.8. This channel alone excludes the presence of a Higgs boson produced with the Standard Model rate between $130 \text{ GeV} < m_H < 260 \text{ GeV}$ at 95% confidence. The analysis loses sensitivity at low mass because the $H \rightarrow WW$ branching fraction falls rapidly at low Higgs masses. However, it is clear that the analysis is close to being sensitive to a 125 GeV Higgs boson and after including data from the full 2012 run the presence of a signal is clear.

9.2.7 Summary

Limits were placed on the allowed mass of a Standard Model Higgs boson using the $H \rightarrow WW$ decay mode. Using 4.6 fb^{-1} recorded at a center of mass energy of $\sqrt{s} = 7 \text{ TeV}$ production of a Standard Model Higgs boson is excluded for masses between 130 GeV and 260 GeV. This analysis did not include enough data to discover the Higgs boson, but when additional data from the 2012 run this channel has sufficient sensitivity to contribute to the discovery.

CHAPTER 10

Search for invisible decays of the Higgs boson

Since the discovery of the Higgs boson a major experimental goal has been to measure its branching fractions. The ATLAS experiment has measured branching fractions in many visible channels including $\gamma\gamma$ [114], ZZ [115], and WW [108]. In addition searches in the $\tau\tau$ [116] and $b\bar{b}$ [117] channels are approaching the sensitivity to where their branching fractions can be measured. An additional possibility exists where the Higgs boson decays to particles that cannot be detected. These decays contribute to the invisible branching fraction. The invisible branching fraction can be inferred from the measured branching fractions, but instead this analysis directly searches for invisible decays. The expected invisible branching fraction is small, so this analysis is only sensitive to anomalous enhancements of it. Many new physics models predict an enhanced branching fraction to invisible particles, but one particularly compelling possibility is that the Higgs boson decays to a pair of dark matter particles. The observed limits on the invisible branching fraction are interpreted as a limit on the coupling between the Higgs boson and the dark matter particle in a simple Higgs Portal model that is discussed in Section 4.4. The limits on the coupling are converted into limits on the coupling between the dark matter particle and the nucleon to compare to the direct detection scattering experiments described in Section 4.3.1.

This search is performed using 4.6 fb^{-1} of data taken at $\sqrt{s} = 7 \text{ TeV}$ from the full 2011 run and 13.1 fb^{-1} of data taken at $\sqrt{s} = 8 \text{ TeV}$ from a portion of the 2012 run. This search has been presented by the ATLAS experiment in Ref [118] and the CMS experiment has recently published preliminary results in this search [119]. In order to tag the event in which the Higgs decays invisibly, it must be produced with one or more visible particles. This search requires the Higgs boson to be produced in association with a Z boson that decays to charged leptons. The Feynman diagram for this process is shown in Figure 10.1. To select this signal this search requires two leptons consistent with the decay of a Z boson plus $E_{\text{T}}^{\text{miss}}$ from the escaping invisible decay products of the Higgs boson.

10.1 Standard Model expectation

Although a Standard Model contribution to the invisible branching fraction of the Higgs boson exists, it is relatively small. Figure 10.2 shows three possible contributions to the Standard Model branching fraction. Diagram 10.2(a) is strongly suppressed because of helicity; a left handed neutrino and right handed anti-neutrino cannot originate from a spin 0 state. Diagram 10.2(b) shows the direct coupling of the Higgs boson to two neutrinos. This diagram is suppressed because neutrinos are extremely light and the coupling to the Higgs boson is expected to be proportional to the neutrino mass. This process is also suppressed by helicity. Diagram 10.2(c) is then the main contribution to the invisible branching fraction. Including the requirement that the associated Z boson decays

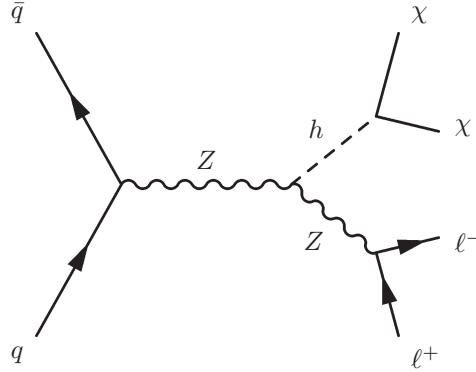


Figure 10.1: Feynman diagram for the associated production of a Higgs boson with a Z boson. The Z boson decays to leptons (e , μ , τ) and the Higgs boson decays to invisible particles, generically represented by χ .

to leptons (e , μ , or τ) the cross section for this process is 0.025 fb so that fewer than one event is expected in the full 2012 dataset.

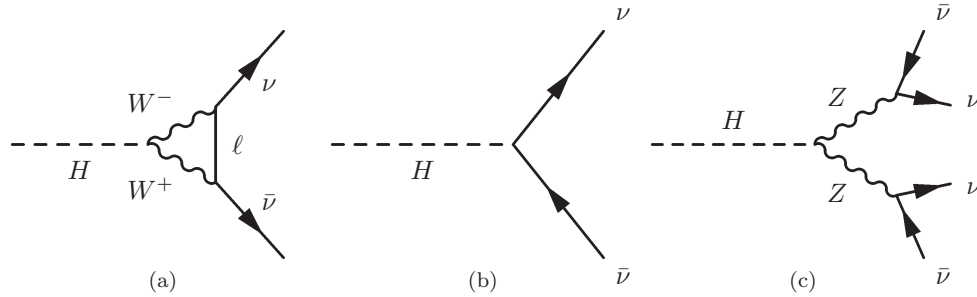


Figure 10.2: Feynman diagrams representing invisible decays of the Higgs boson. Figure (a) shows the production of two neutrinos through two intermediate W bosons. This decay mode is helicity suppressed because the Higgs boson is a spin 0 state. Figure (b) shows the direct coupling of the Higgs boson to two neutrinos. Although the nature of this coupling is not known, it is expected to be extremely small because the neutrino mass is small. It is also highly suppressed by helicity as in Figure (a). Figure (c) is then the main Standard Model invisible decay mode of the Higgs boson. The Higgs boson decays to two Z bosons which both decay to neutrinos

10.2 Analysis overview

In essence this analysis searches for an excess of events over the Standard Model background in the $\ell\ell + E_T^{\text{miss}}$ channel. A number of backgrounds that contribute at different levels must be accounted for. A brief summary of these backgrounds is presented below.

- Continuum $ZZ \rightarrow \ell\nu\nu$ is irreducible and contributes approximately 70% of the total background.

- $WZ \rightarrow \ell\nu\ell\ell$ where the W decay lepton is not identified either by failing lepton identification or by falling below the p_T threshold. The WZ background contributes to approximately 20% of the total background.
- Continuum $WW \rightarrow \ell\nu\ell\nu$ events where the leptons mimic a Z boson constitute approximately 5% of the background.
- $t\bar{t}$ and single top quark events where the leptons mimic a Z boson are largely reduced by applying a jet veto and contribute to approximately 2% of the background.
- Inclusive $Z \rightarrow \ell\ell$ events are largely reduced by requiring large E_T^{miss} . Additional cuts are also applied to further suppress this background. The remaining background contributes less than 1% to the total.
- Inclusive $W \rightarrow \ell\nu$ and dijet events can fake the signal if one or two jets are reconstructed as leptons. These backgrounds are less than 1% of the total.
- $H \rightarrow ZZ^{(*)} \rightarrow \ell\nu\nu$, for a 125 GeV SM Higgs boson, would produce E_T^{miss} that falls below the cut. Thus, this process is considered negligible.
- $H \rightarrow WW^{(*)} \rightarrow \ell\nu\ell\nu$, for a 125 GeV SM Higgs boson, would have a dilepton mass that falls outside the Z peak and is thus also considered to be negligible.

10.3 Data and simulation samples

This search uses 4.7 fb^{-1} of data recorded in 2011 at $\sqrt{s} = 7 \text{ TeV}$ and 13.0 fb^{-1} of data recorded in 2012 at $\sqrt{s} = 8 \text{ TeV}$. The two data taking periods are analyzed separately and the results are combined at the end. Events are selected using a combination of triggers that select single electrons or muons or a pair of electrons or muons. The trigger efficiency for signal events passing the full selection cuts described below is nearly 100% in both data periods in the electron channel, and approximately 95% and 94% in the 2011 and 2012 periods respectively in the muon channel. A Good Runs List (GRL) selects runs and luminosity blocks within (see Section 6.5) where the beam conditions are stable and the detectors and readout are performing nominally.

The POWHEG [94, 95, 96] Monte Carlo generator is used to simulate the signal. In the simulation the associatively produced Z boson is forced to decay to e , μ , or τ . The invisible decay of the Higgs boson is simulated by forcing the Higgs boson to decay to two Z bosons, which are then forced to decay to neutrinos. The sample is normalized assuming the Standard Model production rate of ZH and that 100% of the Higgs branching fraction is to invisible particles. Signal samples are generated

at Higgs boson masses of 115, 120, 125, 130, 150, 200, and 300 GeV. The Higgs boson lineshape is generated using the narrow width approximation which is a valid assumption because this analysis is only sensitive to the p_T of the invisibly decaying Higgs boson.

Background processes are modeled using tree level and NLO MC generators. HERWIG [98] is used to model ZZ , WZ , and WW production for the 2011 data, and Sherpa [97] for the 2012 data. The MC@NLO [80] generator is used to model WW , $t\bar{t}$, Wt , and s-channel single top quark production. ACERMC [120] models t-channel single top quark production. Inclusive W and Z/γ^* production are simulated with ALPGEN [82]. The POWHEG and Sherpa generators are also used to simulate Z/γ^* production. For the ZZ and WZ backgrounds, the prediction from simulation is used to estimate the background contribution. For other processes the simulation is only used to cross-check data driven background estimates. In order to investigate the contributions from $H \rightarrow WW \rightarrow \ell\nu\ell\nu$ and $H \rightarrow ZZ \rightarrow \ell\nu\nu$ for a 125 GeV SM Higgs boson, the simulation samples are generated with POWHEG interfaced with PYTHIA [121] showering.

10.4 Object selection

As with the analyses presented previously that are selected in the $\ell\ell + E_T^{\text{miss}}$ channel, electrons, muons, jets, and E_T^{miss} must be reconstructed. In addition a track based E_T^{miss} is used to suppress fake E_T^{miss} backgrounds.

Electrons are reconstructed following Section 7.3 and must pass the `medium++` identification criteria. Electrons are required to have $p_T > 20$ GeV and $|\eta| < 2.47$. Electrons are also selected with $p_T > 7$ GeV to implement a veto on events that have a third lepton with $7 \text{ GeV} < p_T < 20 \text{ GeV}$. A track isolation of $\text{ptcone20}/p_T < 0.1$ is required. Electrons must not overlap with jets. Therefore any electron having $0.2 < \Delta R_{e,\text{jet}} < 0.4$ are removed. When $\Delta R_{e,\text{jet}} < 0.2$ the jet is removed because every electron is also reconstructed as a jet. To avoid the case where a muon is also reconstructed as an electron, any electrons having $\Delta R_{e,\mu} < 0.2$ are removed.

Muons are identified by the *Staco Combined* algorithm in this analysis as described in Section 7.4. Muons must have $p_T > 20$ GeV and $|\eta| < 2.4$. As in the electron case, muons are reconstructed with $p_T > 7$ GeV to implement a third lepton veto. Muons must be isolated from nearby tracks by requiring $\text{ptcone20}/p_T < 0.1$. The muon track must satisfy $z_0 < 1$ mm and the d_0 significance must be less than 10. Muons are removed if they fall within $\Delta R_{\mu,\text{jet}} < 0.4$.

Jets are reconstructed using the anti- k_t algorithm following the description in Section 7.5. To suppress jets from pileup interactions we require $\text{JVF} < 0.75$ in 2011 data and $\text{JVF} < 0.5$ in 2012 data. The cuts change between the two data taking periods to account for the significant increase in the number of pileup interactions in 2012 (see Figure 5.4).

The E_T^{miss} is measured using the `RefFinal` algorithm described in Section 7.7. Following the procedure in Section 7.7.3.4 the simulated pileup multiplicity is shifted by a factor of 0.89 to correct for the cross section used when determining the number of pileup interactions. Application of the scaling improves the agreement between the simulated fake E_T^{miss} distribution and the data. In addition, a track based E_T^{miss} , $E_T^{\text{miss,track}}$, is used to further suppress fake E_T^{miss} backgrounds. See Section 7.7.2 for a description of the track E_T^{miss} calculation.

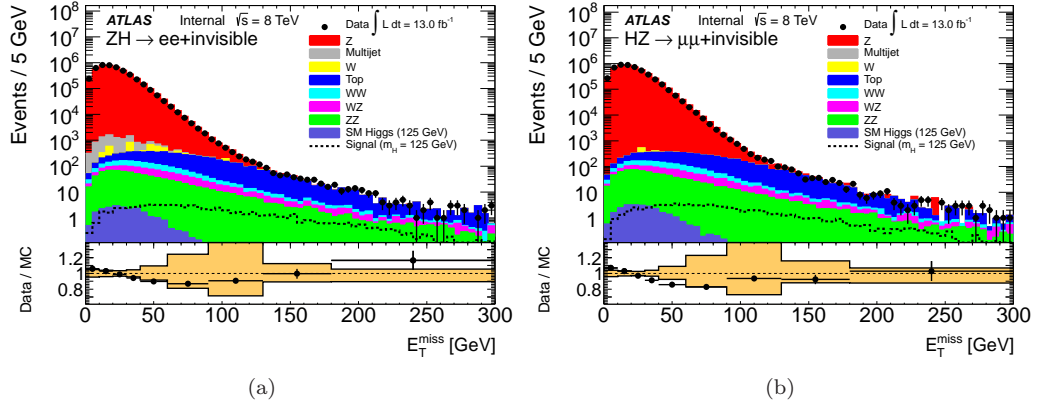
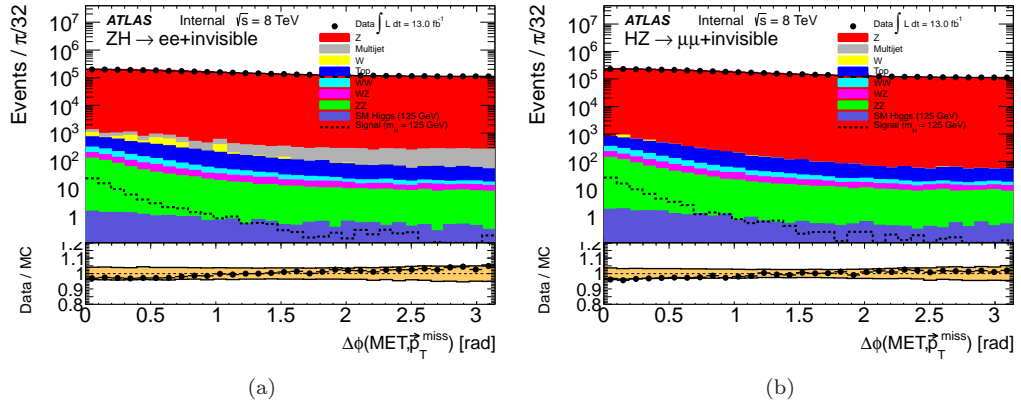
10.5 Event selection

Events are selected using a combination of triggers that select single electrons or muons or a pair of electrons or muons. Events are further pre-selected by requiring that at least one reconstructed vertex that has at least three associated tracks with $p_T > 500$ MeV. This analysis is critically dependent upon the E_T^{miss} performance, so overall data quality criteria is applied to reject events having non-collision backgrounds such as cosmic-ray muons and beam-related backgrounds, or events with degraded detector performance that can cause large mismeasurement of the E_T^{miss} .

Events must have exactly two opposite-charge electrons or muons. Events are divided into an ee and $\mu\mu$ channel based on the final state leptons present. To reduce the background from WZ events where the lepton originating from the W decay has $p_T < 20$ GeV, events are removed if an additional electron or muon is reconstructed with $p_T > 7$ GeV. The invariant mass of the dilepton system ($M_{\ell\ell}$) is required to satisfy $76 \text{ GeV} < M_{\ell\ell} < 106 \text{ GeV}$ to be consistent with leptons decaying from an on shell Z boson.

Figure 10.3 shows the E_T^{miss} distributions after the dilepton mass requirement. A disagreement is observed in the simulated E_T^{miss} distribution, but the discrepancy is within the systematic uncertainty. To reject the majority of the Z background the E_T^{miss} is required to be greater than 90 GeV. $E_T^{\text{miss,track}}$ is used to confirm the presence of true E_T^{miss} . In events having true E_T^{miss} originating from weakly interacting particles, such as neutrinos escaping the detector, the $E_T^{\text{miss,track}}$ is oriented in the same direction in azimuth as the E_T^{miss} vector. Therefore the azimuthal difference between E_T^{miss} and $E_T^{\text{miss,track}}$ ($\Delta\phi(E_T^{\text{miss}}, E_T^{\text{miss,track}})$) is required to be less than 0.2 radians. The distribution of $\Delta\phi(E_T^{\text{miss}}, E_T^{\text{miss,track}})$ in the 2012 data, after the dilepton mass window requirement, is shown in Figure 10.4.

Under the signal assumption the transverse momentum of the reconstructed Z boson is balanced by the transverse momentum of the invisibly decaying Higgs boson. The E_T^{miss} is an accurate measurement of the Higgs transverse momentum if it is sufficiently large (see Section 7.7.3). The E_T^{miss} should therefore be similar in magnitude and back-to-back with the Z momentum measured by the decay leptons. To select this signature the azimuthal separation between the dilepton

Figure 10.3: E_T^{miss} distributions for the ee (a) and $\mu\mu$ (b) channels after the $M_{\ell\ell}$ cut is applied.Figure 10.4: $\Delta\phi(E_T^{\text{miss}}, E_T^{\text{miss, track}})$ distributions for the ee (a) and $\mu\mu$ (b) channels after the $M_{\ell\ell}$ cut is applied.

system and the E_T^{miss} ($\Delta\phi(Z, E_T^{\text{miss}})$) is required to be greater than 2.6 radians. The decay leptons from a boosted Z boson are close in azimuth. To remove additional Z/γ^* background the azimuthal opening angle of the two leptons ($\Delta\phi(\ell, \ell)$) is required to be less than 1.7 radians. Furthermore the magnitude of $p_T^{\ell\ell}$ and E_T^{miss} should be compatible and thus the fractional p_T difference, defined as $|E_T^{\text{miss}} - p_T^{\ell\ell}|/p_T^{\ell\ell}$, is required to be less than 0.2. The distribution of $|E_T^{\text{miss}} - p_T^{\ell\ell}|/p_T^{\ell\ell}$ in the 2012 data, after the dilepton mass window requirement, is shown in Figure 10.5. Finally, a majority of the signal is produced in association with no high p_T jets whereas backgrounds from boosted Z bosons and $t\bar{t}$ pairs tend to have one or more jets. Thus, events are required to have no reconstructed jets with $p_T > 20$ GeV and $|\eta| < 2.5$. The jet multiplicity in the 2012 data after the dilepton mass window requirement is shown in Figure 10.6.

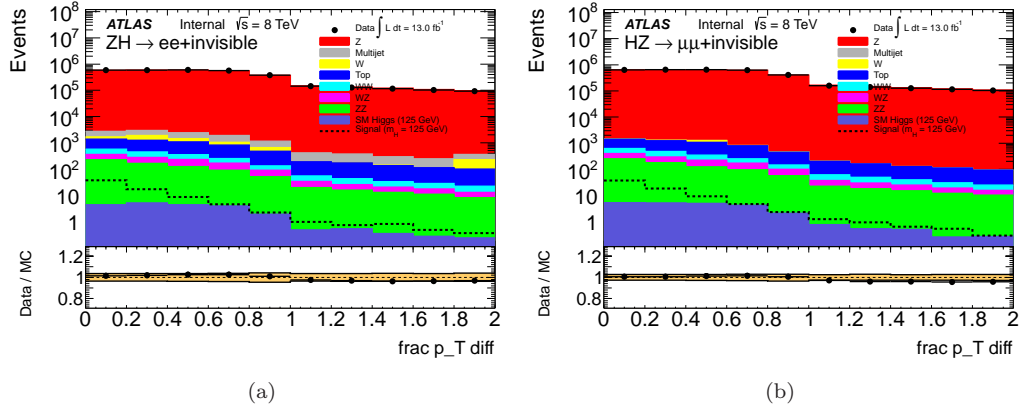


Figure 10.5: Fractional p_T difference distributions for the ee (a) and $\mu\mu$ (b) channels after the $M_{\ell\ell}$ cut is applied.

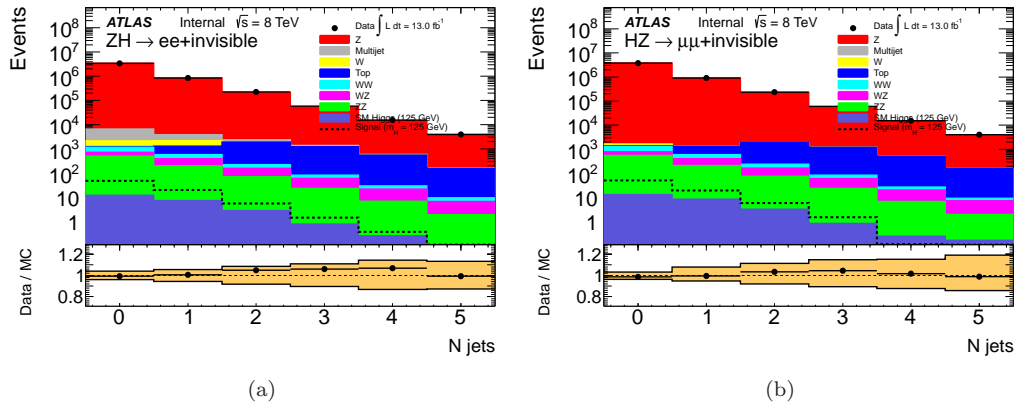


Figure 10.6: Jet multiplicity distributions for the ee (a) and $\mu\mu$ (b) channels after the $M_{\ell\ell}$ cut is applied.

10.6 Background estimation

This analysis searches for an excess of events over the Standard Model background. Therefore it is essential to correctly estimate each background to this search. Many of the methods used here are the same as those used in the $ZZ \rightarrow \ell^+\ell^-\nu\bar{\nu}$ analysis because the signal selection and backgrounds are similar.

10.6.1 ZZ and WZ backgrounds

The ZZ and WZ backgrounds are estimated using the predictions from simulation. The ZZ and the WZ simulations are normalized to NLO cross sections. The cross section of the ZZ process is increased by 6% to account for the gluon fusion process which is not included in the simulation.

Systematic uncertainties are derived from the propagation of reconstructed object uncertainties and from uncertainties on the production cross section. The total systematic uncertainty on these backgrounds is 13% in the 2011 data taking period and 12% in the 2012 data taking period. The simulation of WZ events is validated in a trilepton control region and shows good agreement with the data.

10.6.2 Combined $WW + \text{top} + Z \rightarrow \tau\tau$ estimate

The contributions from WW , $t\bar{t}$, and $Z \rightarrow \tau\tau$ are estimated using the same method as in the ZZ cross section (Section 8.2.5.1). These processes exhibit the flavor symmetry in their final states. The branching fraction to the $e\mu$ final state is twice that of the ee or $\mu\mu$ final states. Therefore, the signal free $e\mu$ control region is used to extrapolate these backgrounds to the ee and $\mu\mu$ channels.

Important sources of systematic uncertainty are uncertainties in the simulation used for the subtraction, and variations in the correction factor, k . The correction factor is measured to be 0.97 in the simulation, and 0.94 in the data in events that pass the dilepton requirement and no additional cuts. The maximum variation of the correction factor, observed at each cut level in the signal selection is used to estimate this uncertainty. The differences in kinematics for the $e\mu$ and dielectron or dimuon events are also considered as systematics. The combined systematic uncertainties from simulation subtraction and the maximum variation of the correction factor is 16% for the 2012 data. The estimated background from these sources is 4.8 ± 2.2 (stat.) ± 0.8 (syst.) for the 2012 data, and is consistent with the expectation from the simulation within the uncertainty. As this data-driven estimate gives a consistent expectation, but with larger uncertainty for the 2011 data, the estimate from for WW , $t\bar{t}$, and single top quark events are from simulation for the 2011 data.

10.6.3 Z/γ^* background estimate using ABCD method

The background from inclusive Z boson production is estimated using an ABCD method utilizing four regions, the signal region, A, and three side-band regions, B-D. The regions are formed by two uncorrelated variables: the $\Delta\phi(E_T^{\text{miss}}, E_T^{\text{miss,track}})$ and fractional p_T difference. Region B is formed by inverting the $\Delta\phi(E_T^{\text{miss}}, E_T^{\text{miss,track}})$ cut and applying the fractional p_T difference cut. Regions C and D invert the fractional p_T difference cut with region C formed by applying the $\Delta\phi(E_T^{\text{miss}}, E_T^{\text{miss,track}})$ cut and region D formed by inverting the cut. The events in the signal region are estimated as follows:

$$N_A^{\text{est}} = N_B^{\text{obs}} \times \frac{N_C^{\text{obs}}}{N_D^{\text{obs}}} \times \alpha \quad (10.1)$$

where, N_A^{est} is the number of estimated Z background in the signal region, and N_X^{obs} is the number of observed events in Region X ($X=B-D$). Contributions from non- Z backgrounds in Regions B-D are subtracted before applying this equation. A small impact from the correlation between the two variables is considered in the correction factor α , which is 1.07 (1.04) for the 2011 (2012) data. Systematic uncertainties are derived by evaluating the compatibility of the E_T^{miss} distributions in the control regions and from the variation in the correction factor after the various selection requirements. The total systematic uncertainty is 38% in the 2011 data and 21% in the 2012 data.

10.6.4 Z/γ^* background estimate using single photon method

The Z/γ^* background is also estimated by using single photon events to model E_T^{miss} in Z/γ^* events. This procedure follows that outlined in Section 8.2.5.2 for the ZZ cross section measurement and only differs in the cuts applied and the quantity of data analyzed. This procedure is described in detail in Chapter 11 and the implementation for this search is described in Section 11.3.15.

10.6.5 Inclusive W background estimate

The background from inclusive W production and multijet events is estimated using the Matrix Method. This method is the same as that described in Section 8.2.5.3. Systematic uncertainties are dominated by the measurement of the lepton fake rates. The selection requirements that define the sample from which the fake rates are derived are varied and the deviations in the obtained results are taken as the systematic uncertainties. These yields an uncertainty of 14% in the 2011 data and 19% in the 2012 data.

10.7 Results

The observed number of events and the estimated contribution from each source of background is shown in Table 10.1. The expectation for a Higgs boson having $m_H = 125$ GeV and a 100% branching ratio to invisible particles is shown. Figure 10.7 shows the final E_T^{miss} distributions for the 2011 and 2012 data taking periods. In both the 2011 and 2012 data a small deficit is observed relative to the background prediction. Since no excess is observed we set limits on the allowed invisible branching fraction of the Higgs boson. Limits are set under two hypotheses; that the invisibly decaying particle is a Standard Model Higgs boson having $m_H = 125$ GeV and that the invisibly decaying particle is an additional Higgs boson that is produced through Standard Model couplings. For the latter case limits are placed on the allowed production cross section times branching ratio for Higgs mass hypotheses between $115 \text{ GeV} < m_H < 300 \text{ GeV}$.

Source	2011	2012
ZZ	$23.5 \pm 0.8 \pm 3.1$	$56.5 \pm 1.2 \pm 6.8$
WZ	$6.2 \pm 0.4 \pm 0.8$	$13.9 \pm 1.2 \pm 2.0$
$t\bar{t} + WW + Z \rightarrow \tau^+\tau^-$	$1.5 \pm 0.2 \pm 0.1$	$4.8 \pm 2.2 \pm 0.8$
$Z + \text{jets}$	$0.16 \pm 0.13 \pm 0.06$	$1.4 \pm 0.4 \pm 0.3$
$W + \text{jets} + \text{multijet}$	$1.4 \pm 1.1 \pm 0.2$	$0.48 \pm 0.64 \pm 0.09$
Total Bkg.	$33.6 \pm 1.7 \pm 3.2$	$77.1 \pm 2.9 \pm 7.1$
Signal $m_h = 125$ GeV	$8.1 \pm 0.2 \pm 0.7$	$25.4 \pm 0.7 \pm 2.0$
Observed	27	71

Table 10.1: Expected background, expected signal, and observed number of events for the 2011 and 2012 data periods. Uncertainties are listed with the statistical uncertainty first and systematics second. The signal expectation is shown for a Higgs boson having $m_H = 125$ GeV and 100% branching ratio to invisible particles.

A profile likelihood is constructed to determine the limits on the allowed invisible branching fraction. Limits are expressed using the CL_s method [122]. This method defines $CL_s = CL_{s+b}/CL_b$. Where CL_{s+b} is the probability that the signal plus background produces the observation and CL_b is the probability that only the background produces the observation. We consider a model to be excluded if $1 - CL_s > 0.95$. Figure 10.8 shows the 95% CL limit on the production cross section times branching ratio for Higgs mass hypotheses between 115 GeV and 300 GeV. The black dashed line shows the background only hypothesis and the solid black line shows the observed exclusion. The observed line is below the expected because a deficit of events was observed. The red dashed line shows the expectation from a Higgs boson having 100% branching ratio to invisible particles. The green and yellow bands show the 68% and 95% uncertainties on the limit. Figure 10.9 shows $1 - CL$ for the invisible branching ratio for a Standard Model Higgs boson having $m_H = 125$ GeV. The dashed black line shows the expected $1 - CL$ and the observation is shown in black. Red lines indicate the 68% and 95% CL . We exclude $BR(H \rightarrow \text{invisible}) > 65\%$ at 68% confidence.

10.8 Dark matter interpretation of branching ratio limits

One possible interpretation for an enhanced branching fraction to invisible particles is that the Higgs boson decays to the dark matter particles that are expected to comprise approximately 24% of the energy density of the universe. Chapter 4 describes the evidence for dark matter and possible models for the nature of dark matter on the particle level. The invisible branching fraction limits are interpreted in terms of a coupling between the Higgs boson and dark matter, $\lambda_{h\chi\chi}$, as described in Section 4.4. Limits on both $\lambda_{h\chi\chi}$ and the coupling constant between the Higgs boson and the nucleon, $\sigma_{\chi N}$, are calculated as a function of m_χ . These results are compared to limits from direct detection scattering experiments interpreted in terms of $\lambda_{h\chi\chi}$ and $\sigma_{\chi N}$. In calculating the limits all

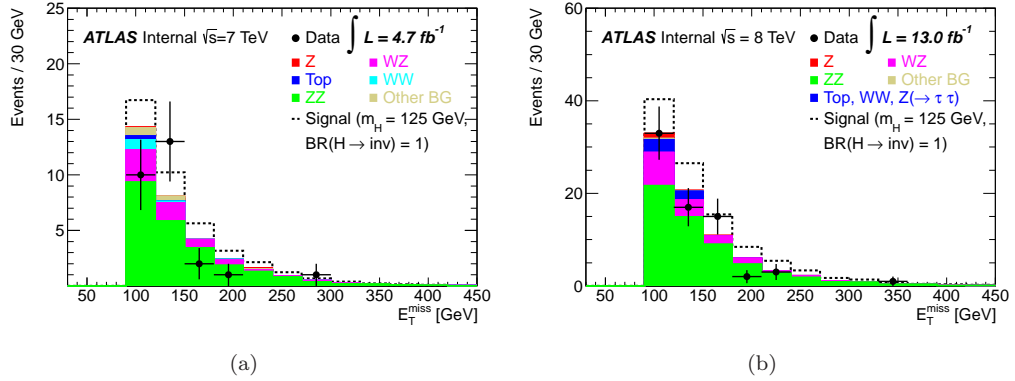


Figure 10.7: Final E_T^{miss} distributions for the 2011 (a) and 2021 (b) data taking periods. The signal expectation is shown for a Higgs boson having $m_H = 125$ GeV and 100% branching ratio to invisible particles.

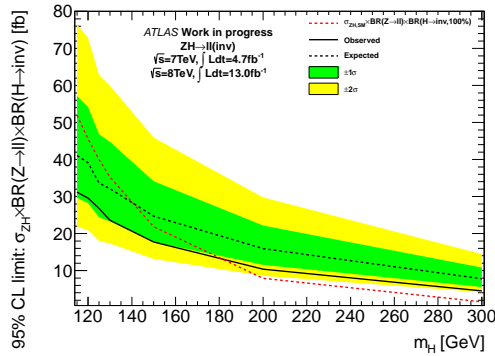


Figure 10.8: The 95% CL limit on the production cross section times branching ratio for Higgs mass hypotheses between 115 GeV and 300 GeV. The black dashed line shows the background only hypothesis and the solid black line shows the observed exclusion. The observed line is below the expected because a deficit of events were observed. The red dashed line shows the expectation from a Higgs boson having 100% branching ratio to invisible particles. The green and yellow bands show the 68% and 95% uncertainties on the limit.

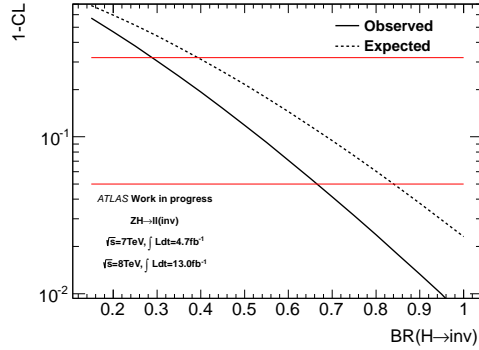


Figure 10.9: $1 - CL$ for the invisible branching ratio for a Standard Model Higgs boson having $m_H = 125$ GeV. The dashed black line shows the expected $1 - CL$ and the observation is shown in black. Red lines indicate the 68% and 95% CL .

variable	value
v	174.0 GeV
m_h	125.0 GeV
m_N	1.0 GeV
f_N	0.326
f_N upper syst.	0.629
f_N lower syst.	0.260
Γ_h^{Total}	4.07 MeV

Table 10.2: Values for variables used in Equations 4.1 through 4.6.

variables in Equations 4.1- 4.6 are constants except for m_χ , $\lambda_{h\chi\chi}$, and $\sigma_{\chi N}$. The inputs used for the remaining variables are given in Table 10.2. Limits on $\lambda_{h\chi\chi}$ vs m_χ are shown in Figure 10.10 for the scalar (10.10(a)), vector (10.10(b)), and majorana (10.10(c)) hypotheses. All direct detection results incur a large uncertainty from the Higgs-Nucleon form factor uncertainty. Figure 10.11 shows limits on $\sigma_{\chi N}$ vs. m_χ . Direct detection results are published as limits on $\sigma_{\chi N}$ vs. m_χ and need no further conversion. The invisible branching ratio limits are shown for the scalar, vector, and majorana fermion hypothesis as three curves. The hashed bands on the invisible branching ratio limits show the uncertainty resulting from the systematic variation of f_N .

It is evident from Figures 10.10 and 10.11 that the invisible branching fraction limits are complementary to the direct detection limits. Direct detection experiments provide the strongest limits at high mass, but they lose all sensitivity below about 10 GeV. The invisible branching fraction limits are sensitive only below $m_h/2$ and provide exclusion below 10 GeV where the direct detection results do not reach. The limits from the scalar, vector, and fermion dark matter species depend differently on the dark matter mass, but all exclude a large range of the coupling strength at low mass. Therefore, within the Higgs portal model – which makes a generic assumption to test the

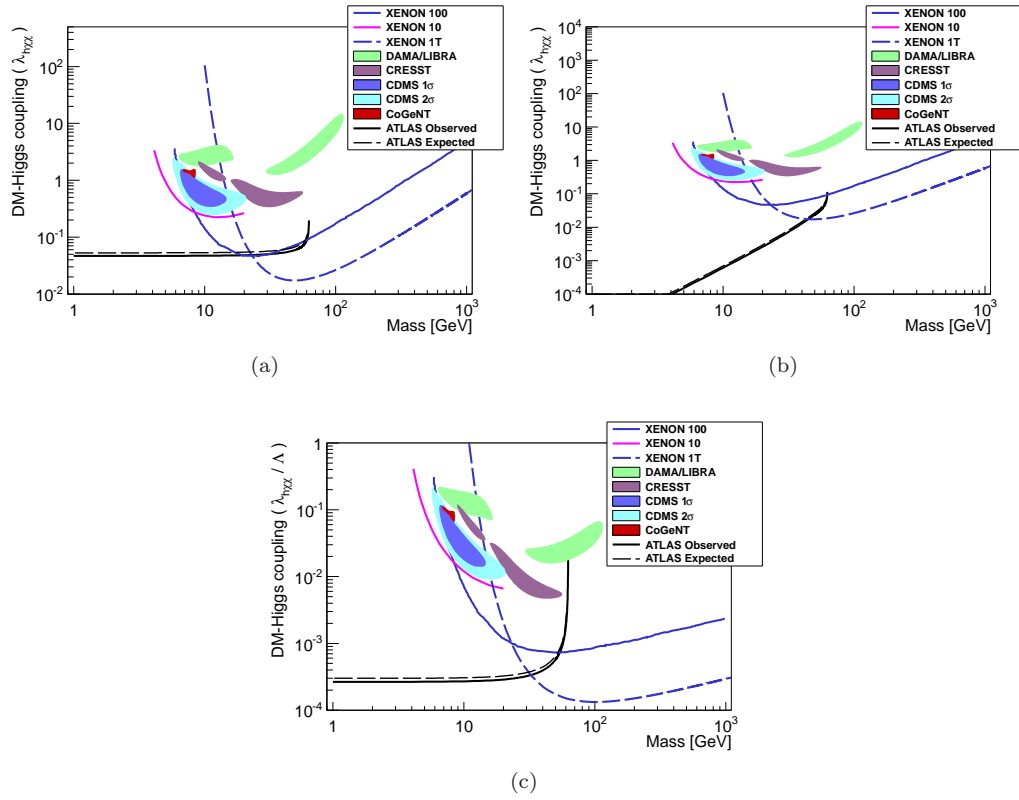


Figure 10.10: Limits on λ_{hXX} vs m_X for scalar (a), vector (b), and majorana fermion (c) dark matter in the Higgs portal model. In the case of fermionic dark matter the limit is placed on λ_{hXX}/Λ to account for the cutoff scale introduced to regulate the non-renormalizable operator. All limits from direct detection limits incur an uncertainty from f_N .

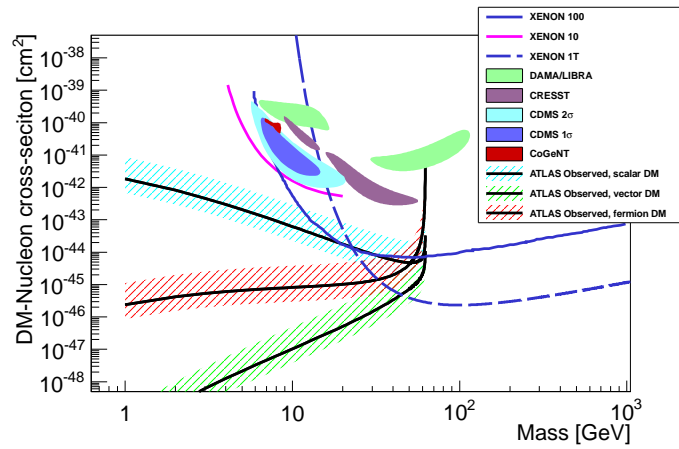


Figure 10.11: Limits on $\sigma_{\chi N}$ vs m_h . Limits calculated from the invisible branching ratio limits presented in this note are shown for the scalar (cyan band), vector (green band), and majorana fermion (red band) cases. Invisible branching ratio limits incur a large uncertainty from f_N .

Higgs-dark matter coupling – the coupling between dark matter and the Higgs boson is strongly limited across a large range of dark matter mass.

CHAPTER 11

Z/γ^* background estimate using single photons

Many processes studied at the LHC produce two charged leptons and one or more undetected neutrinos such as those presented in Sections 8.1, 8.2, 9.2, and 10. In the inclusive dilepton final state Z/γ^* events dominate over other processes by at least a factor of ten. Generally analyses that use the dilepton plus E_T^{miss} final state require large missing transverse momentum (E_T^{miss}) to reject the Z/γ^* background. The remaining Z/γ^* background in the signal region is estimated using data driven techniques. This method determines the shape of the full fake E_T^{miss} distribution in Z/γ^* events using single photon events. The following sections describe the method in detail and show its application in three dilepton + E_T^{miss} analyses.

11.1 Motivation

This method provides a robust data-driven estimate of the Z/γ^* background to a dilepton + E_T^{miss} final state. The similarity between single photon events and Z/γ^* events allows certain event level distributions to be modeled using the corresponding distributions in single photon events. The E_T^{miss} distribution is the primary distribution that the method models. The E_T^{miss} distribution is dominated by fake E_T^{miss} sources in both Z/γ^* events and single photon events because neither process produces final state neutrinos.⁸ The contributions to the fake E_T^{miss} resolution are similar in both types of events making the shapes of the fake E_T^{miss} distributions look similar between the two samples. However, the difference between the p_T distribution of single photons and the $p_T^{\ell\ell}$ distribution in Z/γ^* events prevents complete agreement in the E_T^{miss} distributions. A p_T dependent weight must be applied to the single photon sample to correct the difference in the p_T distribution. Additional weights may be required as well depending on the specific implementation of the method. The corrected single photon E_T^{miss} distribution should accurately reproduce the distribution in Z/γ^* events. The Z/γ^* background passing the E_T^{miss} cut applied by the analysis is simply determined by applying the same cut on the corrected single photon E_T^{miss} distribution. The method can model certain additional distributions; some possibilities are discussed below.

11.2 Compatibility between single photon and Z/γ^* events

The success of the method relies on the similarity between single photon events and Z/γ^* events. Fake E_T^{miss} arises from the same sources in both single photon events and Z/γ^* events. In particular both samples experience the same pileup, underlying event, and hadronic recoil. The pileup and underlying event are the same because on average they are common for all collisions. The similarity in the hadronic recoil is evident in comparing the Feynman diagrams of both processes shown in

⁸Heavy flavor decays can produce neutrinos, but they will be a negligible contribution in the cases considered here.

Figure 11.1. For each diagram in the second row (b-d) the Z/γ^* propagator is replaced with a real photon in the diagram below it (e-g). This replacement is valid for all diagrams except diagram (a). However, diagram (a) produces the Z/γ^* having zero transverse momentum because there is no recoiling quark or gluon. Low momentum Z/γ^* cannot be modeled with the single photon method because photons are triggered only above a minimum p_T of 20 GeV. Fortunately the signal selection of most $\ell\ell + E_T^{\text{miss}}$ analyses require that the dilepton system is boosted. Therefore low momentum Z/γ^* can be ignored and single photon events will only be used to model Z/γ^* events after $p_T^{\ell\ell}$ and p_T^γ cuts of at least 20 GeV are applied. The similarity between single photons and Z/γ^* extends to higher order diagrams as well. This guarantees that the hadronic recoil system is similar in properly matched single photon and Z/γ^* events.

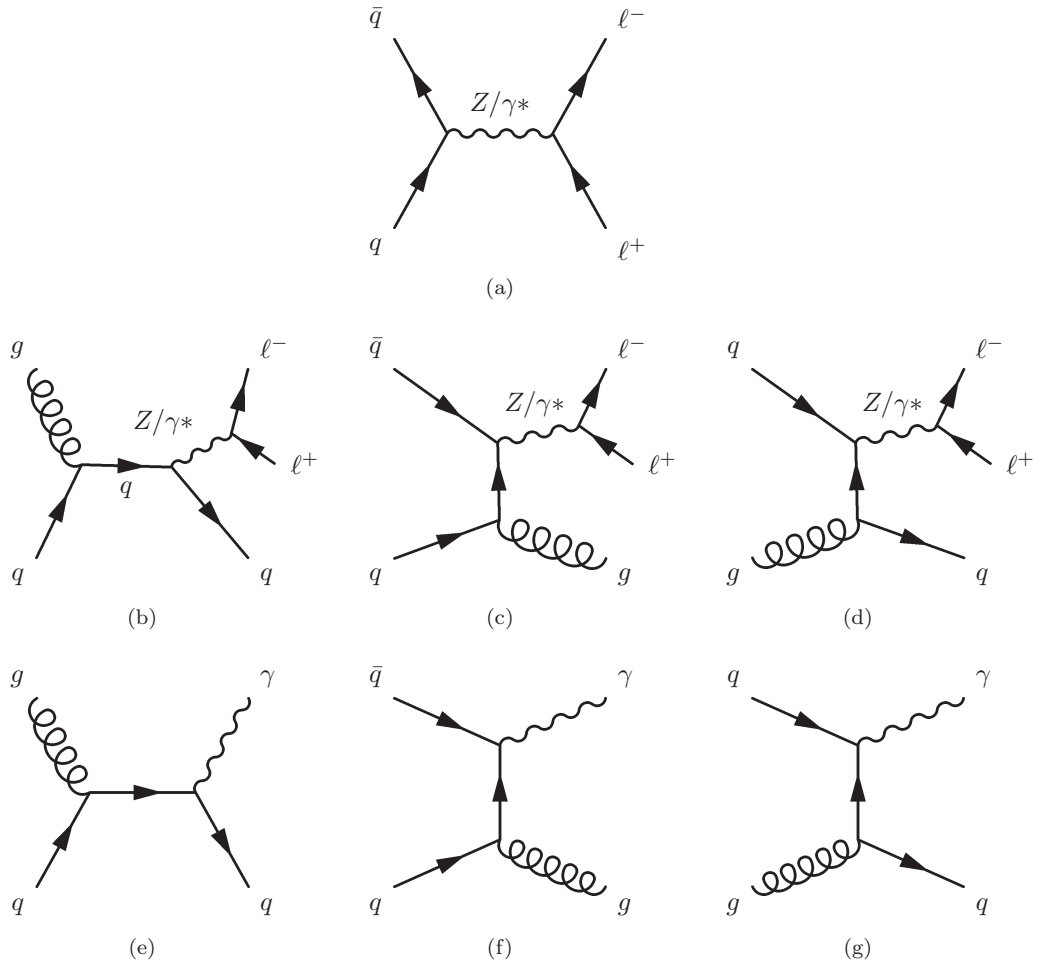


Figure 11.1: Feynman diagrams for the tree level production of Z/γ^* (first and second rows) and single photons (last row). For each Z/γ^* production diagram in the second row the Z/γ^* can simply be replaced with a real photon. Diagram (a) does not allow this replacement, but it also produces Z/γ^* with zero transverse momentum. Low momentum Z/γ^* cannot be modeled with the single photon method because of trigger thresholds, but they are usually rejected in the event selection.

11.3 Basic single photon method

The goal of the single photon method is to model the E_T^{miss} in Z/γ^* events using single photon events. While the E_T^{miss} is the principle distribution to model, other distributions may be modeled as well. The procedure is outlined as follows,

1. Select a sample of single photon events.
2. Select a sample of Z/γ^* events.
3. Apply cuts to the single photon and the Z/γ^* sample so that the samples are compatible.
4. Normalize the single photon sample so that it represents the same number of events as the Z/γ^* sample.
5. Weight the photon p_T spectrum to match the Z/γ^* p_T spectrum.
6. Apply any other weights. Additional weights may be needed to improve the agreement between the single photon and Z/γ^* samples.
7. Subtract real E_T^{miss} contributions to the single photon sample.
8. Apply E_T^{miss} cut and any other cuts that are modeled by the single photon sample to derive the efficiencies of those cuts. The final background estimate is the weighted number of single photon events remaining after all cuts.

These steps are generic to any use case. The following sections will expand on the specific issues in each step.

11.3.1 Modeling possibilities

This method is principally intended to model the E_T^{miss} distribution in Z/γ^* events. The similarity between the two samples means that it is often possible to model additional variables. The possible distributions are separated into three categories.

- Purely leptonic variables. Lepton information is not available in single photon events and therefore variables such as $\Delta\phi(\ell, \ell)$ cannot be modeled with this method. Cuts on these variables must be applied before deriving the photon p_T weighting.
- Purely non-leptonic variables. Such distributions can be modeled using the single photon method and include E_T^{miss} and jet related quantities.

- Partially leptonic variables. Variables that combine lepton information with E_T^{miss} or jet quantities are *a priori* not accessible to this method. For example, $E_T^{\text{miss,rel}}$ requires the angular separation between the E_T^{miss} and the nearest lepton as well as the magnitude of the E_T^{miss} . While the magnitude of the E_T^{miss} is modeled using this method, the angular separation is not. A more advanced method that includes this category of variables will be described in Section 11.4.

11.3.2 Sample compatibility and normalization

The single photon and Z/γ^* selection cuts must be compatible such that both samples represent the same kinematics. In general all cuts that are not modeled using the single photon method should be applied to the Z/γ^* sample before the method is carried out. For example, if a cut on a purely leptonic variable such as $\Delta\phi(\ell, \ell)$ is applied the cut must be applied to the Z/γ^* sample prior to applying the method because $\Delta\phi(\ell, \ell)$ cannot be modeled using single photons. Any kinematic cuts applied in the analysis that can be mapped to the single photon sample should also be applied. For example, the analyses presented here require a jet veto in the signal selection. The jet veto should also be applied to the single photon sample so that only zero jet single photon events are used to model zero jet Z/γ^* events. A cut on p_T^γ is implicit in the trigger selection, and this minimum must also be applied to the $p_T^{\ell\ell}$ distribution. If the Z/γ^* selection applies a higher $p_T^{\ell\ell}$ cut, the same cut should be applied on the photon p_T . In most cases the sample normalization and any weights should be derived and applied after the compatibility cuts are applied.

After selection cuts are applied to both samples the raw number of events is different between the two. In order to predict the correct number of events the single photon sample must be weighted so that it represents the same number of events as the Z/γ^* sample. This normalization can also be accomplished as a part of the p_T^γ weighting described below, but for clarity it is described separately. The normalization is derived in a low E_T^{miss} control region that is chosen to remove real E_T^{miss} contributions in both samples. The control region cut is typically $E_T^{\text{miss}} < 40$ GeV which is a compromise between rejecting real E_T^{miss} contributions but keeping a majority of the single photon and Z/γ^* events.

11.3.3 p_T^γ weighting

Although the single photon and Z/γ^* processes are quite similar, some differences exist and must be corrected for. A significant difference between Z/γ^* production and single photon production is in the mass. The mass of the Z/γ^* causes the dilepton system to have a different p_T distribution than if the Z/γ^* was massless like the photon. In order to account for this difference the single photon

p_T spectrum is weighted to match the $p_T^{\ell\ell}$ spectrum in Z/γ^* events. The application of the weights is given by,

$$N^\gamma(p_T^i) \times C_\gamma^{Z/\gamma^*} \times w^{p_T}(p_T^i) = N^{Z/\gamma^*}(p_T^i) \quad (11.1)$$

Where p_T^i indicates a p_T bin and C_γ^{Z/γ^*} explicitly includes the overall normalization factor discussed in the previous section,

$$C_\gamma^{Z/\gamma^*} = \frac{N_{Z/\gamma^*}^{\text{total}}}{N_\gamma^{\text{total}}}$$

To be pedantic, the weights are given by

$$w^{p_T}(p_T^i) \equiv \frac{1}{C_\gamma^{Z/\gamma^*}} \frac{N^{Z/\gamma^*}(p_T^i)}{N^\gamma(p_T^i)}$$

which is a trivial rearrangement of Equation 11.1. It is important to note that the weights must be derived and applied separately. The weights can only be determined after the full p_T spectra are available while they must be applied event-by-event. One must therefore iterate twice over the data to implement the method, first to derive the weights and second to apply the weights. Equation 11.1 is generalized in Equation 11.2 to include any number of additional weights.

In general, the p_T^γ weighting should be derived using the same samples in which the overall normalization is derived. However correlations between the $p_T^{\ell\ell}$ or p_T^γ and other event kinematics can cause the weights to be incorrect if cuts are applied on the other event kinematics. Special attention should be paid to the $M_{\ell\ell}$ distribution. The p_T^γ weighting is only valid within narrow $M_{\ell\ell}$ windows because the $p_T^{\ell\ell}$ is correlated with $M_{\ell\ell}$. If the signal selection only requires one narrow $M_{\ell\ell}$ window, as in Z tagged analyses, the $p_T^{\ell\ell}$ distribution is approximately constant within this window and one set of weights can be used. If the dilepton signal is selected in a wide $M_{\ell\ell}$ range the p_T^γ weights should be derived separately for events in various $M_{\ell\ell}$ windows. The size of the windows should be chosen such that the shape of the $p_T^{\ell\ell}$ distribution is approximately constant across the $M_{\ell\ell}$ window. Cuts on the jet multiplicity also affect the $p_T^{\ell\ell}$ and p_T^γ distributions. In zero jet events there is little hadronic energy from which the dilepton system can recoil and the $p_T^{\ell\ell}$ and p_T^γ distributions tend to fall much more rapidly. In multijet events the $p_T^{\ell\ell}$ and p_T^γ distributions can extend to much higher values. Therefore the p_T^γ weighting must be derived in bins of jet multiplicity. In many analyses only a single jet bin is selected. In these cases the jet multiplicity cut can simply be applied to both the Z/γ^* and single photon samples before the p_T^γ weighting is derived.

The p_T^γ weighting can be derived either from Z/γ^* data or simulation. If the weighting is derived relative to Z/γ^* data, true E_T^{miss} contributions from processes such as WW , $t\bar{t}$, or ZZ are inevitably included. However the true E_T^{miss} processes are small compared to the number of Z/γ^* events and they can usually be ignored. If a smaller true E_T^{miss} contamination is required a maximum E_T^{miss} cut can be applied to both samples such that a majority of the single photon and Z/γ^* events are used,

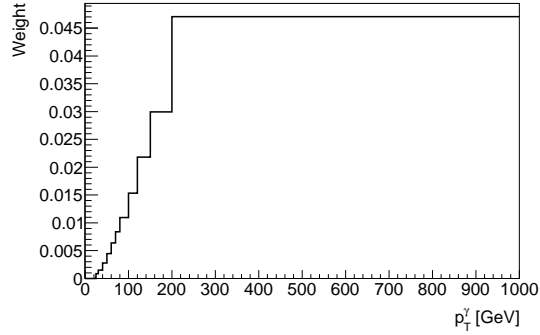


Figure 11.2: An example of p_T^γ weights derived for the single photon method. The weights are determined in variable width bins to reduce statistical fluctuations at high p_T^γ .

but the true E_T^{miss} contribution is reduced. This cut can be the same as the cut used to determine the overall normalization. The E_T^{miss} cut inevitably influences the p_T^γ and $p_T^{\ell\ell}$ distributions, but because the E_T^{miss} cut only removes a small fraction of events the affect on the p_T^γ and $p_T^{\ell\ell}$ distributions is small. To avoid these issues one can instead weight the p_T^γ distribution to the $p_T^{\ell\ell}$ distribution in simulated Z/γ^* events.

The p_T^γ weights should be derived such that they are not susceptible to statistical fluctuations in the single photon or Z/γ^* samples. The p_T^γ and $p_T^{\ell\ell}$ distributions fall off at high p_T and therefore the statistics available for determining the p_T^γ weights is small at high p_T . To account for the changing statistics over the p_T^γ and $p_T^{\ell\ell}$ distributions, a variably binned p_T^γ weight is used. The binning used depends on the statistics available and must be chosen to reduce statistical variations in the weights. Figure 11.2 shows an example set of p_T^γ weights with variable binning.

11.3.4 Additional weights

It may be necessary weight other variables in addition to the p_T^γ . Some specific cases of this will be described below. Any additional weights should be applied in a similar manner as the p_T weight. The weighting scheme can be generalized as,

$$\begin{aligned} C_\gamma^{Z/\gamma^*} \times N^\gamma \left(p_T^i, f_2^j, \dots, f_N^\alpha \right) &\times \left[w^{p_T} (p_T^i) \times w^2 (f_2^j) \times \dots \times w^N (f_N^\alpha) \right] \\ &= N^{Z/\gamma^*} \left(p_T^i, f_2^j, \dots, f_N^\alpha \right) \end{aligned} \quad (11.2)$$

where f_N^α are distributions to which the weighting is applied and α indicates the bin in that distribution. The overall normalization of the single photon sample is included as C_γ^{Z/γ^*} . The w^n are the distributions of weights in bins of f_N such that the average weight is one,

$$w^N (f_N^\alpha) = \frac{1}{C_\gamma^{Z/\gamma^*}} \frac{N^{Z/\gamma^*} (f_N^\alpha)}{N^\gamma (f_N^\alpha)}$$

In other words, the single photon distribution is normalized to the same number of events as the Z/γ^* sample and any number of distributions can be weighted as long as the weights do not change the normalization.

11.3.5 Weighting by the average number of pileup interactions

Weighting by the average number of pileup interactions is an example of an additional weight that is usually necessary. In order to correctly model pileup sensitive quantities such as E_T^{miss} the selected single photon events must experience the same pileup conditions as the selected dilepton events. This condition is satisfied if both Z/γ^* and single photon events are selected using unprescaled triggers. However, if prescaled triggers are used, as is often the case in the single photon selection, they are biased to record events having fewer pileup events on average. The prescale value is higher at the start of a run, when the instantaneous luminosity is the largest. As the instantaneous luminosity decreases during the run the prescale values are lowered so that the trigger rate remains approximately constant throughout the run. The prescaled triggers are therefore biased towards lower instantaneous luminosity and thus events having fewer pileup collisions. The distribution of the average number of pileup interactions ($\langle \mu \rangle$) for each trigger in 2011 and 2012 data is shown in Figure 11.3. To account for these differences the $\langle \mu \rangle$ distribution of events selected with prescaled triggers is weighted to match the $\langle \mu \rangle$ distribution of the unprescaled trigger.

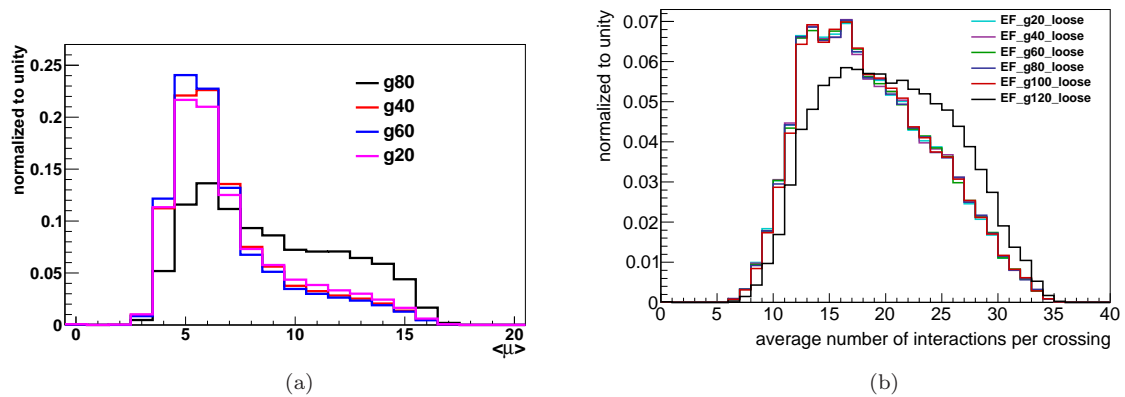


Figure 11.3: Distributions of the average number of pileup interactions for single photon triggers in the 2011 (a) and 2012 (b) data taking periods. The g80 trigger was unprescaled during 2011 data taking and the g120 trigger was unprescaled in the 2012 data taking period. All prescaled triggers are biased to have lower $\langle \mu \rangle$ than the unprescaled triggers.

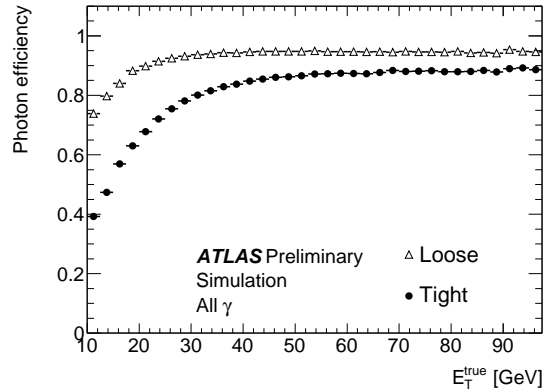


Figure 11.4: Photon reconstruction efficiency with respect to true photons for the `loose` and `tight` working points. Above 90 GeV an efficiency of 90% and 95% is achieved for the `loose` and `tight` working points respectively [123].

11.3.6 Photon identification

Photons are reconstructed from narrow energy deposits in the electromagnetic Calorimeter. Showers originating from photons are very similar to showers originating from electrons so photon reconstruction proceeds similarly to electron reconstruction [59] (see Section 3.4 for descriptions of how electrons and photons interact in the calorimeter). A match between inner detector tracks and the photon calorimeter cluster is attempted. If there is no match the object is labeled as an unconverted photon. When a track match is successful the track is scanned for a secondary vertex that is consistent with a photon conversion in the beam pipe or inner detector material (see Section 3.4.4 for a description of photon conversions). If a secondary vertex is identified the object is labeled as a converted photon. A converted photon may be associated with one or two tracks. Cases when more than two tracks are found are usually fakes and are not considered. Cuts are applied on a number of shower shape variables to distinguish photons from jets. Two working points labeled as `loose` and `tight` are defined by the set of shower shape cuts used. The reconstruction efficiency for true photons for the `loose` and `tight` working points is shown in Figure 11.4 [123].

To provide additional rejection against jets, isolation variables are derived from both calorimeter clusters and inner detector tracks. The calorimeter based isolation sums all calorimeter clusters within $\Delta R = 0.3$ of the photon excluding the photon itself. The calorimeter isolation is corrected by subtracting an average event density determined from soft depositions not associated with a photon or jet. A p_T dependent correction is also applied to correct for leakage of the photon shower into the isolation cone. The track isolation variable sums all tracks having $p_T > 500$ MeV within a cone of $\Delta R = 0.3$. If the photon is converted the associated conversion tracks are not included.

11.3.7 Photon selection

A number of photon triggers that apply the `loose` selection criteria and have p_T thresholds increasing in increments of 20 GeV from 20 GeV to 120 GeV are used to record photon events. In 2012 all thresholds except for the 120 GeV threshold are prescaled such that the rate at which events are recorded is approximately 1 Hz. In 2011 only triggers having thresholds up to 80 GeV are used because the trigger having a threshold of 80 GeV is unprescaled. The three lower threshold triggers were prescaled to a rate of approximately 2 Hz in 2011. In order to obtain a smooth photon p_T distribution, single photon events that pass a given trigger and are within a consistent p_T bin are weighted by the prescale of the trigger. The lower p_T required to be consistent with a trigger is 5 GeV above the trigger threshold so that the trigger efficiency is on plateau (constant as a function of p_T). Figure 11.5 shows the trigger turn-on curve for three of the 2011 triggers. The trigger efficiency reaches a plateau within 5 GeV above the trigger threshold. The upper p_T threshold required to be consistent with a trigger is 5 GeV above the threshold of the trigger having the next higher threshold, except in the case of the unprescaled trigger where there is no upper p_T threshold. Table 11.1 shows each trigger used, its prescale, and the photon p_T binning required for it to be associated with that trigger. Figures 11.6 and 11.7 illustrate the prescale weighting procedure in the 2012 and 2011 data samples respectively. Figures 11.6(a) and 11.7(a) show the photon p_T spectrum for each trigger with no upper p_T cut and without correcting for the trigger prescales. Figures 11.6(b) and 11.7(b) apply the weights to correct for the trigger prescales. The resulting distributions line up with the distribution from the unprescaled trigger as expected. Figures 11.6(c) and 11.7(c) apply the photon p_T binning but with no correction for the trigger prescales. These distributions illustrate the available photon statistics provided by each trigger. Figures 11.6(d) and 11.7(d) apply both the p_T binning and correct for the trigger prescales resulting in a smooth photon p_T distribution.

While applying the `tight` identification criteria reduces the dijet contamination, in many cases photons are produced inside jets causing the jet to pass the tight identification cuts. To further reduce the dijet contamination photon candidates are required to be isolated from nearby calorimeter deposits as described in 11.3.6. The isolation distribution is shown in Figure 11.15. The yellow histogram shows the prediction from single photon simulation and the red histogram shows the prediction from dijet simulation. The corrected isolation is required to be less than 2 GeV to select single photon candidate events. Furthermore for the nominal single photon method photons must be unconverted. Electrons from W boson decays tend to fake converted photons more than unconverted photons, so this requirement reduces the W background. However converted photons have the advantage of being associated with tracks that indicate the vertex from which the photon originated. This case will be described in Section 11.3.11.

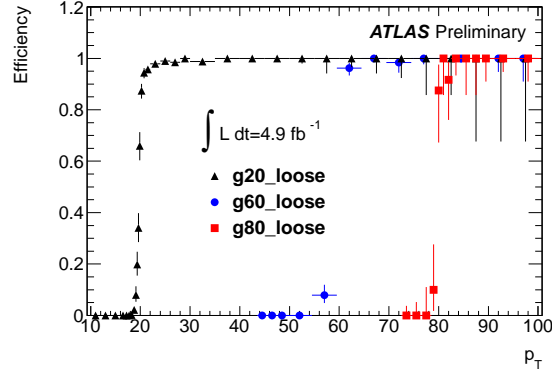


Figure 11.5: Photon trigger efficiency turn-on curves with respect to the offline photon p_T for the thresholds of 20 GeV, 40 GeV, and 60 GeV for 2011 data taking. In all cases the plateau is reached within 5 GeV of the trigger threshold.

Trigger	average prescale factor	photon p_T requirement
2012		
EF_g20_loose	4415.781	$25 \text{ GeV} < p_T < 45 \text{ GeV}$
EF_g40_loose	348.553	$45 \text{ GeV} < p_T < 65 \text{ GeV}$
EF_g60_loose	80.942	$65 \text{ GeV} < p_T < 85 \text{ GeV}$
EF_g80_loose	28.535	$85 \text{ GeV} < p_T < 105 \text{ GeV}$
EF_g100_loose	13.037	$105 \text{ GeV} < p_T < 125 \text{ GeV}$
EF_g120_loose	1.0	$p_T > 125 \text{ GeV}$
2011		
EF_g20_loose	364.73	$25 \text{ GeV} < p_T < 45 \text{ GeV}$
EF_g40_loose	26.46765	$45 \text{ GeV} < p_T < 65 \text{ GeV}$
EF_g60_loose	4.634768	$65 \text{ GeV} < p_T < 85 \text{ GeV}$
EF_g80_loose	1.0	$p_T > 85 \text{ GeV}$

Table 11.1: Single photon triggers and their average prescales for the 2011 and 2012 data samples. The p_T cuts used to bin the triggered samples is also indicated. When the p_T binning and prescale weights are applied to each triggered sample a smooth p_T distribution is achieved.

11.3.8 Single photon kinematic distributions

Figure 11.8 shows relevant kinematic distributions in single photon events. In the order that the plots are shown the distributions are, E_T^{miss} , p_T^γ , track E_T^{miss} , $\Delta\phi(\gamma, E_T^{\text{miss}})$, the jet multiplicity, and the photon calorimeter isolation. All distributions include events that have exactly one tight, isolated, and unconverted photon. The isolation requirement is not applied in the calorimeter isolation plot. In all the use cases given in this dissertation a jet veto is applied in the signal selection and must also be applied to single photon events. Many other event kinematics are affected by the jet veto, so it is important to check the event kinematics after the jet veto is applied. Figure 11.9 shows, in the order of the figure, the E_T^{miss} , p_T^γ , track E_T^{miss} , and $\Delta\phi(\gamma, E_T^{\text{miss}})$ after the jet veto is applied. The processes that contribute to single photon events are,

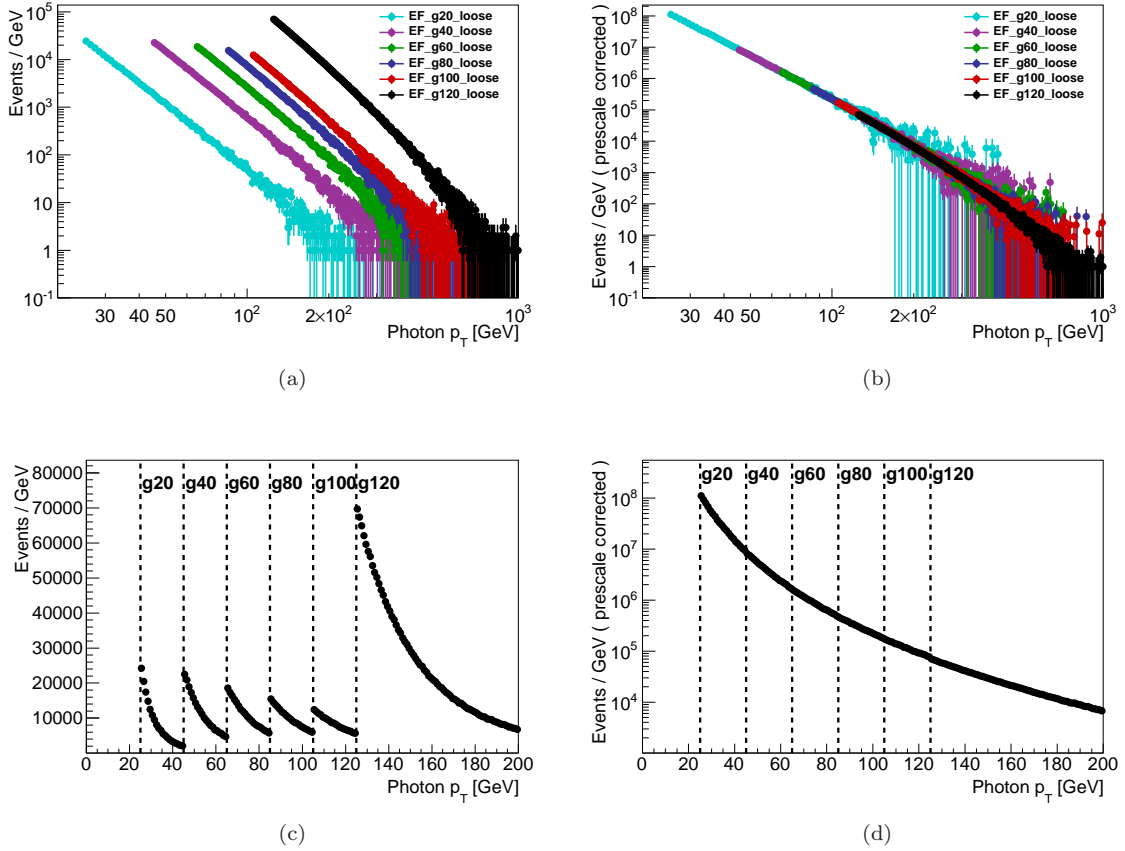


Figure 11.6: Photon trigger weighting scheme in the 2012 data sample. Figure (a) shows the raw photon p_T distributions for each triggered sample. The prescales increase for lower trigger thresholds causing those distributions to be shifted down. Figure (b) corrects for the prescales and all the distributions agree with the unprescaled trigger. Figure (c) applies the p_T binning to avoid overlap between triggers. Figure (d) applies the prescale correction to the binned samples to achieve a smooth p_T distribution.

- Single photon production – The dominant process at low E_T^{miss} . The shape of the E_T^{miss} distribution is dominated by fake sources.
- Dijets – Also contributes at low E_T^{miss} . The E_T^{miss} distribution is dominated by fake sources for dijets as well. The dijet contribution is derived using a data driven estimate that will be described in Section 11.3.12.
- $W \rightarrow \ell\nu_\ell$ – Contributes when the lepton is reconstructed as a photon. The dominant contribution is from electrons that fake a photon. This process tends to have large E_T^{miss} from the escaping neutrino
- Top – In small fraction of events where one or two top quarks are produced a photon will be

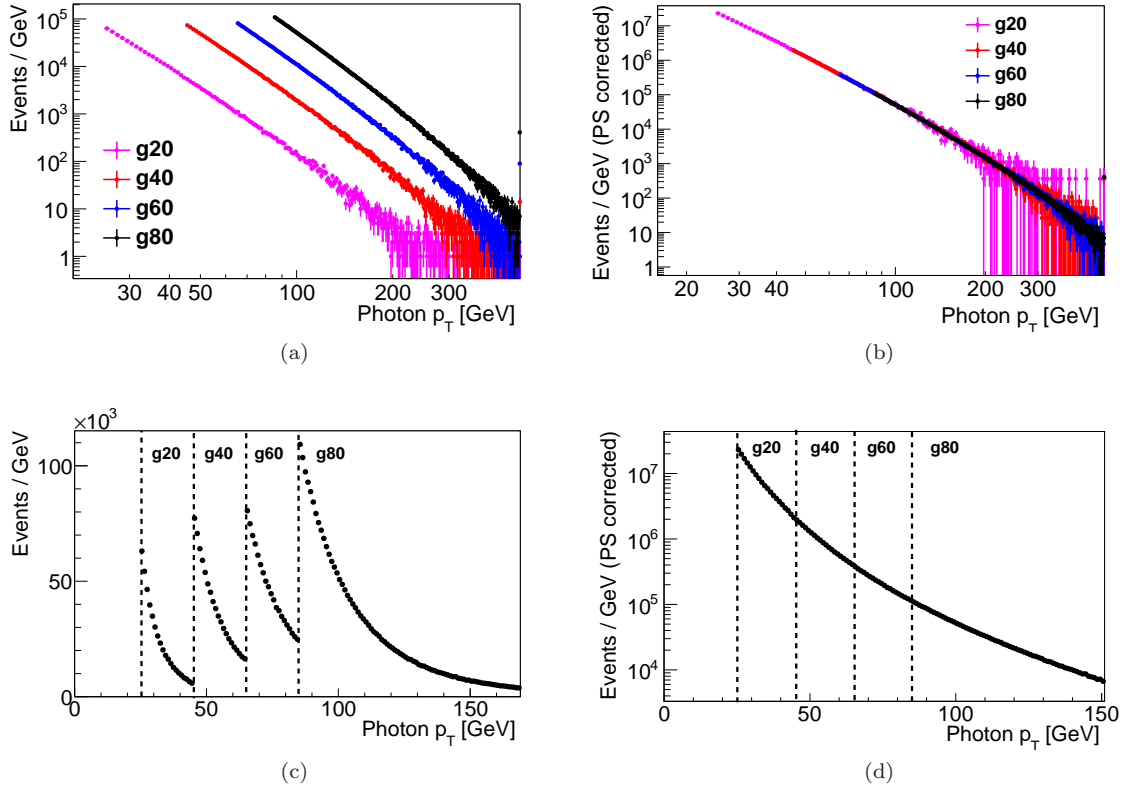


Figure 11.7: Photon trigger weighting scheme in the 2011 data sample. Figure (a) shows the raw photon p_T distributions for each triggered sample. The prescales increase for lower trigger thresholds causing those distributions to be shifted down. Figure (b) corrects for the prescales and all the distributions agree with the unprescaled trigger. Figure (c) applies the p_T binning to avoid overlap between triggers. Figure (d) applies the prescale correction to the binned samples to achieve a smooth p_T distribution.

reconstructed because of lepton or jet fakes.

- $W\gamma \rightarrow \ell\nu\ell\gamma$ – In this process the photon is identified and the decay lepton is lost. These events tend to have large E_T^{miss} from the escaping neutrino.
- $Z(\rightarrow \nu\nu)\gamma$ – The photon is identified along with large E_T^{miss} from the escaping neutrinos. This is a dominant and irreducible contribution at large E_T^{miss} .

11.3.9 Single lepton and dilepton control regions

The photon selection and the performance of the simulation are checked in control regions having one or two leptons and a photon. If the analysis for which this estimate is used requires leptons, the lepton definitions used to define the control regions should be the same as for the analysis. In this

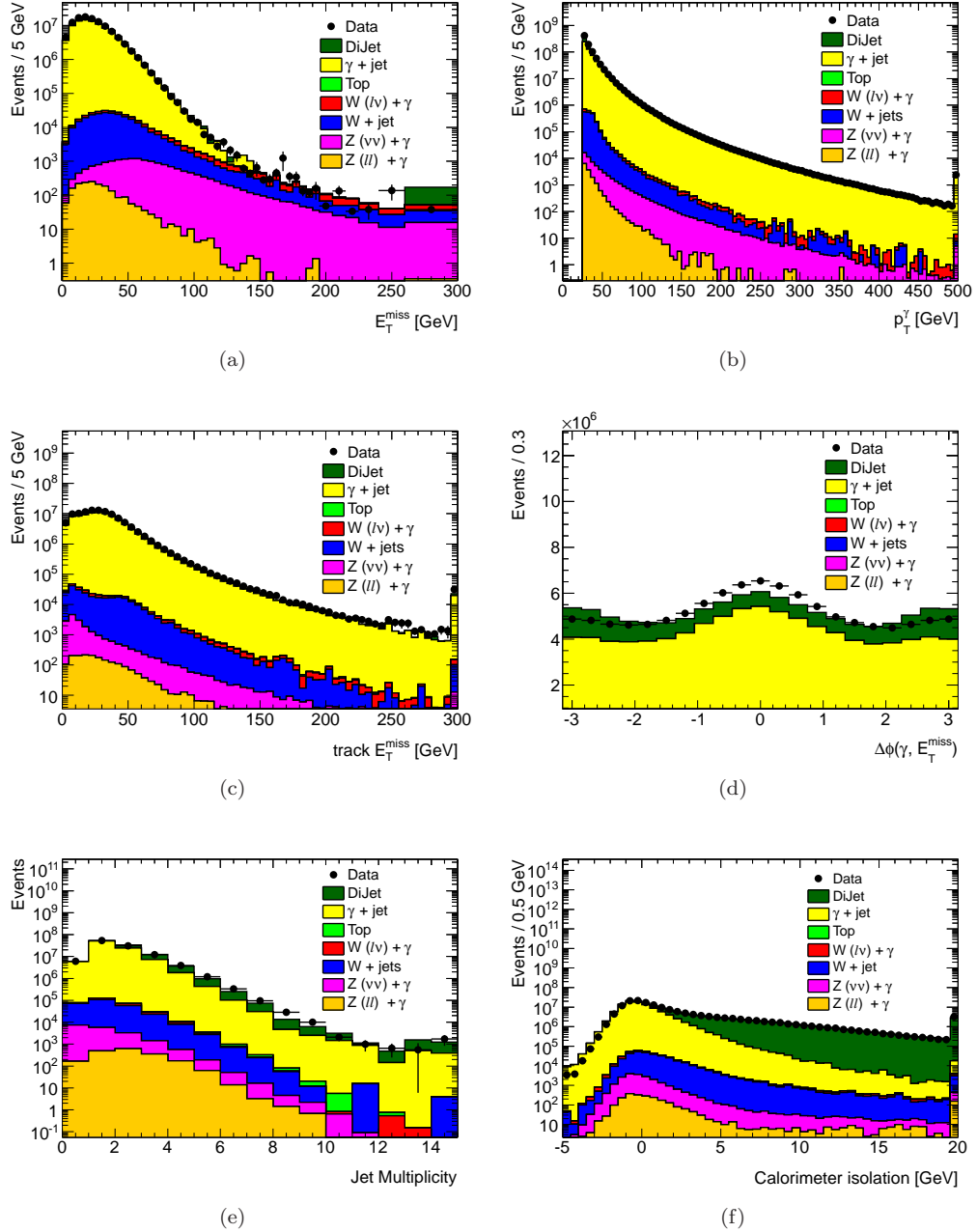


Figure 11.8: Distributions of E_T^{miss} (a), p_T^γ (b), track E_T^{miss} (c), $\Delta\phi(\gamma, E_T^{\text{miss}})$ (d), and jet multiplicity (e) for events having exactly one tight, isolated, unconverted photon and no identified leptons. The calorimeter isolation distribution (e) is shown with the photon isolation cut applied.

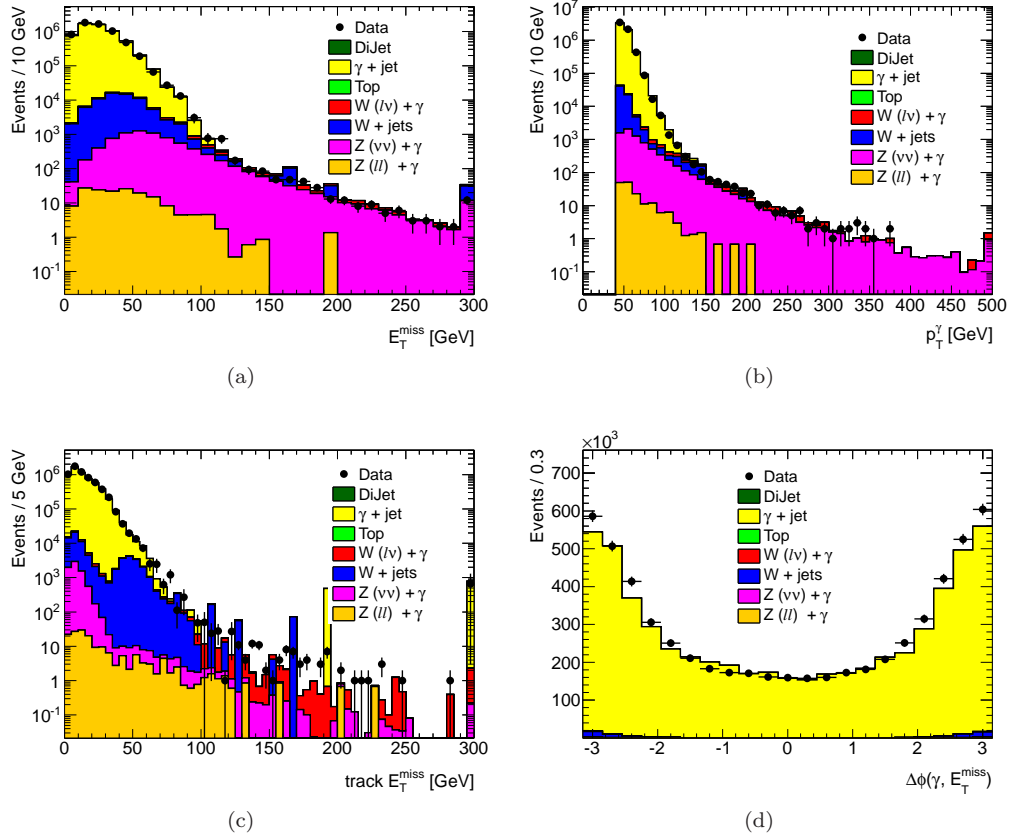


Figure 11.9: Distributions of E_T^{miss} (a), p_T^γ (b), track E_T^{miss} (c), $\Delta\phi(\gamma, E_T^{\text{miss}})$ (d), for events having exactly one tight, isolated, unconverted photon, no reconstructed jets, and no identified leptons.

case the lepton definitions are those used in Chapter 10. The E_T^{miss} distributions in the photon plus one lepton control regions are shown in Figure 11.10(a) for the electron channel and 11.10(b) for the muon channel. In the $\gamma + e$ channel $Z \rightarrow ee$ events where one electron fakes a photon dominate at low E_T^{miss} . In the $\gamma + \mu$ channel, the contribution from $Z \rightarrow \mu\mu$ is smaller because muons rarely fake photons. A small contribution is expected from events where one muon is not reconstructed and a photon is produced or faked by a jet. The high E_T^{miss} region is dominated by $W + \gamma$ events. The $Z \rightarrow \ell\ell$ background does not reproduce the data well, but this is expected because photon fakes are not well described in the simulation. In the region where $W + \gamma$ dominates the simulation and data agree well. Figures 11.10(c) and 11.10(d) show the invariant mass of the photon and two leptons ($M_{\ell\ell\gamma}$) for the photon plus dilepton control regions. The distribution shows two peaks. The lower mass peak reconstructs the Z boson mass and is from final state radiation from a lepton in $Z \rightarrow \ell\ell$ events. The higher mass peak is from events where both a photon and Z boson are produced. In this case the Z mass peak is shifted to higher mass from the inclusion of the photon. In both channels

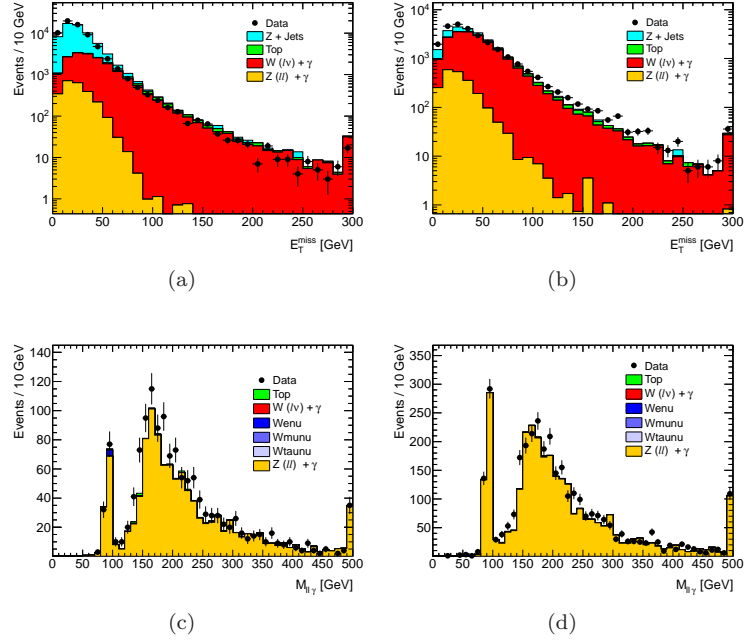


Figure 11.10: Single photon plus lepton control regions. Figures (a) and (b) show the E_T^{miss} distributions of events that have one photon and one electron (a) or muon (b). The distribution is dominated by $W\gamma$ events at high E_T^{miss} and the simulation agrees well with the data. Figures (c) and (d) show the invariant mass of the photon plus dilepton system of events that have one photon and two electrons (a) or two muons (b). The distribution is dominated by $Z + \gamma$ events and the simulation agrees well with the data.

the prediction from simulation agrees well with the data.

11.3.10 Background subtraction

Backgrounds to the single photon selection must be subtracted to obtain the correct E_T^{miss} template. The background subtraction must be implemented after all weights are applied. The final E_T^{miss} distribution is a binned subtraction of the weighted single photon data and the weighted background estimates. The E_T^{miss} tail in single photon events is dominated by real E_T^{miss} backgrounds so the subtraction is sensitive to the normalization of the background estimates. The uncertainty on the background should be propagated to the estimate by varying each background contribution by its uncertainty. The systematic uncertainty on the final estimate is the difference in the final Z/γ^* background prediction between the nominal background prediction and when the backgrounds are varied.

11.3.11 Photon vertexing – converted photons

In most use cases unconverted photons should be used because they have fewer fakes from $W \rightarrow e\nu$ than converted photons. However one drawback of using unconverted photons is that vertexing information is not available. This is especially true in the use cases described in this dissertation because a jet veto is applied in the signal selection. In an event with an unconverted photon and no jets the identified primary vertex is likely to be the incorrect one. Figure 11.11 shows the difference in z between the true hard scatter vertex and the reconstructed primary vertex in the single photon simulation. The probability to reconstruct the correct vertex is 78% if no jet cut is made and 68% if a jet veto is applied. In dilepton events this problem does not arise because the tracks from the two leptons provide vertexing information. This difference between the Z/γ^* and single photons can be ignored unless variables that use primary vertex information are modeled. One example of this is the track based E_T^{miss} . As is described in Section 7.7.2 the track E_T^{miss} includes only tracks that are associated with the primary vertex. If the incorrect primary vertex is reconstructed, the track E_T^{miss} will include tracks from a pileup interaction instead of the hard scatter. This error happens much more often in single photon events than in dilepton events causing track E_T^{miss} to be poorly modeled when using the single photon method. The vertexing of single photons can be improved by attempting to vertex unconverted photons from the calorimeter, or by using converted photons.

Unconverted photons have no tracks with which to identify the primary vertex, but the calorimeter cluster can be used to obtain pointing information. The position of the photon cluster is extrapolated to the primary vertex to obtain the z position from where the photon originated. However, the resolution on z from the calorimeter is much poorer than from tracks. Figure 11.11 shows the difference between the z of the reconstructed primary vertex and the z extrapolated from the calorimeter. The difference shows a broad peak near zero where the calorimeter pointing and primary vertex z values are consistent. To remove events where the primary vertex was reconstructed far from where the calorimeter points to a cut can be applied on this distribution. However one must be careful that the cut does not bias other distributions. For example the primary vertex is more often correct when there is more unclustered hadronic energy, but this also correlated with the E_T^{miss} resolution.

The other solution to photon vertexing is to use converted photons. The tracks from converted photons are used when the primary vertex is identified, improving the efficiency to find the correct vertex. To ensure the best vertex finding only converted photons associated with two tracks are used. Converted photons are essentially treated the same as unconverted photons except that they are selected using different triggers and they have different background compositions. Converted photons are most often triggered with an electron trigger because from the point of view of the trigger algorithm a converted photon is an electron. Therefore the lowest threshold unrescaled

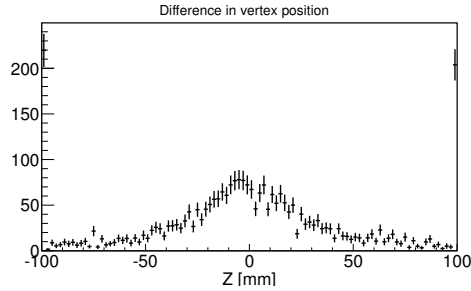


Figure 11.11: The difference between the z positions of the primary vertex and the extrapolated photon origin using the calorimeter cluster. In events that form the wide peak centered at zero the correct primary vertex is likely chosen while in events outside the peak the primary vertex is likely to be incorrectly identified.

electron trigger is used to select converted photons. All photon identification and selection criteria are the same as for unconverted photons. Figure 11.12 shows the E_T^{miss} distribution for converted photons. The distribution looks very similar to the unconverted case in Figure 11.8(a) except that the background from $W \rightarrow e\nu$ is larger. This is not surprising because converted photons look much more similar to electrons than unconverted photons. The fakes often are caused by so-called trident events. As the name indicates, a trident occurs when an electron splits into three tracks; the electron undergoes bremsstrahlung and emits a photon which then converts into an electron-positron pair. When one of the three tracks is lost the electron is reconstructed as a converted photon having two tracks. Additional variables have been developed to reject these backgrounds.

11.3.11.1 Trident suppression

Three variables are constructed to identify the third track from a trident. The third track is missed when the conversion is identified, but it may still be present in the event. If the third track is present it is close to the photon object. The minimum ΔR is calculated between each track, excluding the conversion tracks, and the photon object associated with the photon. Figure 11.13(a) shows the minimum ΔR for $W \rightarrow e\nu$ events and single photon events. In many cases the third trident track is identified. In cases when the third track from the trident is not found additional rejection can be obtained from the tracks that were identified. Trident events tend to have lower p_T tracks because the momentum is divided among three tracks instead of two. Therefore the minimum p_T of the conversion tracks, shown in Figure 11.13(b) can reject tridents. Finally in tridents the conversion can occur at a larger radius and has fewer silicon hits than a real photon conversion. Figure 11.13(c) shows the distribution of the number of silicon hits on both conversion tracks for simulated $W \rightarrow e\nu$ events and simulated single photon events. Electron fakes have zero silicon hits more often than real photon conversions. Therefore both conversion tracks are required to have at least one silicon

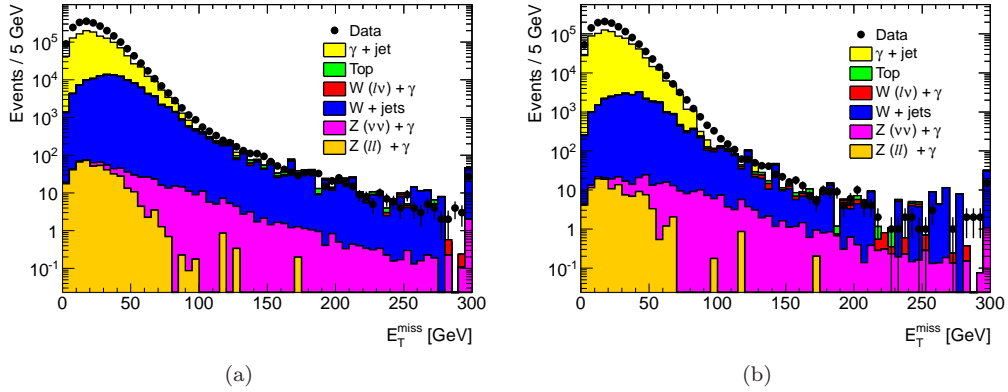


Figure 11.12: E_T^{miss} distributions in events having a 2 track converted photon before suppression of trident fakes from electrons (a) and after (b).

hit. The three distributions are relatively uncorrelated. To check this, the minimum ΔR between the photon and the nearest track in the event is required to be less than 0.1. The minimum conversion track p_T and number of silicon hits on each conversion track are shown in Figures 11.13(d) and 11.13(e) respectively after the cut. Both distributions show that additional rejection of trident fakes can be achieved. The three trident suppression cuts reduces the $W \rightarrow e\nu$ background by 75% while removing only 35% of real photons.

11.3.12 Data driven dijet prediction and normalization of single photon simulation

The dijet background is estimated using a data driven technique. The dijet background is simulated, but lack of statistics causes large statistical fluctuations in the prediction. Figure 11.15 shows the isolation distribution of tight photons where the red histogram is the dijet prediction from simulation and the yellow histogram shows the single photon simulation. The dijet simulation suffers from poor statistics, but shows approximate agreement with the data. A more robust estimate of this background is necessary and will be derived from data.

A two step normalization procedure is used to determine both the dijet background and the normalization of the single photon simulation. Figure 11.14 shows a schematic diagram for this method. This method of obtaining a dijet template has been implemented in the measurement of the single photon cross section at ATLAS [124] and is described in detail in [125]. The isolation template is derived by inverting combinations of three photon PID variables that are fairly uncorrelated with isolation. The template is normalized to the non-isolated control region for photons passing the tight PID. The resulting dijet prediction is then used in the tight, isolated region where the single photon

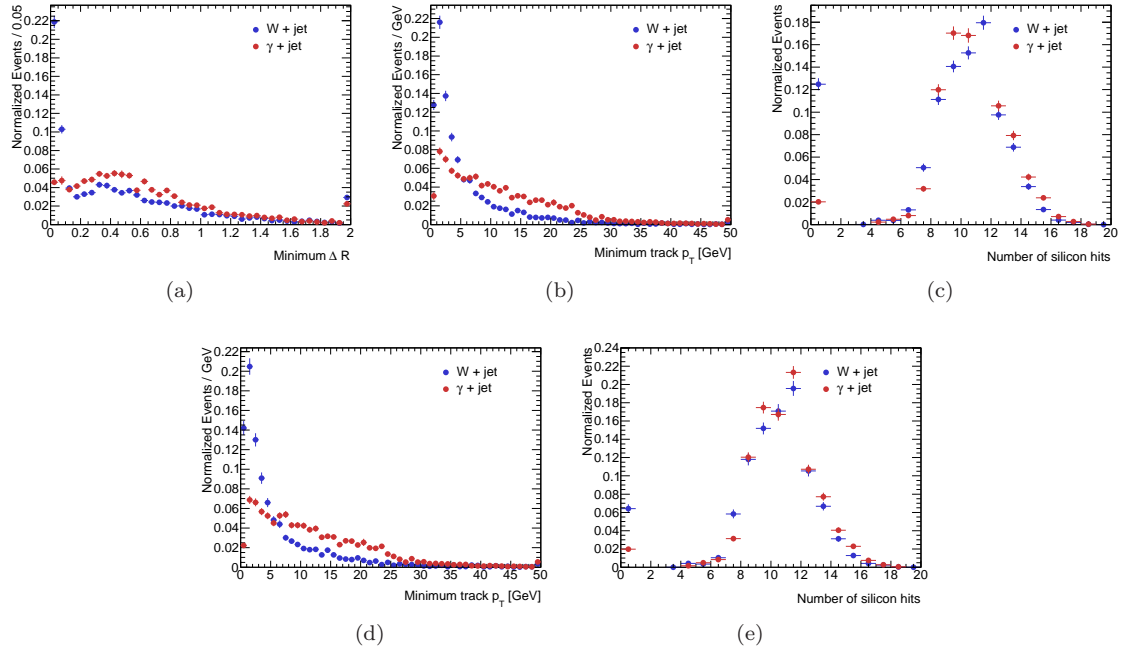


Figure 11.13: Variables used to reject electrons that fake 2 track converted photons. The minimum ΔR between the photon and all other tracks in the event excluding the two conversion tracks (a) is used to identify the third track from an electron trident. The two tracks from the trident tend to have lower p_T than a real conversion. Figure (b) shows the minimum p_T of the two conversion tracks. Tracks from tridents tend to have fewer silicon hits and more often have zero silicon hits (c). Figures (d) and (e) show the minimum p_T distribution and the distribution of the number of silicon hits respectively after the minimum ΔR is required to be greater than 0.1.

simulation is normalized to match the data. The normalization is such that the sum of the dijet prediction and the scaled single photon simulation agrees with the data. The single photon simulation does not correctly reproduce the isolation distribution in data so a fit to the two templates is not possible and instead this two step normalization procedure is used. The normalization is applied in photon p_T bins because the isolation energy is strongly dependent on the photon p_T for both real photons and fake photons from jets. It is important to note that the normalization of the single photon simulation is not essential to the background estimation method; it is purely aesthetic.

Three of the tight photon ID variables are found to be uncorrelated with the isolation energy and are referred to as dijet control region variables. The three variables measure the photon shower shape in the first layer of the electromagnetic calorimeter. The variables used are f_{side} , which measures the width of the shower in η , $ERatio$, which provides pion rejection by measuring relative the energy difference between the largest and second largest energy deposits in the shower, and ΔE , which also provides pion rejection using the energy difference between the largest deposit and the smallest deposit between the largest and second largest deposits.

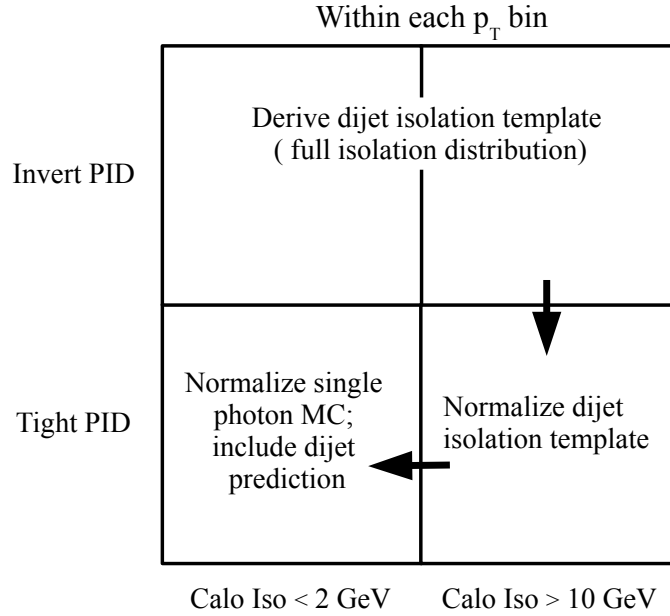


Figure 11.14: A diagrammatic explanation of the dijet background estimate and single photon normalization procedure. An isolation template is derived by inverting combinations of three photon PID variables that are fairly uncorrelated with isolation. The template is normalized to the non-isolated control region for photons passing the tight PID. The resulting dijet prediction is then used in the tight, isolated region where the single photon simulation is normalized to match the data. The procedure is applied in bins of photon p_T .

The three dijet control region variables are inverted using three different schemes that trade off between statistics and dijet purity. The schemes require at least one, at least two, and all three dijet control region variables to fail. Figure 11.18 shows the isolation distribution for each case. The case where at least one cut must fail, Figure 11.18(c), provides the most statistics, but also has contamination from real photons whereas the case where all three must fail, Figure 11.18(a), has fewer statistics but less contamination from real photons. The intermediate case where at least two of the cuts must fail is shown in Figure 11.18(b). A dijet prediction is produced from each scheme and the variation in the prediction between the schemes will be used to estimate a systematic uncertainty.

The normalization of the dijet template is performed in p_T bins in the non-isolated dijet control region where $E_{\text{Tcone30}} > 10$ GeV. The derived p_T dependent weights are shown in Figure 11.16(a). The p_T weighted dijet estimate is then used in the $E_{\text{Tcone30}} < 2$ GeV region and the single photon simulation is weighted to match the data using the same p_T binning. The derived p_T dependent weights for the single photon simulation are shown in Figure 11.16(b). Figure 11.17 compares the isolation and E_T^{miss} distributions from the dijet estimate. The shape of the isolation distribution

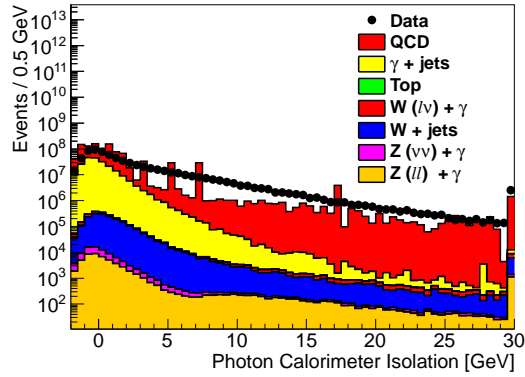


Figure 11.15: Calorimeter isolation distribution of photon candidates that pass the tight identification criteria. The red histogram shows the dijet prediction from simulation. The dijet simulation suffers from large statistical fluctuations, but the simulation qualitatively agrees with the data.

differs somewhat between the three inversion schemes. The case when at least one dijet control region variable fails has the most statistics and has events in the E_T^{miss} tail while the other two cases have fewer events in the E_T^{miss} tail. The case when at least one dijet control region variable fails will be used to predict the dijet background and the largest difference in normalization between the different schemes determines the uncertainty.

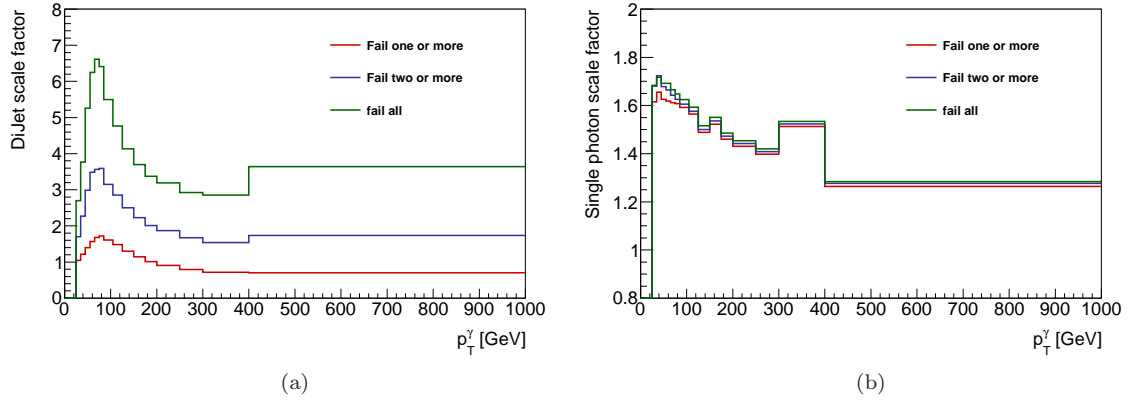


Figure 11.16: Comparison of the weights derived in the three schemes used to estimate the dijet background (a) and the $\gamma + \text{jet}$ process (b). The variation in the normalization of the weights in Figure (a) is because the background statistics vary between the schemes.

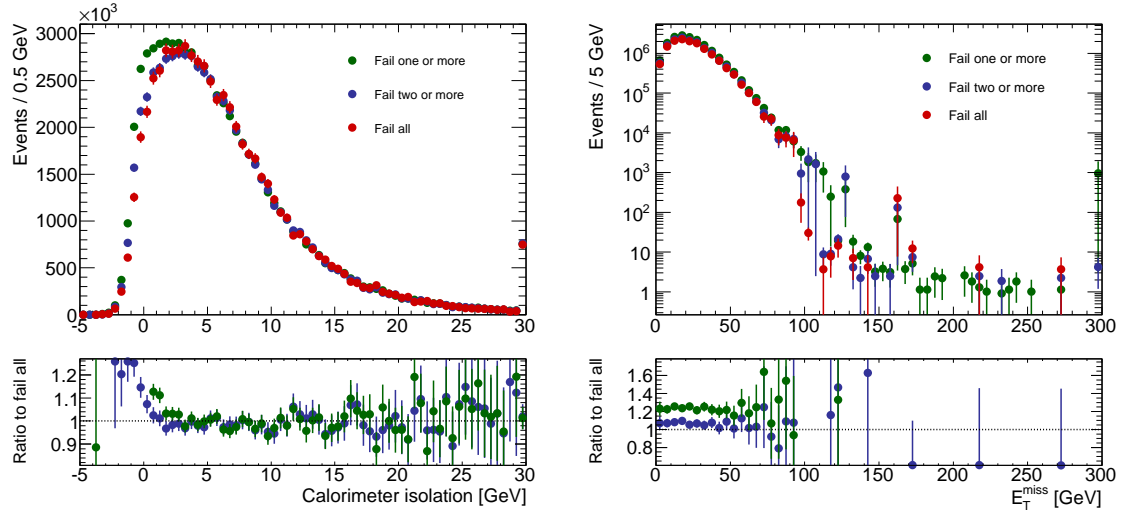


Figure 11.17: Comparison of the isolation distribution (a) the E_T^{miss} distribution (b) for the three dijet estimation schemes. In Figure (b) the nominal isolation cut is applied. The three schemes have different isolation distributions because of background contamination. After a cut is applied on the isolation distribution, the predicted E_T^{miss} distributions have different normalizations but similar shapes.

11.3.13 Improved estimate of $W \rightarrow e\nu_e$ background

The nominal estimate of the $W \rightarrow e\nu_e$ background is derived from simulation. Despite the large sample size of the $W \rightarrow e\nu_e$ simulation, the estimate suffers from statistical uncertainties because the electron must fake a tight photon. To increase the available statistics a scale factor that accounts for the probability for an electron to fake a tight photon is applied to reconstructed electrons in the $W \rightarrow e\nu_e$ simulation. The scale factor is derived in a high statistics Z sample using a tag and probe style method and is determined in bins of p_T and η . The scale factor is derived separately for unconverted and converted photons because the probability for an electron to fake a converted photon is higher.

Events are required to have two reconstructed medium++ electrons (See 7.3) or one medium++ electron and one tight photon. In events having one tight photon and one medium++ electron where the invariant mass of the two objects is near the Z mass, the photon is likely to have originated from a real electron. To select events rich in electrons faking photons the electron-photon mass is required to be between 76 GeV and 106 GeV. Similarly the dielectron mass is required to be within the same range. For the p_T range considered the background from non electron fakes in the electron-photon selection is negligible. The rate at which electrons fake photons in a given p_T or η bin is determined from the ratio of the number of reconstructed photons to the number of reconstructed electrons in

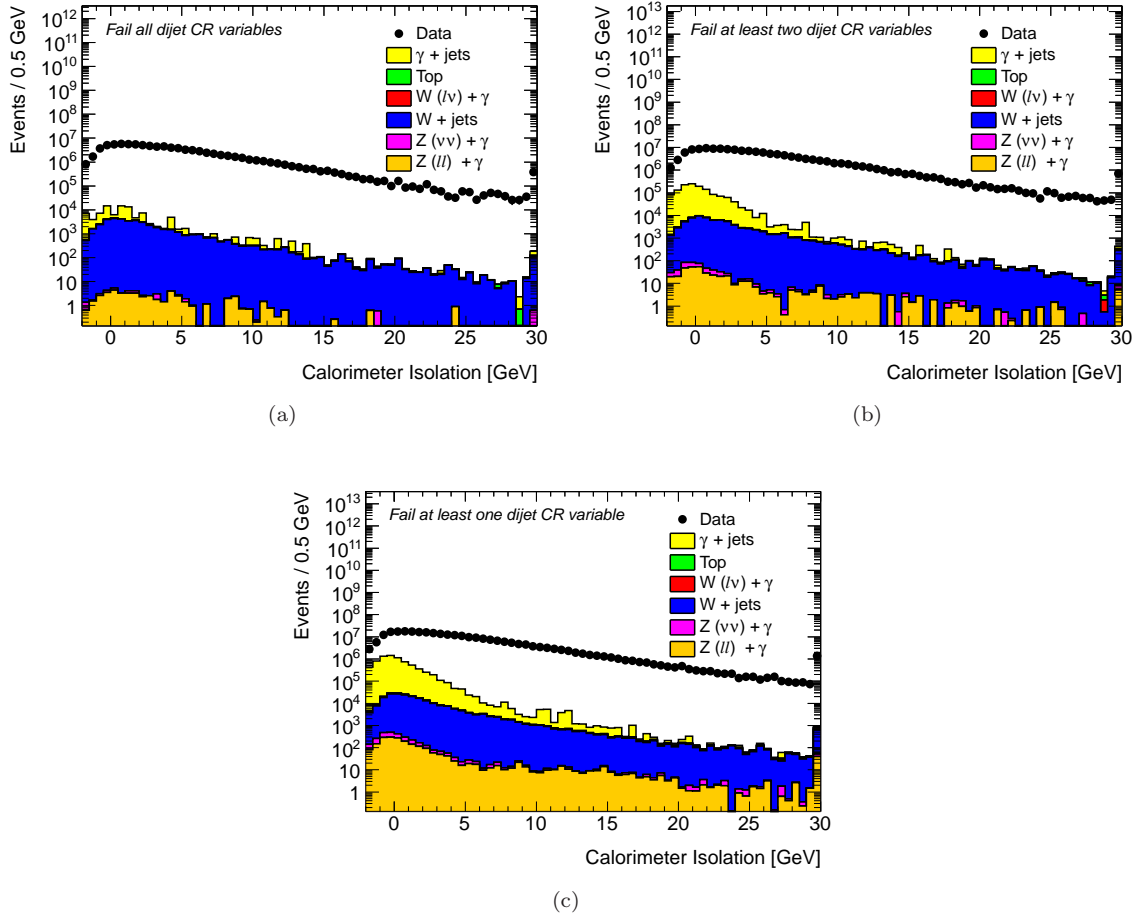


Figure 11.18: Calorimeter isolation distributions of photon candidates where all tight cuts except three variables derived from layer 1 quantities that are largely uncorrelated with isolation. The dijet prediction is not shown; the large discrepancy between data and simulation is attributed to dijet events. Three possibilities for inverting the layer 1 based variables are considered. All three cuts are required to fail in (a), at least two cuts must fail in (b) and any of the three cuts must fail in (c). The different configurations are a trade off between available statistics and the level of contamination from real photons. Configuration (a) has the fewest statistics, but is most pure in dijet events. Configuration (c) has the most statistics, but has the most contamination from real photons, and (b) is intermediate in both statistics and purity.

that bin. The fake rate is not strongly correlated between p_T and η allowing the scale factor to be determined separately in p_T and η bins instead of using 2-d binning. In dielectron events each electron has a chance to fake a photon and therefore each electron is counted in the denominator. Figure 11.19 shows the p_T and η fake factors derived in data and Monte Carlo. The fake factors have a strong dependence in η because of the distribution of material in the inner detector. The fake factors agree well between data and simulation.

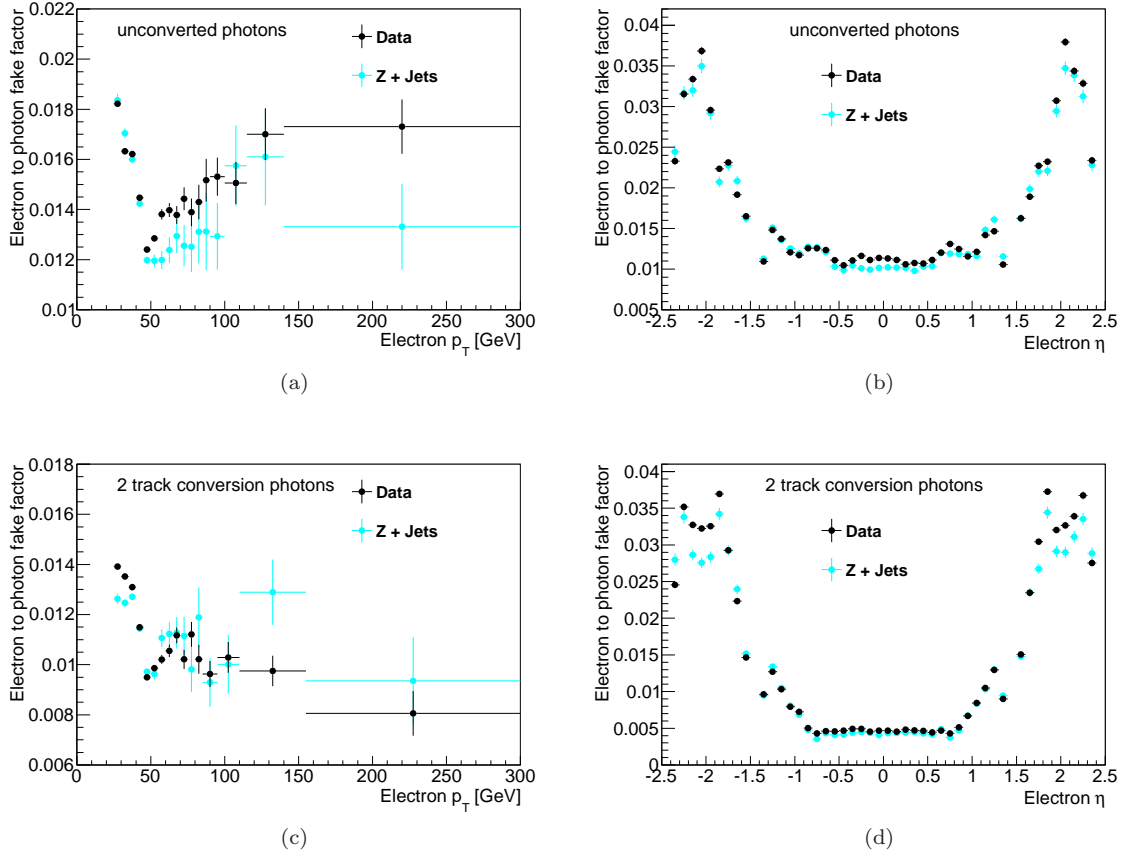


Figure 11.19: Fake factors for an electron that passes the `medium++` identification criteria to fake a photon that passes the tight identification criteria. The probability of an electron to fake a photon is dependent on the electron p_T , η , and whether the faked photon is associated with conversion tracks. Fake factors are derived separately for unconverted (a, b) and 2 track conversion photons (c, d) and are binned in p_T and η . The black points show the fake factors derived from data and the blue points show fake factors derived from $Z + \text{jets}$ simulation. Fake factors agree well between data and simulation.

11.3.14 Application – $ZZ \rightarrow \ell^+ \ell^- \nu \bar{\nu}$

This method was implemented to estimate the Z/γ^* background to the ZZ cross section measurement in the $\ell\ell\nu\nu$ final state. The analysis is described in Section 8.2. The analysis requires $\text{Axial } E_T^{\text{miss}} > 75 \text{ GeV}$ and $|p_T^{\ell\ell} - E_T^{\text{miss}}|/p_T^{\ell\ell} < 0.4$ to reject Z/γ^* events. The $\text{Axial } E_T^{\text{miss}}$ is a function of the magnitude of the E_T^{miss} and the azimuthal difference between the E_T^{miss} and $p_T^{\ell\ell}$, ($\Delta\phi(Z, E_T^{\text{miss}})$). Therefore the single photon method must model E_T^{miss} and $\Delta\phi(Z, E_T^{\text{miss}})$. For a portion of the analysis events are binned in three distributions, $p_T^{\ell\ell}$, $\Delta\phi(\ell, \ell)$, and the transverse mass, m_T . The $p_T^{\ell\ell}$ is modeled by construction because of the p_T^γ weighting. The $\Delta\phi(\ell, \ell)$ is a purely leptonic variable that cannot be modeled with this method. Instead the method must be applied

in each bin of $\Delta\phi(\ell, \ell)$. For each bin the $\Delta\phi(\ell, \ell)$ cuts that define the bin should be applied to the Z/γ^* sample before the single photon normalization or p_T weighting are derived. The full method is carried out in each bin producing independent, but statistically correlated results. The m_T depends only on variables that are already modeled. The definition of m_T is,

$$M_T^2 = \left(\sqrt{M_Z^2 + |p_T^{\ell\ell}|^2} + \sqrt{M_Z^2 + E_T^{\text{miss}2}} \right)^2 - E_T^{\text{miss}2} - p_T^{\ell\ell 2} - 2E_T^{\text{miss}} p_T^{\ell\ell} \cos(\Delta\phi(Z, E_T^{\text{miss}})) \quad (11.3)$$

where M_Z is the world average Z mass [1]. The m_T only depends on E_T^{miss} , $p_T^{\ell\ell}$, and $\Delta\phi(Z, E_T^{\text{miss}})$ so no additional variables need to be modeled. The m_T binning cuts can simply be applied after all other cuts.

The p_T weights and normalization are derived after all cuts are applied except for Axial E_T^{miss} and fractional difference. The p_T^γ weights are derived separately for the ee and $\mu\mu$ channels. The full sample of single photon events are used for both channels, but a different set of p_T^γ weights are applied in each channel. As a result, results are statistically correlated between the ee and $\mu\mu$ channels. Weights to correct the pileup multiplicity distributions for the prescaled photon triggers are also applied.

After the weights are applied the background contributions to the single photon selection are subtracted using the prediction from simulation. The dijet contribution is not subtracted and a systematic uncertainty is derived to account for its contribution. A systematic uncertainty is included to account for uncertainties in the cross sections for the processes simulated. Figure 11.20 shows the Axial E_T^{miss} distributions in both channels after all cuts except Axial E_T^{miss} and fractional difference. The stacked histograms represent the background and signal predictions for each contributing process and the black points show the data. The cyan distributions show the Z/γ^* background predicted from this method. All other processes are modeled using the simulation. Good agreement is observed between the data and the Z/γ^* background prediction, but the $\mu\mu$ channel the prediction is slightly shifted to lower values of Axial E_T^{miss} . This difference is attributed to poor modeling of the $\Delta\phi(Z, E_T^{\text{miss}})$ distribution in the $\mu\mu$ channel. Figure 11.21 compares the $\Delta\phi(Z, E_T^{\text{miss}})$ distribution between the single photon model and the data. The distributions are normalized to have unit area to compare the shapes of the distributions. Good agreement is observed in the ee channel, but the distributions disagree in the $\mu\mu$ channel. The fact that the model agrees better with the data in the ee channel than the $\mu\mu$ channel is not surprising. The $\Delta\phi(Z, E_T^{\text{miss}})$ distribution is affected by lepton mismeasurements. If a lepton is mismeasured, the E_T^{miss} is pulled to point along or opposite to the lepton. Electrons and photons are similar objects, so the effects of electron momentum mismeasurements are modeled by photons. Muons, however, are very different objects than photons. In particular, the muon momentum resolution is different than for photons and can have long tails. The difference in the $\Delta\phi(Z, E_T^{\text{miss}})$ distribution between the model and data in the $\mu\mu$ channel

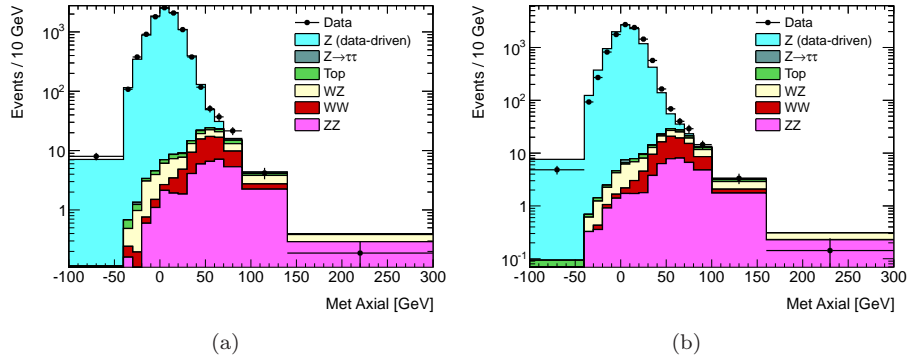


Figure 11.20: Axial E_T^{miss} distributions in the ee (a) and $\mu\mu$ (b) channel for the $ZZ \rightarrow \ell^+\ell^-\nu\bar{\nu}$ analysis. The Z distribution is modeled using the single photon method. Good agreement is observed in the ee channel and a small shift in the Z model is observed in the $\mu\mu$ channel.

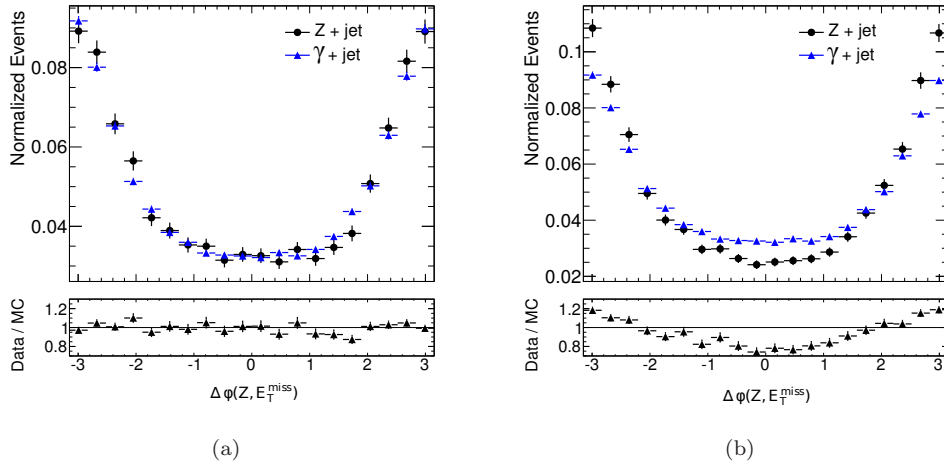


Figure 11.21: Comparison of the $\Delta\phi(Z, E_T^{\text{miss}})$ distributions between the data and the single photon model in the ee (a) and $\mu\mu$ (b) channels. The distributions are normalized to the same area to compare the shape of the distribution between the data and the model. Contributions to the shape from non- Z processes are negligible. Good agreement is observed in the ee channel, but some disagreement exists in the $\mu\mu$ channel. This disagreement causes the shift in Axial E_T^{miss} observed in Figure 11.20(b).

is attributed to this difference. An additional systematic uncertainty is added to the background estimate in the $\mu\mu$ channel to account for this discrepancy.

The ZZ analysis also measures the cross section in bins of $p_T^{\ell\ell}$, $\Delta\phi(\ell, \ell)$, and m_T . Figure 11.22 shows the Axial E_T^{miss} distributions, Figure 11.23 shows the predicted m_T distributions, and Figure 11.24 shows the predicted $\Delta\phi(\ell, \ell)$ distributions. Good agreement is observed in all cases. The m_T is correlated with E_T^{miss} so in the third m_T bin almost all of the Z background has been removed. In the first and second m_T bins the predicted Z background agrees well with the data. Table 11.2

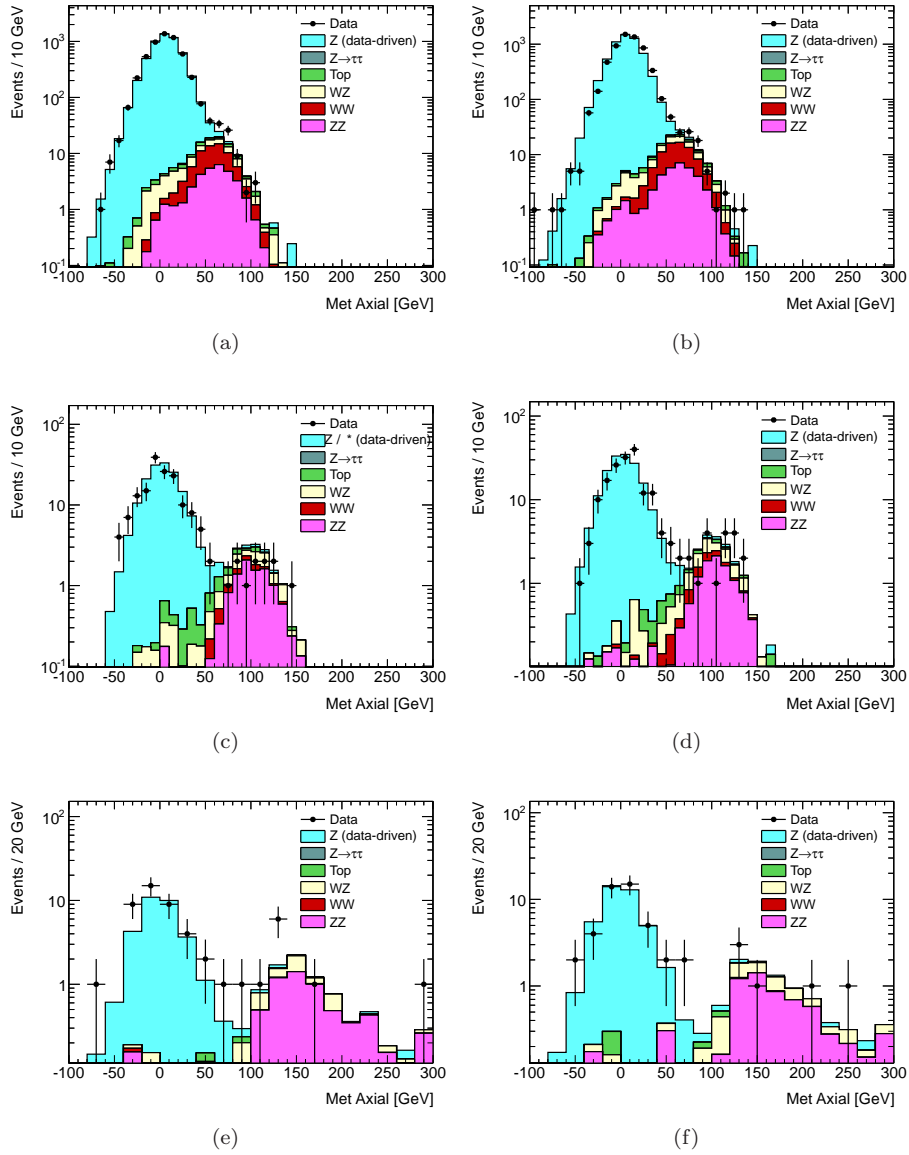


Figure 11.22: Axial E_T^{miss} distributions for each of three bins in $p_T^{\ell\ell}$. In all plots the Z distribution is modeled using the single photon method. Figures (a), (c), and (e) show the ee channel and Figures (b), (d), and (f) show the $\mu\mu$ channel. Figures (a) and (b) require $50 \text{ GeV} < p_T^{\ell\ell} < 90 \text{ GeV}$, Figures (c) and (d) require $90 \text{ GeV} < p_T^{\ell\ell} < 130 \text{ GeV}$ and Figures (e) and (f) require $p_T^{\ell\ell} > 130 \text{ GeV}$. In all cases the Z background predicted from the single photon model agrees well with the data.

shows the predicted Z background for each channel and in each bin of $p_T^{\ell\ell}$, $\Delta\phi(\ell, \ell)$, and m_T .

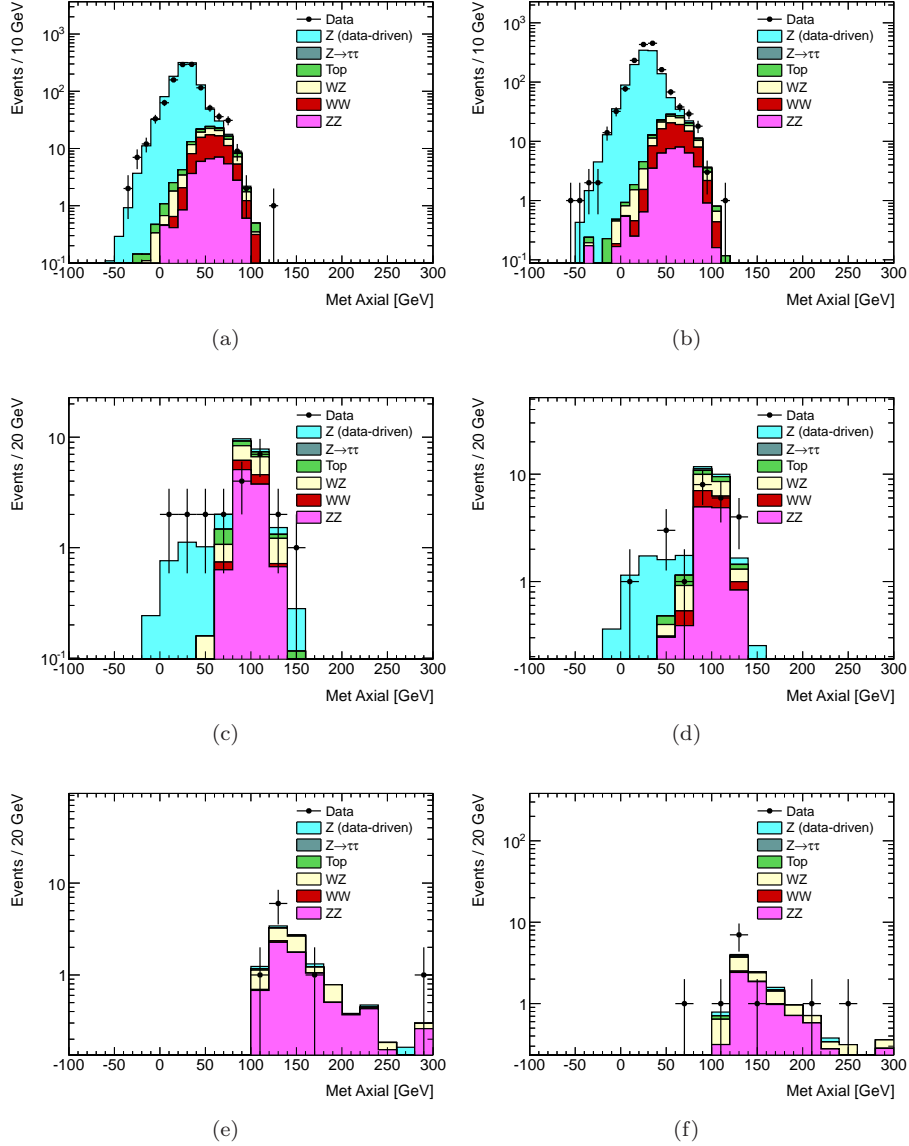


Figure 11.23: Axial E_T^{miss} distributions for each of three bins in m_T . In all plots the Z distribution is modeled using the single photon method. Figures (a), (c), and (e) show the ee channel and Figures (b), (d), and (f) show the $\mu\mu$ channel. Figures (a) and (b) require $220 \text{ GeV} < m_T < 250 \text{ GeV}$, Figures (c) and (d) require $250 \text{ GeV} < m_T < 300 \text{ GeV}$ and Figures (e) and (f) require $m_T > 300 \text{ GeV}$. The m_T distribution is strongly correlated with E_T^{miss} so few Z events remain in the $m_T > 300 \text{ GeV}$ bin. In cases when more statistics are available for the Z background the model agrees well with the data.

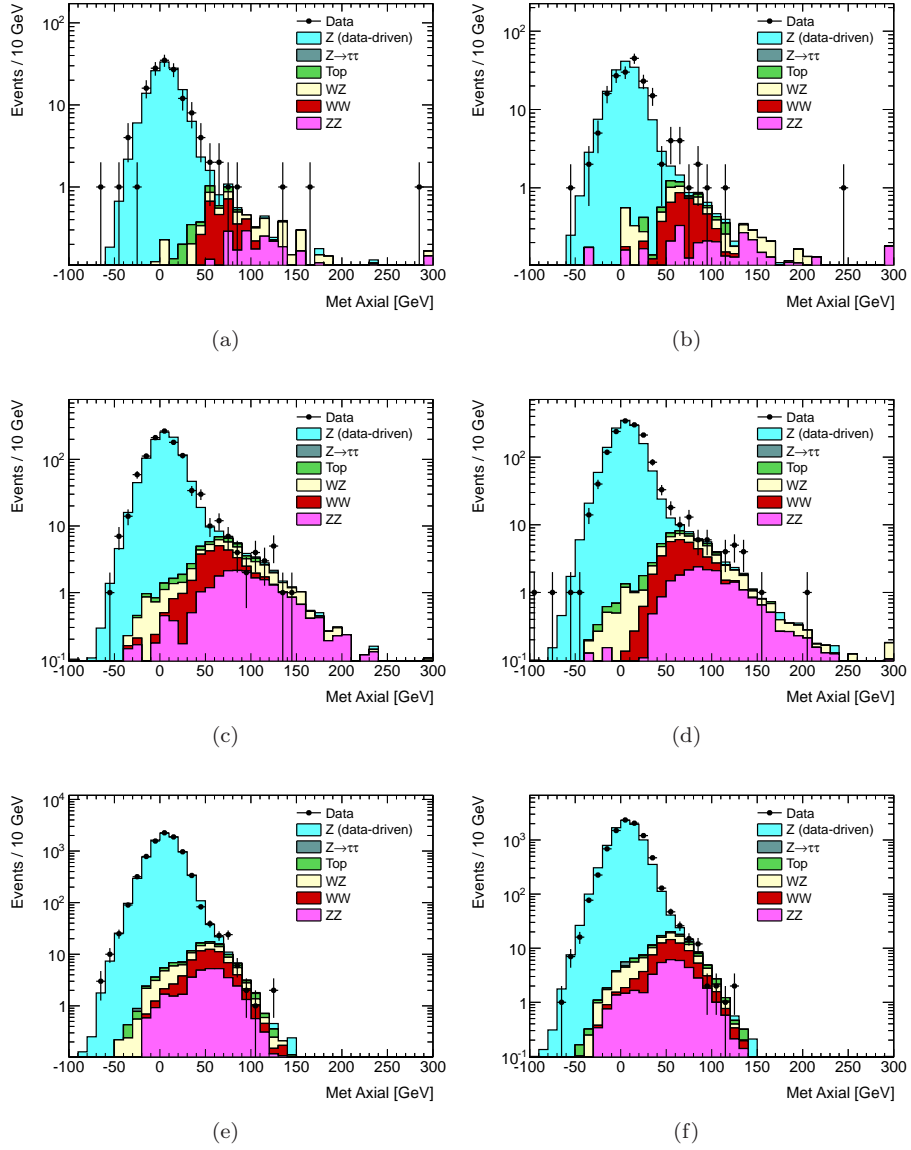


Figure 11.24: Axial E_T^{miss} distributions for each of three bins in $\Delta\phi(\ell, \ell)$. In all plots the Z distribution is modeled using the single photon method. Figures (a), (c), and (e) show the ee channel and Figures (b), (d), and (f) show the $\mu\mu$ channel. Figures (a) and (b) require $0 < \Delta\phi(\ell, \ell) < 0.5$, Figures (c) and (d) require $0.5 < \Delta\phi(\ell, \ell) < 1.7$ and Figures (e) and (f) require $1.7 < \Delta\phi(\ell, \ell) < \pi$. In all cases the Z background predicted from the single photon model agrees well with the data.

channel	Region	estimated Z bkg.	stat. uncert	syst uncert.
ee	Nominal	2.595	0.680	0.991
$\mu\mu$	Nominal	2.676	0.786	1.234
ee	$50 < p_T^{\ell\ell} < 90$	1.371	0.577	0.524
ee	$90 < p_T^{\ell\ell} < 130$	1.070	0.230	0.409
ee	$p_T^{\ell\ell} > 130$	0.158	0.278	0.060
$\mu\mu$	$50 < p_T^{\ell\ell} < 90$	1.428	0.628	0.658
$\mu\mu$	$90 < p_T^{\ell\ell} < 130$	1.126	0.240	0.519
$\mu\mu$	$p_T^{\ell\ell} > 130$	0.121	0.407	0.056
ee	$0.0 < \Delta\phi(\ell, \ell) < 0.5$	0.108	0.104	0.041
ee	$0.5 < \Delta\phi(\ell, \ell) < 1.7$	1.292	0.305	0.494
ee	$\Delta\phi(\ell, \ell) > 1.7$	1.194	0.413	0.456
$\mu\mu$	$0.0 < \Delta\phi(\ell, \ell) < 0.5$	0.246	0.057	0.113
$\mu\mu$	$0.5 < \Delta\phi(\ell, \ell) < 1.7$	1.316	0.447	0.607
$\mu\mu$	$\Delta\phi(\ell, \ell) > 1.7$	1.114	0.419	0.514
ee	$220 < m_T < 250$	1.331	0.525	0.508
ee	$250 < m_T < 300$	1.091	0.296	0.417
ee	$m_T > 300$	0.166	0.314	0.063
$\mu\mu$	$220 < m_T < 250$	1.379	0.566	0.636
$\mu\mu$	$250 < m_T < 300$	1.159	0.330	0.534
$\mu\mu$	$m_T > 300$	0.126	0.434	0.058

Table 11.2: Data-driven Z background estimates using the single photon method. Results are shown for each channel and in each bin of $p_T^{\ell\ell}$, $\Delta\phi(\ell, \ell)$, and m_T .

11.3.15 Application – ZH , $H \rightarrow$ invisible

This method was implemented to estimate the Z/γ^* background to the ZH , $H \rightarrow$ invisible search. Much like the $ZZ \rightarrow \ell^+\ell^-\nu\bar{\nu}$ analysis, a cut on E_T^{miss} and the fractional p_T difference, $|E_T^{\text{miss}} - p_T^{\ell\ell}|/p_T^{\ell\ell}$, are applied to reject the Z/γ^* background. This analysis includes data from the 2012 run that has much higher pileup than in the 2011 run where even a sizeable E_T^{miss} cut does not reject enough Z/γ^* background and other cuts must be added to reduce the background further. To further reject the background the analysis uses the angular separation between the nominal E_T^{miss} and track E_T^{miss} . They are required to be within $\Delta\phi(E_T^{\text{miss}}, E_T^{\text{miss,track}}) < 0.2$ so that both measurements of E_T^{miss} confirm the presence of true E_T^{miss} . An additional cut requires the E_T^{miss} to be back-to-back with $p_T^{\ell\ell}$, $\Delta\phi(Z, E_T^{\text{miss}}) > 2.6$. Therefore the single photon method can be used to model E_T^{miss} , $\Delta\phi(Z, E_T^{\text{miss}})$, $\Delta\phi(E_T^{\text{miss}}, E_T^{\text{miss,track}})$, and the fractional p_T difference. As is described below, the single photon method does not model the $\Delta\phi(Z, E_T^{\text{miss}})$ distribution well and this distribution must be weighted to match the simulation. The remaining signal selection cuts are applied before deriving the p_T^γ weights. These cuts are, the baseline dilepton selection, the third lepton veto, $M_{\ell\ell}$, $\Delta\phi(\ell, \ell)$, and the jet veto. A total of three shaping weights are applied to the single photon sample, the p_T^γ weight, the $\Delta\phi(Z, E_T^{\text{miss}})$ weight and the pileup correction weight.

The $\Delta\phi(Z, E_T^{\text{miss}})$ weight is required because the direction that the E_T^{miss} points relative to a

photon is much different than the relative direction in Z/γ^* events. This discrepancy points to a possible error in the E_T^{miss} calculation for photon objects in 2012. In lieu of a fix for this error the $\Delta\phi(Z, E_T^{\text{miss}})$ distribution is modeled from the Z/γ^* simulation by weighting the $\Delta\phi(\gamma, E_T^{\text{miss}})$ distribution to match the $\Delta\phi(Z, E_T^{\text{miss}})$ distribution. The method is first carried out without applying the $\Delta\phi(\gamma, E_T^{\text{miss}})$ weight to show the discrepancy. Figure 11.25 shows the $\Delta\phi(Z, E_T^{\text{miss}})$ and $\Delta\phi(E_T^{\text{miss}}, E_T^{\text{miss,track}})$ distributions where the Z/γ^* contribution is modeled using this method. A clear difference is apparent in the shape between the data and the model. The E_T^{miss} tends to point along the photon more often than it points along the $p_T^{\ell\ell}$ vector. This can be compared to Figure 11.21 which compares the single photon distribution to the data distribution in 2011 data where the agreement is better. Figure 11.26 shows the $\Delta\phi(Z, E_T^{\text{miss}})$ and $\Delta\phi(E_T^{\text{miss}}, E_T^{\text{miss,track}})$ distributions after the weighting is applied. The $\Delta\phi(Z, E_T^{\text{miss}})$ distribution agree by construction. Weighting the $\Delta\phi(Z, E_T^{\text{miss}})$ distribution also brings the $\Delta\phi(E_T^{\text{miss}}, E_T^{\text{miss,track}})$ distribution into agreement because the two variables are correlated. Therefore the discrepancy is only present in the $\Delta\phi(Z, E_T^{\text{miss}})$ distribution and the modeling of the $\Delta\phi(E_T^{\text{miss}}, E_T^{\text{miss,track}})$ distribution is acceptable.

After all weights are applied the modeling of the E_T^{miss} , $\Delta\phi(E_T^{\text{miss}}, E_T^{\text{miss,track}})$, and fractional p_T difference cuts must be checked. Figure 11.27 Shows the E_T^{miss} distribution and the fractional p_T difference distribution for both channels with the full single photon method applied to estimate the $Z + \text{jets}$ background. Discrepancies of up to 50% are observed in the E_T^{miss} distribution. The single photon model predicts a narrower E_T^{miss} distribution than what is observed in Z/γ^* events. In order to cover for this discrepancy a large systematic uncertainty must be applied to the background estimate. Such a large additional uncertainty is not acceptable and a solution to the root cause of the problem is preferable.

11.4 Extended single photon method

The single photon method has been shown to be successful at modeling E_T^{miss} related variables. However variables that combine lepton and E_T^{miss} information cannot be modeled as described in Section 11.3.1. For example $E_T^{\text{miss,rel}}$, described in Section 7.7.1, uses the magnitude of E_T^{miss} as well as the angular separation between the nearest lepton or jet. Lepton information does not exist in single photon events so $E_T^{\text{miss,rel}}$ cannot be calculated. The extended method allows these variables to be modeled using a procedure that merges single photon and Z/γ^* events.

The extended method follows the same procedure as the basic method, but adds a merging algorithm. The goal of the merging algorithm is to combine variables from single photon events with simulated Z/γ^* events. The particular variables that are merged depend on which distributions are to be modeled with the method. The merging algorithm replicates the nominal Z/γ^* simulation

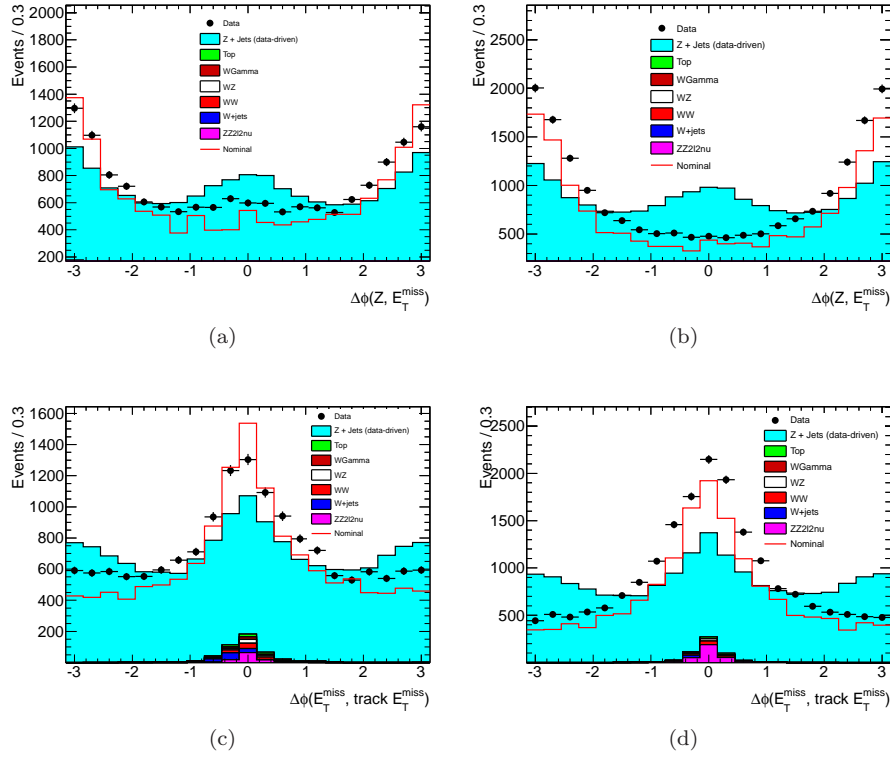


Figure 11.25: Distributions of $\Delta\phi(Z, E_T^{\text{miss}})$ (a-b) and $\Delta\phi(E_T^{\text{miss}}, E_T^{\text{miss,track}})$ (c-d) for the ee (a,c) and $\mu\mu$ (b, d) channels with no $\Delta\phi(Z, E_T^{\text{miss}})$ correction. A large discrepancy between the single photon model and the data is observed.

event by event. Figure 11.28 shows a diagram of the merging procedure. Each Z/γ^* event is matched with one or more single photon events, and variables from the single photon event replace the associated variables in the Z/γ^* event. When multiple single photon events are matched to a Z/γ^* event the Z/γ^* event is replicated for each matched single photon event producing multiple output events per input event. The output events are identical to the input events except that some variables are replaced with variables from a single photon event. Therefore in a simulated Z/γ^* event a variable such as E_T^{miss} is “fixed” by replacing it with the E_T^{miss} in a single photon event that is properly matched to the Z/γ^* event. The output sample can be used exactly as the input sample is.

Merging can only occur between matched events. The matching criteria require that the photon p_T and η closely match the p_T and η of the reconstructed Z/γ^* system. In this case a simple binned matching is used, but different matching schemes can be explored. The p_T matching achieves the p_T^γ weighting as in the basic single photon method. The η matching also weights the photon η distribution to match the dilepton η distribution. The η weight was not used in the basic method

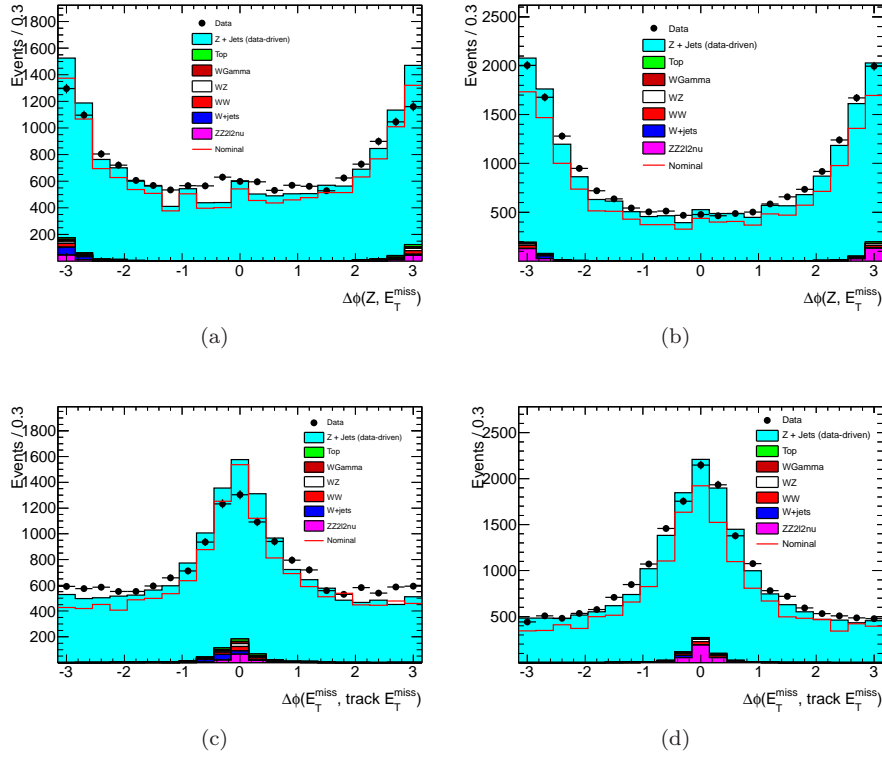


Figure 11.26: Distributions of $\Delta\phi(Z, E_T^{\text{miss}})$ (a-b) and $\Delta\phi(E_T^{\text{miss}}, E_T^{\text{miss, track}})$ (c-d) for the ee (a,c) and $\mu\mu$ (b, d) channels with the $\Delta\phi(Z, E_T^{\text{miss}})$ correction. The correction brings both distributions into good agreement with the data. Although the $\Delta\phi(E_T^{\text{miss}}, E_T^{\text{miss, track}})$ distribution is not weighted, it is correlated with $\Delta\phi(Z, E_T^{\text{miss}})$ so that it too agrees after the correction.

because the η distribution has little correlation with the variables that can be modeled. The extend method, however, requires a more careful event matching. Matching is not performed in ϕ because the detector is fairly symmetric in ϕ . Instead, all objects in the matched single photon events are rotated such that the ϕ component of the photon vector is the same as the ϕ component of the dilepton vector. The matching is additionally performed in jet bins. The p_T distribution is correlated with the number of jets in the event. To ensure that the events are properly matched, single photon events should only be matched to Z/γ^* events that have the same number of reconstructed jets. Many analyses require a jet veto. In this case the merging should only occur between events that have no reconstructed jets. For each of the matched single photon events a new output event is created by copying the full simulated Z event. Then, all variables that are to be modeled using the single photon method are replaced with those from the single photon event. Specific merging procedures are required for some variables; a few cases will be considered below. The replicated and modified Z event is then saved as part of the output sample. It is important to note that

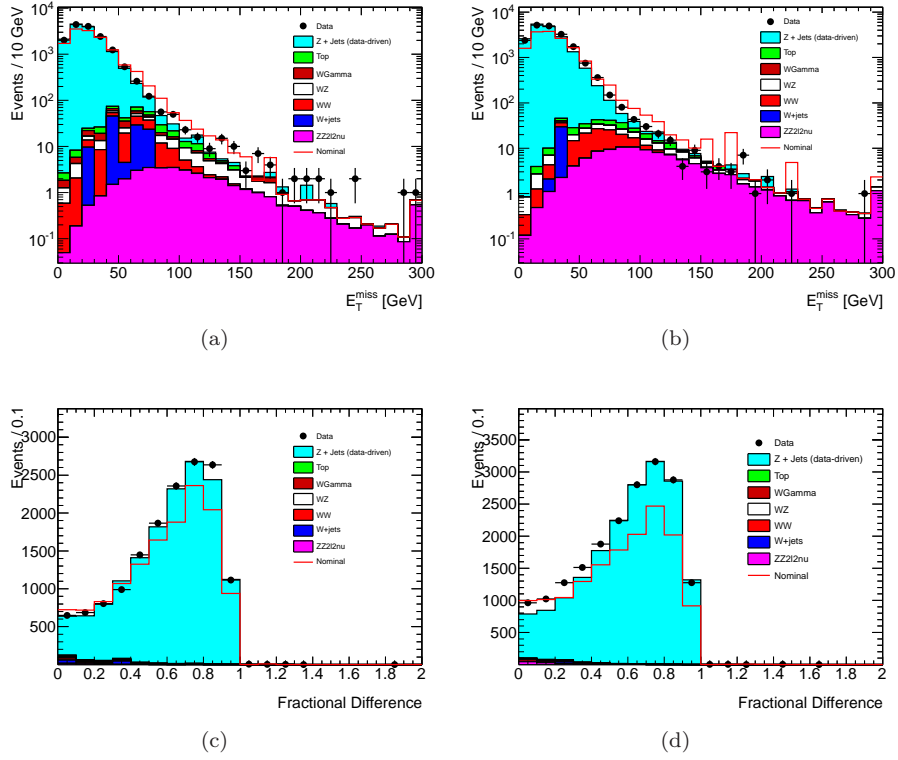


Figure 11.27: Distributions of E_T^{miss} for the ee (a) and $\mu\mu$ (b) channels and fractional p_T difference for the ee (c) and $\mu\mu$ (d) channels.

this merging procedure will create more output dilepton events than input dilepton events. The output events receive an additional event weight that corrects the normalization so that the output sample represents the same number of events as the input sample. In addition individual events in the output dilepton sample cannot be assumed to be statistically independent and a bootstrapping procedure must be used to evaluate the statistical uncertainty.

When variables are merged they must be translated from the single photon event to the Z/γ^* event. Some variables are straightforward, but some require specific procedures for their calculation. A selection of variables with their merging procedures are,

- E_T^{miss} – the full E_T^{miss} vector is replaced
- $E_T^{\text{miss,rel}}$ – the full E_T^{miss} vector and all jets are taken from the single photon event and the reconstructed lepton four-vectors in the dilepton event are used for the angular component of $E_T^{\text{miss,rel}}$. It is important to note that this calculation does not preserve lepton mismeasurements. When the E_T^{miss} vector is replaced from the single photon event the effects on E_T^{miss} from lepton mismeasurement are lost. However the lepton mismeasurement is rarely the cause

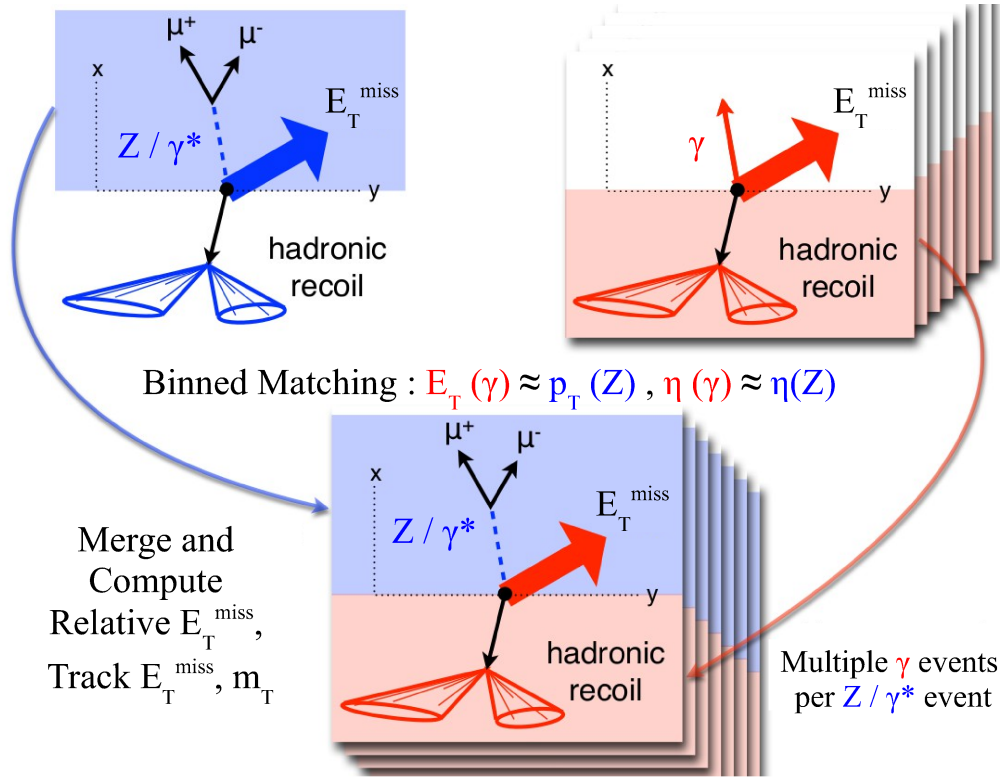


Figure 11.28: Schematic of the merging procedure for a single dilepton event. The dilepton event is shown in blue at the top left with the lepton, E_T^{miss} , and hadronic recoil components labeled. A set of single photon events that have been matched such that the photon p_T and η are close to the dilepton p_T and η are shown in red at the top right. At the bottom the lepton information from the dilepton event is combined with the E_T^{miss} and hadronic recoil from each single photon event. These merged events are saved and replace the nominal Z/γ^* simulation.

of mismeasured E_T^{miss} and in the signal regions suited for this method the E_T^{miss} often points away from the leptons.

- Jets – All jets in the dilepton event are replaced with those from the photon event. Generally jet kinematics are well modeled in the photon sample, but if it is found that some kinematics are not well modeled the jets can instead be used from the Z/γ^* simulation.
- Track E_T^{miss} – All tracks except for those associated to leptons are taken from the single photon event. If the photon is converted, the tracks associated with the photon are excluded
- Transverse mass (m_T) – This variable measures the transverse component of the mass of the dilepton + E_T^{miss} system. The E_T^{miss} vector is taken from the photon event and the leptons are taken from the dilepton event.

The non-single photon contributions to the inclusive photon sample must be subtracted as in

the basic method. To implement the subtraction the backgrounds to the inclusive photon sample must also be merged with the Z/γ^* simulation. Merging single photon simulation follows the same procedure as for single photon data except that the event weight is negated. The output Z/γ^* sample that is merged with the single photon simulation is appended to the output Z/γ^* sample that is merged with single photon data. The full merged sample therefore includes both the single photon data and single photon simulation with a negative weight.

The cut efficiency of any variables that are modeled is simply determined by applying the cut to the merged sample. The final background estimate is given by the number of events remaining in the merged sample after all cuts. A complication of the merged sample, however, is that the statistical uncertainty is not simply the square root of the number of events. Instead, a bootstrapping procedure must be used to evaluate the statistical uncertainty. The merged Z/γ^* sample is divided into subsamples. The final background estimate is determined from each subsample and the statistical variation among the samples gives the statistical uncertainty on the final result. Systematic uncertainties are the same as in the basic method and are applied to the final background estimate.

11.4.1 Application – $H \rightarrow WW$

The extended single photon method was developed for the $H \rightarrow WW$ search described in Section 9.2. This method was in fact applied to a newer version of the analysis that included a fraction of the data from the 2012 run. The analysis uses the $E_T^{\text{miss,rel}}$ variable to remove the Z/γ^* background which requires the extended method. An additional cut is applied on a hadronic recoil variable to achieve more Z/γ^* rejection. A fit in bins of m_T is used as the final discriminating variable in the analysis. It is therefore necessary that the Z/γ^* background estimate predicts a shape for the background. The extended single photon method is ideal to estimate this difficult background.

The merging procedure is implemented as described above. The variables that are to be modeled are $E_T^{\text{miss,rel}}$, Track E_T^{miss} , and a hadronic recoil variable, $fRecoil$, which measures the momenta of tracks recoiling from the dilepton system. It is the vector sum of the momenta of tracks that originate from the primary vertex and lie within a 45 degree azimuthal slice centered exactly opposite to the $p_T^{\ell\ell}$ vector. Figures 11.29 and 11.30 show the E_T^{miss} and $E_T^{\text{miss,rel}}$ distributions where $Z + \text{jets}$ distribution is modeled using this method. All event cuts are applied except for $E_T^{\text{miss,rel}}$ track E_T^{miss} , $fRecoil$, and m_T . However the analysis was blinded and certain blinding criteria were applied to remove the signal region. The shape of the E_T^{miss} and $E_T^{\text{miss,rel}}$ distributions are altered by blinding cuts, but the $Z + \text{jets}$ distribution reproduces it well. Good agreement between the data and $Z + \text{jets}$ prediction in the ee channel is observed. The agreement in the $\mu\mu$ channel is poorer than in the ee channel. The reason for the discrepancy is in the difference in the momentum resolution between

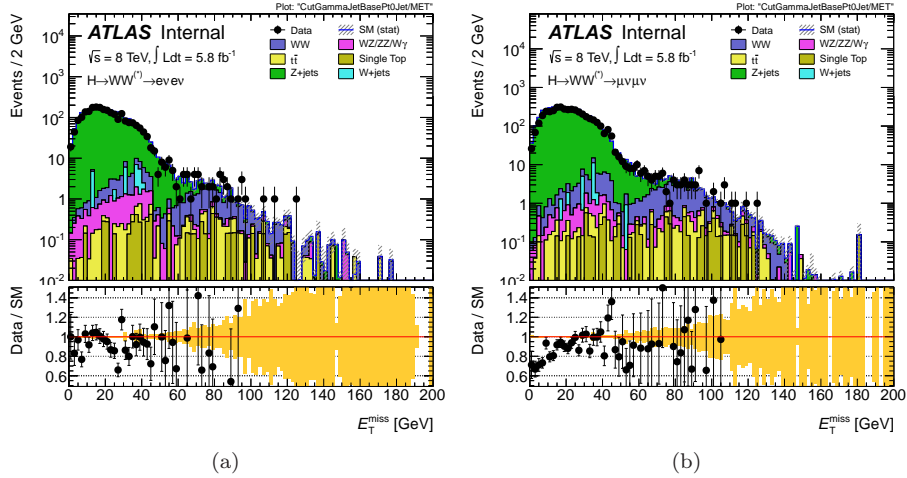


Figure 11.29: E_T^{miss} distributions in the ee (a) and $\mu\mu$ channels (b). The Z + jets histogram is the prediction from the extended single photon method. All other processes are estimated using simulation. The blinding criteria shapes the E_T^{miss} distribution, but the Z + jets model shows good agreement with the data over the full distribution.

photons and muons. This problem was also addressed in Section 11.3.14 in the implementation of the basic method for the $ZZ \rightarrow \ell^+ \ell^- \nu \bar{\nu}$ analysis. The muon momentum resolution tends to have larger tails than the photon momentum resolution. Therefore single photon model does not correctly represent the muon momentum resolution and the model predicts a slightly narrower E_T^{miss} distribution. This is not an issue in the ee channel because electrons and photons are very similar objects. The $E_T^{\text{miss,rel}}$ variable is intended to be insensitive to lepton mismeasurements, but a discrepancy is observed in $E_T^{\text{miss,rel}}$ distribution of the $\mu\mu$ channel as well. This discrepancy is expected because when the samples are merged, lepton mismeasurements are not preserved in the E_T^{miss} since it is replaced with the E_T^{miss} in a single photon event. Therefore $E_T^{\text{miss,rel}}$ suffers from the discrepancy as well. Figures 11.31 and 11.32 show the $fRecoil$ and track E_T^{miss} distributions. In both distributions the Z + jet model shows some disagreement with the data. The shape of $fRecoil$ is not correctly produced and the track E_T^{miss} distribution is over estimated at large values of track E_T^{miss} . These discrepancies are attributed to the inefficiency to reconstruct the correct primary vertex in single photon events. In the cases when the incorrect primary vertex is selected the tracks from a min-bias event are used instead of those from the hard scatter. The solution to this problem is to use converted photons to improve the vertex finding efficiency. Figure 11.33 shows the m_T distribution, the final discriminating variable in the analysis. The ee channel has good agreement and the $\mu\mu$ channel has some disagreement because it depends on E_T^{miss} which has a disagreement in the $\mu\mu$ channel.

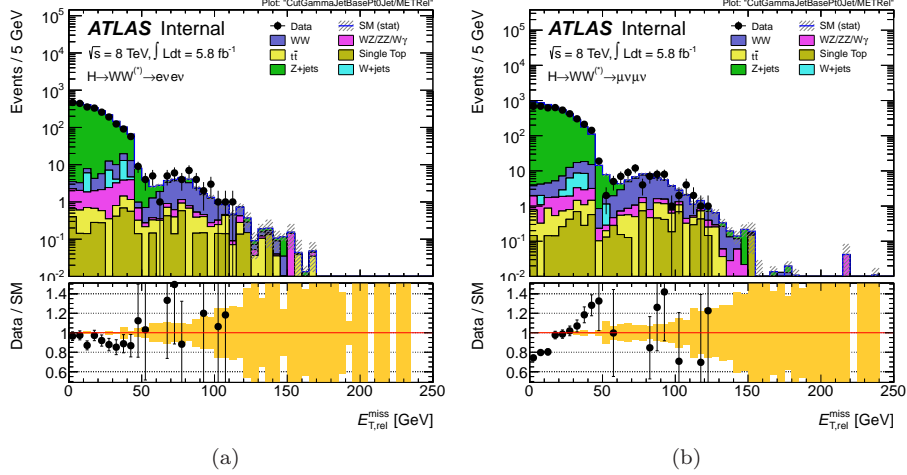


Figure 11.30: $E_T^{\text{miss,rel}}$ distributions in the ee (a) and $\mu\mu$ (b) channels. The $Z + \text{jets}$ histogram is the prediction from the extended single photon method. All other processes are estimated using simulation. The blinding criteria shapes the $E_T^{\text{miss,rel}}$ distribution, but the $Z + \text{jets}$ model shows good agreement with the data over the full distribution.

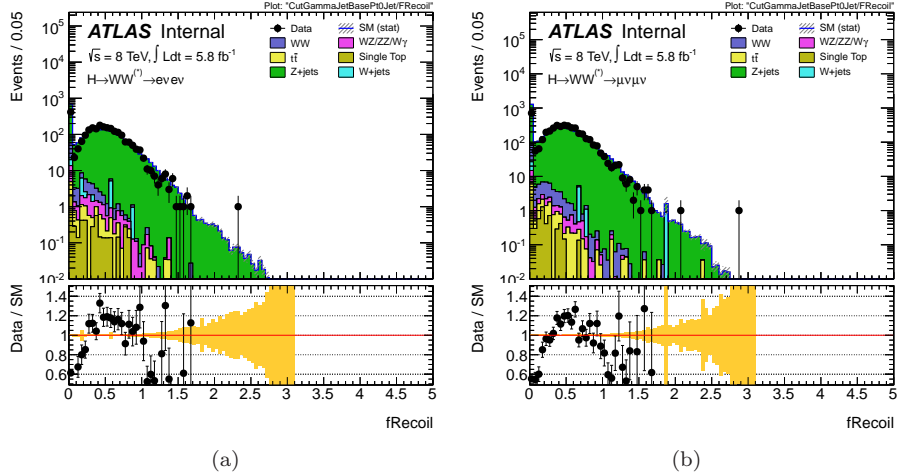


Figure 11.31: $fRecoil$ distributions in the ee (a) and $\mu\mu$ (b) channels. The $Z + \text{jets}$ histogram is the prediction from the extended single photon method. All other processes are estimated using simulation. The shape of the modeled $fRecoil$ distribution has some disagreement with the data. At small values of $fRecoil$ the model predicts too many events and at large values of $fRecoil$. This discrepancy is attributed to the inefficiency to reconstruct the correct primary vertex in single photon events described in Section 11.3.11.

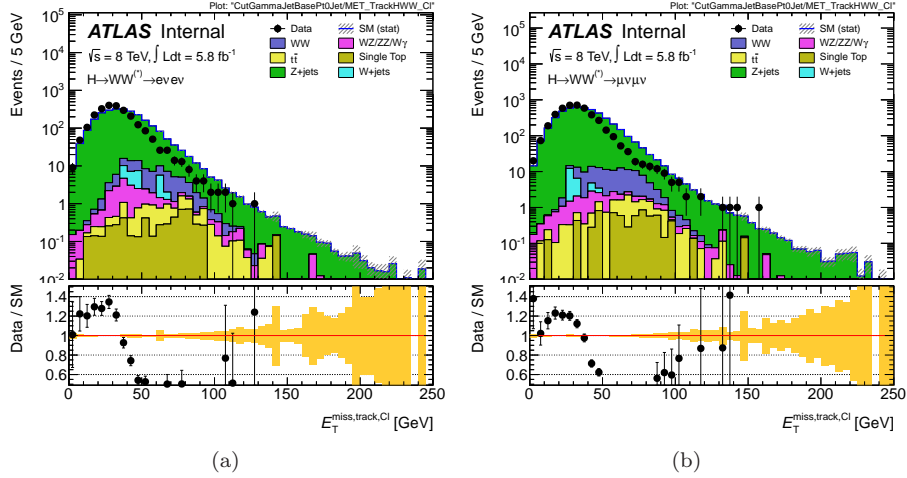


Figure 11.32: Track E_T^{miss} distributions in the ee (a) and $\mu\mu$ (b) channels. The $Z + \text{jets}$ histogram is the prediction from the extended single photon method. All other processes are estimated using simulation. The shape of the modeled track E_T^{miss} distribution disagrees with the data at large values of track E_T^{miss} . This discrepancy is attributed to the inefficiency to reconstruct the correct primary vertex in single photon events described in Section 11.3.11.

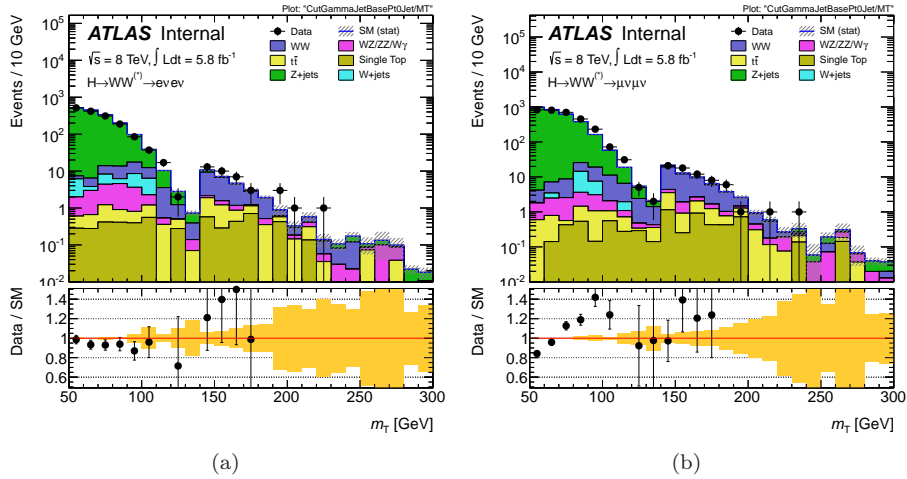


Figure 11.33: m_T distributions in the ee (a) and $\mu\mu$ (b) channels. The $Z + \text{jets}$ histogram is the prediction from the extended single photon method. All other processes are estimated using simulation. The blinding criteria shapes the m_T distribution, but the $Z + \text{jets}$ model shows good agreement with the data over the full distribution.

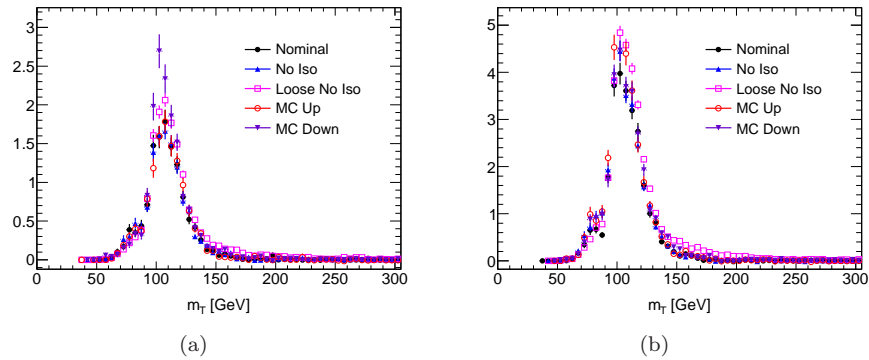


Figure 11.34: The predicted $Z + \text{jet } m_T$ distribution using the extended single photon method in the ee and $\mu\mu$ channels. The distributions from two variations of two systematic sources are shown. The No Iso and Loose No Iso distributions show the predictions of the m_T for dijet enriched events. The No Iso distribution uses photons that pass the `tight` identification criteria, but no isolation cut is applied. The Loose No Iso distribution is further enriched in dijet events by using `loose` photons with no isolation cut. The MC Up and MC Down entries account for the variation of the simulation within its uncertainties.

An advantage of using the single photon method is that the m_T shape is predicted with more statistics than in simulation. The final m_T distribution is shown in Figure 11.34 with the predictions from systematic variations included. The sources of uncertainty considered are dijet contamination and the subtraction of single photon backgrounds using simulation. The systematic uncertainty from dijet contamination is evaluated by using photons that are `tight`, but not isolated and photons that `loose` and not isolated. The uncertainty on the subtraction is evaluated by varying the prediction from simulation up and down within the cross section uncertainties. The method to determine the statistical uncertainty was described above in Section 11.4. The merging is done in five independent and randomized samples. The results from the different measurements are compared and the largest variation between the samples is a conservative estimate of the statistical uncertainty in the nominal estimate. Figure 11.35 shows the prediction from the five independent samples.

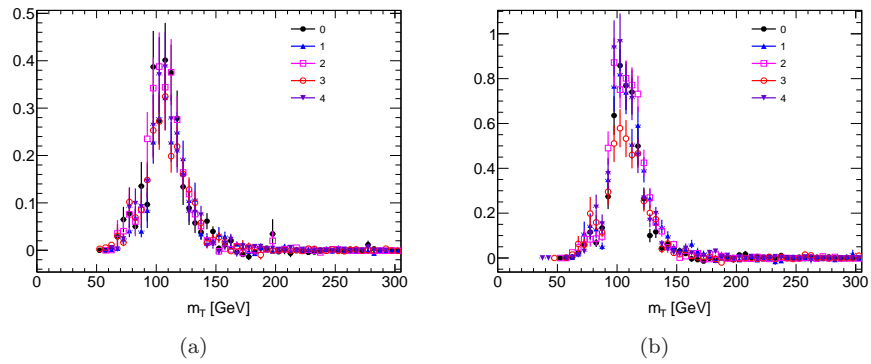


Figure 11.35: Determination of the statistical uncertainty of the $Z + \text{jets}$ prediction using the bootstrapping method. The nominal sample is divided into five equally sized and random samples. The m_T distribution is predicted separately from each sample. The maximum variation between the samples is a conservative estimate of the statistical uncertainty.

CHAPTER 12

Conclusions

This dissertation presented measurements of the WW cross section, the ZZ cross section, a search for the Higgs boson in the WW decay channel, and a search for invisible decays of the Higgs boson. All of these analyses were performed in final states having two leptons and E_T^{miss} . A common issue among dilepton + E_T^{miss} signatures is rejecting the Z/γ^* background and estimating its contamination in the signal region. Special attention was given to studies of fake E_T^{miss} and in estimating the Z/γ^* background.

The WW cross section was measured in the fully leptonic final state to be $40_{-16}^{+20}(\text{stat.}) \pm 7(\text{syst.})\text{pb}$ using 34 pb^{-1} of data recorded at $\sqrt{s} = 7 \text{ TeV}$, in agreement with the theoretical expectation. The ZZ cross section was measured in the $\ell\ell\nu\nu$ final state to be $5.7_{-1.3}^{+1.4}(\text{stat.})_{-0.6}^{+0.7}(\text{syst.}) \pm 0.1(\text{lumi})\text{pb}$ using 4.6 fb^{-1} of data recorded at $\sqrt{s} = 7 \text{ TeV}$. The result agrees well with theoretical expectations as well as the measured cross section in the $\ell\ell\ell\ell$ final state. The cross section was also measured in bins of $p_T^{\ell\ell}$, $\Delta\phi(\ell, \ell)$, and m_T unfolded to the generator level. Limits were placed on anomalous triple gauge couplings which are much more stringent than previous limits.

The discovery of the Higgs boson fulfilled a principle goal of the LHC and marked a major milestone in particle physics. An overview of the discovery of the Higgs boson was given and a search for the Higgs boson in the WW decay channel using 4.6 fb^{-1} of data taken at $\sqrt{s} = 7 \text{ TeV}$ was presented. At that stage a discovery of a $m_H = 125 \text{ GeV}$ Higgs boson was not possible, but the WW channel excluded a large range of Higgs masses between $130 \text{ GeV} < m_H < 260 \text{ GeV}$ with 95% confidence.

The final analysis presented a search for invisible decays of the Higgs boson. This analysis uses the newly discovered Higgs boson to search for new physics that could enhance its invisible branching fraction. The analysis uses 13.1 fb^{-1} of data taken at $\sqrt{s} = 8 \text{ TeV}$ and 4.6 fb^{-1} of data taken at $\sqrt{s} = 7 \text{ TeV}$. No excess of events were observed and a limit of 65% is placed on the invisible branching fraction of a Standard Model Higgs boson having $m_h = 125 \text{ GeV}$. One possible cause of an enhanced invisible branching fraction is decays to dark matter. A Higgs portal model is used to translate the invisible branching fraction limit into a limit on dark matter mass and cross section. The model makes a simple, ad-hoc extension to the Standard Model by including one additional particle (the dark matter particle) that interacts only with the Higgs boson. Because the nature of dark matter is not known, limits are determined for scalar, vector, and majorana fermion dark matter. The limit on the coupling between dark matter and the Higgs boson is compared to the limits from dark matter direct detection experiments. We find that limits from the invisible branching fraction add significant exclusion dark matter having a mass below 10 GeV where direct detection experiments do not reach. Therefore we conclude that the dark matter particle cannot have a strong interaction with the Higgs boson over most of the viable mass range considered for dark matter particles. This

constraint indicates that the dark matter particle must couple to Standard Model by some more complicated mechanism that is yet to be determined.

Given that evidence for dark matter has not yet been found at the LHC, the future prospects for dark matter detection are important. The LHC will soon take data at a higher center of mass energy and will collect much more data. The additional data will allow for more stringent limits on the invisible branching fraction of the Higgs boson. Additional channels will also contribute to the invisible branching fraction limits. The VBF channel has a higher production rate and will provide a more stringent limit than the associated production channel. Improvements can be made to the ZH channel presented here as well. In the ZH channel the dominant systematic uncertainty is on the normalization of the standard model ZZ background. This background is estimated using simulation which has an uncertainty of 11%. In order to place more stringent limits on the invisible branching fraction of the Higgs boson this uncertainty must be reduced. One possibility is to use $Z\gamma$ events as a proxy to ZZ events, much like how single photon events are used to estimate the Z/γ^* background as described in Chapter 11. Such improvements will allow for much stronger constraints on the invisible branching fraction of the Higgs boson.

Bibliography

- [1] Particle Data Group Collaboration, J. Beringer et al., *Review of Particle Physics*, *Phys. Rev. D* **86** (2012) 010001. [3.1](#), [3.4](#), [3.5](#), [8.1](#), [8.1.4](#), [8.7](#), [11.3.14](#)
- [2] T. A. Collaboration, *Combined measurements of the mass and signal strength of the Higgs-like boson with the ATLAS detector using up to 25 fb⁻¹ of proton-proton collision data*, Tech. Rep. ATLAS-CONF-2013-014, CERN, Geneva, Mar, 2013. [3.1](#)
- [3] LEP Working Group for Higgs boson searches, ALEPH, DELPHI, L3, OPAL Collaboration, R. Barate et al., *Search for the standard model Higgs boson at LEP*, *Phys.Lett.* **B565** (2003) 61–75, [arXiv:hep-ex/0306033](#) [hep-ex]. [3.1](#)
- [4] M. Baak, M. Goebel, J. Haller, A. Hoecker, D. Kennedy, et al., *The Electroweak Fit of the Standard Model after the Discovery of a New Boson at the LHC*, *Eur.Phys.J.* **C72** (2012) 2205, [arXiv:1209.2716](#) [hep-ph]. [3.1](#), [3.1](#)
- [5] ALEPH, DELPHI, L3, OPAL, SLD, LEP Electroweak Working Group, SLD Electroweak Group, SLD Heavy Flavour Group Collaboration, S. Schael et al., *Precision electroweak measurements on the Z resonance*, *Phys.Rept.* **427** (2006) 257–454, [arXiv:hep-ex/0509008](#) [hep-ex]. [3.1](#)
- [6] ALEPH, DELPHI, L3, OPAL, LEP Electroweak Working Group Collaboration, S. Schael et al., *Electroweak Measurements in Electron-Positron Collisions at W-Boson-Pair Energies at LEP*, [arXiv:1302.3415](#) [hep-ex]. [3.1](#)
- [7] MuLan Collaboration, D. Webber et al., *Measurement of the Positive Muon Lifetime and Determination of the Fermi Constant to Part-per-Million Precision*, *Phys.Rev.Lett.* **106** (2011) 041803, [arXiv:1010.0991](#) [hep-ex]. [3.1](#)
- [8] G. Altarelli and G. Parisi, *Asymptotic Freedom in Parton Language*, *Nucl.Phys.* **B126** (1977) 298. [3.3](#)
- [9] Y. L. Dokshitzer, *Calculation of the Structure Functions for Deep Inelastic Scattering and e+ e- Annihilation by Perturbation Theory in Quantum Chromodynamics.*, *Sov.Phys.JETP* **46** (1977) 641–653. [3.3](#)
- [10] V. Gribov and L. Lipatov, *Deep inelastic e p scattering in perturbation theory*, *Sov.J.Nucl.Phys.* **15** (1972) 438–450. [3.3](#)
- [11] A. Martin, W. Stirling, R. Thorne, and G. Watt, *Parton distributions for the LHC*, *Eur.Phys.J.* **C63** (2009) 189–285, [arXiv:0901.0002](#) [hep-ph]. [3.4](#), [8.1.5](#)

- [12] S. Tavernier, *Experimental Techniques in Nuclear and Particle Physics*. Springer, 2010. 3.4
- [13] V. Balashov, *Interaction of Particles and Radiation with Matter*. Springer, 1993. 3.4
- [14] S. Meroli, D. Passeri, and L. Servoli, *Energy loss measurement for charged particles in very thin silicon layers*, *Journal of Instrumentation* **6** (2011) no. 06, P06013. <http://stacks.iop.org/1748-0221/6/i=06/a=P06013>. 3.4, 3.4.1
- [15] V. C. Rubin and W. K. Ford, Jr., *Rotation of the Andromeda Nebula from a Spectroscopic Survey of Emission Regions*, *The Astrophysical Journal* **159** (1970) 379. 4.2
- [16] T. S. van Albada, J. N. Bahcall, K. Begeman, and R. Sancisi, *Distribution of dark matter in the spiral galaxy NGC 3198*, *The Astrophysical Journal* **295** (1985) 305–313. 4.2
- [17] D. M. Wittman, J. A. Tyson, D. Kirkman, I. Dell’Antonio, and G. Bernstein, *Detection of weak gravitational lensing distortions of distant galaxies by cosmic dark matter at large scales*, *Nature* **405**, 2000/05/11/print. <http://dx.doi.org/10.1038/35012001>. 4.2
- [18] A. N. Taylor, S. Dye, T. J. Broadhurst, N. Bentez, and E. van Kampen, *Gravitational Lens Magnification and the Mass of Abell 1689*, *The Astrophysical Journal* **501** (1998) no. 2, 539. <http://stacks.iop.org/0004-637X/501/i=2/a=539>. 4.2
- [19] K. Garrett and G. Duda, *Dark Matter: A Primer*, *Adv.Astron.* **2011** (2011) 968283, [arXiv:1006.2483 \[hep-ph\]](https://arxiv.org/abs/1006.2483). 4.2, 4.3
- [20] N. Jarosik, C. L. Bennett, J. Dunkley, B. Gold, M. R. Greason, M. Halpern, R. S. Hill, G. Hinshaw, A. Kogut, E. Komatsu, D. Larson, M. Limon, S. S. Meyer, M. R. Nolte, N. Odegard, L. Page, K. M. Smith, D. N. Spergel, G. S. Tucker, J. L. Weiland, E. Wollack, and E. L. Wright, *Seven-year Wilkinson Microwave Anisotropy Probe (WMAP) Observations: Sky Maps, Systematic Errors, and Basic Results*, *The Astrophysical Journal* **192** (2011) 14, [arXiv:1001.4744 \[astro-ph.CO\]](https://arxiv.org/abs/1001.4744). 4.2
- [21] XENON100 Collaboration, E. Aprile et al., *Dark Matter Results from 225 Live Days of XENON100 Data*, *Phys.Rev.Lett.* **109** (2012) 181301, [arXiv:1207.5988 \[astro-ph.CO\]](https://arxiv.org/abs/1207.5988). 4.3.1, 4.4
- [22] XENON10 Collaboration, J. Angle et al., *Constraints on inelastic dark matter from XENON10*, *Phys.Rev.* **D80** (2009) 115005, [arXiv:0910.3698 \[astro-ph.CO\]](https://arxiv.org/abs/0910.3698). 4.3.1
- [23] CDMS-II, CDMS Collaboration, Z. Ahmed et al., *Search for inelastic dark matter with the CDMS II experiment*, *Phys.Rev.* **D83** (2011) 112002, [arXiv:1012.5078 \[astro-ph.CO\]](https://arxiv.org/abs/1012.5078). 4.3.1
- [24] EDELWEISS Collaboration, E. Armengaud et al., *Final results of the EDELWEISS-II WIMP search using a 4-kg array of cryogenic germanium detectors with interleaved electrodes*, *Phys.Lett.* **B702** (2011) 329–335, [arXiv:1103.4070 \[astro-ph.CO\]](https://arxiv.org/abs/1103.4070). 4.3.1
- [25] EDELWEISS Collaboration, E. Armengaud et al., *A search for low-mass WIMPs with EDELWEISS-II heat-and-ionization detectors*, *Phys.Rev.* **D86** (2012) 051701, [arXiv:1207.1815 \[astro-ph.CO\]](https://arxiv.org/abs/1207.1815). 4.3.1
- [26] D. Y. Akimov, H. Araujo, E. Barnes, V. Belov, A. Bewick, et al., *WIMP-nucleon cross-section results from the second science run of ZEPLIN-III*, *Phys.Lett.* **B709** (2012) 14–20, [arXiv:1110.4769 \[astro-ph.CO\]](https://arxiv.org/abs/1110.4769). 4.3.1
- [27] E. Behnke, J. Behnke, S. Brice, D. Broemmelsiek, J. Collar, et al., *Improved Limits on Spin-Dependent WIMP-Proton Interactions from a Two Liter CF₃I Bubble Chamber*, *Phys.Rev.Lett.* **106** (2011) 021303, [arXiv:1008.3518 \[astro-ph.CO\]](https://arxiv.org/abs/1008.3518). 4.3.1

- [28] M. Felizardo, T. Girard, T. Morlat, A. Fernandes, A. Ramos, et al., *Final Analysis and Results of the Phase II SIMPLE Dark Matter Search*, *Phys.Rev.Lett.* **108** (2012) 201302, [arXiv:1106.3014 \[astro-ph.CO\]](#). 4.3.1
- [29] G. Angloher, M. Bauer, I. Bavykina, A. Bento, C. Bucci, et al., *Results from 730 kg days of the CRESST-II Dark Matter Search*, *Eur.Phys.J.* **C72** (2012) 1971, [arXiv:1109.0702 \[astro-ph.CO\]](#). 4.3.1
- [30] DAMA, LIBRA Collaboration, R. Bernabei et al., *New results from DAMA/LIBRA*, *Eur.Phys.J.* **C67** (2010) 39–49, [arXiv:1002.1028 \[astro-ph.GA\]](#). 4.3.1
- [31] C. Aalseth, P. Barbeau, J. Colaresi, J. Collar, J. Diaz Leon, et al., *Search for an Annual Modulation in a P-type Point Contact Germanium Dark Matter Detector*, *Phys.Rev.Lett.* **107** (2011) 141301, [arXiv:1106.0650 \[astro-ph.CO\]](#). 4.3.1
- [32] CDMS Collaboration, R. Agnese et al., *Dark Matter Search Results Using the Silicon Detectors of CDMS II*, *Phys.Rev.Lett.* (2013) , [arXiv:1304.4279 \[hep-ex\]](#). 4.3.1, 4.4
- [33] AMS Collaboration, M. Aguilar et al., *First Result from the Alpha Magnetic Spectrometer on the International Space Station: Precision Measurement of the Positron Fraction in Primary Cosmic Rays of 0.5–350 GeV*, *Phys. Rev. Lett.* **110** (2013) 141102. <http://link.aps.org/doi/10.1103/PhysRevLett.110.141102>. 4.3.2, 4.5
- [34] PAMELA Collaboration, O. Adriani et al., *An anomalous positron abundance in cosmic rays with energies 1.5–100 GeV*, *Nature* **458** (2009) 607–609, [arXiv:0810.4995 \[astro-ph\]](#). 4.3.2, 4.5
- [35] Fermi LAT Collaboration, M. Ackermann et al., *Measurement of Separate Cosmic-Ray Electron and Positron Spectra with the Fermi Large Area Telescope*, *Phys. Rev. Lett.* **108** (2012) 011103. <http://link.aps.org/doi/10.1103/PhysRevLett.108.011103>. 4.3.2, 4.5
- [36] ATLAS Collaboration, G. Aad et al., *Search for dark matter candidates and large extra dimensions in events with a photon and missing transverse momentum in pp collision data at $\sqrt{s} = 7$ TeV with the ATLAS detector*, *Phys.Rev.Lett.* **110** (2013) 011802, [arXiv:1209.4625 \[hep-ex\]](#). 4.3.3
- [37] CMS Collaboration, S. Chatrchyan et al., *Search for Dark Matter and Large Extra Dimensions in pp Collisions Yielding a Photon and Missing Transverse Energy*, *Phys.Rev.Lett.* **108** (2012) 261803, [arXiv:1204.0821 \[hep-ex\]](#). 4.3.3
- [38] ATLAS Collaboration, G. Aad et al., *Search for dark matter candidates and large extra dimensions in events with a jet and missing transverse momentum with the ATLAS detector*, *JHEP* **1304** (2013) 075, [arXiv:1210.4491 \[hep-ex\]](#). 4.3.3
- [39] CMS Collaboration, S. Chatrchyan et al., *Search for dark matter and large extra dimensions in monojet events in pp collisions at $\sqrt{s} = 7$ TeV*, *JHEP* **1209** (2012) 094, [arXiv:1206.5663 \[hep-ex\]](#). 4.3.3
- [40] A. Djouadi, O. Lebedev, Y. Mambrini, and J. Quevillon, *Implications of LHC searches for Higgs–portal dark matter*, *Phys.Lett.* **B709** (2012) 65–69, [arXiv:1112.3299 \[hep-ph\]](#). 4.4, 4.4
- [41] L. Lopez-Honorez, T. Schwetz, and J. Zupan, *Higgs portal, fermionic dark matter, and a Standard Model like Higgs at 125 GeV*, *Phys.Lett.* **B716** (2012) 179–185, [arXiv:1203.2064 \[hep-ph\]](#). 4.4
- [42] P. J. Fox, R. Harnik, J. Kopp, and Y. Tsai, *Missing Energy Signatures of Dark Matter at the LHC*, *Phys.Rev.* **D85** (2012) 056011, [arXiv:1109.4398 \[hep-ph\]](#). 4.4

- [43] O. S. Brning, P. Collier, P. Lebrun, S. Myers, R. Ostojic, J. Poole, and P. Proudlock, *LHC Design Report*. CERN, Geneva, 2004. [5](#)
- [44] C. Hill, K. Prelec, and M. Weiss, *Design of the preinjector for the CERN RFQ2 project*, Tech. Rep. CERN-PS-88-72-HI. CERN-PS-HI-88-72, CERN, Geneva, 1988. [5.2](#)
- [45] Stokes, Richard and Wangler, Thomas, *Radiofrequency Quadrupole Accelerators and their applications*, Ann. Rev. Nucl. Part. Sci **38** (1988) 97–118. [5.2](#)
- [46] M. Weiss, *The RFQ2 complex: The future injector to CERN Linac 2*, Conf.Proc. C920324 (1992) 539–541. [5.2](#)
- [47] A. Feschenko, C. Hill, A. Lombardi, A. Liou, R. Scrivens, et al., *Tests of the CERN proton linac performance for LHC-type beams*, tech. rep., CERN, 2000. [5.2](#)
- [48] B. Mikulec, A. Blas, C. Carli, A. Findlay, K. Hanke, G. Rumolo, and J. Tan, *LHC Beams from the CERN PS Booster*, Tech. Rep. CERN-ATS-2009-070, CERN, May, 2009. [5.2](#)
- [49] M. Barnes, M. Benedikt, E. W. Blackmore, A. Blas, J. Borburgh, R. Cappi, M. Chanel, V. Chohan, F. Cifarelli, G. Clark, G. Daems, L. R. Evans, A. B. Fowler, R. Garoby, J. Gonzalez, D. G. Grier, J. Gruber, S. Hancock, C. E. Hill, A. Jansson, E. Jensen, S. R. Koscielniak, A. Krusche, R. Losito, P. Maesen, F. Mammarella, K. D. Metzmacher, A. Mitra, J. Olsfors, M. Paoluzzi, J. Pedersen, R. Poirier, U. Raich, K. W. Reiniger, T. C. Ries, J. P. Riunaud, J. P. Royer, M. Sassowsky, K. Schindl, H. O. Schnauer, L. Sermeus, M. Thivent, H. M. Ullrich, W. Van Cauter, M. Vretenar, and F. V. Vlker, *The PS complex as proton pre-injector for the LHC: design and implementation report*, tech. rep., CERN, Geneva, 2000. [5.2](#)
- [50] M. Benedikt, A. Blas, J. Borburgh, R. Cappi, M. Chanel, V. Chohan, G. Cyvoct, R. Garoby, D. G. Grier, J. Gruber, S. Hancock, C. E. Hill, E. Jensen, A. Krusche, M. Lindroos, E. Mtral, G. Mtral, K. D. Metzmacher, J. Olsfors, F. Pedersen, U. Raich, J. P. Riunaud, J. P. Royer, M. Sassowsky, K. Schindl, H. O. Schnauer, M. Thivent, H. M. Ullrich, F. V. Vlker, M. Vretenar, M. Barnes, E. W. Blackmore, F. Cifarelli, G. Clark, F. Jones, S. R. Koscielniak, F. Mammarella, A. Mitra, R. Poirier, K. W. Reiniger, and T. C. Ries, *The PS complex produces the nominal LHC beam*, Tech. Rep. CERN-PS-2000-039-OP, CERN, Jul, 2000. [5.2](#)
- [51] G. Arduini, P. Baudrenghien, T. Bohl, P. Collier, K. Cornelis, W. Hfle, T. P. R. Linnecar, E. Shaposhnikova, J. Tckmantel, and J. Wenninger, *Status of the LHC proton beam in the CERN SPS*, Tech. Rep. CERN-SL-2002-054-OP, CERN, Jun, 2002. [5.2](#)
- [52] ATLAS Collaboration, G. Aad et al., *Improved luminosity determination in pp collisions at $\sqrt{s} = 7$ TeV using the ATLAS detector at the LHC*, [arXiv:1302.4393 \[hep-ex\]](#). [5.3](#)
- [53] G. Anders, N. Bacchetta, V. Balabara, C. Barschel, D. Belohrad, D. Berge, H. Burkhardt, S. I. Cooper, M. Ferro-Luzzi, G. Franzoni, C. Gabaldon, M. Gagliardi, J. J. Gras, V. Halyo, B. Heinemann, P. Hopchev, A. Hunt, W. Kozanecki, S. Kwan, M. Ludwig, D. Marlow, P. Odier, S. Pagan Griso, J. Panman, T. Pauly, S. Thoulet, S. White, J. C. Yun, and M. Zanetti, *LHC Bunch Current Normalisation for the April-May 2010 Luminosity Calibration Measurements*, tech. rep., CERN, Feb, 2011. [5.3](#)
- [54] ATLAS Collaboration, *The ATLAS Experiment at the CERN Large Hadron Collider*, JINST **3** (2008) S08003. [6](#)
- [55] N. Vermes and G. Hallewel, *ATLAS pixel detector: Technical Design Report*. Technical Design Report ATLAS. CERN, Geneva, 1998. [6.1.1](#)

- [56] G. Aad et al., *ATLAS pixel detector electronics and sensors*, *Journal of Instrumentation* **3** (2008) no. 07, P07007. <http://stacks.iop.org/1748-0221/3/i=07/a=P07007>. 6.1.1
- [57] T. Cornelissen, M. Elsing, S. Fleischmann, W. Liebig, E. Moyses, and A. Salzburger, *Concepts, Design and Implementation of the ATLAS New Tracking (NEWT)*, Tech. Rep. ATL-SOFT-PUB-2007-007. ATL-COM-SOFT-2007-002, CERN, Geneva, Mar, 2007. 7.1
- [58] R. Frhwirth, *Application of Kalman filtering to track and vertex fitting*, *Nuclear Instruments and Methods in Physics Research Section A: Accelerators, Spectrometers, Detectors and Associated Equipment* **262** (1987) no. 23, 444 – 450. <http://www.sciencedirect.com/science/article/pii/0168900287908874>. 7.1
- [59] ATLAS Collaboration, G. Aad et al., *Expected Performance of the ATLAS Experiment - Detector, Trigger and Physics*, [arXiv:0901.0512 \[hep-ex\]](https://arxiv.org/abs/0901.0512). 7.2, 7.3, 7.4, 11.3.6
- [60] ATLAS Collaboration, G. Aad et al., *Electron performance measurements with the ATLAS detector using the 2010 LHC proton-proton collision data*, *Eur.Phys.J.* **C72** (2012) 1909, [arXiv:1110.3174 \[hep-ex\]](https://arxiv.org/abs/1110.3174). 7.3
- [61] T. A. Collaboration, *Improved electron reconstruction in ATLAS using the Gaussian Sum Filter-based model for bremsstrahlung*, Tech. Rep. ATLAS-CONF-2012-047, CERN, Geneva, May, 2012. 7.3
- [62] T. A. Collaboration, *Muon Momentum Resolution in First Pass Reconstruction of pp Collision Data Recorded by ATLAS in 2010*, Tech. Rep. ATLAS-CONF-2011-046, CERN, Geneva, Mar, 2011. 7.4
- [63] M. Cacciari, G. P. Salam, and G. Soyez, *The Anti-k(t) jet clustering algorithm*, *JHEP* **0804** (2008) 063, [arXiv:0802.1189 \[hep-ph\]](https://arxiv.org/abs/0802.1189). 7.5
- [64] T. A. Collaboration, *Properties of Jets and Inputs to Jet Reconstruction and Calibration with the ATLAS Detector Using Proton-Proton Collisions at $\sqrt{s} = 7$ TeV*, Tech. Rep. ATLAS-CONF-2010-053, CERN, Geneva, Jul, 2010. 7.5
- [65] T. A. Collaboration, *Jet energy scale and its systematic uncertainty in proton-proton collisions at $\sqrt{s} = 7$ TeV with ATLAS 2011 data*, Tech. Rep. ATLAS-CONF-2013-004, CERN, Geneva, Jan, 2013. 7.5
- [66] G. Aad et al., *Commissioning of the ATLAS high-performance b-tagging algorithms in the 7 TeV collision data*, Tech. Rep. ATLAS-CONF-2011-102, CERN, Geneva, Jul, 2011. 7.5
- [67] ATLAS Collaboration, G. Aad et al., *Performance of Missing Transverse Momentum Reconstruction in Proton-Proton Collisions at 7 TeV with ATLAS*, *Eur.Phys.J.* **C72** (2012) 1844, [arXiv:1108.5602 \[hep-ex\]](https://arxiv.org/abs/1108.5602). 7.7
- [68] G. Aad et al., *Performance of Missing Transverse Momentum Reconstruction in ATLAS with 2011 Proton-Proton Collisions at $\sqrt{s} = 7$ TeV*, Tech. Rep. ATLAS-CONF-2012-101, CERN, Geneva, Jul, 2012. 7.7
- [69] ATLAS Collaboration, G. Aad et al., *Measurement of the Inelastic Proton-Proton Cross-Section at $\sqrt{s} = 7$ TeV with the ATLAS Detector*, *Nature Commun.* **2** (2011) 463, [arXiv:1104.0326 \[hep-ex\]](https://arxiv.org/abs/1104.0326). 7.7.3.4
- [70] T. A. Collaboration, *Charged particle multiplicities in p p interactions at $\sqrt{s} = 0.9$ and 7 TeV in a diffractive limited phase-space measured with the ATLAS detector at the LHC and new PYTHIA6 tune*, Tech. Rep. ATLAS-CONF-2010-031, CERN, Geneva, Jul, 2010. 7.7.3.5

- [71] ATLAS Collaboration, G. Aad et al., *Measurement of the W^+W^- Cross Section in $\sqrt{s} = 7$ TeV pp Collisions with ATLAS*, *Phys. Rev. Lett.* **107** 041802. <http://link.aps.org/doi/10.1103/PhysRevLett.107.041802>. 8.1
- [72] ATLAS Collaboration, G. Aad et al., *Measurement of W^+W^- production in pp collisions at $\sqrt{s} = 7$ TeV with the ATLAS detector and limits on anomalous WWZ and $WW\gamma$ couplings*, [arXiv:1210.2979](https://arxiv.org/abs/1210.2979) [hep-ex]. 8.1
- [73] CMS Collaboration, S. Chatrchyan et al., *Measurement of W^+W^- and ZZ production cross sections in pp collisions at $\sqrt{s} = 8$ TeV*, *Phys.Lett.* **B721** (2013) 190–211, [arXiv:1301.4698](https://arxiv.org/abs/1301.4698) [hep-ex]. 8.1, 8.2
- [74] T. A. Collaboration, *Measurement of W -pair production in e^+e^- collisions at centre-of-mass energies from 183 to 209 GeV*, *The European Physical Journal C - Particles and Fields* **38** (2004) no. 2, 147–160. <http://dx.doi.org/10.1140/epjc/s2004-02048-3>. 8.1
- [75] F. Cossutti, *Measurement of the W pair production cross section and W branching ratios with the DELPHI detector*, *Int. J. Mod. Phys. A* **16** (2001) no. Suppl.1, 348–50. 8.1
- [76] M. Acciarri et al., *Measurement of W -pair cross sections in e^+e^- interactions at $\sqrt{s} = 172$ GeV and W -decay branching fractions*, *Physics Letters B* **407** (1997) no. 34, 419 – 431. <http://www.sciencedirect.com/science/article/pii/S0370269397008022>. 8.1
- [77] OPAL Collaboration, G. Abbiendi et al., *Measurement of the $e^+e^- \rightarrow W^+W^-$ cross section and W decay branching fractions at LEP*, *Eur.Phys.J.* **C52** (2007) 767–785, [arXiv:0708.1311](https://arxiv.org/abs/0708.1311) [hep-ex]. 8.1
- [78] CDF Collaboration, T. Aaltonen et al., *Measurement of the W^+W^- Production Cross Section and Search for Anomalous WW gamma and WWZ Couplings in p p -bar Collisions at $\sqrt{s} = 1.96$ TeV*, *Phys.Rev.Lett.* **104** (2010) 201801, [arXiv:0912.4500](https://arxiv.org/abs/0912.4500) [hep-ex]. 8.1
- [79] D0 Collaboration, V. Abazov et al., *Measurement of the WW production cross section with dilepton final states in p anti- p collisions at $\sqrt{s} = 1.96$ TeV and limits on anomalous trilinear gauge couplings*, *Phys.Rev.Lett.* **103** (2009) 191801, [arXiv:0904.0673](https://arxiv.org/abs/0904.0673) [hep-ex]. 8.1
- [80] S. Frixione and B. R. Webber, *Matching NLO QCD computations and parton shower simulations*, *JHEP* **0206** (2002) . 8.1.2, 8.2.2, 10.3
- [81] T. Binoth, M. Ciccolini, N. Kauer, M. Kramer, *Gluon-induced W -boson pair production at the LHC*, *JHEP* **0612** (2006) . 8.1.2
- [82] M. L. Mangano, M. Moretti, F. Piccinini, R. Pittau and A. D. Polosa, *ALPGEN, a generator for hard multiparton processes in hadronic collisions*, *JHEP* **0307** (2003) , [arXiv:hep-ph/0206293](https://arxiv.org/abs/hep-ph/0206293). 8.1.2, 8.2.2, 10.3
- [83] S. Agostinelli et al., *Geant4a simulation toolkit*, *Nuclear Instruments and Methods in Physics Research Section A: Accelerators, Spectrometers, Detectors and Associated Equipment* **506** (2003) no. 3, 250 – 303. <http://www.sciencedirect.com/science/article/pii/S0168900203013688>. 8.1.2, 8.2.2
- [84] Atlas Collaboration, G. Aad et al., *Measurement of the $W \rightarrow \ell\nu$ and $Z/\gamma^* \rightarrow \ell\ell$ production cross sections in proton-proton collisions at $\sqrt{s} = 7$ TeV with the ATLAS detector*, *JHEP* **1012** (2010) 060, [arXiv:1010.2130](https://arxiv.org/abs/1010.2130) [hep-ex]. 8.1.3.1
- [85] P. M. Nadolsky, H.-L. Lai, Q.-H. Cao, J. Huston, J. Pumplin, et al., *Implications of CTEQ global analysis for collider observables*, *Phys.Rev.* **D78** (2008) 013004, [arXiv:0802.0007](https://arxiv.org/abs/0802.0007) [hep-ph]. 8.1.5

- [86] T. A. Collaboration, *Updated Luminosity Determination in pp Collisions at $\sqrt{s}=7$ TeV using the ATLAS Detector*, Tech. Rep. ATLAS-CONF-2011-011, CERN, Geneva, Mar, 2011. [8.1.5](#)
- [87] G. Aad et al., *Measurement of ZZ production in pp collisions at $\sqrt{s} = 7$ TeV and limits on anomalous ZZZ and ZZ γ couplings with the ATLAS detector*, *Journal of High Energy Physics* **2013** (2013) no. 3, 1–48. <http://dx.doi.org/10.1007/JHEP03%282013%29128>. [8.2](#)
- [88] T. A. Collaboration, *Measurement of Z-pair production in e^+e^- collisions and constraints on anomalous neutral gauge couplings*, *Journal of High Energy Physics* **2009** (2009) no. 04, 124. <http://stacks.iop.org/1126-6708/2009/i=04/a=124>. [8.2](#)
- [89] L3 Collaboration, M. Acciarri et al., *Study of neutral current four fermion and Z Z production in e^+e^- collisions at $\sqrt{s} = 183$ GeV*, *Phys.Lett.* **B450** (1999) 281–293. [8.2](#)
- [90] L3 Collaboration, M. Acciarri et al., *Study of Z boson pair production in e^+e^- interactions at $\sqrt{s} = 192$ -GeV - 202-GeV*, *Phys.Lett.* **B497** (2001) 23–38, [arXiv:hep-ex/0010004 \[hep-ex\]](#). [8.2](#)
- [91] OPAL Collaboration, G. Abbiendi et al., *Study of Z pair production and anomalous couplings in e^+e^- collisions at \sqrt{s} between 190-GeV and 209-GeV*, *Eur.Phys.J.* **C32** (2003) 303–322, [arXiv:hep-ex/0310013 \[hep-ex\]](#). [8.2](#)
- [92] CDF Collaboration, T. Aaltonen et al., *Measurement of ZZ production in leptonic final states at \sqrt{s} of 1.96 TeV at CDF*, *Phys.Rev.Lett.* **108** (2012) 101801, [arXiv:1112.2978 \[hep-ex\]](#). [8.2](#)
- [93] D0 Collaboration, V. M. Abazov et al., *A measurement of the WZ and ZZ production cross sections using leptonic final states in 8.6 fb $^{-1}$ of $p\bar{p}$ collisions*, *Phys.Rev.* **D85** (2012) 112005, [arXiv:1201.5652 \[hep-ex\]](#). [8.2](#)
- [94] P. Nason, *A New method for combining NLO QCD with shower Monte Carlo algorithms*, *JHEP* **0411** (2004) 040, [arXiv:hep-ph/0409146](#). [8.2.2](#), [9.2.2](#), [10.3](#)
- [95] S. Frixione, P. Nason and C. Oleari, *Matching NLO QCD computations with Parton Shower simulations: the POWHEG method*, *JHEP* **0711** (2007) 070, [arXiv:0709.2092 \[hep-ph\]](#). [8.2.2](#), [9.2.2](#), [10.3](#)
- [96] S. Alioli, P. Nason, C. Oleari and E. Re, *A general framework for implementing NLO calculations in shower Monte Carlo programs: the POWHEG BOX*, *JHEP* **1006** (2010) 043, [arXiv:1002.2581 \[hep-ph\]](#). [8.2.2](#), [9.2.2](#), [10.3](#)
- [97] T. Gleisberg, S. Hoche, F. Krauss, M. Schonherr, S. Schumann, F. Siegert, and J. Winter, *Event generation with Sherpa 1.1*, *JHEP* **0902** (2009) 007, [arXiv:0811.4622 \[hep-ph\]](#). [8.2.2](#), [10.3](#)
- [98] G. Corcella, I. Knowles, G. Marchesini, S. Moretti, K. Odagiri, P. Richardson, M. Seymour, and B. Webber, *HERWIG 6.5*, *JHEP* **0101** (2001) 010, [arXiv:hep-ph/0011363](#). [8.2.2](#), [10.3](#)
- [99] J. Alwall, P. Demin, S. de Visscher, R. Frederix, M. Herquet, et al., *MadGraph/MadEvent v4: The New Web Generation*, *JHEP* **0709** (2007) 028, [arXiv:0706.2334 \[hep-ph\]](#). [8.2.2](#)
- [100] R. Frederix, S. Frixione, V. Hirschi, F. Maltoni, R. Pittau, et al., *Four-lepton production at hadron colliders: aMC@NLO predictions with theoretical uncertainties*, *JHEP* **1202** (2012) 099, [arXiv:1110.4738 \[hep-ph\]](#). [8.2.7](#)

- [101] T. Binoth, N. Kauer, and P. Mertsch, *Gluon-induced QCD corrections to $pp \rightarrow ZZ ; l$ anti- l prime anti- l prime*, [arXiv:0807.0024 \[hep-ph\]](#). [8.2.7](#)
- [102] U. Baur and D. L. Rainwater, *Probing neutral gauge boson selfinteractions in ZZ production at hadron colliders*, *Phys.Rev.* **D62** (2000) 113011, [arXiv:hep-ph/0008063 \[hep-ph\]](#). [8.2.9](#)
- [103] ALEPH, DELPHI, L3, OPAL, LEP Electroweak Working Group Collaboration, J. Alcaraz et al., *A Combination of preliminary electroweak measurements and constraints on the standard model*, [arXiv:hep-ex/0612034 \[hep-ex\]](#). [8.2.9](#)
- [104] D0 Collaboration, V. Abazov et al., *Search for ZZ and $Z\gamma^*$ production in $p\bar{p}$ collisions at $\sqrt{s} = 1.96$ TeV and limits on anomalous ZZZ and $ZZ\gamma^*$ couplings*, *Phys.Rev.Lett.* **100** (2008) 131801, [arXiv:0712.0599 \[hep-ex\]](#). [8.2.9](#)
- [105] ATLAS Collaboration, *Observation of a new particle in the search for the Standard Model Higgs boson with the ATLAS detector at the LHC*, *Phys. Lett.* **B716** (2012) 1–29, [arXiv:1207.7214 \[hep-ex\]](#). [9.1](#)
- [106] CMS Collaboration, *Observation of a new boson at a mass of 125 GeV with the CMS experiment at the LHC*, *Phys. Lett.* **B716** (2012) 30–61, [arXiv:1207.7235 \[hep-ex\]](#). [9.1](#)
- [107] T. A. Collaboration, *Study of the spin of the new boson with up to 25 fb⁻¹ of ATLAS data*, Tech. Rep. ATLAS-CONF-2013-040, CERN, Geneva, Apr, 2013. [9.1](#)
- [108] ATLAS Collaboration, G. Aad et al., *Search for the Standard Model Higgs boson in the $H \rightarrow WW^{(*)} \rightarrow \ell\nu\ell\nu$ decay mode with 4.7 /fb of ATLAS data at $\sqrt{s} = 7$ TeV*, *Phys.Lett.* **B716** (2012) 62–81, [arXiv:1206.0756 \[hep-ex\]](#). [9.2.1](#), [10](#)
- [109] T. A. Collaboration, *Measurements of the properties of the Higgs-like boson in the $WW^{(*)} \rightarrow \ell\nu\ell\nu$ decay channel with the ATLAS detector using 25 fb⁻¹ of proton-proton collision data*, Tech. Rep. ATLAS-CONF-2013-030, CERN, Geneva, Mar, 2013. [9.2.1](#)
- [110] CMS Collaboration, *Search for the standard model Higgs boson decaying to W^+W^- in the fully leptonic final state in pp collisions at $\sqrt{s} = 7$ TeV*, *Phys. Lett. B* **710** (2012) no. [arXiv:1202.1489](#). CMS-HIG-11-024. CERN-PH-EP-2012-018, 91–113. 35 p. [9.2.1](#)
- [111] T. C. Collaboration, *Evidence for a particle decaying to $W+W^-$ in the fully leptonic final state in a standard model Higgs boson search in pp collisions at the LHC*, Tech. Rep. CMS-PAS-HIG-13-003, CERN, Geneva, 2013. [9.2.1](#)
- [112] Tevatron New Physics Higgs Working Group, CDF, D0 Collaboration, C. Group, D. Collaborations, the Tevatron New Physics, and H. Working, *Updated Combination of CDF and D0 Searches for Standard Model Higgs Boson Production with up to 10.0 fb⁻¹ of Data*, [arXiv:1207.0449 \[hep-ex\]](#). [9.2.1](#)
- [113] LHC Higgs Cross Section Working Group Collaboration, S. Dittmaier et al., *Handbook of LHC Higgs Cross Sections: 1. Inclusive Observables*, [arXiv:1101.0593 \[hep-ph\]](#). [9.2.2](#)
- [114] ATLAS Collaboration, G. Aad et al., *Search for the Standard Model Higgs boson in the diphoton decay channel with 4.9 fb⁻¹ of pp collisions at $\sqrt{s} = 7$ TeV with ATLAS*, *Phys.Rev.Lett.* **108** (2012) 111803, [arXiv:1202.1414 \[hep-ex\]](#). [10](#)
- [115] ATLAS Collaboration, G. Aad et al., *Search for the Standard Model Higgs boson in the decay channel $H \rightarrow ZZ^{(*)} \rightarrow 4\ell$ with 4.8 fb⁻¹ of pp collision data at $\sqrt{s} = 7$ TeV with ATLAS*, *Phys.Lett.* **B710** (2012) 383–402, [arXiv:1202.1415 \[hep-ex\]](#). [10](#)

- [116] ATLAS Collaboration, G. Aad et al., *Search for the Standard Model Higgs boson in the H to $\tau^+\tau^-$ decay mode in $\sqrt{s} = 7$ TeV pp collisions with ATLAS*, *JHEP* **1209** (2012) 070, [arXiv:1206.5971 \[hep-ex\]](#). [10](#)
- [117] ATLAS Collaboration, G. Aad et al., *Search for the Standard Model Higgs boson produced in association with a vector boson and decaying to a b -quark pair with the ATLAS detector*, *Phys.Lett.* **B718** (2012) 369–390, [arXiv:1207.0210 \[hep-ex\]](#). [10](#)
- [118] *The ATLAS Collaboration*, Tech. Rep. ATLAS-CONF-2013-011, CERN, Geneva, Mar, 2013. [10](#)
- [119] *The CMS Collaboration*, Tech. Rep. CMS-PAS-HIG-13-018, CERN, Geneva, 2013. [10](#)
- [120] B. P. Kersevan and E. Richter-Was, *The Monte Carlo event generator AcerMC versions 2.0 to 3.8 with interfaces to PYTHIA 6.4, HERWIG 6.5 and ARIADNE 4.1*, *Computer Physics Communications* **184** (2013) no. 3, 919 – 985. [10.3](#)
- [121] T. Sjostrand, S. Mrenna and P. Z. Skands, *PYTHIA 6.4 Physics and Manual*, *JHEP* **0605** (2006) 026, [arXiv:hep-ph/0603175](#). [10.3](#)
- [122] A. L. Read, *Presentation of search results: the CL_s technique*, *Journal of Physics G: Nuclear and Particle Physics* **28** (2002) no. 10, 2693. <http://stacks.iop.org/0954-3899/28/i=10/a=313>. [10.7](#)
- [123] T. A. Collaboration, *Evidence for prompt photon production in $p p$ collisions at $\sqrt{s} = 7$ TeV with the ATLAS detector*, Tech. Rep. ATLAS-CONF-2010-077, CERN, Geneva, Jul, 2010. [11.4](#), [11.3.6](#)
- [124] ATLAS Collaboration, G. Aad et al., *Measurement of the inclusive isolated prompt photon cross section in pp collisions at $\sqrt{s} = 7$ TeV with the ATLAS detector*, *Phys.Rev.* **D83** (2011) 052005, [arXiv:1012.4389 \[hep-ex\]](#). [11.3.12](#)
- [125] M. Hance and H. H. Williams, *Measurement of Inclusive Isolated Prompt Photon Production in Proton-Proton Collisions at $\sqrt{s} = 7$ TeV with the ATLAS Detector*. PhD thesis, Pennsylvania U., Philadelphia, 2011. Presented 11 Jul 2011. [11.3.12](#)